

On the Myelin-Axon Interaction

Structural Studies of Myelin-Associated Glycoprotein,
Olfactomedin-1 and the Nogo Receptor

Matti F. Pronker

Voor mijn ouders

Committee:
Prof.dr. M. Baldus
Prof.dr. J.A. Killian
Prof.dr. F. Förster
Prof.dr. R.J. Pasterkamp
Prof.dr. A.B. Smit

On the Myelin-Axon Interaction

Structural Studies of Myelin-Associated Glycoprotein, Olfactomedin-1 and the Nogo Receptor

Over de Myeline-Axon Interactie
Structurele Studies van Myeline-Geassocieerd Glycoproteïne,
Olfactomedin-1 en de Nogo Receptor
(met een samenvatting in het Nederlands)

Proefschrift

ter verkrijging van de graad van doctor aan de Universiteit Utrecht op gezag van
de rector magnificus, prof.dr. G.J. van der Zwaan, ingevolge het besluit van het
college voor promoties in het openbaar te verdedigen op dinsdag 5 april 2017
des ochtends te 10.30 uur

door

Matti Feije Pronker

geboren op 15 juni 1989,
te Leiderdorp

Matti F. Pronker

On the Myelin-Axon Interaction – Structural Studies of Myelin-Associated
Glycoprotein, Olfactomedin-1 and the Nogo Receptor Dissertation, Utrecht
University, The Netherlands

The research described in this dissertation was performed from 2012-2016 in the
Crystal and Structural Chemistry section, Bijvoet Center for Biomolecular Research,
Department of Chemistry, Faculty of Science, Utrecht University, The Netherlands
ISBN: 978-94-6295-620-9

Cover design by: Matti F. Pronker

Printed by: ProefschriftMaken on FSC-certified paper

Promotor: Prof.dr. P. Gros
Co-promotor: Dr. B.J.C. Janssen

Table of Contents:

Chapter 1	
General introduction	7
Chapter 2	
Structural basis of myelin-associated glycoprotein adhesion and signaling	29
Chapter 3	
Nogo Receptor crystal structures with correct disulfide pattern suggest a novel mode of self-interaction	81
Chapter 4	
Olfactomedin-1 has a V-shaped disulfide-linked tetrameric structure	107
Chapter 5	
General discussion	131
English Summary	148
Nederlandse samenvatting	150
Dankwoord	153
Curriculum Vitae	156
List of abbreviations	157

Dit proefschrift werd mogelijk gemaakt met financiële steun van de Nederlandse organisatie voor Wetenschappelijk Onderzoek (NWO), gebied Chemische Wetenschappen.

Chapter 1

General introduction

Matti F. Pronker

The nervous system

The nervous system of vertebrates consists of the central nervous system (CNS; brain, spinal cord, optic nerves and retina) and the peripheral nervous system (PNS; all other nerves). In the nervous system, specialized cells called neurons form connections with other neurons to form functional circuits. These connections between neurons are called synapses, where neurons transmit electric signals to other neurons. The electrochemical signals that travel through neurons are called actions potentials, which can either activate or inhibit signaling in the post-synaptic target neuron.

The processes that sprout from the cell body of the neuron and branch out to form these connections are called neurites, of which there are two types: dendrites and axons. A neuron can have many dendrites to receive signals from other neurons, but has only one axon to generate an output signal. During early neuronal development, the axon has not yet specialized and therefore all processes sprouting from neurons are referred to as neurites. Both axon and dendrites can each form many synapses to establish functional circuitry^{1,2}.

Apart from neurons, the nervous system comprises glial cells that support the neurons in their function. The four types of glia are myelin cells (Schwann cells in the PNS, oligodendrocytes in the CNS), astrocytes, microglia (macrophage-like cells of the CNS) and ependymal cells (epithelial cells of the ventricular system of the CNS)^{1,2}. Myelination by Schwann cells or oligodendrocytes provides enhanced conductance velocity, a decrease in the electrical capacitance, electrical insulation, physical protection and metabolic support of long axons³. Whereas Schwann cells individually wrap around a segment of axon, a single oligodendrocyte can sprout multiple processes that each wrap around a segment of axon. These processes resemble individual Schwann cells and can enwrap the same or different axons. The gaps in between these Schwann cells or oligodendrocyte processes are known as the nodes of Ranvier. The primary myelin-axon interface enclosed by these nodes of Ranvier is known as the internode, whereas the sections bordering the node of Ranvier are called paranode and juxtaparanode (paranode being the closest to the node of Ranvier, see fig. 1)³. The high lipid content of myelin cells gives myelinated tissue a white appearance, hence the term white matter. Grey matter on the other hand consists mostly of the cell bodies of neurons and astrocytes, rather than myelinated axons^{1,2}.

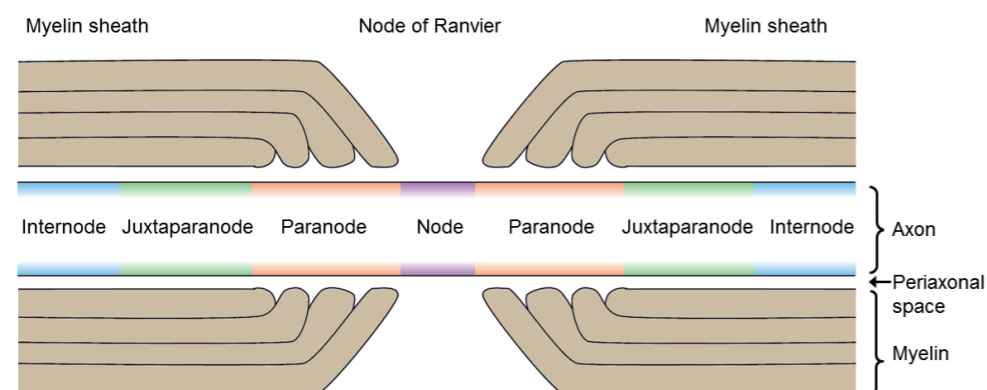


Figure 1: Overview of myelin domains

Slice through a myelinated axon, indicating the different regions around a node of Ranvier, as well as the periaxonal space.

Nervous system regeneration upon injury

Damage of the nervous system by injury or disease can be very debilitating if not deadly. However, neurons have regenerative capacity and are plastic by nature to allow learning⁴. Neurons can sprout new neurites to form alternative connections and if an axon is cut, an axonal growth cone can be formed that extends to new target neurons to restore circuitry⁴. Whereas regeneration in the PNS can be robust⁵, regeneration in the adult CNS is generally very limited^{4,6}. Physical damage to the CNS (e.g. spinal cord or brain injury) causes the formation of a glial scar at the site of injury, containing myelin debris, reactive astrocytes, microglia and extracellular matrix components⁷. Molecules present at this glial scar inhibit neurite outgrowth and induce collapse of axonal growth cones⁷. In particular, molecules expressed by oligodendrocytes were found to inhibit plasticity and regeneration⁸⁻¹⁰. Often, these molecules are also involved in guiding axons and neurites to their targets during early development of the nervous system⁴. However, in case of injury, they pose barriers that limit the capacity of neurons to regenerate⁴. Interfering with this signaling could be an approach to stimulate regeneration and enhance recovery after CNS injury.

Apart from external factors that influence the plasticity of neurons, intrinsic neuronal signaling mechanisms have been recognized that limit the regeneration potential of adult neurons even if all external factors are removed (e.g. the presence of certain transcription factors required for synthesis of proteins involved in regeneration processes)¹¹. However, in this work, I will focus on external guidance cues and more specifically, the myelin-associated inhibitors of regeneration and their signaling through the central Nogo Receptor (NgR).

Myelin-associated inhibitors of regeneration: MAG, Nogo and OMgp

Three myelin-expressed proteins were identified as having regeneration-inhibiting properties, called myelin-associated inhibitors of regeneration (MAIs). Myelin-associated glycoprotein (MAG; also known as Siglec4a) is a myelin-expressed cell adhesion molecule normally expressed at the axon-myelin interface along the internode. It is a type 1 single-pass transmembrane protein with an extracellular segment comprising five immunoglobulin-(Ig)-like domains. Recombinantly-expressed extracellular domain of MAG was found to inhibit neurite outgrowth and immuno-depletion of MAG from an inhibitory fraction of CNS myelin protein restored neurite outgrowth on that myelin substrate¹². Simultaneously, another lab identified MAG as a MAI by showing that neurite outgrowth was reduced when neurons were grown on a support of MAG-expressing COS-7 cells as compared to controls¹³.

Later, the myelin-expressed protein Nogo, also known as Reticulon-4, was found to inhibit neurite outgrowth similar to MAG^{14,15}. Three different isoforms of Nogo, known as Nogo-A, Nogo-B and Nogo-C share a sequence of 66 amino acids that is responsible for neurite outgrowth inhibition. This sequence, known as Nogo66, is flanked by two transmembrane helices and exposed to the extracellular side of the plasma membrane¹⁴. Nogo-A, -B and -C have been reported to form a heteromeric complex on the cell surface¹⁶.

Thirdly, Oligodendrocyte myelin glycoprotein (OMgp) was found to have a similar neurite outgrowth-inhibiting effect as MAG and Nogo66^{17,18}. OMgp is predicted to consist of an N-terminal leucine-rich repeat (LRR) domain followed by a glycosylated stalk and a glycosylphosphatidylinositol (GPI)-anchoring sequence^{17,18}. Interestingly, OMgp is expressed by oligodendrocytes as well as neurons¹⁹. OMgp was later found to also bind MAG²⁰, but it remains unclear whether this interaction happens *in cis* or *in trans*.

In short, the three myelin proteins MAG, Nogo and OMgp were identified as inhibitory molecules towards regeneration. These three MAIs are all expressed at the oligodendrocyte plasma membrane yet they are structurally and topologically dissimilar, as MAG is a type 1 single-pass transmembrane protein, Nogo has two membrane-spanning helices enclosing an extracellular domain and OMgp is GPI-anchored, thus lacks an intracellular domain (Fig. 2).

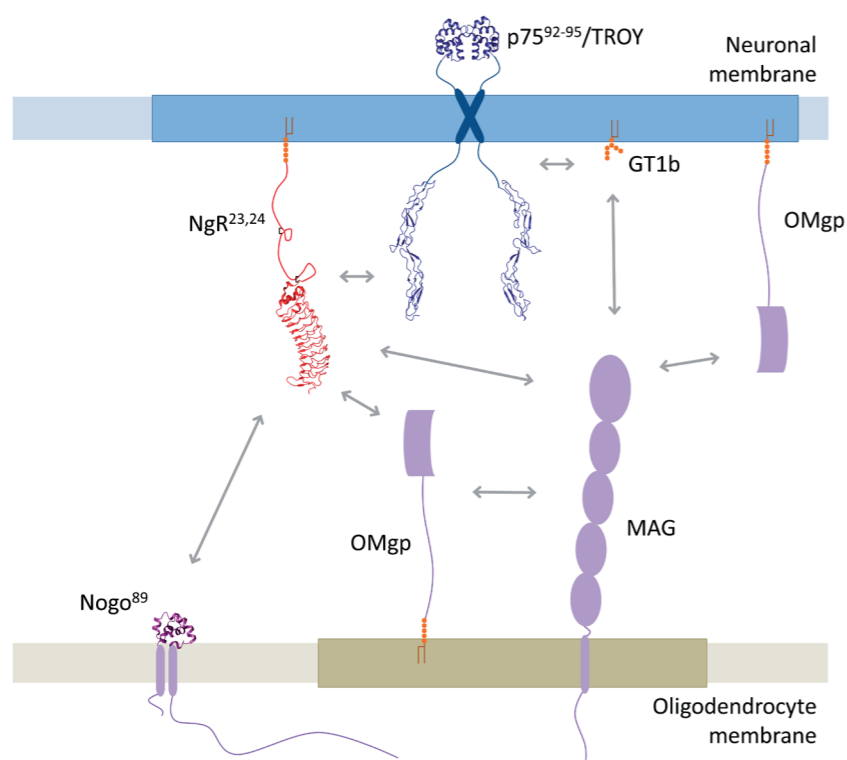


Figure 2: Overview of MAI interactions at the neuronal cell surface

Coloring is the same as in table 1; MAIs are represented in purple, the receptor NgR in red, co-receptors in blue and carbohydrates are orange. Previously-reported interactions are represented by grey arrows and lipid rafts are indicated as thicker and darker patches of membrane. Two disulfides, in the NgR glycosylated stalk and C-terminal LRR capping domain, are represented in black²⁵. When possible, structures were used to represent the proteins. For p75/TROY, structures of p75 are shown.

MAI receptors

MAG, Nogo66 and OMgp have completely different folds and share no sequence homology. Remarkably, these three MAIs were found to signal via a common receptor known as NgR^{18,21,22} (Fig. 2). NgR mediates both neurite outgrowth inhibition and axonal growth cone collapse elicited by all three MAIs^{18,21,22}. NgR is expressed on the neuronal plasma membrane and comprises an N-terminal LRR domain^{23,24}, followed by a glycosylated stalk and a C-terminal GPI-anchoring sequence²⁵. All three MAIs bind to the N-terminal LRR domain of NgR^{22,23,26-30}, rather than the membrane-proximal glycosylated stalk³¹. Furthermore, NgR can self-associate, also via its LRR domain^{23,27,32}.

Table 1: Overview of molecules involved in MAI signaling

Protein name	Cell-type	Intracellular domain?	Reported interactions:	Structures:
MAIs:				
MAG	myelin cells	yes	NgR, NgR2, PirB, LRP1, GT1b, p75, β 1-integrins, OMgp	
Nogo66	myelin cells	yes	NgR, PirB	2KO2
OMgp	myelin cells, neurons	no	NgR, MAG	
Other ligands:				
CSPGs	secreted, astrocytes, neurons	yes/no	NgR, NgR3	4CM4, 2C4S
BlyS	secreted, neurons	yes/no	NgR	1KXG, 3V56, 1JH5, 1OQD, 1OQE, 1KD7, 4V46, 4ZCH
(Co-)Receptors:				
NgR	neurons	no	MAG, Nogo66, OMgp, CSPGs, BlyS, LIG1, LOTUS, Olfm1, p75, TROY, LINGO-1, AMIGO3, GT1b	1OZN, 1P8T, 3KJ4
NgR2	neurons	no	MAG	4P91, 4P8S
NgR3	neurons	no	CSPGs	
PirB	neurons	yes	MAG, Nogo66, p75	4LLA, 2DYP
LRP1	neurons	yes	MAG, p75	
β 1-integrins	neurons	yes	MAG	4WK0, 4WK2, 4WK4, 4WJK
p75	neurons	yes	MAG, NgR, PirB, LRP1, GT1b, (LINGO-1)	1SG1, 3BUK, 1NGR, 4F42, 4F44, 2MIC, 2MJO, 2N80, 2N83, 2N97, 3IJ2
TROY	neurons	yes	NgR, AMIGO3, (LINGO-1)	
LINGO-1	neurons	yes	NgR, GT1b, (p75, TROY)	2ID5, 4OQT
AMIGO3	neurons	yes	NgR, p75, TROY	
GT1b ganglioside	neurons	no	MAG, NgR, p75, LINGO-1	
Antagonists:				
LIG1	secreted	no	NgR	
LOTUS	secreted, neurons	no	NgR	
Olfm1	secreted	no	NgR, LINGO-1	

A dimerized soluble construct of the NgR LRR could block the inhibitory effects on regeneration of CNS myelin, MAG and Nogo66^{22,27}. However, the stalk and GPI anchor of NgR are required for efficient signal transduction²⁷.

Knockout of NgR in mice resulted in a rather modest increase in regeneration potential^{33,34}. This led to the discovery of Paired Ig receptor B (PirB; also known as LILRB2 in humans) as a functional receptor for both MAG and Nogo66, mediating neurite outgrowth inhibition and axonal growth cone collapse³⁵.

Apart from NgR and PirB, several other receptors were found to be capable of mediating the neurite outgrowth inhibition signaling specifically by MAG. The NgR paralog NgR2 was found to be a functional substitute for NgR as a MAG receptor, but did not bind Nogo66^{28,36}. Low-density lipoprotein receptor-related protein-1 (LRP1) was also found to be a receptor for neurite-outgrowth inhibition by MAG³⁷. Finally, β 1-integrins were found to mediate MAG-dependent axonal growth cone-turning responses, whereas repulsion by OMgp was not affected by β 1-integrin function³⁸.

Summarizing, NgR is a receptor for all three MAIs and PirB for both MAG and Nogo66. NgR2, LRP1 and β 1-integrins have been identified as functional regeneration-inhibition signaling receptors only for MAG.

Co-receptors

NgR is a GPI-anchored protein and thus lacks an intracellular domain, so it cannot transduce the signal across the membrane by itself. Several neuronal co-receptors were found to be involved in the transduction of MAI signaling through the neuronal plasma membrane. The tumor-necrosis factor receptor superfamily member p75 (also known as p75-ntr; p75 neurotrophin receptor) was identified as a co-receptor for all three MAIs³⁹⁻⁴¹ (Fig. 2). p75 is also involved in neuronal growth factor signaling and has an intracellular death domain (DD)⁴².

LRR and Ig-like domain-containing NgR-interacting protein 1 (LINGO-1) is a co-receptor that can mediate MAI signal transduction in a reconstituted system of non-neuronal COS-7 cells, when co-transfected with NgR and p75⁴³. TROY, like p75, is a member of the tumor-necrosis factor receptor superfamily. It is more widely expressed in the adult CNS than p75 and can substitute for p75 in the NgR/LINGO-1 receptor complex^{44,45}.

The widely held view^{4,46,47} of LINGO-1 as a co-receptor in a ternary complex with NgR and p75 at the plasma membrane has been disputed. Full-length (FL) LINGO-1 was found to predominantly reside in secretory or endosomal compartments, instead of at the plasma membrane. Moreover, LINGO-1 and NgR compete for p75-binding⁴⁸. These results suggest that these proteins are involved in sequential interactions, rather

than forming a trimeric complex. More recently, the amphoterin-induced gene and open reading frame 3 (AMIGO3) was identified as another possible co-receptor that forms complexes together with NgR and either p75 or TROY⁴⁹.

The alternative MAG and Nogo66 receptor PirB also relies on p75 as a co-receptor for signal transduction into the neuron⁵⁰. Furthermore, for the alternative MAG receptor LRP1 it was demonstrated that p75 acts as a co-receptor for MAG signaling⁵¹.

Concluding, either p75 or TROY (depending on the type of neuron) and possibly AMIGO3 are the most important co-receptors for signal transduction of MAIs at the neuronal plasma membrane, whereas LINGO-1 might play a role further downstream in signal transduction (Fig. 2).

Intracellular downstream effectors

Whereas the MAIs are extracellular, the effectors mediating the neuronal response to these cues act in the neuronal cytosol. Several downstream effectors have been identified that are responsible for intracellular signal transduction culminating in altered cytoskeleton dynamics. Whereas NgR and GT1b gangliosides do not have an intracellular domain, PirB, p75, TROY, LINGO-1 and AMIGO3 do. In particular, the intracellular DD of p75 is held responsible for signal transduction of MAIs.

Ras homolog gene family member A (RhoA) is a member of a family of small GTPases that function as molecular switches, being in either GTP- (active) or GDP-bound (inactive) states. RhoA is a downstream effector of p75 and association with its DD leads to an increase of GTP-bound RhoA^{41,52,53}. RhoA functions downstream of MAIs, since stimulation of neurons with MAIs results in RhoA activation⁵⁴.

Activation of RhoA is mediated by Rho GDP dissociation inhibitor (RhoGDI), a protein that directly binds both the DD of p75 and to RhoA^{53,55}. Association of RhoGDI with the p75 DD reduces its affinity for RhoA via an allosteric mechanism⁵³. RhoGDI prevents nucleotide exchange and membrane association of RhoA, thereby keeping RhoA in a silent signaling state. Binding of RhoGDI to the DD of p75 allows RhoA to dissociate from RhoGDI, associate with the membrane and with Rho GDP/GTP exchange factors (RhoGEFs). These RhoGEFs allow RhoA-bound GDP to exchange for GTP, thus activating RhoA^{53,55,56}. More recently, the alternative co-receptor TROY, that can substitute for p75 in MAI signaling^{44,45}, was shown to bind to RhoGDI with its intracellular domain and could activate RhoA, similar to p75⁵⁷.

Once in the GTP-bound state, RhoA can activate Rho-associated, coiled-coil-containing protein kinase (ROCK)^{58,59}. ROCK is recognized as a master regulator of cytoskeleton dynamics in different cell types, phosphorylating a wide variety of cytoskeletal proteins and regulators upon activation⁶⁰ (e.g. myosin light chain, tau, neurofilaments and LIM

kinase 1, which phosphorylates the actin depolymerization factor cofilin^{60,61}). ROCK functions downstream in the MAI signal transduction cascade, as pharmacological inhibition of ROCK promotes neurite outgrowth in the presence of MAIs^{56,62,63}.

Although many other proteins have been implicated in the downstream signaling of MAIs, a signaling axis of direct interactions can be formed from the intracellular domains of p75 and TROY to RhoGDI, RhoA and ROCK, a master regulator of cytoskeleton dynamics capable of modulating local neuronal morphology and plasticity⁶⁰.

GT1b as a MAG receptor and a role for lipid rafts in MAI signal transduction

Before its identification as a MAI, MAG was primarily known for being the principal cell adhesion molecule at the myelin-axon interface along the internode⁶⁴. It was found to establish myelin-axon contacts by binding to axonal glycosphingolipids called gangliosides⁶⁵. With its N-terminal V-type Ig domain it specifically recognizes certain sialylated gangliosides, most notably the major brain gangliosides GT1b and GD1a⁶⁶. Before NgR was identified as a MAG receptor, these gangliosides were investigated as possible receptors for MAG's regeneration-inhibiting properties⁶⁷. Pre-incubating MAG with gangliosides or mutating the ganglioside binding site alleviates the neurite outgrowth-inhibiting effects of MAG⁶⁷. Moreover, GalNAcT knockout mice that cannot biosynthesize complex gangliosides like GD1a and GT1b were insensitive to MAG-mediated neurite outgrowth inhibition^{68,69}.

Both gangliosides and GPI-anchored proteins are known to reside preferentially in lipid rafts⁷⁰. Indeed, both NgR and GT1b associate with lipid rafts⁷¹⁻⁷³. During MAG signaling lipid rafts play a double role. Apart from myelin-to-axon signaling, MAG also engages in axon-to-myelin signaling to regulate processes during early myelination involving the non-receptor tyrosine kinase Fyn⁷⁴. Fyn kinase is a member of the Src family and is myristoylated and palmitoylated at the N-terminus. Fyn kinase activation is associated with lipid raft localization⁷⁵. MAG was also shown to reside in lipid rafts in myelin cells and to bind exclusively to neuronal lipid raft fractions of membranes containing NgR and GT1b gangliosides⁷⁶. These results suggest that both on the myelin membrane and on the axonal membrane, lipid rafts play a role to mediate bidirectional MAG signaling⁷⁶.

More evidence for GT1b ganglioside involvement in MAG-dependent regeneration inhibition came from studies involving p75. A sodium dodecyl sulfate (SDS)-resistant interaction between p75 and GT1b ganglioside was found⁴¹. Also, the downstream cytosolic signaling protein RhoA can be prenylated and recruited to lipid rafts⁷⁷. GT1b was shown to partially co-localize with p75 and RhoA on cultured neurons⁷⁶. In another study, NgR and p75 were also found to co-localize in lipid raft fractions derived from

brain tissue, in which NgR was shown to interact with p75⁷³.

Both Nogo66-dependent RhoA activation and MAG- and Nogo-dependent axonal growth cone collapse were abolished by treatment of the neurons with the cholesterol-sequestering agent β -methylcyclodextrin^{72,73}. Moreover, stimulation with a dimerized soluble MAG construct or a Nogo peptide was shown to recruit p75 to lipid rafts⁷². Even antibodies to GD1a or GT1b gangliosides could recruit p75 to lipid rafts^{67,68,72}, suggesting that p75 interacts with these gangliosides. These results suggest that recruitment of co-receptors such as p75 to lipid rafts may play an important role in MAI signaling.

Other inhibitors of regeneration signaling via NgR

Although chondroitin sulfate proteoglycans (CSPGs) are not myelin-associated, they inhibit neurite outgrowth and regeneration in the CNS and were found to signal through NgR⁷⁸. CSPGs are proteoglycans decorated with long linear chondroitin sulfate glycosaminoglycan chains, made up of alternating repeating units of β -glucuronic acid and N-acetylgalactosamine. Upon injury, secretion (e.g. by reactive astrocytes) of different CSPGs, such as neurocan, NG2, versican, brevican and phosphacan is increased⁷⁹⁻⁸⁷. The glycosaminoglycan chains of CSPGs bind to both NgR and its paralog NgR3, via a positively-charged segment in the membrane-proximal stalks of NgR and NgR3. Combined knockout of NgR and NgR3 showed improved axonal regeneration upon injury, which could be enhanced even further when combined with knockout of Rptp σ , another known receptor for CSPGs⁷⁸.

B lymphocyte stimulator (BlyS) is an additional inhibitor of regeneration that is not myelin-associated yet signals through NgR⁸⁸. BlyS is a homotrimeric protein from the tumor necrosis factor family that exists as both a membrane-bound and a secreted form. BlyS is expressed at spinal cord injury sites, collapses axonal growth cones and inhibits neurite outgrowth. Regeneration inhibition by BlyS was shown to be mediated by NgR, similar to the MAIs⁸⁸.

Summarizing, CSPGs and BlyS are non-myelin-associated inhibitors of regeneration that signal through NgR. Whether their signal transduction through the membrane relies on p75/TROY or LINGO-1/AMIGO3 as for MAIs remains to be determined.

Structures of MAIs and their (co-)receptors provide insights into signaling mechanisms

Although many insights into MAI signaling were gained by neurobiology and molecular biology studies, the exact mechanisms of signal transduction are still not completely understood. Structural data are available for different MAIs and their (co-)receptors, providing additional clues for determining the signaling mechanisms.

Nogo66 was studied by NMR without the flanking transmembrane helices. Only in a salt-free solution of pure water and upon addition of the detergent dodecylphosphocholine (DPC), the 66-residue construct adopts a defined α -helical structure⁸⁹. This could be explained by the fact that Nogo66 is normally partly embedded in the membrane. Indeed, the structure revealed a large fraction of surface-exposed hydrophobic sidechains⁸⁹. It was described later that DPC also specifically stabilizes Nogo66, as the choline head forms a stabilizing salt-bridge with a buried glutamate sidechain⁹⁰. In its native environment, phosphocholine heads that are part of phosphatidylcholine phospholipids likely stabilize the Nogo66 fold⁹⁰.

The structure of the LRR domain of NgR, which is responsible for MAI binding as well as for self-association, was solved by X-ray crystallography by two groups independently (Fig. 3)^{23,24}. However, a later study revealed that both groups used a domain truncation that results in an artificial disulfide pattern in the C-terminal capping domain²⁵. Extensive site-directed mutagenesis studies, as well as evolutionary conservation of surface residues suggest that it is the concave rather than the convex surface of the NgR LRR that is responsible for binding to MAG, Nogo66, OMgp and LINGO-1^{20,23,24}. The structure of the LRR domain of NgR2 was also solved, showing a similar LRR fold as NgR, but with different surface residues, which may explain the different ligand specificities of these paralogs⁹¹.

The structure of the four consecutive N-terminal cysteine-rich domains of p75 was determined in complex with different neurotrophin ligands^{92,93}. Also, the structure of the intracellular DD of p75 was solved⁹⁴, and shown to have a propensity to dimerize⁹⁵. It was shown that p75 forms disulfide-linked dimers via a cysteine in the transmembrane region⁹⁶⁻⁹⁸. The intracellular dimeric DDs of p75 are separated if the extracellular cysteine-rich domains of p75 are dimerized by dimeric neurotrophins, possibly by a scissoring mechanism^{53,96,97}. NgR preferentially binds to dimeric p75 in the conformation with associating intracellular DDs⁹⁸, as opposed to the neurotrophin-bound conformation. Interestingly, TROY also has a cysteine in its transmembrane helix at a similar depth in the membrane, suggesting it might undergo similar mechanisms. However, MAG could still signal into non-neuronal COS-7 cells expressing NgR, LINGO-1 and p75 lacking this cysteine, although RhoA activation was not as pronounced as with *wildtype* (WT) p75⁹⁶. Crystal structures were also solved for the LRR and Ig-like domains of LINGO-1, which constitute most of the extracellular region⁹⁹. LINGO-1 crystallized as a tetramer with its C-termini oriented in the same direction. This tetramer was confirmed in solution,

suggesting it could also form on a cell surface⁹⁹. Although the structure of the extracellular domain of AMIGO3 was never solved, crystal structures of the LRR and Ig domains of its paralog AMIGO1 (39% sequence identity) were solved¹⁰⁰. AMIGO1 crystallized as a dimer that was confirmed in solution by small-angle X-ray scattering (SAXS). SAXS was also used to show that AMIGO3 forms dimers with a similar arrangement¹⁰⁰.

Crystal structures of the non-myelin-associated inhibitor of regeneration BlyS show that it forms homotrimers^{101,102}. In its membrane-detached form, these trimers can further assemble into icosahedral 60-mers^{103,104}, suggesting a potential to cluster cell surface receptors like NgR.

These structures have informed on the organization of the folded domains of several MAI signaling components (Fig. 2 and 3). In addition, many crystal structures are available for integrins, including β 1-type integrins¹⁰⁵ and several truncation constructs of double Ig domains of the human PirB ortholog LILRB2 have been solved^{106,107}. However, a detailed discussion of the integrin and PirB receptor structures goes beyond the scope of this thesis. Instead of those receptors, I will focus on signaling via the NgR receptor complex in this thesis.

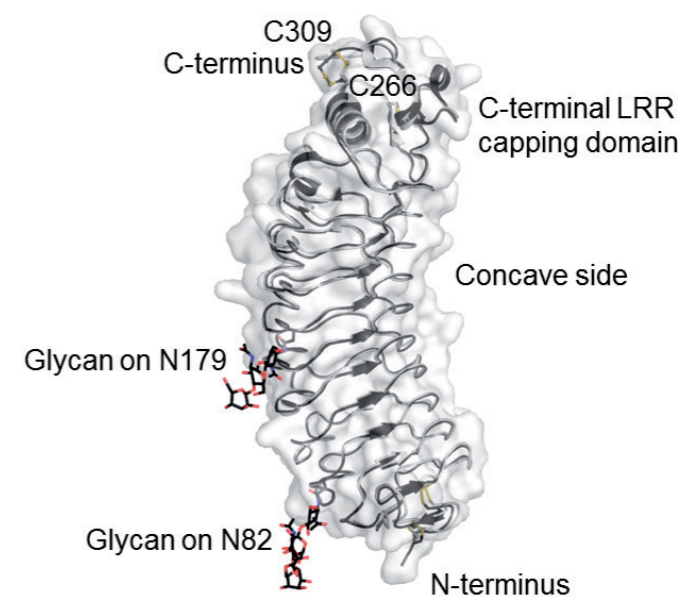


Figure 3: Previously-published structures of NgR

The two previously-published NgR structures are aligned and overlaid, 1OZN²⁴ in black and 1P8T²³ in white. Disulfides and glycans are represented as sticks, the artificial C266-C309 disulfide as thicker ball-and-sticks.

Physiological function of MAI signaling

Considering their negative effects on regeneration upon injury, one could wonder why vertebrates have evolved this signaling pathway. In other words, what could be the physiological function of MAI signaling?

Early brain development is characterized by critical periods in which certain neuronal circuitry is plastic and has the ability to rewire¹⁰⁸. One classic example is the period in which ocular dominance is still plastic^{108,109}. NgR knockout mice have severely extended periods in which ocular dominance could be altered, suggesting that signaling via NgR negatively regulates plasticity to consolidate neuronal circuitry involved in ocular dominance^{110,111}. Interestingly, knockout of the alternative MAI receptor PirB leads to a similar increase of the period of ocular dominance plasticity¹¹².

Apart from axonal growth cone collapse and neurite outgrowth inhibition, signaling through NgR regulates synapse formation and determines synaptic strength, processes that are connected with memory and learning. Knockout studies of NgR show it controls dendritic spine morphology and negatively regulates activity-dependent synaptic plasticity^{113,114}. Further studies have revealed that genetic ablation of NgR does not affect synaptic anatomy in adolescent mice, when it is still very plastic. However, in adult mice adolescent-like anatomical plasticity could be restored by conditional knockout of NgR¹¹⁵. Knockout of NgR also resulted in enhanced generation of dendritic spines upon sensory stimulation in adult mice compared to *WT*¹¹⁶.

Overexpression of NgR in mice forebrain neurons leads to impaired long-term (months) memory, whereas short-term memory was unaffected¹¹⁷. A role in memory was further strengthened by NgR knockout studies that compared the erasure of fear memories in adult and juvenile mice. A role for NgR in preventing erasure of these fear memories was found in adult mice, whereas juveniles could successfully erase fear memories upon extinction training in both *WT* and knockout mice¹¹⁵.

As signaling through NgR reduces neuronal plasticity by collapsing axonal growth cones, inhibiting neurite outgrowth and sprouting, but also inhibiting dendritic spine generation and synaptic plasticity, the general consensus is that NgR signaling complexes function as receptors for external cues that reduce plasticity to consolidate neuronal circuitry in the adult nervous system^{118,119}.

Antagonists of MAI signaling

Since MAI signaling is thought to negatively regulate neuronal plasticity, the existence of positive regulators to balance out this signaling is expected. Three proteins have been identified that antagonize the regeneration inhibition by the MAIs by specifically

interfering with their signaling.

Olfactomedin-1 (Olfm1), also known as Noelin or Pancortin, binds to NgR and suppresses MAI-dependent axonal growth cone collapse¹²⁰. Olfm1 is a secreted glycoprotein expressed in the nervous system^{121,122}. Different Olfm1 isoforms play varying roles in nervous system development^{121,122}. Olfm1 is a member of the Olfactomedin (Olf) superfamily that share an Olfactomedin domain^{123,124}. For Olfm1, this domain is close to its C-terminus and it is preceded by a coiled-coil domain and an N-terminal domain that is found in several Olf family members^{123,124}. Olfm1 was found to covalently self-associate via its cysteines, but the exact oligomeric state has not been reported^{125,126}. Olfm1 does not compete directly with MAIs for NgR-binding, but rather competes with binding of the co-receptors p75 and LINGO-1 to NgR. Interestingly, Olfm1 also binds LINGO-1, but not p75¹²⁰.

Leucine-rich glioma inactivated 1 (LGI1) is a secreted protein that does not influence neurite outgrowth by itself, but enhances neurite outgrowth on an inhibitory myelin support. It binds to NgR and competes with Nogo66 binding to NgR, thereby preventing Nogo66-dependent neurite outgrowth inhibition¹²⁷. Similar to Olfm1, LGI1 has been shown to be involved in brain development¹²⁸.

Lateral olfactory tract usher substance (LOTUS), also known as cartilage acidic protein-1B, was identified as an NgR ligand important for neural circuit formation in the lateral olfactory tract. It is also secreted and like LGI1, LOTUS competes with Nogo66 for NgR binding. It prevents Nogo66-dependent axonal growth cone collapse¹²⁹. LOTUS also competes with MAG and OMgp for NgR binding and suppresses axonal growth cone collapse by these two NgR ligands¹³⁰.

Summarizing, the secreted NgR ligands Olfm1, LGI1 and LOTUS antagonize MAI signaling either by direct competition (LGI1 and LOTUS) or by blocking co-receptor recruitment (Olfm1). These proteins have been implicated in neuronal development, possibly due to their MAI-antagonizing signaling through NgR.

Scope of this thesis

In spite of a wealth of available neurobiological, biochemical and structural data regarding MAI signaling, important questions remain. Especially the mechanisms at the extracellular side, that orchestrate signal transduction through the membrane, are unresolved. Many studies have shown conflicting results with regards to the involvement of specific (classes of) molecules in regeneration inhibition, which has been linked to cell-type-specific mechanisms¹³¹. It is not clear how the structurally distinct MAIs can signal via the same receptor complex (Fig. 2). The notion of a ternary receptor complex of NgR, p75 and LINGO-1 has been disputed⁴⁸, suggesting that the mechanism might

be more complicated than simple co-receptor recruitment. Recent work on p75 and its downstream effectors RhoGDI and RhoA indicates that conformational changes might be transduced through the membrane^{53,96–98}. The fact that the (co-)receptors NgR, p75, LINGO-1 and AMIGO3 all oligomerize^{23,27,32,96,97,99,100}, suggests receptor clustering could play a role in MAI signaling. Receptor clustering could also enhance lipid raft formation and *vice versa*⁷⁰ and lipid raft formation was shown to be required for MAG- and Nogo-dependent axonal growth cone collapse⁷².

This thesis addresses the molecular mechanisms of myelin-associated inhibition of regeneration in the CNS, focusing on the initial extracellular signaling events and the central NgR receptor protein. A structural biology approach was used to characterize the myelin-associated inhibitor of regeneration MAG, its receptors NgR and GT1b and an antagonist of MAG signaling through NgR; Olfm1.

In Chapter 2, the structure of the extracellular domain of MAG is described. Structures of MAG-oligosaccharide complexes and *in vitro* binding studies reveal how MAG recognizes gangliosides such as GT1b. Neurite outgrowth inhibition assays provide new insights into the mechanisms of MAG-dependent regeneration inhibition. Implications for MAG-dependent adhesion at the myelin-axon interface as well as axon-to-myelin signaling (during myelination) will be discussed. Chapter 3 describes new crystal structures of NgR, for the first time with its native disulfide structure. Chapter 4 focuses on Olfm1, which was found to form disulfide-linked tetramers. The architecture of the tetrameric assembly and a crystal structure of a dimeric C-terminal segment are described. Chapter 6 discusses the implications of these results for the molecular mechanisms of MAI signaling.

References:

1. Purves, D. *et al. Neuroscience, fifth edition.* (Sinauer, 2012).
2. Squire, L. R. *et al. Fundamental Neuroscience.* (Elsevier, 2008).
3. Simons, M. & Nave, K. Oligodendrocytes: Myelination and axonal support. *Cold Spring Harb. Perspect. Biol.* a020479 (2015). doi:10.1101/cshperspect.a020479
4. Akbik, F., Cafferty, W. B. J. & Strittmatter, S. M. Myelin associated inhibitors: A link between injury-induced and experience-dependent plasticity. *Exp. Neurol.* **235**, 43–52 (2011).
5. Fawcett, J. W. & Keynes, R. J. Peripheral nerve regeneration. *Annu. Rev. Neurosci.* **13**, 43–60 (1990).
6. Kim, W.-Y. & Snider, W. D. Neuroscience. Overcoming inhibitions. *Science* **322**, 869–72 (2008).
7. Silver, J. & Miller, J. H. Regeneration beyond the glial scar. *Nat. Rev. Neurosci.* **5**, 146–156 (2004).
8. Schwab, M. E. & Caroni, P. Oligodendrocytes and CNS myelin are nonpermissive substrates for neurite growth and fibroblast spreading *in vitro*. *J. Neurosci.* **8**, 2381–2393 (1988).
9. Caroni, P. & Schwab, M. E. Two membrane protein fractions from rat central myelin with inhibitory properties for neurite growth and fibroblast spreading. *J. Cell Biol.* **106**, 1281–1288 (1988).
10. Schwab, M. E. & Caroni, P. Antibody against myelin-associated inhibitor of neurite growth neutralizes nonpermissive substrate properties of CNS white matter. *Neuron* **1**, 85–96 (1988).
11. Sun, F. & He, Z. Neuronal intrinsic barriers for axon regeneration in the adult CNS Fang Sun and Zhigang He. *Curr. Opin. Neurobiol.* **20**, 510–518
12. McKerracher, L. *et al.* Identification of myelin-associated glycoprotein as a major myelin-derived inhibitor of neurite growth. *Neuron* **13**, 805–11 (1994).
13. Mukhopadhyay, G., Doherty, P., Walsh, F. S., Crocker, P. R. & Filbin, M. T. A novel role for myelin-associated glycoprotein as an inhibitor of axonal regeneration. *Neuron* **13**, 757–67 (1994).
14. GrandPré, T., Nakamura, F., Vartanian, T. & Strittmatter, S. M. Identification of the Nogo inhibitor of axon regeneration as a Reticulon protein. *Nature* **7199**, 439–444 (2000).
15. Chen, M. S. *et al.* Nogo-A is a myelin-associated neurite outgrowth inhibitor and an antigen for monoclonal antibody IN-1. *Nature* **403**, 434–9 (2000).
16. Dodd, D. *et al.* Nogo-A, -B, and -C are found on the cell surface and interact together in many different cell types. *J. Biol. Chem.* **280**, 12494–12502 (2005).
17. Kottis, V. *et al.* Oligodendrocyte-myelin glycoprotein (OMgp) is an inhibitor of neurite outgrowth. *J. Neurochem.* **82**, 1566–1569 (2002).
18. Wang, K., Koprivica, V., Kim, J. & Sivasankaran, R. Oligodendrocyte-myelin glycoprotein is a Nogo receptor ligand that inhibits neurite outgrowth. *Nature* **417**, 941–944 (2002).
19. Habib, a *et al.* Expression of the oligodendrocyte-myelin glycoprotein by neurons in the mouse central nervous system. *J. Neurochem.* **70**, 1704–1711 (1998).
20. Laurén, J. *et al.* Characterization of myelin ligand complexes with neuronal Nogo-66 receptor family members. *J. Biol. Chem.* **282**, 5715–5725 (2007).
21. Fournier, A. E., GrandPré, T. & Strittmatter, S. M. Identification of a receptor mediating Nogo-66 inhibition of axonal regeneration. *Nature* **409**, 341–346 (2001).
22. Liu, B. P., Fournier, A., GrandPré, T. & Strittmatter, S. M. Myelin-associated glycoprotein as a functional ligand for the Nogo-66 receptor. *Science* **297**, 1190–3 (2002).
23. Barton, W. *et al.* Structure and axon outgrowth inhibitor binding of the Nogo-66 receptor and related proteins. *EMBO J.* **22**, 3291–302 (2003).
24. He, X. L. *et al.* Structure of the Nogo receptor ectodomain: a recognition module implicated in myelin inhibition. *Neuron* **38**, 177–85 (2003).
25. Wen, D. *et al.* Disulfide structure of the leucine-rich repeat C-terminal cap and C-terminal stalk region of Nogo-66 receptor. *Biochemistry* **44**, 16491–16501 (2005).
26. Wang, K. C., Koprivica, V., Kim, J. A. & Sivasankaran, R. Oligodendrocyte-myelin glycoprotein is a Nogo receptor ligand that inhibits neurite outgrowth. *Nature* **417**, 941–944 (2002).
27. Fournier, A. E., Gould, G. C., Liu, B. P. & Strittmatter, S. M. Truncated soluble Nogo receptor binds Nogo-66 and blocks inhibition of axon growth by myelin. *J. Neurosci.* **22**, 8876–83 (2002).
28. Venkatesh, K. *et al.* The Nogo-66 receptor homolog NgR2 is a sialic acid-dependent receptor selective for myelin-associated glycoprotein. *J. Neurosci.* **25**, 808–22 (2005).
29. Laurén, J. *et al.* Characterization of myelin ligand complexes with neuronal Nogo-66 receptor family members. *J. Biol. Chem.* **282**, 5715–25 (2007).

30. Robak, L. A. *et al.* Molecular Basis of the Interactions of the Nogo-66 Receptor and Its Homolog NgR2 with Myelin-Associated Glycoprotein : Development of NgR OMNI -Fc , a Novel Antagonist of CNS Myelin Inhibition. *J. Neurosci.* **29**, 5768–5783 (2009).
31. Wen, D. *et al.* Disulfide structure of the leucine-rich repeat C-terminal cap and C-terminal stalk region of Nogo-66 receptor. *Biochemistry* **44**, 16491–501 (2005).
32. Saha, N., Kolev, M. V, Semavina, M., Himanen, J. & Nikolov, D. B. Ganglioside mediate the interaction between Nogo receptor 1 and LINGO-1. *Biochem. Biophys. Res. Commun.* **413**, 92–97 (2011).
33. Zheng, B. *et al.* Genetic deletion of the Nogo receptor does not reduce neurite inhibition in vitro or promote corticospinal tract regeneration in vivo. *Proc. Natl. Acad. Sci. U. S. A.* **102**, 1205–10 (2005).
34. Chivatakarn, O., Kaneko, S., He, Z., Tessier-Lavigne, M. & Giger, R. J. The Nogo-66 receptor NgR1 is required only for the acute growth cone-collapsing but not the chronic growth-inhibitory actions of myelin inhibitors. *J. Neurosci.* **27**, 7117–24 (2007).
35. Arwal, J. K. *et al.* PirB is a functional receptor for myelin inhibitors of axonal regeneration. *Science* (80-.). **322**, 967–970 (2008).
36. Laurén, J. *et al.* Characterization of myelin ligand complexes with neuronal Nogo-66 receptor family members. *J. Biol. Chem.* **282**, 5715–25 (2007).
37. Stiles, T. L. *et al.* LDL receptor-related protein-1 is a sialic-acid-independent receptor for myelin-associated glycoprotein that functions in neurite outgrowth inhibition by MAG and CNS myelin. *J. Cell Sci.* **126**, 209–20 (2013).
38. Goh, E. L. K. *et al.* Beta1-Integrin Mediates Myelin-Associated Glycoprotein Signaling in Neuronal Growth Cones. *Mol. Brain* **1**, 10 (2008).
39. Wang, K. C., Kim, J. a, Sivasankaran, R., Segal, R. & He, Z. P75 interacts with the Nogo receptor as a co-receptor for Nogo, MAG and OMgp. *Nature* **420**, 74–8 (2002).
40. Wong, S. T. *et al.* A p75(NTR) and Nogo receptor complex mediates repulsive signaling by myelin-associated glycoprotein. *Nat. Neurosci.* **5**, 1302–1308 (2002).
41. Yamashita, T., Higuchi, H. & Tohyama, M. The p75 receptor transduces the signal from myelin-associated glycoprotein to Rho. *J. Cell Biol.* **157**, 565–70 (2002).
42. Hempstead, B. The many faces of p75NTR. *Curr. Opin. Neurobiol.* **12**, 260–267 (2002).
43. Mi, S. *et al.* LINGO-1 is a component of the Nogo-66 receptor/p75 signaling complex. *Nat. Neurosci.* **7**, 221–228 (2004).
44. Shao, Z. *et al.* TAJ/TROY, an orphan TNF receptor family member, binds Nogo-66 receptor 1 and regulates axonal regeneration. *Neuron* **45**, 353–359 (2005).
45. Park, J. B. *et al.* A TNF receptor family member, TROY, is a coreceptor with Nogo receptor in mediating the inhibitory activity of myelin inhibitors. *Neuron* **45**, 345–351 (2005).
46. Saha, N., Kolev, M. & Nikolov, D. B. Structural Features of the Nogo receptor Signaling Complexes at the Neuron/Myelin Interface. *Neurosci. Res.* **87**, 1–7 (2014).
47. Schwab, M. E. Functions of Nogo proteins and their receptors in the nervous system. *Nat. Rev. Neurosci.* **11**, 799–811 (2010).
48. Meabon, J. S. *et al.* LINGO-1 Interacts with the p75 Neurotrophin Receptor in Intracellular Membrane Compartments. *J. Biol. Chem.* jbc.M114.608018 (2015).
49. Ahmed, Z., Douglas, M. R., John, G., Berry, M. & Logan, A. AMIGO3 is an NgR1/p75 co-receptor signalling axon growth inhibition in the acute phase of adult central nervous system injury. *PLoS One* **8**, e61878 (2013).
50. Fujita, Y., Takashima, R., Endo, S., Takai, T. & Yamashita, T. The p75 receptor mediates axon growth inhibition through an association with PIR-B. *Cell Death Dis.* **2**, e198 (2011).
51. Mantuano, E., Lam, M. S. & Gonias, S. L. LRP1 assembles unique co-receptor systems to initiate cell signaling in response to tissue-type plasminogen activator and Myelin-associated glycoprotein. *J. Biol. Chem.* **288**, 34009–34018 (2013).
52. Yamashita, T., Tucker, K. L. & Barde, Y. a. Neurotrophin binding to the p75 receptor modulates Rho activity and axonal outgrowth. *Neuron* **24**, 585–93 (1999).
53. Lin, Z. *et al.* Structural basis of death domain signaling in the p75 neurotrophin receptor. *Elife* **4**, 1–21 (2015).
54. Niederöst, B., Oertle, T., Fritsche, J., McKinney, R. A. & Bandtlow, C. E. Nogo-A and myelin-associated glycoprotein mediate neurite growth inhibition by antagonistic regulation of RhoA and Rac1. *J. Neurosci.* **22**, 10368–76 (2002).
55. Yamashita, T. & Tohyama, M. The p75 receptor acts as a displacement factor that releases Rho from Rho-GDI. *Nat. Neurosci.* **6**, 461–467 (2003).
56. Fournier, A. E., Takizawa, B. T. & Strittmatter, S. M. Rho kinase inhibition enhances axonal regeneration in the injured CNS. *J. Neurosci.* **23**, 1416–1423 (2003).
57. Lu, Y. *et al.* TROY interacts with Rho guanine nucleotide dissociation inhibitor α (RhoGDI α) to mediate Nogo-induced inhibition of neurite outgrowth. *J. Biol. Chem.* **288**, 34276–86 (2013).
58. Ishizaki, T. *et al.* The small GTP-binding protein Rho binds to and activates a 160 kDa Ser/Thr protein kinase homologous to myotonic dystrophy kinase. *EMBO J.* **15**, 1885–1893 (1996).
59. Amano, M. *et al.* Formation of Actin Stress Fibers and Focal Adhesions Enhanced by Rho-Kinase. *Science* (80-.). **275**, 1308–1311 (1997).
60. Amano, M., Nakayama, M. & Kaibuchi, K. Rho-kinase/ROCK: A key regulator of the cytoskeleton and cell polarity. *Cytoskeleton* **67**, 545–554 (2010).
61. Ohashi, K. *et al.* Rho-associated kinase ROCK activates LIM-kinase 1 by phosphorylation at threonine 508 within the activation loop. *J. Biol. Chem.* **275**, 3577–3582 (2000).
62. Hirose, M. *et al.* Molecular dissection of the Rho-associated protein kinase (p160ROCK)-regulated neurite remodeling in neuroblastoma N1E-115 cells. *J. Cell Biol.* **141**, 1625–36 (1998).
63. Niederöst, B., Oertle, T., Fritsche, J., McKinney, R. A. & Bandtlow, C. E. Nogo-A and myelin-associated glycoprotein mediate neurite growth inhibition by antagonistic regulation of RhoA and Rac1. *J. Neurosci.* **22**, 10368–10376 (2002).
64. Quarles, R. H. Myelin-associated glycoprotein (MAG): past, present and beyond. *J. Neurochem.* **100**, 1431–1448 (2007).
65. Kelm, S., Pelz, A., Schauer, R., Filbin, M. T. & Tang, S. Sialoadhesin, myelin-associated glycoprotein and CD22 define a new family of sialic acid-dependent adhesion molecules of the immunoglobulin superfamily. *Curr. Biol.* **4**, (1994).
66. Collins, B. E. *et al.* Sialic acid specificity of myelin-associated glycoprotein binding. *J. Biol. Chem.* **272**, 1248–1255 (1997).
67. Vinson, M. *et al.* Myelin-associated glycoprotein interacts with ganglioside GT1b. A mechanism for neurite outgrowth inhibition. *J. Biol. Chem.* **276**, 20280–5 (2001).
68. Vyas, A. a *et al.* Gangliosides are functional nerve cell ligands for myelin-associated glycoprotein (MAG), an inhibitor of nerve regeneration. *Proc. Natl. Acad. Sci. U. S. A.* **99**, 8412–7 (2002).
69. Fujitani, M. *et al.* Binding of soluble myelin-associated glycoprotein to specific gangliosides induces the association of p75NTR to lipid rafts and signal transduction. *J. Neurochem.* **94**, 15–21 (2005).
70. Simons, K. & Toomre, D. Lipid rafts and signal transduction. *Nat. Rev. Mol. Cell Biol.* **1**, 31–39 (2000).
71. Pignot, V. *et al.* Characterization of two novel proteins, NgRH1 and NgRH2, structurally and biochemically homologous to the Nogo-66 receptor. *J. Neurochem.* **85**, 717–728 (2003).
72. Fujitani, M. *et al.* Binding of soluble myelin-associated glycoprotein to specific gangliosides induces the association of p75NTR to lipid rafts and signal transduction. *J. Neurochem.* **94**, 15–21 (2005).
73. Yu, W., Guo, W. & Feng, L. Segregation of Nogo66 receptors into lipid rafts in rat brain and inhibition of Nogo66 signaling by cholesterol depletion. *FEBS Lett.* **577**, 87–92 (2004).
74. Umemori, H., Sato, S., Yagi, T., Aizawa, S. & Yamamoto, T. Initial events of myelination involve Fyn tyrosine kinase signalling. *Nature* **367**, 572–576 (1994).
75. Krämer-Albers, E.-M., White, R., Kramer-Albers, E. M. & White, R. From axon-glia signalling to myelination: the integrating role of oligodendroglial Fyn kinase. *Cell. Mol. Life Sci.* **68**, 2003–12 (2011).
76. Vinson, M. *et al.* Lipid rafts mediate the interaction between myelin-associated glycoprotein (MAG) on myelin and MAG-receptors on neurons. *Mol. Cell. Neurosci.* **22**, 344–352 (2003).
77. Michaely, P. A., Mineo, C., Ying, Y. S. & Anderson, R. G. W. Polarized distribution of endogenous Rac1 and RhoA at the cell surface. *J. Biol. Chem.* **274**, 21430–21436 (1999).
78. Dickendesher, T. L. *et al.* NgR1 and NgR3 are receptors for chondroitin sulfate proteoglycans. *Nat. Neurosci.* **15**, (2012).
79. Jones, L. L., Margolis, R. U. & Tuszynski, M. H. The chondroitin sulfate proteoglycans neurocan, brevican, phosphacan, and versican are differentially regulated following spinal cord injury. *Exp. Neurol.* **182**, 399–411 (2003).
80. Mckeon, R. J., Hocke, A. & Silver, J. Injury-induced proteoglycans inhibit the potential for laminin-mediated axon growth on astrocytic scars. *Exp. Neurol.* **136**, 32–43 (1995).
81. Asher, R. a *et al.* Neurocan is upregulated in injured brain and in cytokine-treated astrocytes. *J. Neurosci.* **20**, 2427–38 (2000).

82. Haas, C. a, Rauch, U., Thon, N., Merten, T. & Deller, T. Entorhinal cortex lesion in adult rats induces the expression of the neuronal chondroitin sulfate proteoglycan neurocan in reactive astrocytes. *J. Neurosci.* **19**, 9953–9963 (1999).
83. McKeon, R. J., Jurynek, M. J. & Buck, C. R. The chondroitin sulfate proteoglycans neurocan and phosphacan are expressed by reactive astrocytes in the chronic CNS glial scar. *J. Neurosci.* **19**, 10778–10788 (1999).
84. Levine, J. M. Increased Expression after Brain Injury of the NG2 Chondroitin-Sulfate Proteoglycan. *J. Neurosci.* **14**, 4716–4730 (1994).
85. Ong, W. Y. & Levine, J. M. A light and electron microscopic study of NG2 chondroitin sulfate proteoglycan-positive oligodendrocyte precursor cells in the normal and kainate-lesioned rat hippocampus. *Neuroscience* **92**, 83–95 (1999).
86. Rhodes, K. E., Moon, L. D. F. & Fawcett, J. W. Inhibiting cell proliferation during formation of the glial scar: effects on axon regeneration in the CNS. *Neuroscience* **120**, 41–56 (2003).
87. Tang, X., Davies, J. E. & Davies, S. J. A. Changes in Distribution, Cell Associations, and Protein Expression Levels of NG2, V2, and Tenascin-C During Acute to Chronic Maturation of Spinal Cord Scar Tissue. *J. Neurosci. Res.* **71**, 427–444 (2003).
88. Zhang, L. *et al.* Identification of BlyS (B lymphocyte stimulator), a non-myelin-associated protein, as a functional ligand for Nogo-66 receptor. *J. Neurosci.* **29**, 6348–6352 (2009).
89. Vasudevan, S. V., Schulz, J., Zhou, C. & Cocco, M. J. Protein folding at the membrane interface, the structure of Nogo-66 requires interactions with a phosphocholine surface. *Proc. Natl. Acad. Sci. U. S. A.* **107**, 6847–6851 (2010).
90. Alhoshani, A. *et al.* Glutamate provides a key structural contact between reticulon-4 (Nogo-66) and phosphocholine. *Biochim. Biophys. Acta - Biomembr.* **1838**, 2350–2356 (2014).
91. Semavina, M. *et al.* Crystal structure of the Nogo-receptor-2. *Protein Sci.* **20**, 684–689 (2011).
92. He, X.-L. & Garcia, K. C. Structure of nerve growth factor complexed with the shared neurotrophin receptor p75. *Science (80-)*. **304**, 870–5 (2004).
93. Gong, Y., Cao, P., Yu, H. & Jiang, T. Crystal structure of the neurotrophin-3 and p75NTR symmetrical complex. *Nature* **454**, 789–793 (2008).
94. Liepinsh, E., Ilag, L. L., Otting, G. & Ibáñez, C. F. NMR structure of the death domain of the p75 neurotrophin receptor. *EMBO J.* **16**, 4999–5005 (1997).
95. Qu, Q. *et al.* Structural characterization of the self-association of the death domain of p75(NTR). *PLoS One* **8**, e57839 (2013).
96. Vilar, M. *et al.* Activation of the p75 Neurotrophin Receptor through Conformational Rearrangement of Disulphide-Linked Receptor Dimers. *Neuron* **62**, 72–83 (2009).
97. Vilar, M. *et al.* Ligand-independent signaling by disulfide-crosslinked dimers of the p75 neurotrophin receptor. *J. Cell Sci.* **122**, 3351–3357 (2009).
98. Vilar, M. *et al.* Heterodimerization of p45-p75 modulates p75 signaling: structural basis and mechanism of action. *PLoS Biol.* **12**, e1001918 (2014).
99. Mosyak, L. *et al.* The structure of the Lingo-1 ectodomain, a module implicated in central nervous system repair inhibition. *J. Biol. Chem.* **281**, 36378–90 (2006).
100. Kajander, T., Kuja-Panula, J., Rauvala, H. & Goldman, A. Crystal Structure and Role of Glycans and Dimerization in Folding of Neuronal Leucine-Rich Repeat Protein AMIGO-1. *J. Mol. Biol.* **413**, 1001–1015 (2011).
101. Karpusas, M. *et al.* Crystal structure of extracellular human BAFF, a TNF family member that stimulates B lymphocytes. *J. Mol. Biol.* **315**, 1145–54 (2002).
102. Oren, D. *et al.* Structural basis of BlyS receptor recognition. *Nat. Struct. Biol.* **9**, 288–292 (2002).
103. Liu, Y. *et al.* Crystal structure of sTALL-1 reveals a virus-like assembly of TNF family ligands. *Cell* **108**, 383–394 (2002).
104. Kim, H. M. *et al.* Crystal structure of the BAFF-BAFF-R complex and its implications for receptor activation. *Nat. Struct. Biol.* **10**, 342–348 (2003).
105. Xia, W. & Springer, T. A. Metal ion and ligand binding of integrin $\alpha 5 \beta 1$. *Proc. Natl. Acad. Sci. U. S. A.* **111**, 17863–8 (2014).
106. Shiroishi, M. *et al.* Structural basis for recognition of the nonclassical MHC molecule HLA-G by the leukocyte Ig-like receptor B2 (LILRB2/LIR2/ILT4/CD85d). *Proc. Natl. Acad. Sci. U. S. A.* **103**, 16412–7 (2006).
107. Nam, G. *et al.* Crystal structures of the two membrane-proximal Ig-like domains (D3D4) of LILRB1/B2: Alternative models for their involvement in peptide-HLA binding. *Protein Cell* **4**, 761–770 (2013).
108. Morishita, H. & Hensch, T. K. Critical period revisited: impact on vision. *Curr. Opin. Neurobiol.* **18**, 101–107 (2008).
109. Hofer, S. B., Mrcic-Flogel, T. D., Bonhoeffer, T. & Hübener, M. Lifelong learning: ocular dominance plasticity in mouse visual cortex. *Curr. Opin. Neurobiol.* **16**, 451–459 (2006).
110. McGee, A. W., Yang, Y., Fischer, Q. S., Daw, N. W. & Strittmatter, S. M. Experience-driven plasticity of visual cortex limited by myelin and Nogo receptor. *Science (80-)*. **309**, 2222–2226 (2005).
111. Frantz, M. G., Kast, R. J., Dorton, H. M., Chapman, K. S. & McGee, a. W. Nogo Receptor 1 Limits Ocular Dominance Plasticity but not Turnover of Axonal Boutons in a Model of Amblyopia. *Cereb. Cortex* 1–11 (2015). doi:10.1093/cercor/bhv014
112. Syken, J., Grandpre, T., Kanold, P. O. & Shatz, C. J. PirB restricts ocular-dominance plasticity in visual cortex. *Science (80-)*. **313**, 1795–800 (2006).
113. Lee, H. *et al.* Synaptic function for the Nogo-66 receptor NgR1: regulation of dendritic spine morphology and activity-dependent synaptic strength. *J. Neurosci.* **28**, 2753–65 (2008).
114. Raiker, S. J. *et al.* Oligodendrocyte-myelin glycoprotein and Nogo negatively regulate activity-dependent synaptic plasticity. *J. Neurosci.* **30**, 12432–12445 (2010).
115. Akbik, F. V., Bhagat, S. M., Patel, P. R., Cafferty, W. B. J. & Strittmatter, S. M. Anatomical Plasticity of Adult Brain Is Titrated by Nogo Receptor 1. *Neuron* **77**, 859–866 (2013).
116. Jitsuki, S. *et al.* Nogo Receptor Signaling Restricts Adult Neural Plasticity by Limiting Synaptic AMPA Receptor Delivery. *Cereb. cortex* **26**, 427–39 (2016).
117. Karlen, A. *et al.* Nogo receptor 1 regulates formation of lasting memories. *Proc.* **106**, 20476–20481 (2009).
118. Mironova, Y. A. & Giger, R. J. Where no synapses go: gatekeepers of circuit remodeling and synaptic strength. *Trends Neurosci.* **36**, 363–373 (2013).
119. Baldwin, K. T. & Giger, R. J. Insights into the physiological role of CNS regeneration inhibitors. *Front. Mol. Neurosci.* **8**, 1–8 (2015).
120. Nakaya, N., Sultana, A., Lee, H. S. & Tomarev, S. I. Olfactomedin 1 interacts with the Nogo A receptor complex to regulate axon growth. *J. Biol. Chem.* **287**, 37171–37184 (2012).
121. Barembaum, M., Moreno, T. a, LaBonne, C., Sechrist, J. & Bronner-Fraser, M. Noelin-1 is a secreted glycoprotein involved in generation of the neural crest. *Nat. Cell Biol.* **2**, 219–225 (2000).
122. Moreno, T. a. & Bronner-Fraser, M. Noelins modulate the timing of neuronal differentiation during development. *Dev. Biol.* **288**, 434–447 (2005).
123. Tomarev, S. I. & Nakaya, N. Olfactomedin domain-containing proteins: Possible mechanisms of action and functions in normal development and pathology. *Mol. Neurobiol.* **40**, 122–138 (2009).
124. Anholt, R. R. H. Olfactomedin proteins: central players in development and disease. *Front. Cell Dev. Biol.* **2**, 1–10 (2014).
125. Anholt, R. R., Petro, a E. & Rivers, a M. Identification of a group of novel membrane proteins unique to chemosensory cilia of olfactory receptor cells. *Biochemistry* **29**, 3366–3373 (1990).
126. Ando, K. *et al.* Expression and characterization of disulfide bond use of oligomerized A2-Pancortins: Extracellular matrix constituents in the developing brain. *Neuroscience* **133**, 947–957 (2005).
127. Thomas, R. *et al.* LGI1 is a Nogo receptor 1 ligand that antagonizes myelin-based growth inhibition. *J. Neurosci.* **30**, 6607–12 (2010).
128. Su, L.-D., Xie, Y.-J., Zhou, L., Shen, Y. & Hu, Y.-H. LGI1 is Involved in the Development of Mouse Brain. *Cerebellum* 14–16 (2014).
129. Sato, Y. *et al.* Cartilage acidic protein-1B (LOTUS), an endogenous Nogo receptor antagonist for axon tract formation. *Science* **333**, 769–73 (2011).
130. Kurihara, Y. *et al.* LOTUS suppresses axon growth inhibition by blocking interaction between Nogo receptor-1 and all four types of its ligand. *Mol. Cell. Neurosci.* **61**, 211–218 (2014).
131. Giger, R. J. *et al.* Mechanisms of CNS myelin inhibition: evidence for distinct and neuronal cell type specific receptor systems. *Restor. Neurol. Neurosci.* **26**, 97–115 (2008).
132. Poliak, S. & Peles, E. The local differentiation of myelinated axons at nodes of Ranvier. *Nat. Rev. Neurosci.* **4**, 968–980 (2003).

Chapter 2

Structural basis of myelin-associated glycoprotein adhesion and signaling

Matti F. Pronker¹, Suzanne Lemstra², Joost Snijder³, Albert J.R. Heck³,
Dominique M.E. Thies-Weesie⁴, R. Jeroen Pasterkamp², Bert J.C. Janssen¹

¹: *Crystal and Structural Chemistry, Bijvoet Center for Biomolecular Research, Department
of Chemistry, Faculty of Science, Utrecht University, Padualaan 8, 3584 CH Utrecht,
The Netherlands*

²: *Department of Translational Neuroscience, Brain Center Rudolf Magnus, University
Medical Center Utrecht, Universiteitsweg 100, 3584 CG Utrecht, The Netherlands*

³: *Biomolecular Mass Spectrometry and Proteomics, Bijvoet Center for Biomolecular
Research and Utrecht Institute for Pharmaceutical Sciences, Faculty of Science, Utrecht
University, Padualaan 8, 3584 CH Utrecht, The Netherlands*

⁴: *Van't Hoff Laboratory for Physical and Colloid Chemistry, Debye Institute of
Nanomaterials Science, Department of Chemistry, Faculty of Science, Utrecht University,
Padualaan 8, 3584 CH Utrecht, The Netherlands*

Nature Communications 7, 13584 (2016).

Abstract

Myelin-associated glycoprotein (MAG) is a myelin-expressed cell-adhesion and bi-directional signaling molecule. MAG maintains the myelin-axon spacing by interacting with specific neuronal glycolipids (gangliosides), inhibits axon regeneration and controls myelin formation. The mechanisms underlying MAG adhesion and signaling are unresolved. We present crystal structures of the MAG full ectodomain, which reveal an extended conformation of five Ig domains and a homodimeric arrangement involving membrane-proximal domains Ig4 and Ig5. MAG-oligosaccharide complex structures and biophysical assays show how MAG engages axonal gangliosides at domain Ig1. Two post-translational modifications were identified – N-linked glycosylation at the dimerization interface and tryptophan C-mannosylation proximal to the ganglioside binding site – that appear to have regulatory functions. Structure-guided mutations and neurite outgrowth assays demonstrate MAG dimerization and carbohydrate recognition are essential for its regeneration-inhibiting properties. The combination of *trans* ganglioside binding and *cis* homodimerization explains how MAG maintains the myelin-axon spacing and provides a mechanism for MAG-mediated bi-directional signaling.

Introduction

Myelination of axons enables enhanced conductance velocity in both the central and peripheral nervous system (CNS and PNS) of vertebrates. It also provides electrical insulation and a decrease of the capacitance, as well as physical protection and metabolic support of long axons¹. Myelin-associated glycoprotein (MAG) adhesion and signaling at the myelin-axon interface regulates the formation and maintenance of myelinated axons, thus playing an important role in the development and function of the nervous system^{2,3}. Aberrant MAG function, for example from mutations that likely cause misfolding, or anti-MAG autoimmunity, has been associated with demyelination and neurodegenerative disorders, such as corticospinal motor neuron disease also known as hereditary spastic paraplegias⁴, Pelizaeus-Merzbacher disease-like disorder⁵, demyelinating anti-MAG peripheral neuropathy^{6,7} and multiple sclerosis^{2,8}.

MAG is a type 1 single-pass transmembrane protein expressed on myelinating oligodendrocytes in the CNS and Schwann cells in the PNS^{2,3}. MAG is the fifth highest expressed protein in myelin of the CNS⁹. It is highly enriched at the innermost (adaxonal) myelin membrane along the internode, where it contacts the axon. MAG is also found on other myelin structures, such as the mesaxon, Schmidt-Lanterman incisures and paranodal loops^{2,3}. MAG adhesion maintains the myelin-axon spacing (periaxonal diameter) by interacting with specific neuronal gangliosides (glycolipids), such as the major brain gangliosides GT1b and GD1a¹⁰⁻¹³. More recently, the Nectin-like (Necl) proteins 1 and 4 have also been found to contribute to myelin-axon adhesion along the internode^{14,15}, although they are expressed less than MAG in mature myelin⁹ and knockout of Necl4 does not affect myelination¹⁶.

MAG, also known as Siglec4a, is evolutionarily the oldest member of the Siglec family¹⁷. Unlike all other Siglecs, MAG plays no role in the immune system and is exclusively expressed in the nervous system¹⁷. Based on the primary sequence its extracellular region is predicted to consist of five Ig-domains; an N-terminal V-type Ig domain that is typical for Siglecs and four C2-type Ig domains. This is followed by a single membrane-spanning helix and an intracellular region predicted to be unstructured and of different length for two MAG isoforms, L-MAG and S-MAG. Like other Siglecs, MAG recognizes sialic acid groups and the specificity of MAG has been established to be Neu5Ac- α 2,3-Gal- β 1,3-GalNAc¹⁸. This trisaccharide is part of several neuronal gangliosides, most notably the major brain gangliosides GT1b and GD1a, but also GM1b, GT1 β and GQ1b α . MAG bridges the periaxonal space by interacting with these axonal gangliosides *in trans* via the canonical Siglec site at a conserved arginine (R118 in MAG) in the N-terminal domain^{19,20}.

MAG signaling is bidirectional, engaging in both axon-to-myelin as well as myelin-to-axon signaling. MAG has been extensively studied as one of three classic myelin-

associated inhibitors of central nervous system regeneration, the other ligands being Nogo66 and Oligodendrocyte Myelin glycoprotein (OMgp)^{2,3}. MAG inhibits neurite outgrowth and collapses axonal growth cones in a sialic acid binding-dependent manner. It does so as full-length transmembrane^{20,21}, but also as a proteolytically shed and soluble form called dMAG²². As a receptor, MAG controls myelin formation and integrity. How MAG transduces the extracellular signal into the myelinating cell is not well understood, but it has been shown that the cytosolic domain of the L-MAG isoform binds to the cytoplasmic non-receptor tyrosine kinase Fyn²³ and that antibody-induced crosslinking of L-MAG triggers its localization to lipid rafts²⁴ and activates Fyn in oligodendrocytes²³. This activation of Fyn is essential for the initiation of myelination²⁵. In contrast, the shorter MAG isoform S-MAG binds to zinc and microtubules and this is postulated to have a structural function in mature myelin^{26,27}.

From earlier rotary-shadowed electron microscopy (EM) and sedimentation velocity Analytical Ultracentrifugation (AUC) studies it was hypothesized that the extracellular segment of MAG has a back-folded Ig-horseshoe type structure, but the estimated maximum dimensions of 8.8 and 18.5 nm determined by AUC and EM, respectively, deviate substantially^{28,29}. In the absence of any high-resolution structural data on MAG or its interaction with ganglioside ligands, the conformation of the five Ig domains, the extracellular specificity-determining parameters and the mechanisms underlying MAG adhesion and bidirectional signaling are unresolved. Using a combination of structural, biophysical and cellular techniques, we provide the structural basis of MAG-mediated adhesion and identify a dimerization-dependent mechanism that explains how MAG regulates axon-to-myelin and myelin-to-axon signaling, and controls myelin-axon spacing.

Results

MAG has an extended conformation

We determined crystal structures of the full extracellular segment of mouse MAG (MAG₁₋₅) in two different crystal forms that diffracted to a maximum resolution of 3.8 and 4.3 Å. These crystals were obtained by enzymatic deglycosylation of MAG₁₋₅ or reductive lysine methylation of glycosylated MAG₁₋₅ (see Materials and Methods). In addition, crystals of a shorter construct, consisting of the three N-terminal domains (MAG₁₋₃), diffracted to a maximum resolution of 2.1 Å. The structures were solved by molecular replacement with individual Ig domains from homologous proteins. The exceptionally high solvent content of the two MAG₁₋₅ crystal forms (91 and 85 %, Supplementary Fig. 1) aided in obtaining phases of sufficient quality for initial model building (see also table 1 and Materials and Methods for details).

Table 1. Data collection and refinement statistics

	MAG ₁₋₃ unliganded	MAG ₁₋₃ ligand bound	MAG ₁₋₅ deglycosylated	MAG ₁₋₅ lysine-methylated
Data collection				
Space group	<i>P</i> 1	<i>P</i> 1	<i>P</i> 3 ₂	<i>P</i> 6 ₅ 22
Cell dimensions				
<i>a</i> , <i>b</i> , <i>c</i> (Å)	43.06, 60.4, 79.22	43.61, 60.12, 79.47	278.9, 278.9, 62.52	101.2, 101.2, 687.5
α , β , γ (°)	72.70, 86.71, 83.01	71.86, 86.51, 82.95	90, 90, 120	90, 90, 120
Resolution (Å)	42.73-2.12 (2.19- 2.12)	56.79-2.30 (2.38- 2.30)	69.72-3.80 (4.03- 3.80)	114.62-4.30 (4.81-4.30)
No. of reflections	42,931	42,931	35,257	15,430
<i>R</i> _{merge}	0.064 (1.118)	0.157 (0.981)	0.234 (1.683)	0.115 (3.937)
Mean <i>I</i> / σ <i>I</i>	8.8 (0.9)	5.9 (1.6)	9.2 (1.6)	15.6 (1.3)
CC _{1/2}	0.998 (0.558)	0.985 (0.565)	0.997 (0.565)	0.998 (0.242)
Completeness (%)	96.2 (95.7)	97.5 (95.7)	100.0 (100.0)	100.0 (100.0)
Redundancy	3.6 (3.5)	4.5 (4.3)	9.6 (9.7)	35.7 (36.9)
Refinement				
Resolution (Å)	2.1	2.3	3.8	4.3
<i>R</i> _{work} / <i>R</i> _{free}	0.224 / 0.262	0.224 / 0.254	0.203 / 0.230	0.266 / 0.282
No. atoms	5162	5095	3887	3942
Average <i>B</i> -factors (Å ²)				
Protein	71.1	70.9	144.2	414.5
Ligand/ion	106.8	102.5	129.4	N/A
Water	60.8	59.7	N/A	N/A
R.M.S. deviations				
Bond lengths (Å)	0.003	0.002	0.006	0.008
Bond angles (°)	0.700	0.583	1.218	1.384
Molprobability score	1.69	1.49	2.38	2.36

*Each dataset was collected from a single crystal.

In all three crystal forms MAG has an extended collinear conformation (Fig. 1). Only consecutive Ig domains interact with each other via hydrophobic interfaces (buried-surface area ranging from 243 to 690 Å²) and short inter-domain linkers of up to two residues (Fig. 1a). Domains Ig1 and Ig2 form the largest interface in which the Ig2 loops at the N-terminal “head” side interact with the A2-B (Ig domain β -strand numbering) side of Ig1 (Fig. 1a). The three other inter-domain interfaces are exclusively formed in a head-to-tail fashion involving loops at the N-terminal “head” and C-terminal “tail” side of the Ig domains (Fig. 1a). As predicted from the primary sequence the N-terminal Ig1

domain of MAG has a V-type Ig fold like other Siglec family members^{30–32} and domains Ig3 and Ig4 are of the C2 type. Domains Ig2 and Ig5, however, have a C1-type Ig fold, contrary to the predicted C2-fold (Supplementary Fig. 2). The three crystal structures of MAG are similar to each other with only small differences within the domains (RMSD ranging from 0.93 to 2.13 Å) and inter-domain angle rotation differences ranging from 3.4 to 17.4°, the largest difference is in the domain Ig2-Ig3 angle (Fig. 1b). The combination of hydrophobic inter-domain interfaces, the lack of flexible linker residues and a previously predicted inter-domain disulfide between Ig1 and Ig2 (C37 to C165)³³ explains the limited inter-domain flexibility observed between the three different crystal forms.

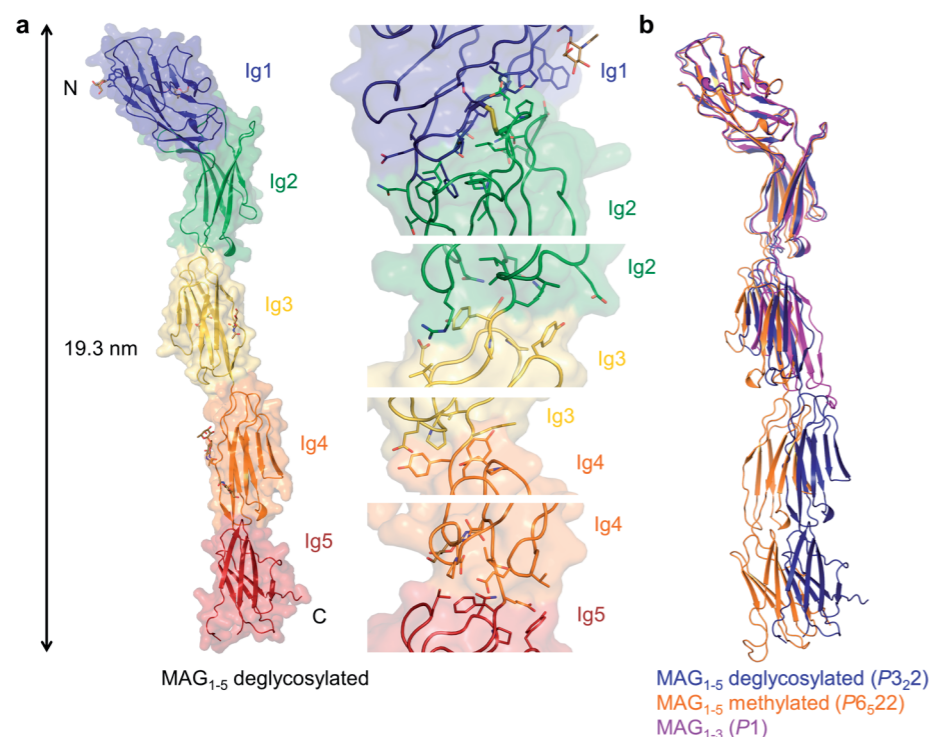


Figure 1. Crystal structures of MAG reveal an extended conformation with limited inter-domain flexibility.

(a) Crystal structure of deglycosylated MAG₁₋₅ colored by domain, glycosylation sites indicated in stick representation and N- and C-termini indicated with N and C (left panel). Close-up views of the inter-domain interfaces with sidechains of interacting residues and the inter-domain disulfide between Ig1 and Ig2 shown in stick representation (right panel). (b) Superposition, based on domain Ig1, of the three crystal structures of MAG; deglycosylated MAG₁₋₅ (blue), lysine-methylated MAG₁₋₅ (orange) and MAG₁₋₃ (purple), space groups indicated in brackets.

MAG is post-translationally modified

The structures reveal MAG is post-translationally modified at several sites. MAG contains seven disulfides, five of which are canonical for Ig domains. Cysteines 37 and 165 form an inter-domain disulfide between Ig1 and Ig2 and cysteines 421 and 430 form an additional intra-domain disulfide in Ig5, as shown previously³³ (Supplementary Fig. 3). In addition, MAG carries N-linked glycans and previously eight N-linked glycosylation sites were determined in human MAG by mass spectrometry analysis³⁴. We observe glycan electron density for five of those equivalent sites in the mouse MAG structures (on asparagine 99, 223, 246, 315 and 406, Supplementary Fig. 4). The differences in these observations arise from one N-linked glycosylation site that is not conserved (N106 in human MAG is a threonine in mouse) and from poorly resolved electron density for the other two sites (on N450 and N454) that are situated in a flexible loop. One additional N-linked glycan is revealed by clear electron density on N332, in contrast to the previous study that did not find this residue in a glycopeptide analysis³⁴. Electron density at the N332-linked glycan suggests it is fucosylated in our recombinantly-produced MAG (Supplementary Fig. 5). In native mass spectrometry experiments of intact recombinant MAG, we also observed internal mass shifts of +147 Da on MAG monomers (Supplementary Fig. 6), further indicating fucosylation as a post-translational modification. Thus the combination of our data and that of others³⁴ indicates that mouse MAG has eight N-linked glycosylation sites (on N99, N223, N246, N315, N323, N406, N450 and N454).

Additionally, MAG carries a tryptophan C-mannosylation on W22. In all three crystal forms, electron density proximal to the sidechain of W22 suggests this residue is C-mannosylated (Supplementary Fig. 6). Indeed, analysis of the MAG primary sequence reveals that this tryptophan is part of the canonical WxxW motif (W22 is the first tryptophan) for C-mannosylation, a rare post-translational modification present on several secreted proteins³⁵. The W22-attached α -D-mannopyranosyl group has an unusual ring-flipped 1C4 chair conformation in the structures (regular mannose is 4C1, Supplementary Fig. 6). This ring-flipped conformation is in agreement with previous NMR studies on mannosyl-tryptophan³⁶ and can be explained by the preference of the bulky tryptophan, covalently attached to the C1 of the mannose, to be in the equatorial position. We confirmed the C-mannosylation of W22 by in-gel trypsin digestion of MAG₁₋₅ followed by LC-MS/MS analysis of the (glyco)peptide fragments (Supplementary Fig. 7). In addition, native mass spectrometry of wild-type and mutated MAG₁₋₅, in which the second tryptophan of the C-mannosylation motif is substituted for glutamine (W25Q, resulting in WxxQ), showed a mass shift of -221 Da in accordance with a loss of C-mannosylation and confirming the importance of the WxxW motif (Supplementary Fig. 6).

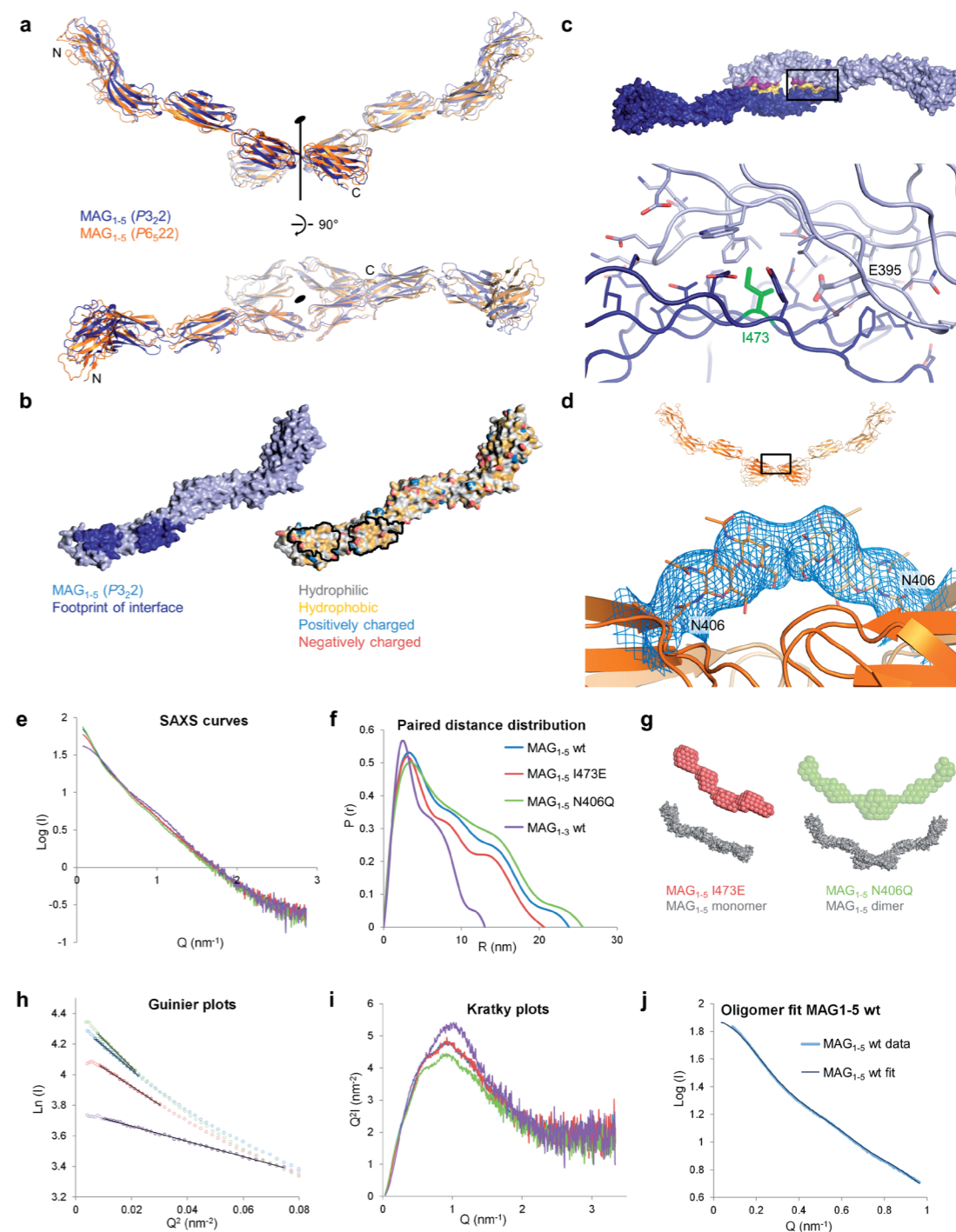
MAG₁₋₅ crystal structures reveal a dimeric arrangement

MAG₁₋₅ forms a symmetry-related dimer at a crystallographic twofold rotation axis in both MAG₁₋₅ crystal forms. They share the same interface (Fig. 2a) on domains Ig4 and Ig5, which buries a surface area of 2037 Å². The CC'FG face of Ig4 binds to the ABDE face of Ig5 of the symmetry-related molecule and *vice versa*, thus forming two equivalent hemi-interfaces. The interface is mostly hydrophobic apart from the negatively-charged E395 in Ig4, with hydrophilic residues lining the edges of the interface (Fig. 2b).

To validate the interface we generated two interface mutations based on the structures, that we predicted to either disrupt dimerization (I473 to E) or enhance it (N406 to Q). The hydrophobic I473 in the middle of the hydrophobic interface of Ig5 was mutated to a negatively-charged glutamate, to ensure disturbance of the hydrophobic effect as well as introducing electrostatic repulsion with the opposing E395 in Ig4 (Fig. 2c). N406 carries an N-linked glycan and in the glycosylated lysine-methylated crystals of MAG₁₋₅, the density for this glycan suggests that it sterically clashes with its symmetry partner in the dimer (Fig. 2d). We hypothesized that a dimer with increased affinity would form, were this glycan absent. Remarkably, the N406Q mutant that lacks this glycan was the only MAG construct that showed a distinct dimer peak in size exclusion chromatography (Supplementary Fig. 8). The other glycans are not expected to interfere with dimerization, also not when considering myelin-specific N-linked glycans³⁷. We confirmed that MAG dimerizes in solution via the Ig4-Ig5 interface by analyzing glycosylated and deglycosylated forms of MAG₁₋₅, MAG₁₋₃ (that lacks the dimerization domains) and the aforementioned mutants in Small Angle X-ray Scattering (SAXS) and AUC experiments.

Figure 2. MAG forms dimers via domains Ig4 and Ig5.

(a) Superposition of the crystallographic dimers observed in the crystals of MAG₁₋₅ deglycosylated (blue) and MAG₁₋₅ lysine-methylated (orange). The twofold axis is indicated by a black line with an ellipse on top, N- and C-termini indicated with N and C for one monomer. (b) The dimer is formed by two equivalent symmetry-related hemi-interfaces, which are mostly hydrophobic (yellow) with hydrophilic (grey), positively charged (blue) and negatively charged (red) residues lining the edges. (c) Zoom of the interface in deglycosylated MAG₁₋₅, indicating isoleucine 473, which was mutated to glutamate to disturb the interface. (d) $2F_o - F_c$ electron density at a contour level of 1.0 σ of the N-linked glycan on N406 in the lysine methylated MAG₁₋₅ crystal structure, showing the steric hindrance with its symmetry mate. Glycosylation at this site was prevented by mutating N406 to glutamine to obtain a MAG variant with enhanced dimerization properties. (e) SAXS Log I versus Q plots for glycosylated MAG variants: MAG₁₋₅ wt (blue), MAG₁₋₅ I473E (red), MAG₁₋₅ N406Q (green) and MAG₁₋₃ (purple), same coloring used in panels e to j. (f) Paired distance distribution functions of the same MAG variants as in panel e. (g) DAMMIF *ab-initio* modeling for deglycosylated MAG₁₋₅ I473E (red) and MAG₁₋₅ N406Q (green), showing remarkable similarity to the crystal structures of monomeric MAG (left, grey) and the crystallographic dimer (right, grey), respectively (see Supplementary Fig. 13 for fits). (h) Guinier plots of the glycosylated MAG variants show the same size-related trends as the paired distance distribution function in panel f. (i) Kratky plots for the different glycosylated MAG variants confirm that MAG behaves as a semi-rigid rod in solution and not as flexible beads-on-a-string. (j) OLIGOMER fit of the MAG monomer and crystallographic dimer to the glycosylated MAG₁₋₅ wt data, using the glycosylated and lysine-methylated crystal structures. OLIGOMER gives a 0.72 : 0.28 (monomer : dimer) ratio at a MAG concentration of 52 μ M.



Small Angle X-ray Scattering confirms dimerization interface

As predicted, SAXS analysis indicated disruption of dimerization for MAG₁₋₃ and MAG₁₋₅ I473E, whereas dimerization is enhanced for MAG₁₋₅ N406Q and deglycosylated MAG₁₋₅ compared to wt MAG₁₋₅. The molecular mass (M_m) based on the extrapolated intensity at zero scattering angle (I_0 , scaled for concentration to BSA), the radius of gyration (R_g), the maximum interatomic distance (D_{max}) and the Porod volume all show these trends (Fig. 2, Supplementary Fig. 9 and table 2). The data show that at similar concentrations, MAG₁₋₅ I473E appears smaller than wt MAG₁₋₅ and MAG₁₋₅ N406Q appears larger than wt MAG₁₋₅. This can be attributed to a shift in the monomer-dimer equilibrium; MAG₁₋₅ I473E has a lesser and MAG₁₋₅ N406Q a greater propensity to dimerize compared to wt MAG₁₋₅.

Furthermore, the MAG₁₋₅ I473E pair distance distribution function $P(r)$ and derived D_{max} , the *ab initio* models as well as the Kratky plots confirm that MAG has an extended conformation and behaves as a semi-rigid rod in solution (Fig. 2f, 2g and 2i). Whereas the SAXS data for glycosylated MAG₁₋₃ and MAG₁₋₅ I473E fit best to scattering curves calculated from single chains of the crystal structures of MAG₁₋₃ and MAG₁₋₅, respectively ($\chi=2.87$ and 2.95, Supplementary Fig. 10), the glycosylated MAG₁₋₅ N406Q SAXS data fits best to scattering curves calculated from the dimer structure ($\chi=3.45$, Supplementary Fig. 10). Both glycosylated and deglycosylated MAG₁₋₅ wt SAXS data fit best to scattering curves calculated from a combination of monomeric and dimeric crystal structures ($\chi=4.05$ for glycosylated and 3.72 for deglycosylated MAG₁₋₅, Fig. 2j and Supplementary Fig. 11). Furthermore, *ab-initio* models based on the SAXS data of deglycosylated MAG₁₋₅ I473E and MAG₁₋₅ N406Q agree remarkably well with the crystal structures of the monomer and dimer of MAG₁₋₅, respectively (Fig. 2g, Supplementary Fig. 12, χ^2 of the model-to-data fit are 1.05 and 1.33 for MAG₁₋₅ I473E and MAG₁₋₅ N406Q, respectively). These data confirm MAG dimerizes via domains Ig4 and Ig5 and that the MAG₁₋₅ chains have an extended and relatively rigid conformation.

Table 2. SAXS data collection and parameters

Sample	Model:	M_m floated/fixed	M_m (kDa)	$\log^{10}(K_d)$	K_d (μ M)	χ^2
MAG ₁₋₅ wt glycosylated	Monomer-dimer equilibrium	floated	62.6	3.42	382	1.17
MAG ₁₋₅ I473E glycosylated	Single species	floated	62.3	-	-	1.18
MAG ₁₋₃ glycosylated	Single species	floated	40.8	-	-	1.31
MAG ₁₋₅ wt deglycosylated	Monomer-dimer equilibrium	fixed	56.9	3.78	167	0.94

The MAG₁₋₅ dimer is weak in solution with a K_d of $3.8 \times 10^2 \mu$ M

To quantify the affinity of MAG dimerization in solution, we performed sedimentation equilibrium Analytical Ultra Centrifugation (SE-AUC) experiments for wt MAG₁₋₅, deglycosylated wt MAG₁₋₅, MAG₁₋₃, MAG₁₋₅ I473E and MAG₁₋₅ N406Q constructs. For each sample a global analysis was performed for different concentrations, centrifugal speeds and wavelengths together (Supplementary Fig. 13-16), except for MAG₁₋₅ N406, which appeared to suffer from aggregation during the experiment. Similar to the SAXS analysis, the MAG₁₋₅ I473E and MAG₁₋₃ SE-AUC data fit best to a single species that agrees with the molecular mass of a monomer (table 3). For wt MAG₁₋₅ and deglycosylated MAG₁₋₅, we could fit the data to a monomer-dimer equilibrium, with K_d 's of 3.8×10^2 and $1.7 \times 10^2 \mu$ M, respectively (table 3). Based on a monomer-dimer equilibrium with these K_d 's, dimer fractions of 18 % for glycosylated wt MAG₁₋₅ and 24 % for deglycosylated wt MAG₁₋₅ are expected to be present in the SAXS experiments (calculated at 52.2 and 37.5 μ M for glycosylated and deglycosylated MAG, respectively). Indeed, the presence of a mix of monomers and dimers is observed in the SAXS data of both glycosylated and deglycosylated MAG₁₋₅ (Fig. 2J, Supplementary Fig. 11). The lack of dimers in the AUC experiments for MAG₁₋₅ I473E and MAG₁₋₃ and the higher affinity for deglycosylated MAG₁₋₅ compared to glycosylated MAG₁₋₅ further confirm that MAG forms dimers via domains Ig4 and Ig5 (table 3).

Structural basis of ligand recognition by Ig1

MAG binds to sialic acids of gangliosides with its N-terminal V-type Ig domain and has a preference for a Neu5Ac- α 2,3-Gal- β 1,3-GalNAc moiety¹⁸. We observed unmodeled electron density in the $2F_o - F_c$ and $F_o - F_c$ maps of the deglycosylated MAG₁₋₅ structure close to R118 in the putative ligand binding site²⁰ (Fig. 3a). Native mass spectrometry of purified MAG₁₋₅ revealed a mixture of free and two ligand-bound MAG₁₋₅ forms with mass differences of 835 ± 2 and 854 ± 2 Da compared to free MAG₁₋₅ (Fig. 3b). The 835 Da ligand possibly corresponds to a tetrasaccharide comprising the aforementioned Neu5Ac- α 2,3-Gal- β 1,3-GalNAc trisaccharide plus another hexose. The 854 Da ligand might correspond to a similar tetrasaccharide where Neu5Ac is replaced by Neu5Gc, a mammalian sialic acid variant not produced by humans. These ligands are likely copurified in complex with MAG from the expression medium that contains beef digest (Primatone). We do not observe clear electron density for any ligands in the two other crystal forms (lysine-methylated MAG₁₋₅ and MAG₁₋₃). In these crystal forms, the unliganded MAG is apparently preferentially crystallized over the ligand-bound forms. The resolution of the MAG₁₋₅-ligand complex (to 3.8 Å) is not sufficient to determine the detailed structure of the bound oligosaccharide. However, the unmodeled electron density is compatible with either of the suggested compounds.

Table 3. SE-AUC parameters

Sample	M _{in} (kDa)	Concentration (μM)	Temperature (K)	R _g (nm)	M _{in} based on I ₀ (kDa)	D _{max} (nm)	Porod volume (nm ³)	SASDB accession code
MAG ₁₋₅ wt glycosylated	64.9	52.2	293	6.8	76.8	23.8	153.8	SASDB55
MAG ₁₋₅ I473E glycosylated	64.9	46.2	293	6.0	64.4	20.6	117.1	SASDB26
MAG ₁₋₅ N406Q glycosylated	63.7	33.3	293	7.3	82.0	25.6	193.2	SASDB36
MAG ₁₋₃ glycosylated	39.8	43.7	293	3.9	43.0	13.0	59.3	SASDB46
MAG ₁₋₅ wt deglycosylated	56.8	37.5	293	7.3	75.4	25.5	166.2	SASDBF6
MAG ₁₋₅ I473E deglycosylated	56.8	45.1	293	6.0	61.1	21.2	99.6	SASDB56
MAG ₁₋₅ N406Q deglycosylated	56.8	33.6	277	7.8	93.9	29.0	216.4	SASDB66
MAG ₁₋₃ deglycosylated	36.6	38.2	293	3.9	39.9	12.6	49.4	SASDB76

To obtain more detailed information on MAG-ligand interactions, the commercially available trisaccharide 3'-N-Acetylneuraminy-N-acetylglucosamine (Neu5Ac-α2,3-Gal-β1,4-GlcNAc) was soaked into the MAG₁₋₃ crystals, as these provided higher resolution data. For the soaked crystals, diffraction data was collected to 2.3 Å resolution. The crystals were isomorphous to the unsoaked MAG₁₋₃ crystals (table 1) and a F_o(soaked)-F_o(unsoaked) map revealed clear electron density in the oligosaccharide binding site for one of the two MAG₁₋₃ chains in the asymmetric unit (Fig. 3c). Most likely the other

chain remained unliganded due to occlusion of the binding site by crystal packing.

The ganglioside binding site is formed by the CC' loop and the F and G β-strands of the N-terminal V-type Ig1 domain. In agreement with previous data²⁰, the side chain of R118 in strand F forms a key salt bridge with the carboxylic acid group of the sialic acid in the trisaccharide ligand. Y65 in the CC' loop forms extensive van der Waals' contacts with the ligand as well as a hydrogen bond to the O9 of the Neu5Ac sialic acid. Other contributing interactions are made by: 1) the backbone carbonyls of N126 and T128 in strand G that form hydrogen bonds with H-N5 and the H-O9 of the sialic acid respectively, 2) the backbone amide proton of T128 that forms a hydrogen bond with the O8 of the sialic acid and 3) the sidechain of Y127 that forms van der Waals' contacts with the glycerol group (C7-C9) of the sialic acid (Fig. 3d).

We validated the ganglioside binding properties of MAG by mutating ligand-binding residues to alanine in MAG₁₋₅ and probed their interaction with GT1b ganglioside incorporated into liposomes. The setup we used, MAG₁₋₅ coupled at the C-terminus to a streptavidin-coated surface plasmon resonance (SPR) chip and GT1b-containing liposomes in the mobile phase, enables avidity-enhanced interactions that also occur in *trans* between cells (Fig. 3f, see also Methods). Indeed we observed specific binding of GT1b liposomes to wt MAG₁₋₅, no interactions with the ligand-binding mutants MAG₁₋₅ R118A, T128A and Y127A and reduced interaction with MAG₁₋₅ Y65A (Fig. 3f). In addition, the MAG₁₋₅ W25Q mutant that lacks the tryptophan mannosylation on W22, still interacted with GT1b liposomes in this assay. Remarkably, this W25Q mutant appeared to have a higher affinity for the GT1b liposomes compared to wt MAG. This suggests that rather than contributing to the interaction strength, this tryptophan mannosylation on W22 may play a regulatory role in binding (membrane-embedded) gangliosides. In summary, we have shown that MAG interacts with membrane-bound gangliosides via the side chain of R118, the CC'-loop and the F and G β-strands of the N-terminal V-type Ig1 domain and that the W22 mannosylation does not enhance ganglioside binding.

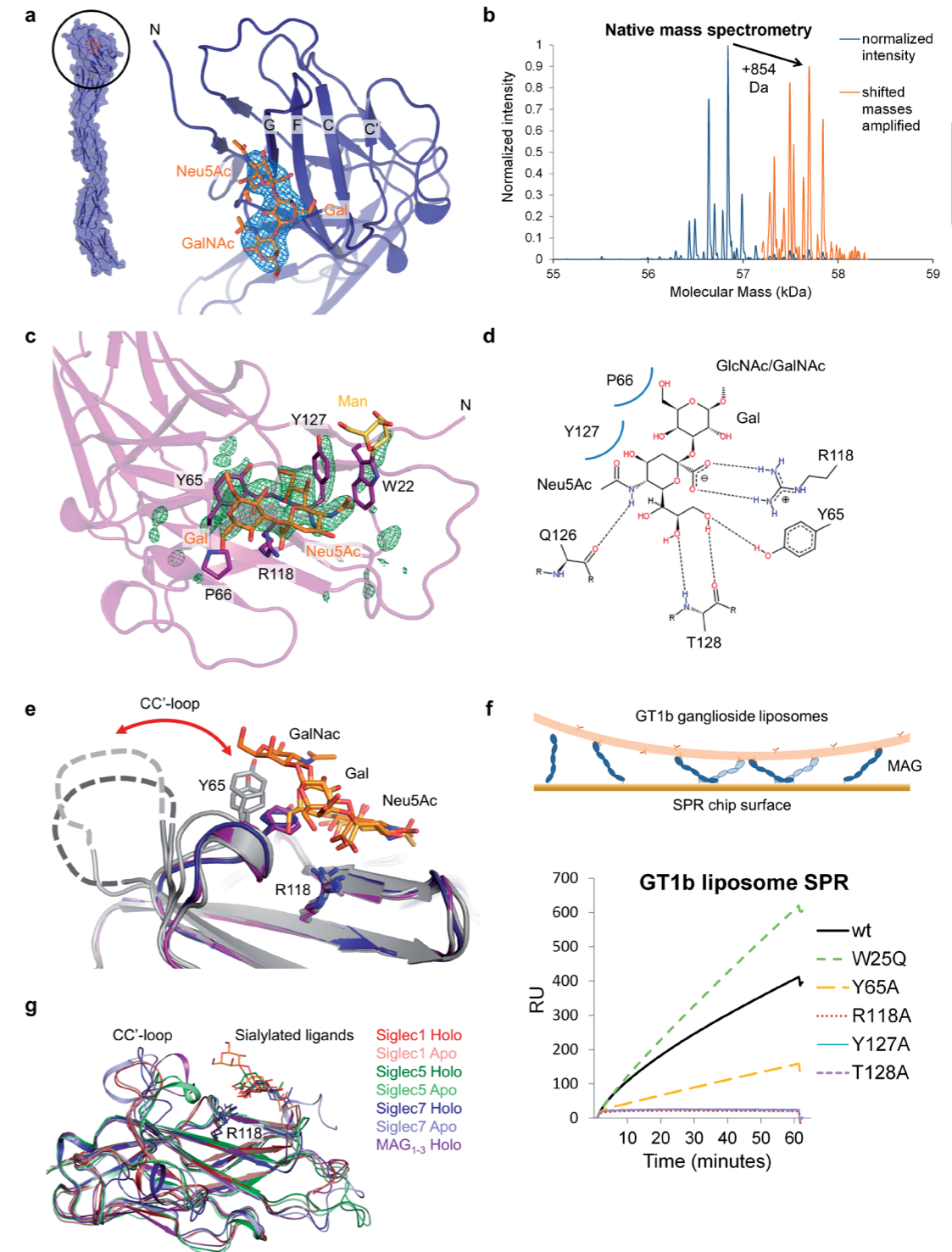
Ligand interaction of MAG is similar to the sialic acid recognition of other Siglec family members (Fig. 3g)^{30,32}. As in Siglec5³², the MAG Ig1 CC'-loop (residues 64-70) seems to undergo conformational selection upon ligand binding. This loop adopts a single conformation when a ligand is bound, whereas it can have several conformations (including the ligand-bound conformation) or is unstructured in the different unliganded MAG crystal forms (Fig. 3e). Furthermore, this loop adopts different conformations in the Siglec-1, -5 and -7 structures (both unliganded and ligand-bound forms, Fig. 3g)³⁰⁻³². The combination of our structural and biophysical data on MAG-ganglioside interaction, with that of others on MAG's specificity for Neu5Ac-α2,3-Gal-β1,3-GalNAc¹⁸ establishes the structural basis of ganglioside recognition by MAG.

Neurite outgrowth inhibition depends on MAG dimerization

We tested different MAG variants in neurite outgrowth assays to determine the role of MAG dimerization for neuronal plasticity inhibition (Fig. 4). In agreement with previous data^{20,38}, MAG₁₋₅ wt on cover slips inhibited neurite outgrowth of hippocampal neurons compared to poly-L-lysine-covered slips (Fig. 4a and 4b). Other dimeric variants (MAG₁₋₅ N406Q and MAG₁₋₅-Fc) inhibited neurite outgrowth to a similar level (Fig. 4d and 4f). The monomeric MAG₁₋₅ I473E and MAG₁₋₃ wt, on the other hand, showed no significant neurite outgrowth inhibition (Fig. 4c and 4e). Interestingly, MAG₁₋₅-Fc R118A, which is dimeric but lacks sialic acid binding properties, showed neurite outgrowth stimulation instead of inhibition, compared to poly-L-lysine (Fig. 4g). These data indicate that dimerization through domains Ig4-Ig5 and the ability to bind sialic acid moieties on the neuronal surface are required for neurite outgrowth inhibition signaling by MAG for hippocampal neurons.

Figure 3. Structural characterization of ligand recognition by the N-terminal domain Ig1 of MAG

(a) $2F_o - F_c$ electron density map displayed at a contour level of 1.3σ before placing any ligand for refinement in the MAG₁₋₅ deglycosylated crystal structure (blue), showing a density that fits well with the Neu5Ac- α 2,3-Gal- β 1,3-GalNAc trisaccharide (orange). (b) Native mass spectrometry reveals two species that have a mass difference of 854 ± 1.4 Da, presumably because of oligosaccharide ligand binding. The deconvolved mass *versus* intensity spectrum (blue) is shown together with the 20x amplified version of this spectrum for masses above 57.2 kDa (orange) to highlight the similar pattern of trimmings between the unliganded and ligand-bound form. (c) $F_o - F_o$ (soaked-unsoaked) electron density at a contour level of 3.0σ of MAG₁₋₃ at the ganglioside binding site of chain B, showing the unbiased electron density changes that resulted from binding of the 3'-Sialyl-N-acetylglucosamine (Neu5Ac- α 2,3-Gal- β 1,4-GlcNAc) ligand and concomitant small conformational rearrangements. Residues involved in ligand engagement (sticks), as well as the C-mannosylation (yellow) on W22 are shown. The first two sugars of the 3'-Sialyl-N-acetylglucosamine (orange) fit the density well. (d) Protein-ligand interactions with hydrogen bonds indicated by dashes and Van Der Waals' contacts by curved blue lines. (e) Comparison of the four unliganded (grey) and the two ligand-bound structures of MAG; MAG₁₋₅ deglycosylated (blue) and soaked MAG₁₋₃ (purple). The CC' loop adopts different conformations in the unliganded structures yet appears to undergo conformational selection by interactions of Y65 in this loop with the ligand. (f) GT1b ganglioside liposome SPR confirms the contribution of contact residues from the crystal structures. Liposome and MAG molecules are displayed approximately to scale in schematic representation. Surprisingly, the W25Q mutant that lacks the tryptophan mannosylation on W22 shows enhanced ligand binding. (g) Similar ligand recognition by four different Siglec family members; MAG (purple, MAG₁₋₃ structures), Siglec1 (red), Siglec5 (green) and Siglec7 (blue). Shown are unliganded forms (lighter colors), ligand-bound forms (darker colors) with sialylated ligands and the conserved arginine (stick representation, R118 in MAG) that forms a salt bridge with the carboxylic acid group of the sialic acid. The structurally heterogeneous CC' loop is also indicated.



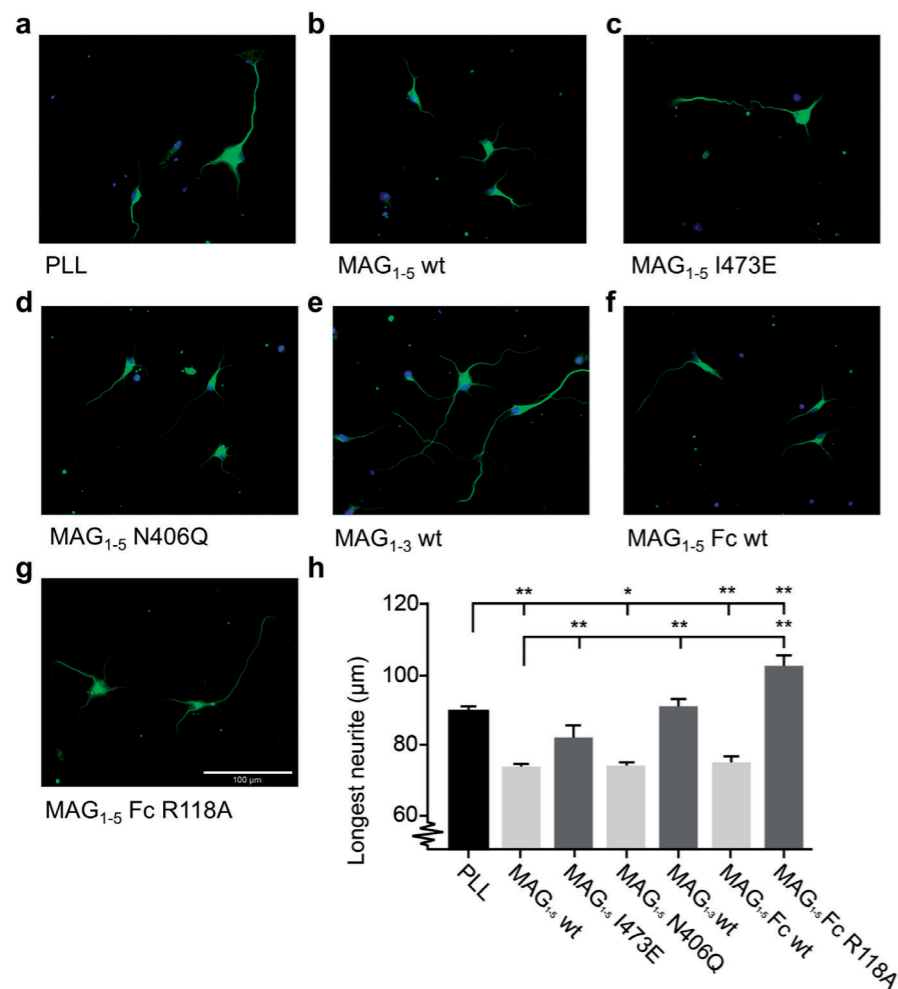


Figure 4. MAG dimerization and sialic acid-binding are required for neurite outgrowth inhibition of hippocampal neurons.

Dissociated neuron cultures were prepared from postnatal day 1 (P1) hippocampus and grown for 2 days *in vitro* (DIV2) on (a) Poly-L-lysine (PLL) ($20 \mu\text{g mL}^{-1}$) as a control or on coverslips coated with PLL and MAG proteins ($60 \mu\text{g mL}^{-1}$): (b) MAG₁₋₅ wt, (c) MAG₁₋₅ I473E, (d) MAG₁₋₅ N406Q, (e) MAG₁₋₃ wt, (f) MAG₁₋₅-Fc wt, or (g) MAG₁₋₅-Fc R118A. Cultures are immunostained with antibodies against β III-tubulin and 4',6-diamidino-2-phenylindole (DAPI). Quantification of the length of the longest neurite is shown in μm in (h). $n = 6$ mice, One-way ANOVA with Tukey posthoc test was used, *: $P < 0.05$. **: $P < 0.01$. Error bars represent standard error of the mean. Only dimeric and not monomeric MAG constructs inhibit neurite outgrowth compared to PLL. Surprisingly, a dimeric variant that does not bind sialic acids (MAG₁₋₅-Fc R118A) appears to stimulate neurite outgrowth.

Discussion

MAG controls adhesion and signaling between myelinating cells and axons. In contrast to earlier studies^{28,29}, we find that MAG does not fold back onto itself like an Ig-horseshoe as in the L1CAM and axonin neuronal adhesion molecules. Instead, our data show that the extracellular region of MAG has an extended shape with limited inter-domain flexibility, similar to several other cell adhesion molecules such as SYG, Cadherin and Nectin family members³⁹⁻⁴¹.

The structure of MAG is the first of a full extracellular portion of a Siglec family member. Besides the common N-terminal V-type Ig domain for recognizing sialic acid moieties, Siglecs vary in the number of additional Ig domains; from 1 up to 16. Comparison of the structures of MAG and Siglec5 reveals a different inter-domain orientation between domains Ig1 and Ig2, likely due to differences in amino acids at the interface (Supplementary Fig. 17 and Supplementary notes).

By binding to axonal gangliosides, MAG maintains a defined spacing between the innermost myelin surface and the axon surface^{10-12,42}. This myelin-axon spacing has been reported to be 12-14 nm based on electron micrographs of chemically fixed myelin tissue¹⁰⁻¹². However, analysis of more recent electron micrographs of high-pressure frozen myelin that does not suffer from fixation induced artifacts⁴³ reveals an axon-myelin spacing of 9-12 nm. This periaxonal diameter matches well with a straightforward model that follows from our structural data of the MAG dimer and the MAG-ganglioside interaction: two opposing membrane surfaces are spaced 10 nm apart when the membrane-proximal C-termini of the MAG dimer are positioned on one membrane (the structures lack only two residues to the transmembrane helix) and the MAG dimer-bound gangliosides are positioned on the other membrane (Fig. 5). Although the two crystal forms of the full extracellular segment of MAG have different inter-domain angles (3.4 to 17.4°), the overall arrangement and resulting structure-based axon-myelin spacing is similar (see also Fig. 2a). The agreement of intermembrane distance determined from high-pressure frozen electron microscopy on myelin tissue⁴³ and here by structural and biophysical data on the extracellular segment of MAG indicates that in the periaxonal space, MAG is dimerized *in cis* via domains Ig4-Ig5 when bound to axonal gangliosides *in trans*.

Intriguingly, in this model, the unusual tryptophan C-mannosylation on W22 is positioned at the interface of MAG and the extracellular leaflet of the axonal membrane (Fig. 5, Supplementary Fig. 18). The WxxW motif is conserved among MAG orthologues in vertebrates from fish to human, but is absent in all other Siglec paralogs (Supplementary Fig. 6). This suggests that tryptophan mannosylation is specific for the function of MAG. We showed that the mannosyl-group does not enhance the binding of MAG to GT1b ganglioside liposomes but may weaken it. Possibly, tryptophan mannosylation of MAG

provides specificity to sialylated ligand interactions. Alternatively, the close proximity of the mannosyl group to the axonal membrane during MAG-ganglioside interaction may indicate a regulatory role in axonal membrane engagement.

The surface area of the MAG dimerization interface formed by Ig4 and Ig5 is large (2037 Å²) and hydrophobic. We find, however, that the affinity of MAG dimerization via this interface in solution is low (K_d of 3.8×10^2 μM). The weak interaction is probably important in the native context, where MAG is expressed on the cell surface, as the *cis*-dimer can be *trans*-stabilized by interaction with gangliosides on the opposing axonal membrane. For the N-Cadherin family of cell adhesion molecules it has been shown that affinities as weak as 10 mM in solution are functionally important in the context of a *trans*-stabilized *cis*-dimer³⁹.

Dimerization of MAG may serve two purposes. It provides a mechanism to restrain the intermembrane distance, since a *cis-trans* stabilized MAG dimer would restrict angular freedom with respect to the membrane more than a *trans* only stabilized MAG monomer. In this sense, the MAG dimer could function as a “molecular leaf spring” that maintains the well-defined spacing between the axonal membrane and the adaxonal myelin membrane along the internode. Additionally, dimerization of MAG could enable compaction of the periaxonal space. The weak *cis*-interaction of MAG, if not stabilized in *trans*, may ensure enough monomer is available to bridge a wider periaxonal spacing (of up to 16 nm, based on the length of a MAG monomer) that may exist during myelin formation. Even greater distances could be bridged if MAG binds to sialylated N- or O-linked glycans of axonal surface glycoproteins before reaching the gangliosides. When *trans*-interactions with gangliosides have been established and possibly local concentrations are elevated due to the abundance of ganglioside ligands, the formation of MAG *cis*-dimers is triggered concomitant with compaction of the periaxonal diameter to its final spacing (Fig. 5).

Dimerization of MAG can be regulated by modulating glycosylation on N406. Large and charged glycans on N406 can obstruct dimerization because of steric clashes and coulombic repulsion. Trimming all MAG N-linked glycans down to single N-Acetylglucosamines by deglycosylation with Endo-Hf or preventing glycosylation on N406 by mutating it to glutamine enhances dimerization (Fig 2, Supplementary Fig. 8-12 and 16, table 2 and 3). This glycosylation site might play a regulatory role during myelin development and myelination-related pathologies. MAG glycosylation changes during development⁴⁴ and abnormal glycosylation of MAG correlates with myelination deficiencies⁴⁵⁻⁴⁷. Possibly, modulation of N406 glycosylation, either at the biosynthesis level or by extracellular trimming, affects MAG dimerization and thereby impacts on the myelin-axon interaction (see Supplementary notes for details).

Myelin-to-neuron signaling with MAG as a ligand can inhibit neurite outgrowth^{2,3,20,21,48}. Studies based on MAG truncations, chimeras and mutant versions suggested that the

inhibitory properties reside in domains Ig4 and Ig5, and in the sialic acid binding site^{20,49,50}. For example, a chimeric protein consisting of Siglec1 Ig domains 1-3 plus MAG Ig4-5, but not Siglec1 domains 1-3 alone, has neurite outgrowth inhibition properties similar to MAG⁴⁹. We confirmed that the sialic acid-binding properties of MAG are required for neurite outgrowth inhibition in hippocampal neurons as the MAG₁₋₅-Fc R118A mutant that lacks ganglioside binding properties does not inhibit, but surprisingly, stimulates neurite outgrowth (Fig. 4g). This has not been reported before and may be an interesting new avenue for therapeutic intervention to enhance central nervous system regeneration. In addition, we show that domains Ig4 and Ig5 are essential for MAG dimerization and that neurite outgrowth inhibition is abrogated by the I473E point mutation that monomerizes MAG (Fig. 4e and 4c). Thus, it is the dimerization of MAG that is required for neurite outgrowth inhibition, rather than direct interactions of domains Ig4 and Ig5 with neuronal receptors, as previously suggested^{49,50}. Although other protein receptors have been identified that mediate the neurite outgrowth-inhibiting signaling by MAG³, it has been shown that direct clustering of gangliosides by antibodies also leads to inhibition of neurite outgrowth of hippocampal neurons²⁰. The combination of our data and that of others indicates that MAG dimerization at domains Ig4 and Ig5 and sialic acid binding at domain Ig1 induces neurite outgrowth inhibition for hippocampal neurons, by clustering of gangliosides. Axon-to-myelin signaling with MAG as a receptor controls myelin formation. Antibody-mediated extracellular clustering of the L-MAG isoform activates Fyn kinase²³ and Fyn activation is essential for the initiation of myelination²⁵. Our structures show that the C-termini of MAG₁₋₅ are separated by 5.4 nm in the dimer, bringing the cytosolic regions into close proximity (Fig. 5). Probably, L-MAG dimerization as a result of *trans* interaction with gangliosides on the axon brings the cytosolic regions of MAG into close proximity to trigger activation of Fyn, similar to Fyn activation by Signaling Lymphocytic Activation Molecule (SLAM) clustering in immune cells⁵¹. Whether MAG forms higher-order clusters that are triggered by dimerization needs to be established, but a preference of both MAG and Fyn for lipid rafts^{24,52} suggests that both proteins can be locally enriched in the membrane to assist clustering.

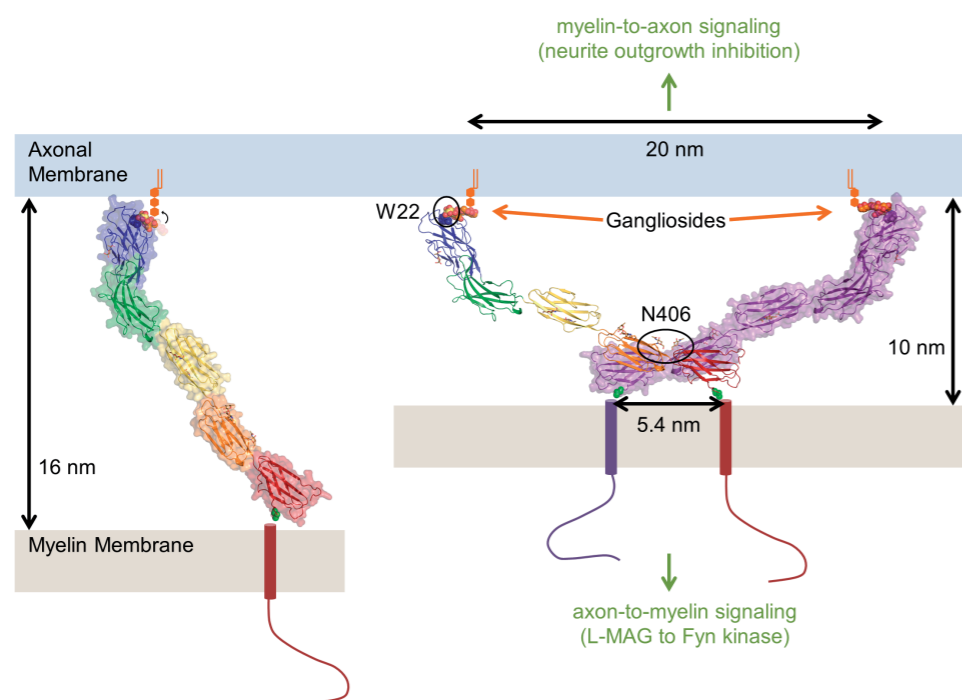


Figure 5. Model for MAG-mediated myelin-axon engagement and signaling

The MAG_{1-5} (cartoon and surface representation) monomer and dimer are indicated, with the trisaccharide ligand (orange spheres, coloring as in Fig. 1) and the tryptophan mannose on W22 (yellow spheres). Whereas monomeric MAG could span intermembrane distances of approximately 16 nm (left), the *cis* dimerization of MAG restricts the periaxonal diameter to 10 nm (right). The arrow at the ganglioside binding site in the left panel indicates that the third sugar, which has the highest B-factors in the deglycosylated MAG_{1-5} structure and is not visible in the ligand-bound MAG_{1-3} structure, needs to be in a different conformation to accommodate such binding. The dimerization of MAG brings the cytosolic regions into close proximity. This possibly triggers signaling into the myelin-forming oligodendrocyte cell. See also Supplementary Fig. 18.

Methods

Generation of constructs and mutagenesis

MAG constructs were generated by polymerase chain reaction (PCR) using mouse S-MAG (IMAGE 40039200) as a template and primers to start at (UNIPROT) residue number 20 (after the signal peptide) and end at residue 325 for MAG_{1-3} and residue 508 for MAG_{1-5} . Point mutants were also created by PCR, either by a two-step PCR with overlapping primers (W22A, W25Q, Y65A, R118A, Y127A, T128A, I473E,) or by a single-step PCR using non-overlapping phosphorylated primers (N406Q). All constructs were subcloned using BamHI/NotI sites in pUPE107.03 (cystatin secretion signal peptide, C-terminal His₆-tag), unless indicated otherwise.

Large-scale expression and purification

Constructs were transiently expressed in N-acetylglucosaminyltransferase I-deficient (GnTI-) Epstein-Barr virus nuclear antigen 1 (EBNA1)-expressing HEK293 cells in suspension (U-Protein Express). The medium was harvested six days after transfection and cells were spun down by 10 minutes of centrifugation at 1000× g. Supernatant was concentrated fivefold and diafiltered against 500 mM NaCl, 25 mM HEPES pH 7.8 (IMAC A) using a Quixstand benchtop system (GE Healthcare) with a 10 kDa molecular weight cut-off (MWCO) membrane. Cellular debris was spun down for 10 minutes at 9500× g and the concentrate was filtered with a glass fiber prefilter (Minisart, Sartorius). Protein was purified by Nickel-nitrilotriacetic acid (Ni-NTA) affinity chromatography followed by size exclusion chromatography (SEC) on a Superdex200 Hiload 16/60 column (GE Healthcare) equilibrated in SEC buffer (150 mM NaCl, 20 mM HEPES pH 7.5). Protein was concentrated to 7–14 mg/mL using a 30 kDa MWCO concentrator before plunge freezing in liquid nitrogen and storage at -80 °C.

Crystallization and data collection

Since initial crystallization attempts did not yield diffraction-quality crystals, several methods were employed to enhance crystallization. Deglycosylation was performed by adding Endo-Hf (1.0×10^6 U mL⁻¹, New England Biolabs) 1:100 (v/v) directly to the concentrated protein and incubating overnight at 37 °C. Completeness of the reaction was analyzed by SDS-PAGE and sample quality was assessed by SAXS (see table 2). As an alternative approach, reductive lysine methylation was performed on glycosylated MAG_{1-5} diluted to 1 mg/mL, by two steps of two hours incubation at 4 °C with 1 M dimethylamine-borane complex (added 1:50, v/v), and 1 M formaldehyde (added 1:25, v/v)⁵³. The reaction was completed by a final addition of 1 M dimethylamine-borane complex (added 1:100, v/v) and incubated overnight at 4 °C, after which the reaction was quenched by performing a SEC run on a Superdex200 (GE Healthcare) column equilibrated in 20 mM Tris/HCl pH 7.5, 200 mM NaCl. Therefore, this was the buffer used to set up crystallization experiments of the lysine-methylated protein. Sitting-drop vapor diffusion at 18 °C was used for all crystallization trials, by mixing 150 nL of protein solution with 150 nL of reservoir solution. Crystals of deglycosylated MAG_{1-5} (6.7 mg/mL) appeared in a condition of 100 mM NaCl, 20 mM Tris/HCl pH 7.0, 7.7 % PEG 4000 (w/v). Crystals of lysine-methylated MAG_{1-5} (8.4 mg/mL) appeared in a condition containing 200 mM NaOAc, 20 % PEG3350 (w/v). Crystals of MAG_{1-3} (12.2 mg/mL) appeared in a condition containing 0.05 M tri-sodium citrate, 1.2 M ammonium sulfate, 3 % (w/v) isopropanol. MAG_{1-3} crystals were soaked overnight by addition of 1 μL reservoir solution containing 10 mM 3'-N-Acetylneuraminy-N-acetyllactosamine (Neu5Ac-α2,3-Gal-β1,4-GlcNAc, Sigma-Aldrich product A6936) to the drop. Crystals were cryo-protected with reservoir solution supplemented with 25

% of glycerol for deglycosylated MAG₁₋₅ and MAG₁₋₃ and with 25 % ethylene glycol for lysine-methylated MAG₁₋₅. After brief incubation in the cryo-protectant solution, crystals were plunge-cooled in liquid nitrogen. Datasets were collected at 100 K at the Deutsches Elektronen-Synchrotron (DESY) PETRA III beamline P14 (lysine-methylated MAG₁₋₅, $\lambda = 0.97553 \text{ \AA}$), the European Synchrotron Radiation Facility (ESRF) beamline ID23-1 (MAG₁₋₃, $\lambda = 0.97599 \text{ \AA}$) and Swiss Light Source (SLS) beamline PX (deglycosylated MAG₁₋₅ and soaked MAG₁₋₃, $\lambda = 0.99998 \text{ \AA}$).

Structure solution and refinement

Data were integrated by IMOSFLM⁵⁴ (MAG₁₋₅ deglycosylated, MAG₁₋₅ lysine-methylated and MAG₁₋₃ ligand bound) or XDS⁵⁵ (MAG₁₋₃ unliganded) and scaled and merged by the AIMLESS pipeline⁵⁶. All structures were solved by molecular replacement using PHASER⁵⁷. Initial search models were PDB IDs 1URL⁵⁸ for Ig1, 4FRW⁴¹ residues 150-242 for Ig2, 1CS6⁵⁹ residues 308-388 for domain Ig3, 3P3Y⁶⁰ residues 55-185 for Ig4 and 2YD6⁶¹ residues 132-221 for Ig5. First MAG₁₋₃ was solved by searching for two copies of 1URL, followed by two copies of 1CS6 and finally two copies of 4FRW. Search models were trimmed to polyalanine chains by CHAINSAW⁶² to obtain better starting density. Next, deglycosylated MAG₁₋₅ was solved by searching for the first two (refined) domains of MAG₁₋₃, followed by SCULPTOR⁶³-trimmed versions of 3P3Y and 2YD6 respectively. Lastly, the Ig3 domain was searched using the refined Ig3 of MAG from MAG₁₋₃ as this domain had a much higher B-factor in the MAG₁₋₅ crystals, likely because of the lack of any crystal packing contacts for this domain. It was important to realize that the unit cell only contained a single copy of MAG, resulting in a solvent content of 91%, which was used in PHASER to estimate the total scattering. Lysine-methylated MAG₁₋₅ was solved by searching for the Ig1, Ig2, Ig4, Ig5 and Ig3 from the refined MAG₁₋₃ and deglycosylated MAG₁₋₅ structures, in that order. Again, Ig3 was searched last because of the high B-factor. After molecular replacement, models were improved by iterative density modification by DM (CCP4)⁶⁴, manual model building in COOT⁶⁵ and refinement with REFMAC⁶⁶. Final refinement was performed with PHENIX⁶⁷ and validation with Molprobity⁶⁸. In both MAG₁₋₅ structures, Ig3 from the higher resolution MAG₁₋₃ structure was used as a reference structure to restrain refinement, because of the high B-factor and the resulting poor density for that domain. Ramachandran statistics were (% Ramachandran favored / % allowed / % outliers): 93/7/0 (MAG₁₋₅ deglycosylated), 91/9/0 (MAG₁₋₅ lysine-methylated), 97/3/0 (MAG₁₋₃ unliganded) and 96/4/0 (MAG₁₋₃ ligand bound). The buried surface area for MAG dimerization was calculated by PISA⁶⁹.

Small angle X-ray scattering

Small-angle X-ray scattering (SAXS) was performed at the ESRF BM29 BioSAXS beamline equipped with a 2D Pilatus 1M detector (DECTRIS, Switzerland), operated

at an energy of 12.5 keV. MAG constructs were diluted with and dialyzed against SEC buffer using a 10 kDa MWCO membrane. The concentrations were determined by UV-Vis spectroscopy on a nanodrop ND-1000 spectrophotometer. Similar concentrations were selected for all samples to allow comparison (see table 2). SAXS data were collected at 20 °C unless indicated otherwise. The data were radially averaged, normalized to the intensity of the transmitted beam and exposure time and the scattering of the solvent-blank (SEC buffer) was subtracted, following standard procedures. The curve was scaled using a BSA reference so that the I_0 represents the molecular mass of the sample. Radiation damage was monitored by comparing curves collected from the same sample, only curves without radiation damage were merged. A single concentration was used for all measurements, no extrapolation to zero concentration was performed. Data were analyzed by PRIMUS⁷⁰, GNOM⁷¹, DAMMIF⁷², CRY SOL⁷³ and OLIGOMER⁷⁰ of the ATSAS⁷⁴ suite.

Analytical ultracentrifugation

Sedimentation equilibrium experiments were carried out in a Beckman Coulter Proteomelab XL-I and a Beckman Optima XL-A analytical ultracentrifuge. Either 12 or 3 mm centerpieces with quartz windows were used, 12 mm for the lowest concentrations and 3 mm for the others. An-60 and An-50 Ti rotors (Beckman) were used to carry out the measurements. MAG constructs were diluted with and dialyzed against SEC buffer using a 10 kDa MWCO membrane. Input concentrations of 3.8, 35.3 and 89.0 μM (MAG₁₋₅ wt glycosylated), 16.8, 27.2, 35.5 and 144 μM (MAG₁₋₅ wt deglycosylated), 3.6, 8.3, 41.4 and 102.8 μM (MAG₁₋₅ I473E glycosylated), 7.2, 57.4 and 332 μM (MAG₁₋₃ wt glycosylated) were used. Sedimentation equilibrium runs were performed at 20 °C and at 7500, 14000 and 20000 rpm. Absorbance was determined at 250, 280 and 300 nm with SEC buffer as a reference. Buffer density and viscosity were determined by SEDNTERP as 0.99823 g mL⁻¹ and 0.001002 Pa·s, respectively.

In-gel digestion and LC-MS/MS

MAG₁₋₅ was separated by SDS-PAGE, and cut from gel for digestion with trypsin (Promega). The gel band was cut to small pieces, washed in Milli-Q water and treated with acetonitrile to shrink the gel pieces. The sample was then incubated in 1 g/L 1,4-dithiothreitol (DTT) for 60 minutes at 60 °C, treated with acetonitrile, alkylated with 10 g/L iodoacetamide for 30 minutes at room temperature in the dark and subsequently washed with ammonium bicarbonate and treated with acetonitrile, twice. The gel pieces were then incubated on ice for 90 minutes with 30 mg/L trypsin. Excess trypsin was removed, the gel pieces were covered in ammonium bicarbonate, and the samples were subsequently incubated overnight at 37 °C. The digested samples were collected and remaining sample was extracted from the gel pieces by treatment with

acetonitrile. The solution with the peptides was subsequently dried in a speedvac and the peptides resuspended in 10% formic acid, 5% dimethylsulfoxide (DMSO) in water. Peptides were separated by reversed phase liquid chromatography (LC) coupled on-line to an Orbitrap Elite for MS/MS analysis. The nano-LC consists of an Agilent 1200 series LC system equipped with a 20 mm ReproSil- Pur C18-AQ (Dr. Maisch GmbH) trapping column (packed in-house, i.d., 100 μ m; resin, 5 μ m) and a 400 mm ReproSil-Pur C18-AQ (Dr. Maisch GmbH) analytical column (packed in-house, i.d., 50 μ m; resin, 3 μ m) arranged in a vented-column configuration. The flow was passively split to 100 nL/min. We used a standard 45-minute gradient from 7-30% acetonitrile in aqueous 0.1% formic acid. All precursors were fragmented by both ETcaD and HCD. Data were searched against a custom database of recombinant protein sequences, including the MAG constructs used here, with trypsin as protease, allowing up to 2 missed cleavages. We used a 50 ppm precursor mass window and 0.02 Da fragment mass window. The C-mannosylated peptide, with 3+ precursor charge, eluted after 33-34 minutes and was identified by both HCD and ETcaD MS/MS, with matched fragment ions supporting site localization for the C-mannosylation.

Native mass spectrometry

Purified protein samples were deglycosylated with Endo-H_f as for crystallization, followed by buffer exchange to 150 mM ammonium acetate pH 7.5, using Vivaspins 500 10 kDa MWCO centrifugal filter units. Samples were loaded onto gold-coated borosilicate capillaries prepared in-house for nanoelectrospray ionization. Samples were analyzed on a modified Orbitrap extended mass range (EMR) for high mass ions⁷⁵.

Surface plasmon resonance

MAG₁₋₅ wt and mutants cloned in-frame with an N-terminal cystatin secretion signal and a C-terminal Biotin Acceptor Peptide (BAP) and His₆-tag (sequence AAAGSGLNDIFEAQKIEWHEGRTKHHHHHH), were biotinylated in HEK293 cells by co-transfection with *E. coli* BirA biotin ligase with a sub-optimal secretion signal (in a pUPE5.02 vector), using a DNA ratio of 9:1 (MAG DNA : BirA DNA, m/m). Additional sterile biotin (100 μ L of 10 mg/mL Tris-buffered biotin per 4 mL HEK293 culture) was supplemented to the medium a few hours after transfection. MAG mutants were purified from the medium by Ni-NTA affinity purification. Purity was evaluated by SDS-PAGE and coomassie staining and biotinylation by a streptavidin gel-shift assay followed by α -His₆ Western blot (Supplementary Fig. 19). C-terminally biotinylated MAG proteins were spotted on a G-STREP SensEye chip (Ssens) with a Continuous Flow Microspotter (CFM, Wasatch Microfluidics) using an 8x6 format. The C-terminal coupling of MAG to the surface mimics the native, membrane attached topology. SEC buffer with 0.005% tween was used as a spotting buffer and the coupling was quenched using 1 mM biotin in SEC buffer solution.

GT1b ganglioside liposomes were prepared as described previously⁷⁶. In brief, the lipids dipalmitoyl phosphatidylcholine, dipalmitoyl phosphatidylglycerol, cholesterol and GT1b gangliosides were mixed in a molar ratio of 40.3:4.2:40.9:1.3 in a chloroform/methanol mixture (6:1, v/v). The lipid mixture was dried under vacuum on a rotary evaporator to create a thin film of lipids. Liposomes were formed by the addition of 1 mL of SEC buffer per 21.7 μ mol of lipid mixture and 11 freeze-thaw cycles. As a negative control, liposomes with the same lipid composition but lacking GT1b were prepared using the same protocol. Liposomes were extruded through a 100 nm membrane with a mini-extruder (Avanti Polar Lipids) at 70 °C.

Surface plasmon resonance experiments, with the liposomes in the mobile phase and the MAG constructs attached to the surface, were performed on an MX96 SPRi instrument (IBIS Technologies) equipped with a CX flowcell, using the CX vesicle run protocol and an association time of 60 minutes at a temperature of 25 °C. As a running buffer, SEC buffer without any detergent was used. Preliminary removal of co-purified ligands before the runs and regeneration after runs was performed by washes with 0.5 % SDS in phosphate-buffered saline (PBS) followed by 5 M NaCl. Data was zeroed and referenced using SprintX 1.11 (IBIS Technologies).

Animals

All animal use and care was in accordance with institutional guidelines and approved by the animal experimentation committee (DEC). Littermate C57BL/6 (Charles River) mice were killed by decapitation at postnatal day 1 (P1) before the brain was removed to prepare hippocampal neuronal cultures.

Neurite outgrowth assays

MAG₁₋₅-Fc constructs were generated by subcloning into pUPE7.12 vector using BamHI/NotI restriction sites (Fc is C-terminal of MAG), expressed in HEK293 cells and purified by protein-A affinity purification using standard protocols. Coverslips were all coated overnight at 4 °C with poly-L-lysine (PLL) (20 μ g/mL) and 2 hours at 37 °C with different MAG proteins (60 μ g/mL): phosphate-buffered saline (PBS) (PLL control), MAG₁₋₅ wt, MAG₁₋₅ I473E, MAG₁₋₅ N406Q, MAG₁₋₃ wt, MAG₁₋₅-Fc wt or MAG₁₋₅-Fc R118A (at least three independent experiments were conducted). It is expected that proteins immobilize non-specifically to the coverslips, therefore the immobilization efficiency of the different MAG variants was not experimentally verified. Hippocampal cultures were prepared as described previously⁷⁷. In brief, the hippocampus was dissected at P1 and collected in L15 dissection medium (Gibco) containing 7 mM HEPES (L15-HEPES). Cells were dissociated by incubation in 0.25% trypsin in L15-HEPES at 37 °C for 20 minutes. Following 3 washes with L15-HEPES, cells were triturated using a fire-polished Pasteur pipette in growth medium (neurobasal medium (Gibco)

with B-27 supplement (Thermo-Fisher), L-glutamine, penicillin/streptomycin and β -mercaptoethanol). Hippocampal neurons were resuspended in fresh growth medium and plated onto PLL- and MAG-coated glass coverslips. After two days in vitro (DIV2), hippocampal cultures were fixed for 10 minutes in 4 % paraformaldehyde followed by three washing steps with PBS, blocking with 5 % normal donkey serum and 0.1 % triton in PBS, and incubated overnight at 4 °C with mouse anti- β III-tubulin primary antibody (Covance, 1:500 (v/v)). The next day, cultures were washed three times with PBS and incubated with the secondary antibody (donkey anti-mouse Alexa Fluor 488, 1:750) for 2 hours at room temperature. After three PBS washing steps, coverslips were incubated with 4',6-diamidino-2-phenylindole (DAPI - Sigma) for 10 minutes. After several PBS washes, coverslips were mounted with FluorSave. Hippocampal neurons were visualized using a Zeiss Axioskop A1 using a 20 \times objective. Images were analyzed using FIJI (version 2.0.0)⁷⁸ by tracing the longest neurite of a hippocampal neuron (positive for tubulin and DAPI). Significance was determined using a one-way ANOVA ($p=0.0001$) with a Bonferroni posthoc test for multiple comparisons (GraphPad Prism version 6.07). Every construct was compared to control PLL or MAG wt. All quantitative assessments in this manuscript were performed while being unaware of the condition to avoid observer bias. During analysis, raw data were named in a descriptive way, without revealing experimental group information. Fluorescent microscopic imaging was always done with the same settings within experiments, and analyzing techniques were standardized. A single person analyzed all data obtained from the experiments. Significant levels were reached for the following proteins: MAG₁₋₅ wt (**, 348 neurons counted), MAG₁₋₅ N406Q (*, 385 neurons counted), MAG₁₋₅-Fc wt (**, 364 neurons counted) and MAG₁₋₅-Fc R118A (*, 369 neurons counted) compared to PLL (395 neurons counted). Constructs MAG₁₋₅ I473E (*, 342 neurons counted), MAG₁₋₃ wt (***, 353 neurons counted) and MAG₁₋₅-Fc R118A (****, 348 neurons counted) were significant compared to MAG₁₋₅ wt. * $P < 0.05$, ** $P < 0.01$, *** $P < 0.001$, **** $P < 0.0001$.

References

1. Simons, M. & Nave, K. Oligodendrocytes: Myelination and axonal support. *Cold Spring Harb. Perspect. Biol.* a020479 (2015). doi:10.1101/cshperspect.a020479
2. Quarles, R. H. Myelin-associated glycoprotein (MAG): past, present and beyond. *J. Neurochem.* **100**, 1431–1448 (2007).
3. Lopez, P. H. H. Role of myelin-associated glycoprotein (siglec-4a) in the nervous system. *Adv. Neurobiol.* **9**, 245–62 (2014).
4. Novarino, G. *et al.* Exome sequencing links corticospinal motor neuron disease to common neurodegenerative disorders. *Science* **343**, 506–11 (2014).
5. Lossos, A. *et al.* Myelin-associated glycoprotein gene mutation causes Pelizaeus-Merzbacher disease-like disorder. *Brain* **138**, 2521–2536 (2015).
6. Braun, P. E., Frail, D. E. & Latov, N. Myelin-associated glycoprotein is the antigen for a monoclonal IgM in polyneuropathy. *J. Neurochem.* **39**, 1261–5 (1982).
7. Poltorak, M., Steck, A. J. & Schachner, M. Reactivity with neural cell adhesion molecules in sera from patients with demyelinating diseases. *Neurosci. Lett.* **65**, 199–203 (1986).
8. Wajgt, A. & Górný, M. CSF antibodies to myelin basic protein and to myelin-associated glycoprotein in multiple sclerosis. Evidence of the intrathecal production of antibodies. *Acta Neurol. Scand.* **68**, 337–43 (1983).
9. Jahn, O., Tenzer, S. & Werner, H. B. Myelin proteomics: molecular anatomy of an insulating sheath. *Mol. Neurobiol.* **40**, 55–72 (2009).
10. Trapp, B. D. & Quarles, R. H. Presence of the myelin-associated glycoprotein correlates with alterations in the periodicity of peripheral myelin. *J. Cell Biol.* **92**, 877–882 (1982).
11. Trapp, B. D., Quarles, R. H. & Suzuki, K. Immunocytochemical studies of quaking mice support a role for the myelin-associated glycoprotein in forming and maintaining the periaxonal space and periaxonal cytoplasmic collar of myelinating Schwann cells. *J. Cell Biol.* **99**, 594–606 (1984).
12. Li, C. *et al.* Myelination in the absence of myelin-associated glycoprotein. *Nature* **369**, 747–50 (1994).
13. Pan, B. *et al.* Myelin-associated glycoprotein and complementary axonal ligands, gangliosides, mediate axon stability in the CNS and PNS: neuropathology and behavioral deficits in single- and double-null mice. *Exp. Neurol.* **195**, 208–17 (2005).
14. Spiegel, I. *et al.* A central role for Necl4 (SynCAM4) in Schwann cell–axon interaction and myelination. *Nat. Neurosci.* **10**, 861–869 (2007).
15. Maurel, P. *et al.* Nectin-like proteins mediate axon-Schwann cell interactions along the internode and are essential for myelination. *J. Cell Biol.* **178**, 861–874 (2007).
16. Zhu, Y. *et al.* Necl-4/SynCAM-4 Is Expressed in Myelinating Oligodendrocytes but Not Required for Axonal Myelination. *PLoS One* **8**, 4–11 (2013).
17. Lehmann, F., Gähje, H., Kelm, S. & Dietz, F. Evolution of sialic acid-binding proteins: Molecular cloning and expression of fish siglec-4. *Glycobiology* **14**, 959–968 (2004).
18. Kelm, S., Pelz, A., Schauer, R., Filbin, M. T. & Tang, S. Sialoadhesin, myelin-associated glycoprotein and CD22 define a new family of sialic acid-dependent adhesion molecules of the immunoglobulin superfamily. *Curr. Biol.* **4**, (1994).
19. Collins, B. E. *et al.* Sialic acid specificity of myelin-associated glycoprotein binding. *J. Biol. Chem.* **272**, 1248–55 (1997).
20. Vinson, M. *et al.* Myelin-associated glycoprotein interacts with ganglioside GT1b. A mechanism for neurite outgrowth inhibition. *J. Biol. Chem.* **276**, 20280–5 (2001).
21. McKerracher, L. *et al.* Identification of myelin-associated glycoprotein as a major myelin-derived inhibitor of neurite growth. *Neuron* **13**, 805–11 (1994).
22. Tang, S. *et al.* Myelin-associated glycoprotein interacts with neurons via a sialic acid binding site at ARG118 and a distinct neurite inhibition site. *J. Cell Biol.* **138**, 1355–66 (1997).
23. Umemori, H., Sato, S., Yagi, T., Aizawa, S. & Yamamoto, T. Initial events of myelination involve Fyn tyrosine kinase signalling. *Nature* **367**, 572–576 (1994).
24. Marta, C. B. *et al.* Myelin associated glycoprotein cross-linking triggers its partitioning into lipid rafts, specific signaling events and cytoskeletal rearrangements in oligodendrocytes. *Neuron Glia Biol.* **1**, 35–46 (2004).

25. Yamauchi, J. *et al.* Phosphorylation of Cytohesin-1 by Fyn Is Required for Initiation of Myelination and the Extent of Myelination During Development. *Sci. Signal.* **5**, ra69-ra69 (2012).
26. Kursula, P., Meriläinen, G., Lehto, V. P. & Heape, A. M. The small myelin-associated glycoprotein is a zinc-binding protein. *J. Neurochem.* **73**, 2110–2118 (1999).
27. Kursula, P., Lehto, V. P. & Heape, A. M. The small myelin-associated glycoprotein binds to tubulin and microtubules. *Mol. Brain Res.* **87**, 22–30 (2001).
28. Fahrig, T. *et al.* Functional Topography of the Myelin-associated Glycoprotein. I. Mapping of Domains by Electron Microscopy. *Eur. J. Neurosci.* **5**, 1118–1126 (1993).
29. Attia, J., Hicks, L., Oikawa, K., Kay, C. M. & Dunn, R. J. Structural properties of the myelin-associated glycoprotein ectodomain. *J. Neurochem.* **61**, 718–726 (1993).
30. May, A. P., Robinson, R. C., Vinson, M., Crocker, P. R. & Jones, E. Y. Crystal structure of the N-terminal domain of sialoadhesin in complex with 3' sialyllactose at 1.85 Å resolution. *Mol. Cell* **1**, 719–728 (1998).
31. Alphey, M. S., Attrill, H., Crocker, P. R. & van Aalten, D. M. F. High resolution crystal structures of Siglec-7. Insights into ligand specificity in the Siglec family. *J. Biol. Chem.* **278**, 3372–7 (2003).
32. Zhuravleva, M. a., Trandem, K. & Sun, P. D. Structural Implications of Siglec-5-Mediated Sialoglycan Recognition. *J. Mol. Biol.* **375**, 437–447 (2008).
33. Pedraza, L., Owens, G. C., Green, L. a & Salzer, J. L. The myelin-associated glycoproteins: membrane disposition, evidence of a novel disulfide linkage between immunoglobulin-like domains, and posttranslational palmitoylation. *J. Cell Biol.* **111**, 2651–61 (1990).
34. Burger, D., Pidoux, L. & Steck, A. J. Identification of the glycosylated sequons of human myelin-associated glycoprotein. *Biochem. Biophys. Res.* **197**, 457–464 (1993).
35. Furmanek, A. & Hofsteenge, J. Protein C-mannosylation: Facts and questions. *Acta Biochim. Pol.* **47**, 781–789 (2000).
36. de Beer, T., Vliegenthart, J. F., Löffler, A. & Hofsteenge, J. The hexopyranosyl residue that is C-glycosidically linked to the side chain of tryptophan-7 in human RNase Us is alpha-mannopyranose. *Biochemistry* **34**, 11785–11789 (1995).
37. Sedzik, J., Jastrzebski, J. P. & Grandis, M. Glycans of myelin proteins. *J. Neurosci. Res.* **93**, 1–18 (2015).
38. McKerracher, L. *et al.* Identification of myelin-associated glycoprotein as a major myelin-derived inhibitor of neurite growth. *Neuron* **13**, 805–811 (1994).
39. Wu, Y., Vendome, J., Shapiro, L., Ben-Shaul, A. & Honig, B. Transforming binding affinities from three dimensions to two with application to cadherin clustering. *Nature* **475**, 510–513 (2011).
40. Özkan, E. *et al.* Extracellular architecture of the SYG-1/SYG-2 adhesion complex instructs synaptogenesis. *Cell* **156**, 482–494 (2014).
41. Harrison, O. J. *et al.* Nectin ectodomain structures reveal a canonical adhesive interface. *Nat. Struct. Mol. Biol.* **19**, 906–15 (2012).
42. Kinter, J. *et al.* An essential role of MAG in mediating axon-myelin attachment in Charcot-Marie-Tooth 1A disease. *Neurobiol. Dis.* **0**, 221–231 (2013).
43. Snaidero, N. *et al.* Myelin Membrane Wrapping of CNS Axons by PI(3,4,5)P3-Dependent Polarized Growth at the Inner Tongue. *Cell* **156**, 277–290 (2014).
44. Quarles, R. H. Effects of pronase and neuraminidase treatment on a myelin-associated glycoprotein in developing brain. *Biochem J* **156**, 143–150 (1976).
45. Konat, G., Hogan, E. L., Leskawa, K. C., Gantt, G. & Singh, I. Abnormal glycosylation of myelin-associated glycoprotein in quaking mouse brain. *Neurochem. Int.* **10**, 555–8 (1987).
46. Bartoszewicz, Z. P. *et al.* Abnormal expression and glycosylation of the large and small isoforms of myelin-associated glycoprotein in dysmyelinating quaking mutants. *J. Neurosci. Res.* **41**, 27–38 (1995).
47. Bartoszewicz, Z. P., Lauter, C. J. & Quarles, R. H. The myelin-associated glycoprotein of the peripheral nervous system in trembler mutants contains increased α 2-3 sialic acid and galactose. *J. Neurosci. Res.* **43**, 587–593 (1996).
48. Schnaar, R. L. & Lopez, P. H. H. Myelin-associated glycoprotein and its axonal receptors. *J. Neurosci. Res.* **87**, 3267–3276 (2009).
49. Cao, Z. *et al.* The inhibition site on myelin-associated glycoprotein is within Ig-domain 5 and is distinct from the sialic acid binding site. *J. Neurosci.* **27**, 9146–54 (2007).
50. Wörter, V. *et al.* Inhibitory activity of myelin-associated glycoprotein on sensory neurons is largely independent of NgR1 and NgR2 and resides within Ig-Like domains 4 and 5. *PLoS One* **4**, e5218 (2009).
51. Chan, B. *et al.* SAP couples Fyn to SLAM immune receptors. *Nat Cell Biol* **5**, 155–160 (2003).
52. Vinson, M. *et al.* Lipid rafts mediate the interaction between myelin-associated glycoprotein (MAG) on myelin and MAG-receptors on neurons. *Mol. Cell. Neurosci.* **22**, 344–352 (2003).
53. Walter, T. S. *et al.* Lysine Methylation as a Routine Rescue Strategy for Protein Crystallization. *Structure* **14**, 1617–1622 (2006).
54. Battye, T. G. G., Kontogiannis, L., Johnson, O., Powell, H. R. & Leslie, A. G. W. iMOSFLM: A new graphical interface for diffraction-image processing with MOSFLM. *Acta Crystallogr. Sect. D Biol. Crystallogr.* **67**, 271–281 (2011).
55. Kabsch, W. Xds. *Acta Crystallogr. Sect. D Biol. Crystallogr.* **66**, 125–132 (2010).
56. Evans, P. R. & Murshudov, G. N. How good are my data and what is the resolution? *Acta Crystallogr. Sect. D Biol. Crystallogr.* **69**, 1204–1214 (2013).
57. McCoy, A. J. *et al.* Phaser crystallographic software. *J. Appl. Crystallogr.* **40**, 658–674 (2007).
58. Bukrinsky, J. T., St. Hilaire, P. M., Meldal, M., Crocker, P. R. & Henriksen, A. Complex of sialoadhesin with a glycopeptide ligand. *Biochim. Biophys. Acta - Proteins Proteomics* **1702**, 173–179 (2004).
59. Freigang, J. *et al.* The crystal structure of the ligand binding module of axonin-1/TAG-1 suggests a zipper mechanism for neural cell adhesion. *Cell* **101**, 425–433 (2000).
60. Liu, H., Focia, P. J. & He, X. Homophilic adhesion mechanism of neurofascin, a member of the L1 family of neural cell adhesion molecules. *J. Biol. Chem.* **286**, 797–805 (2011).
61. Coles, C. H. *et al.* Proteoglycan-specific molecular switch for RPTP σ clustering and neuronal extension. *Science* **332**, 484–8 (2011).
62. Stein, N. CHAINSAW: A program for mutating pdb files used as templates in molecular replacement. *J. Appl. Crystallogr.* **41**, 641–643 (2008).
63. Bunkóczi, G. & Read, R. J. Improvement of molecular-replacement models with *Sculptor*. *Acta Crystallogr. Sect. D Biol. Crystallogr.* **67**, 303–312 (2011).
64. Cowtan, K. DM: an automated procedure for phase improvement by density modification. *Jt. CCP4 ESF-EACBM Newsl. protein Crystallogr.* **31**, 34–38 (1994).
65. Emsley, P. & Cowtan, K. Coot: Model-building tools for molecular graphics. *Acta Crystallogr. Sect. D Biol. Crystallogr.* **60**, 2126–2132 (2004).
66. Murshudov, G. N. *et al.* REFMAC5 for the refinement of macromolecular crystal structures. *Acta Crystallogr. Sect. D Biol. Crystallogr.* **67**, 355–367 (2011).
67. Afonine, P. V. *et al.* Towards automated crystallographic structure refinement with phenix.refine. *Acta Crystallogr. Sect. D Biol. Crystallogr.* **68**, 352–367 (2012).
68. Chen, V. B. *et al.* MolProbity: All-atom structure validation for macromolecular crystallography. *Acta Crystallogr. Sect. D Biol. Crystallogr.* **66**, 12–21 (2010).
69. Krissinel, E. & Henrick, K. Inference of Macromolecular Assemblies from Crystalline State. *J. Mol. Biol.* **372**, 774–797 (2007).
70. Konarev, P. V., Volkov, V. V., Sokolova, A. V., Koch, M. H. J. & Svergun, D. I. PRIMUS: A Windows PC-based system for small-angle scattering data analysis. *J. Appl. Crystallogr.* **36**, 1277–1282 (2003).
71. Svergun, D. I. Determination of the regularization parameter in indirect-transform methods using perceptual criteria. *J. Appl. Crystallogr.* **25**, 495–503 (1992).
72. Franke, D. & Svergun, D. I. DAMMIF, a program for rapid ab-initio shape determination in small-angle scattering. *J. Appl. Crystallogr.* **42**, 342–346 (2009).
73. Svergun, D., Barberato, C. & Koch, M. H. J. CRYSOLE - a Program to Evaluate X-ray Solution Scattering of Biological Macromolecules from Atomic Coordinates. *J. Appl. Crystallogr.* **28**, 768–773 (1995).
74. Petoukhov, M. V. *et al.* New developments in the ATSAS program package for small-angle scattering data analysis. *J. Appl. Crystallogr.* **45**, 342–350 (2012).
75. Rose, R. J., Damoc, E., Denisov, E., Makarov, A. & Heck, A. J. R. High-sensitivity Orbitrap mass analysis of intact macromolecular assemblies. *Nat. Methods* **9**, 1084–6 (2012).
76. Ahn-Yoon, S., Decory, T. R. & Durst, R. a. Ganglioside-liposome immunoassay for the detection of botulinum toxin. *Anal. Bioanal. Chem.* **378**, 68–75 (2004).
77. Van Battum, E. Y. *et al.* The intracellular redox protein MICAL-1 regulates the development of hippocampal mossy fibre connections. *Nat. Commun.* **5**, 4317 (2014).
78. Schindelin, J. *et al.* Fiji: an open-source platform for biological-image analysis. *Nat. Methods* **9**, 676–82 (2012).

Acknowledgements

We thank the staff of the European Synchrotron Radiation Facility (ESRF) beamline ID23-1, Swiss Light Source (SLS) beamline PX and Deutsches Elektronen-Synchrotron (DESY) beamline PETRA III P14 for assistance with diffraction data collection and the staff of ESRF beamline BM29 for SAXS measurements. We thank Mike F. Renne and Jonas M. Dörr for assistance in preparing the GT1b liposomes used in the SPR experiment.

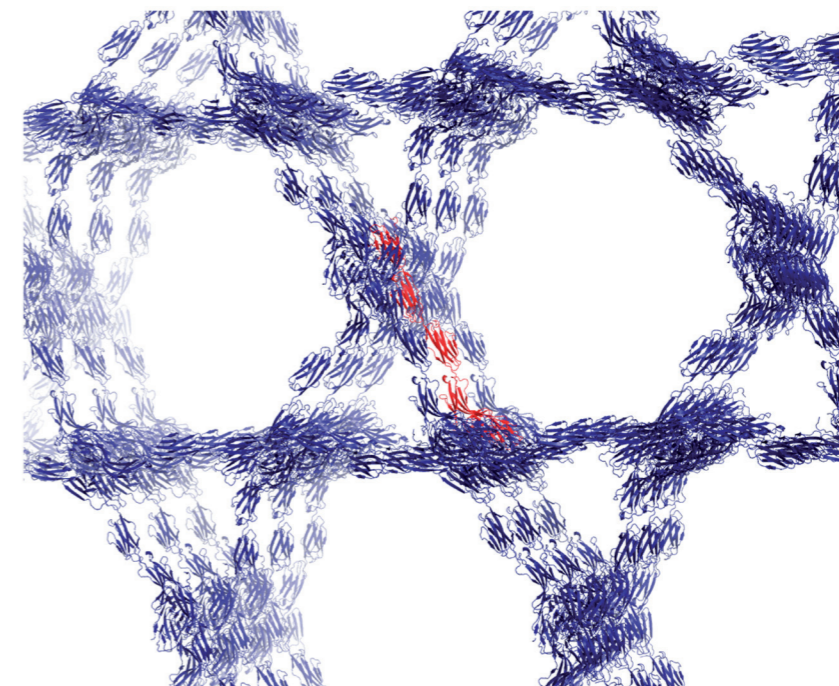
Author contributions

M.F.P. and B.J.C.J. designed the experiments. M.F.P. generated constructs, purified proteins and did all the structural biology (SAXS and X-ray diffraction). M.F.P. and D.T.W. performed SE-AUC experiments and analyzed the data. J.S. performed mass spectrometry experiments and analyzed the data together with A.J.R.H.. S.L. performed neurite outgrowth experiments and analyzed the data together with R.J.P.. B.J.C.J. supervised the project. M.F.P. and B.J.C.J. wrote the manuscript with input from all authors.

Data availability

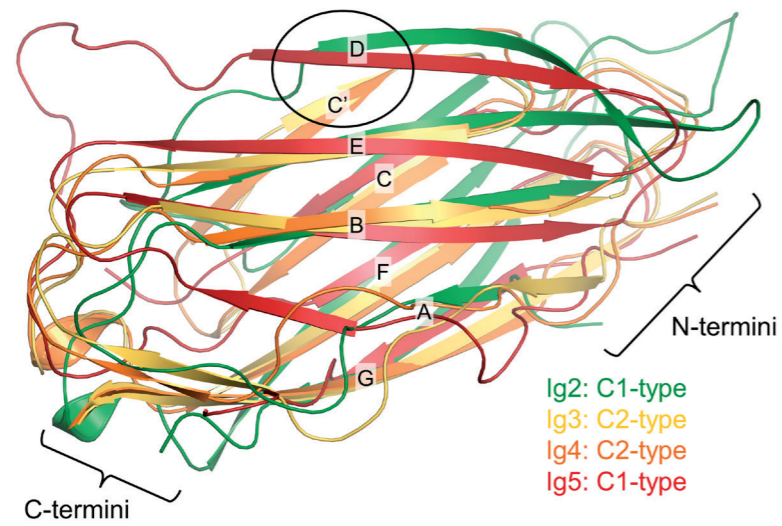
Coordinates and structure factors for MAG₁₋₅ deglycosylated (space group $P3_22$), MAG₁₋₅ methylated (space group $P6_522$), MAG₁₋₃ (space group $P1$) and MAG₁₋₃ ligand bound (space group $P1$) have been deposited in the Protein Data Bank with succession numbers 5LF5, 5LFU, 5LFR and 5LFV, respectively. All SAXS data is made available at the small angle scattering databank (SASBDB) with the accession codes SASDB55 (glycosylated MAG₁₋₅ wt), SASDB26 (glycosylated MAG₁₋₅ I473E), SASDB36 (glycosylated MAG₁₋₅ N406Q), SASDB46 (glycosylated MAG₁₋₃), SASDBF6 (deglycosylated MAG₁₋₅ wt) SASDB56 (deglycosylated MAG₁₋₅ I473E), SASDB66 (deglycosylated MAG₁₋₅ N406Q), SASDB76 (deglycosylated MAG₁₋₃).

Supplementary Figures



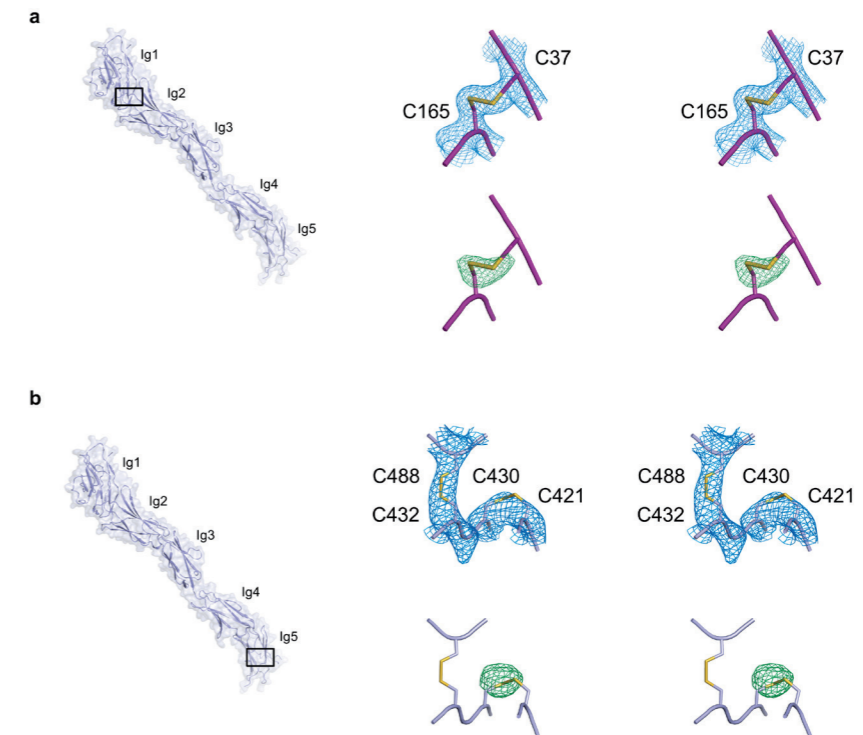
Supplementary Figure 1: High solvent content for MAG₁₋₅ deglycosylated crystals

The MAG₁₋₅ deglycosylated crystals in space group $P3_22$ have large solvent channels, explaining the high solvent content (91%) for these crystals. The MAG lattice is shown in blue, along the threefold screw axis, with a single MAG monomer highlighted in red.



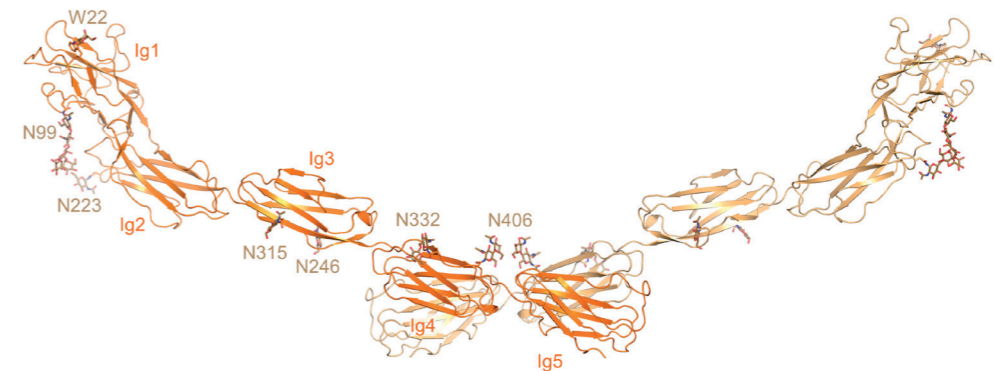
Supplementary Figure 2: Comparison of the MAG Ig2-5 domains, highlighting the different β -strand topology of strand D or C' for the C1- and C2-type Ig folds.

MAG Ig2-5 are all C-type Ig domains, colored as in figure 1a in this figure. Ig3 and Ig4 have a C2-type Ig fold as predicted. Ig2 and Ig5 on the other hand are of the C1-type, contrary to predictions. The C1- and C2-type Ig folds have a different β -strand topology of strand C' and D, indicated by a circle. Whereas the C1-type Ig fold has the D-strand aligning to the ABE sheet (in the frontal sheet from this point of view), this strand is aligning to the bottom CFG sheet in the C2-type fold, where it is referred to as the C'-strand.



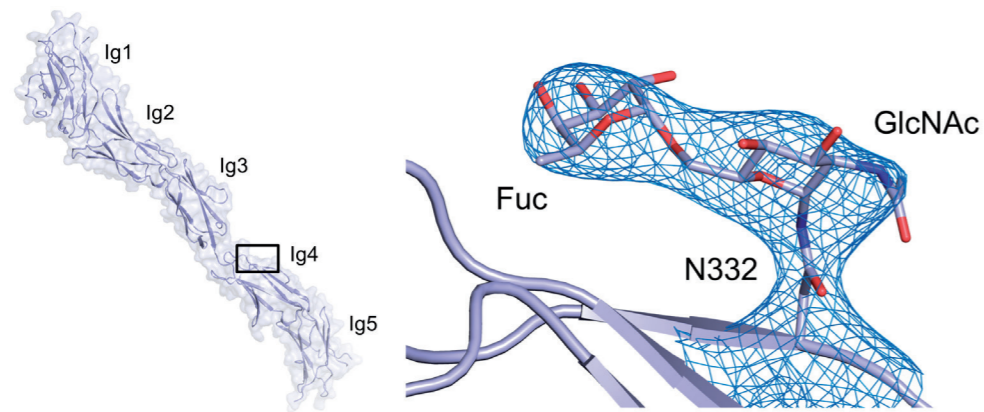
Supplementary Figure 3: Electron density around non-canonical disulfides

(a) Stereo image of the electron density around the disulfide of C37-C165 between Ig1 and Ig2 at a contour level of 1.3σ from the unliganded MAG_{1-3} structure (top) and simulated annealing omit map of the sulfur atoms of this disulfide at a contour level of 3.5σ (bottom) (b) Stereo image of the electron density around the disulfides of C421-C430 (non-canonical) and the adjacent canonical disulfide C432-C488 of Ig5 at a contour level of 1.2σ from the deglycosylated MAG_{1-5} structure (top) and simulated annealing omit map of the sulfur atoms of the C421-C430 disulfide at a contour level of 6σ (bottom).

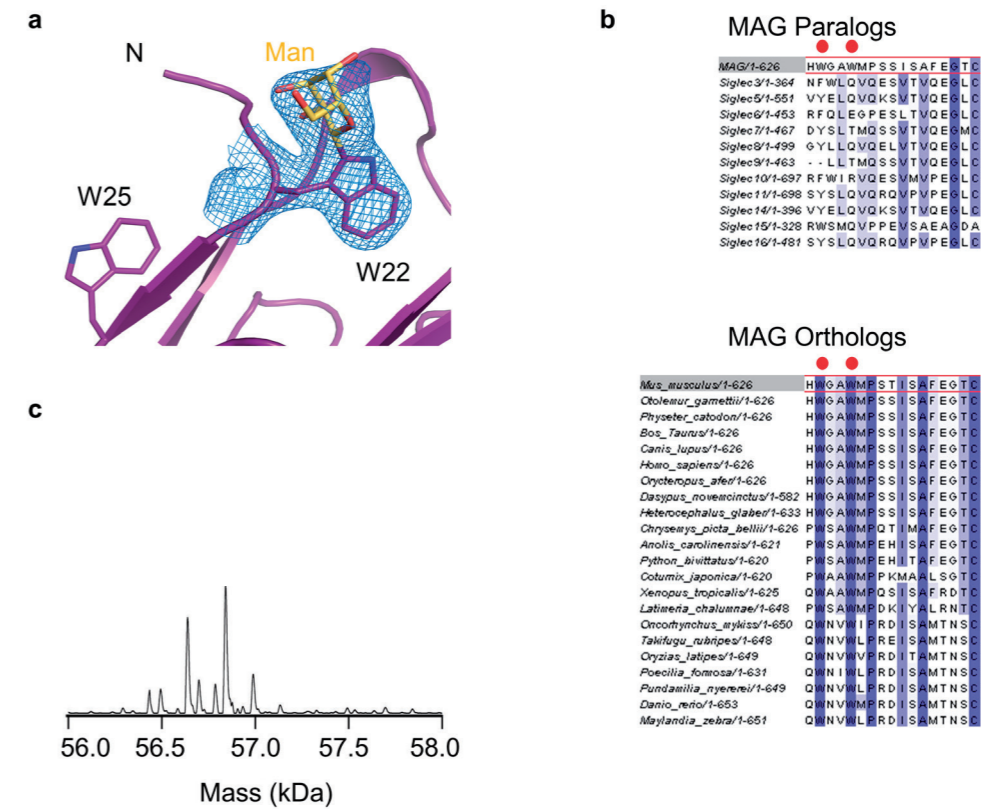


Supplementary Figure 4: Glycosylation of MAG in the lysine-methylated MAG_{1-5} crystal form

Glycans are shown (sticks) based on the electron density for the lysine-methylated MAG_{1-5} crystal form (orange, cartoon representation). Numbering for the frontal/left monomer of MAG (darker orange).



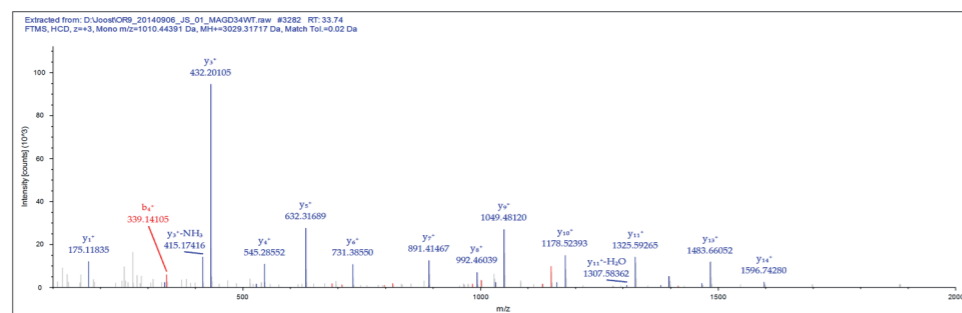
Supplementary Figure 5: Electron density for the fucosylation of the N-linked glycan on N332
The $2F_o - F_c$ electron density map contoured at 1.3σ around N332 is shown for the deglycosylated MAG_{1-5} crystals, with the N-linked glycan after Endo- H_1 treatment modeled (sticks).



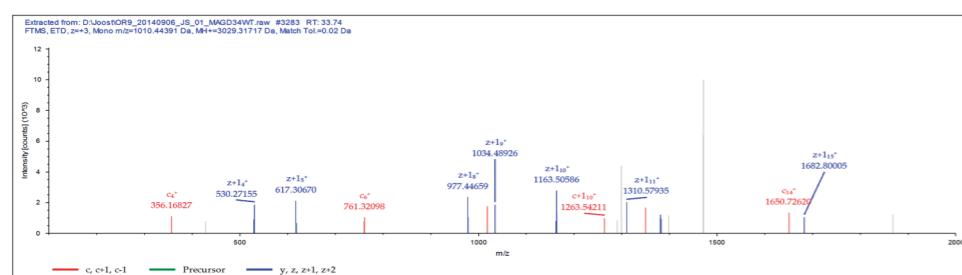
Supplementary Figure 6: Tryptophan mannosylation proximal to the ligand binding site

(a) $2F_o - F_c$ electron density map contoured at 1.0σ around W22 in the MAG_{1-3} unliganded crystals, also showing W25 that is part of the canonical $WxxW$ motif for tryptophan mannosylation. **(b)** Sequence alignments show that the $WxxW$ motif is conserved among MAG orthologs in different vertebrate species, but not in any of the Siglec family paralogs, suggesting functional specificity of this modification for MAG. **(c)** Native mass spectra of MAG_{1-5} wt and MAG W25Q, showing a mass shift corresponding to the mutation plus loss of the mannosyl group.

Higher-energy Collision Dissociation MS/MS

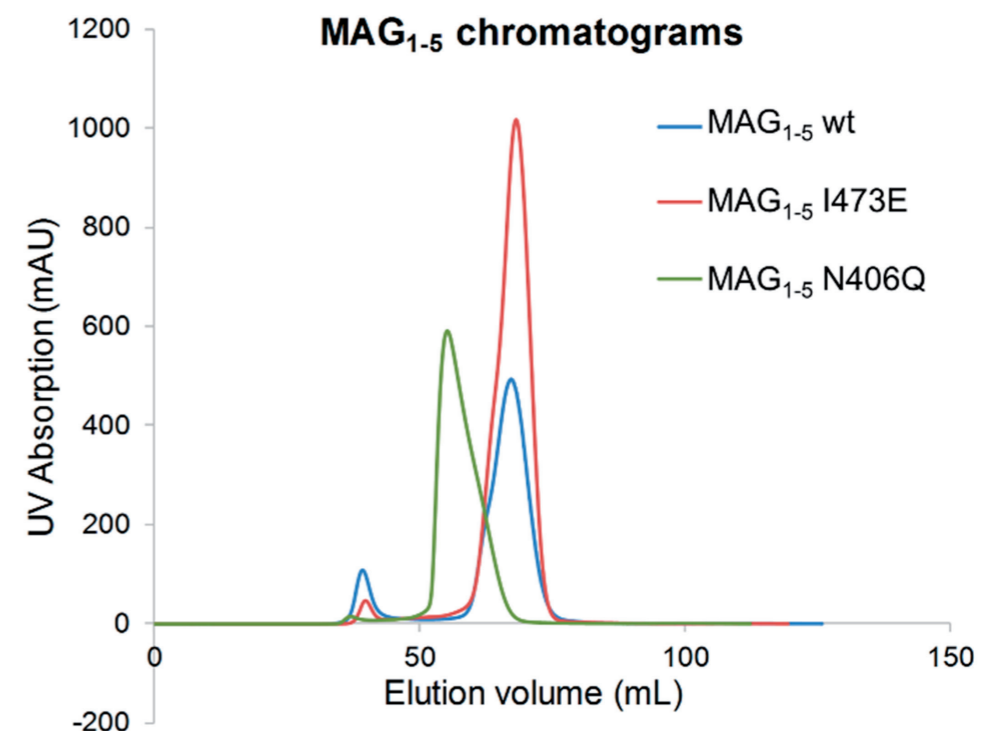


Electron Transfer Dissociation MS/MS

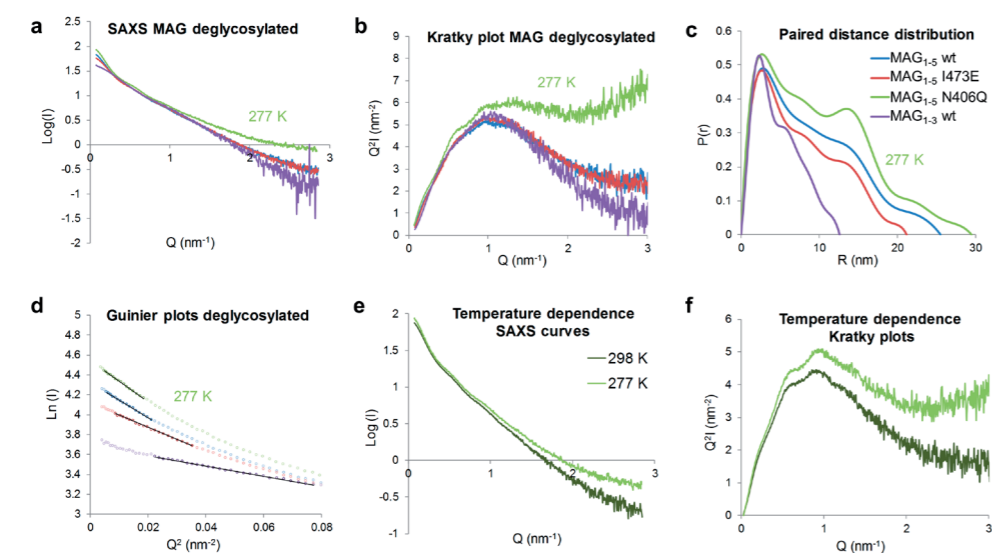


Supplementary Figure 7: Tryptophan-mannosylation is confirmed to be on W22.

MS/MS spectra (by higher-energy collision dissociation or electron transfer dissociation) of the tryptophan-mannosylated N-terminal peptide after trypsinization of wt MAG₁₋₅ show fragment ions corresponding to mannosylation on W22. The sequence was assigned as: GSGHWGAWmPSTISAFEGTcVSIPcR with the following post-translational modifications and adducts: +hexose (tryptophan-mannosylation) on W5, +oxidation of M9, +carbamidomethylation of C20, +carbamidomethylation of C25).

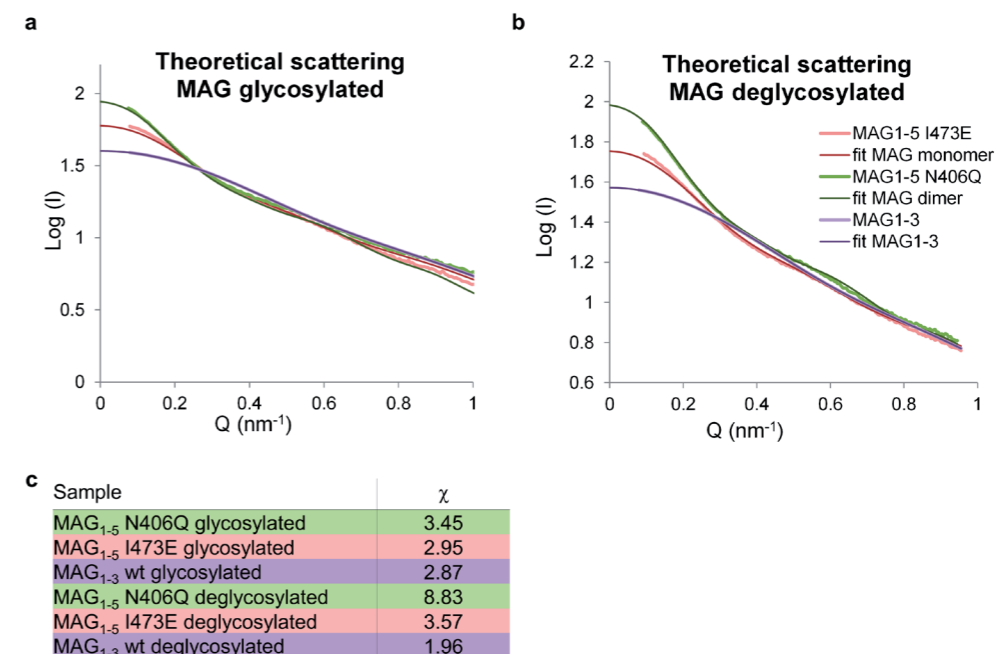
MAG₁₋₅ chromatogramsSupplementary Figure 8: Size-exclusion chromatograms of MAG₁₋₅ wt, MAG₁₋₅ I473E and MAG₁₋₅ N406Q

Size exclusion chromatography was performed in large scale as part of the purification procedure on a Hiload 16/60 Superdex200 column as described in the methods section. Absorption was measured at 280 nm. A clear shift to a dimer is observed for the MAG₁₋₅ N406Q mutant.



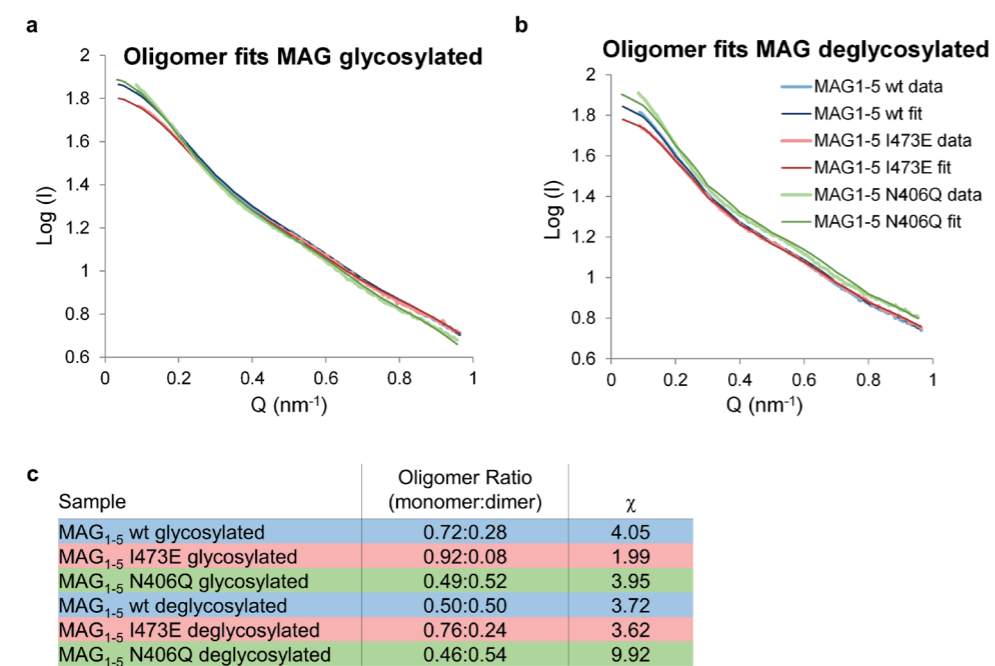
Supplementary Figure 9: SAXS analysis of the deglycosylated MAG variants

(a) Log I vs. Q plot of the different deglycosylated MAG variants. The higher I values at larger scattering angles for the MAG₁₋₅ N406Q variant might be explained by the fact that this was the only construct measured at 277 rather than 293 K (see also panel e), since it was too sensitive to radiation damage and aggregation at 293 K. (b) Kratky plot of the different deglycosylated MAG variants. Again, the MAG₁₋₅ N406Q curve is the only spectrum measured at 277 rather than 293 K (see also panel f). (c) Paired distance distribution function for the different deglycosylated MAG variants. (d) Guinier plots for the different deglycosylated MAG variants. (e) Analysis of the effects of temperature for glycosylated MAG₁₋₅ N406Q at similar concentrations. The Log I vs Q plot is shown, revealing higher scattering intensities (I) for larger scattering angles (Q) when measuring at lower temperatures (277 instead of 293 K). This might explain the similar effect observed for deglycosylated MAG₁₋₅ N406Q in panel a, which was measured at 277 K instead of 293 K. (f) Kratky plot of glycosylated MAG₁₋₅ N406Q at 277 and 293 K, showing a similar effect as seen for the deglycosylated MAG₁₋₅ N406Q in panel b.

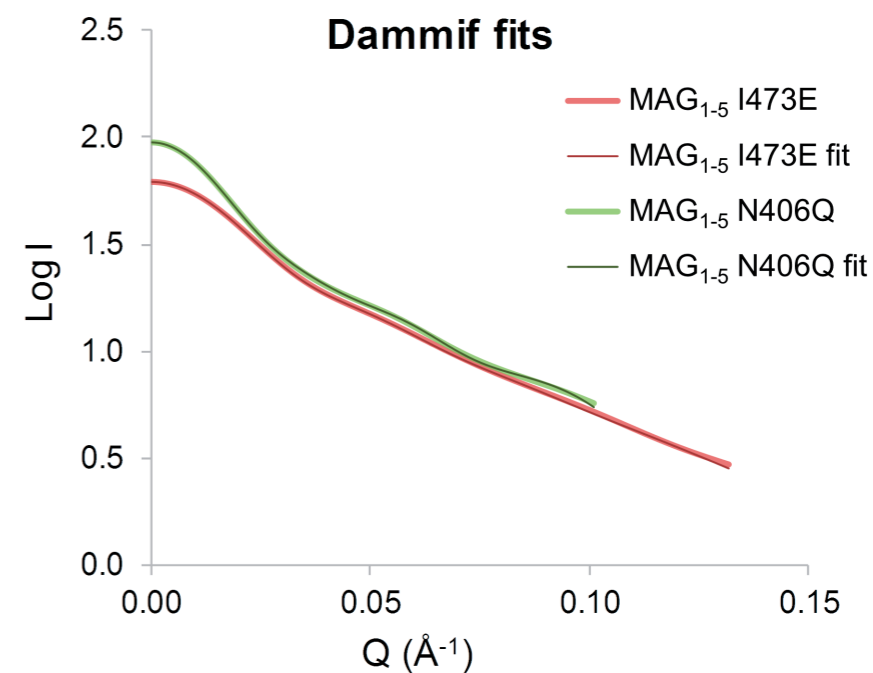


Supplementary Figure 10: Theoretical scattering of crystal structures as determined by CRYSOLO compared to experimental SAXS curves

(a) Theoretical scattering of the glycosylated crystal forms, calculated using the crystal structure of lysine-methylated MAG₁₋₅ in monomeric or dimeric form and of glycosylated MAG₁₋₃, compared to the experimental SAXS curves for the indicated glycosylated MAG forms. Only coordinates of glycans observed in the electron density were used, no extra glycan moieties were modeled. (b) Same for the deglycosylated crystal forms, using the crystal structure of the deglycosylated MAG₁₋₅ monomer and dimer and of MAG₁₋₃ with the glycan coordinates removed, except for the asparagine-attached GlcNAc residues and the tryptophan mannosylation, which are not removed by Endo-H₁ deglycosylase. The MAG₁₋₃ scattering curves agree very well with the theoretical scattering of the monomeric structures of MAG₁₋₃. (c) Table with χ values of fits.

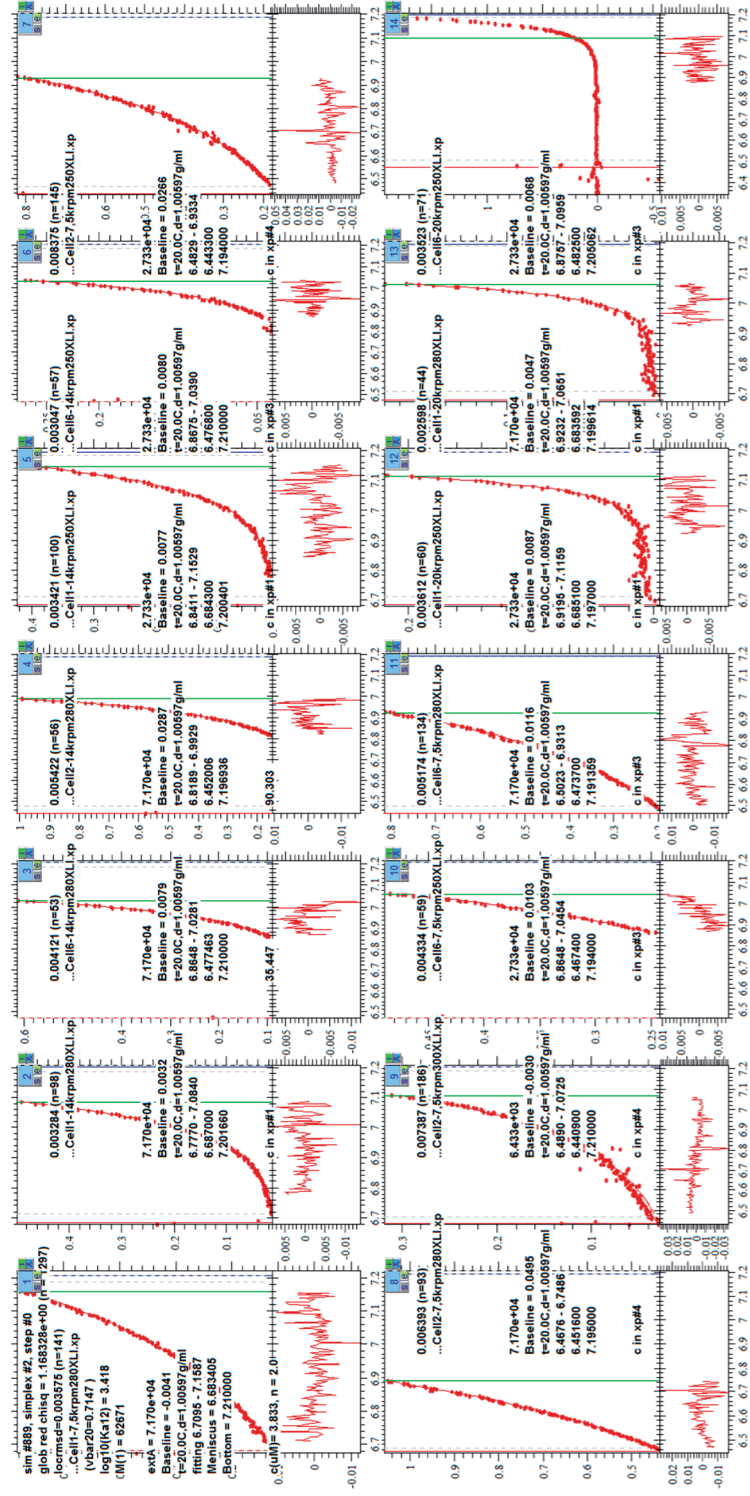


Supplementary Figure 11: OLIGOMER fits to experimental SAXS curves for MAG₁₋₅ wt and mutants
 OLIGOMER fits to SAXS curves of glycosylated (a) and deglycosylated (b) MAG₁₋₅, using the same models as in Supplementary Fig. 10. (c) Monomer-dimer ratios determined by OLIGOMER and χ of the fits.



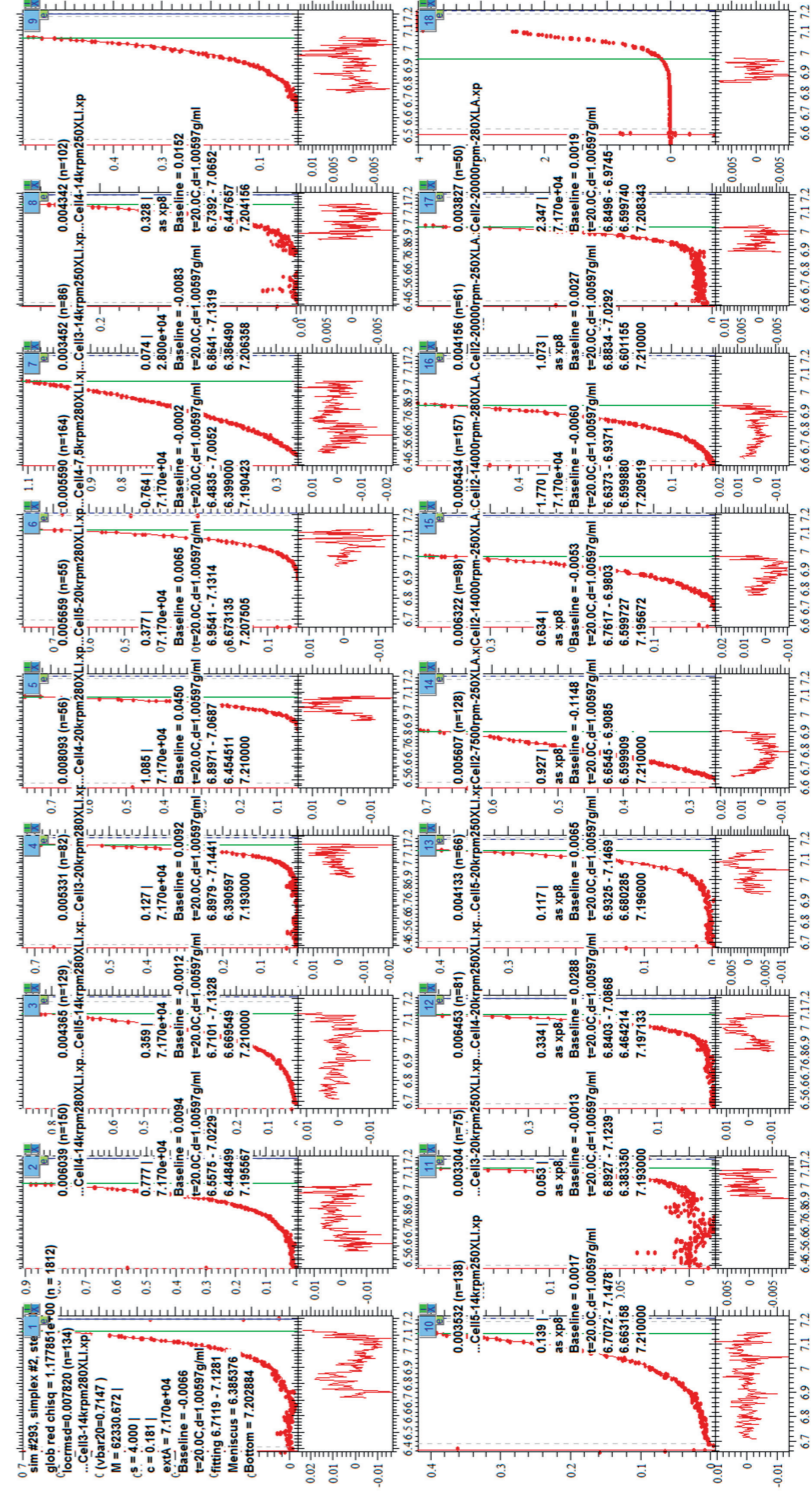
Supplementary Figure 12: Fits of Dammif ab-initio modeling to the SAXS data of deglycosylated MAG₁₋₅ mutants

Dammif fits corresponding to the bead models shown in figure 2g, corresponding to the data of deglycosylated MAG₁₋₅ I473E ($\chi^2=1.05$) and MAG₁₋₅ N406Q ($\chi^2=1.33$). Twofold rotational symmetry was enforced for the MAG₁₋₅ N406Q model.



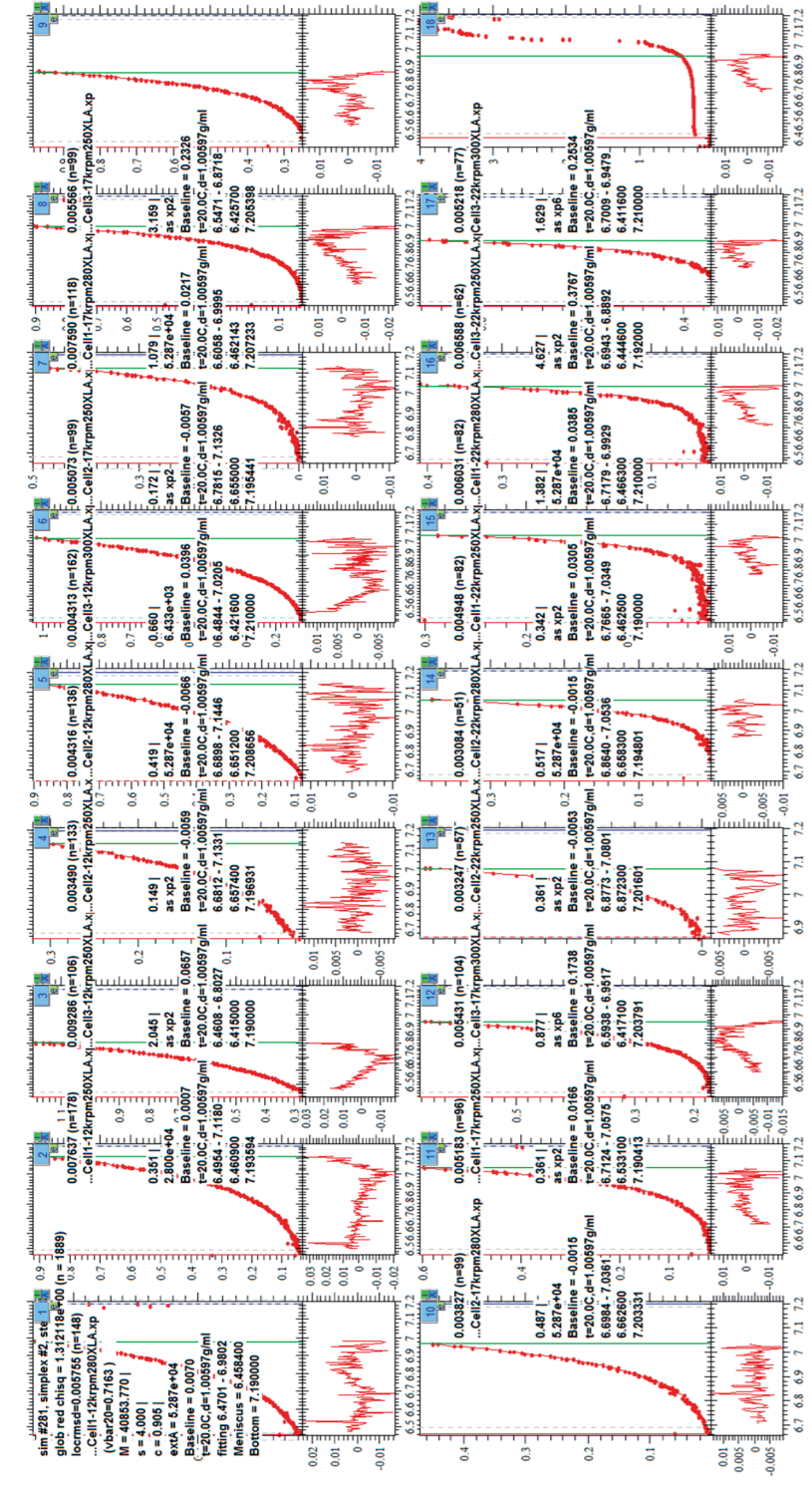
Supplementary Figure 13: SEDPHAT analysis of se-AUC data for MAG_{1.5} wt glycosylated

A global analysis was performed using different concentrations and different rotation speeds, in which MAG was modeled as a monomer-dimer equilibrium with the M₁ floated. Rotation speed can be read from the second line in each panel (7.5, 14 or 20 krpm) and concentration in μM from the bottom line (after c) in each panel. In the panels beneath the curves the residuals from the fit are shown.

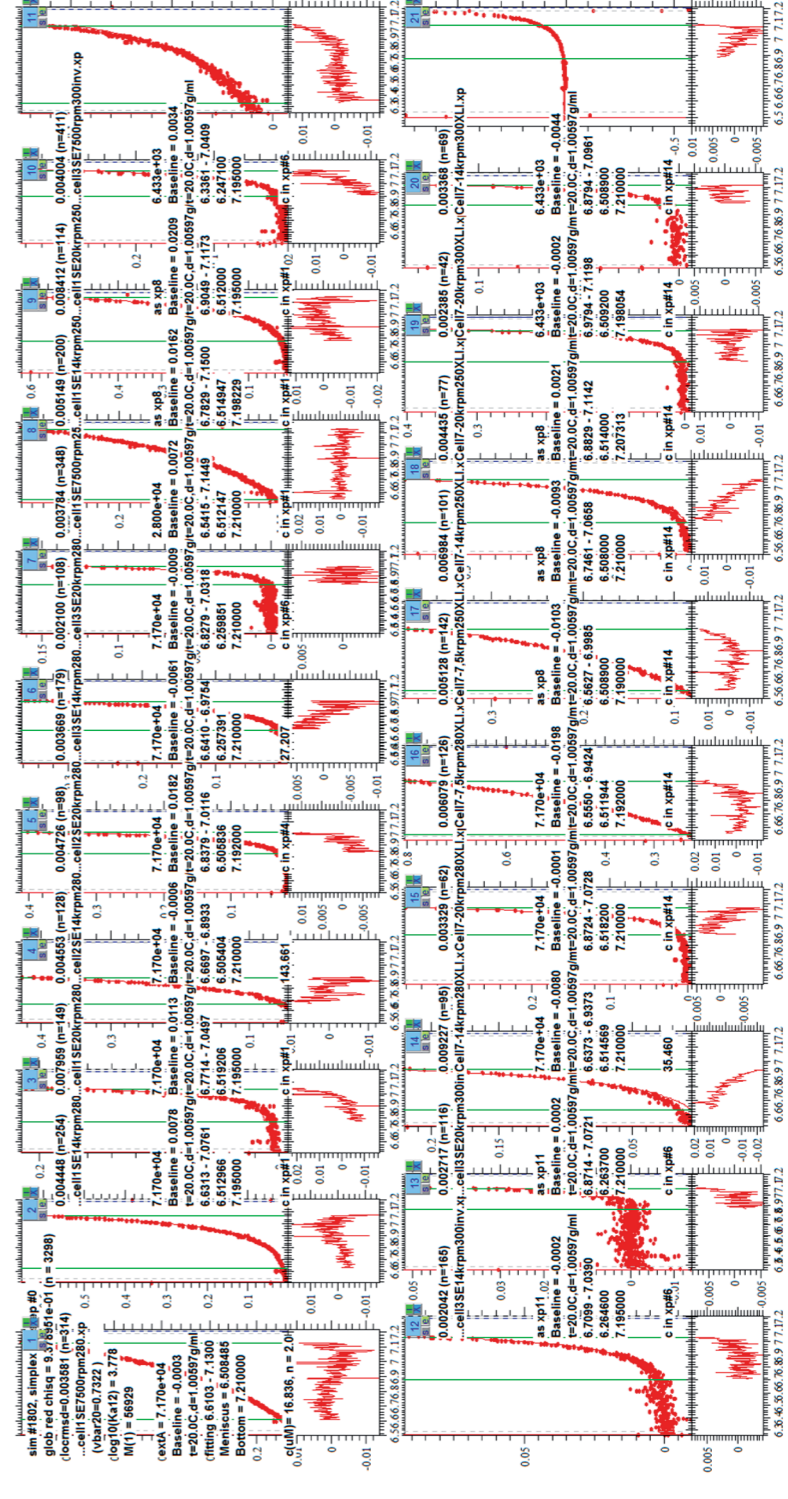


Supplementary Figure 14: SEDPHAT analysis of se-AUC data for MAG_{1.5} I473E glycosylated

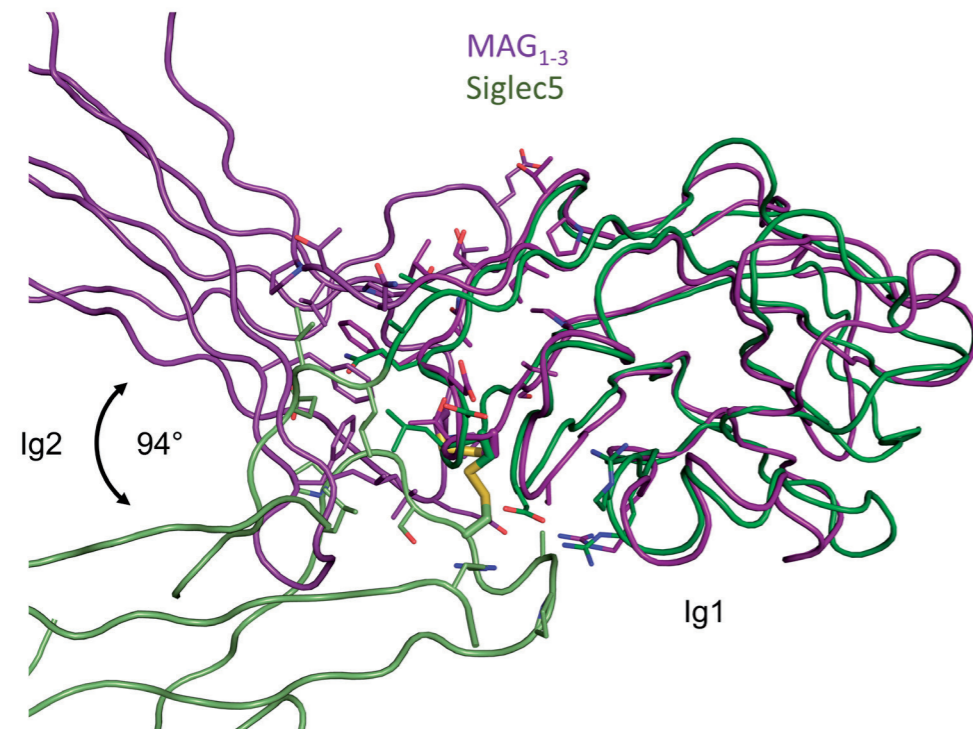
Same as Supplementary Fig. 13, but modeled as a single species, M₁ floated



Supplementary Figure 15: SEDPHAT analysis of se-AUC data for MAG₁₃ wt glycosylated Same as Supplementary Fig. 13, but modeled as a single species, M₁₃ floated

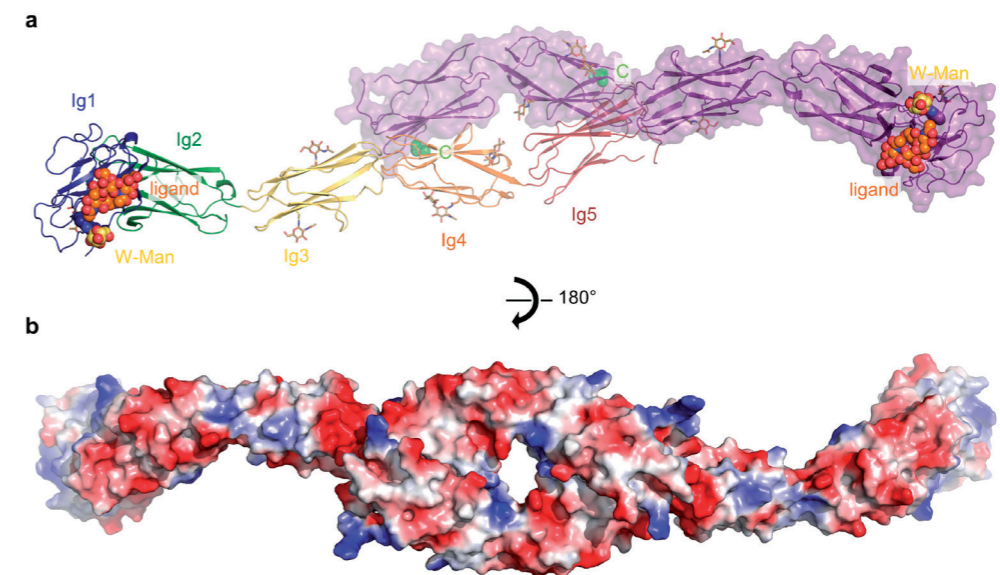


Supplementary figure 16: SEDPHAT analysis of se-AUC data for MAG₁₅ wt deglycosylated Same as Supplementary Fig. 13, but modeled as a monomer-dimer equilibrium, M₁₅ fixed



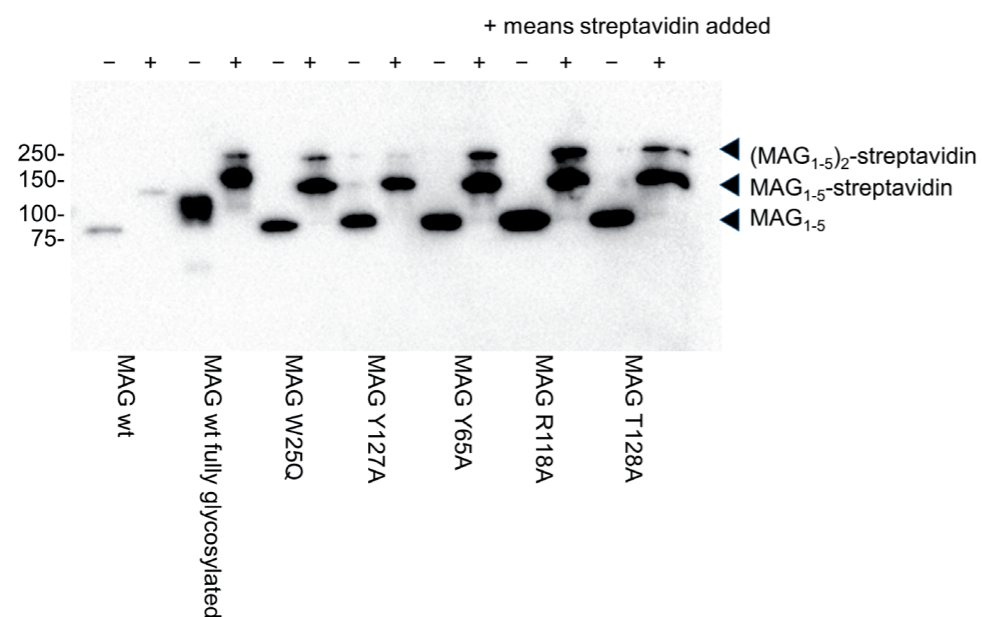
Supplementary Figure 17: Comparison of the inter-domain orientation between the two N-terminal domains of MAG and siglec5

Siglec5 is the only other siglec family member for which a structure is available comprising more than one domain. Comparison of the MAG_{1-3} (purple) and siglec5 (green) structures, aligned by their N-terminal V-type Ig domains, reveals a marked domain rotation of 94° of the second Ig domain (light) with respect to the first Ig domain (dark). Both have a conserved inter-domain disulfide between the first two domains (shown as thick sticks), as do most other siglec family members. The domain rotation is probably the result of variations of the other residues at the inter-domain interface (shown as sticks) as well as differences in the structure of the second domain.



Supplementary Figure 18: Top and bottom views of the MAG dimer

(a) Top view of deglycosylated MAG_{1-5} dimer (representation as in Fig. 5, but rotated 90°), one molecule colored by domain and the other purple with the surface shown. The co-purified carbohydrate ligand (orange spheres), the tryptophan mannosylation (yellow spheres, labelled W-Man), the other glycosylation sites (brown sticks) and the membrane-proximal C-termini (green spheres) are indicated. (b) Bottom view of deglycosylated MAG_{1-5} dimer with electrostatic surface potential shown (red is negatively charged, blue is positive, white is neutral).



Supplementary Figure 19: Gel-shift assay confirms biotinylation of MAG mutants as ligands for GT1b ganglioside liposome SPR.

The different binding-site mutants were expressed with a biotin acceptor peptide (BAP) and His₆-tag and co-expressed with BirA biotin transferase in HEK cells as described in the Methods section. After small-scale Ni-affinity purification, biotinylation was confirmed by a gel-shift after addition of an excess of streptavidin. The second sample is the same construct as the first, but expressed in HEK cells without the GnT1^{-/-}, thus having mature N-linked glycans, but this construct was not used for further analyses. All samples appear fully biotinylated as the lower band completely disappears, the extra top band that appears sometimes for the samples with streptavidin likely corresponds to two biotinylated MAG proteins binding to a single streptavidin tetramer.

Supplementary notes

Comparison of Siglec structures

We present the first structure of a full extracellular domain of a Siglec family member. All other Siglecs function in the immune system rather than in the nervous system, but they share an N-terminal V-type Ig domain for recognizing sialic acid moieties, followed by 1 to 16 C-type Ig domains¹.

Other available Siglec structures comprise either only the N-terminal V-type Ig (Siglec1/Sialoadhesin² and Siglec7³), or the two N-terminal domains (Siglec5⁴). Comparison of the two N-terminal domains of Siglec5 with those of MAG reveals a markedly different inter-domain orientation (rotation of 94°, Supplementary Fig. 17). This is surprising, since Siglec5 and MAG, as well as most other Siglecs, have a conserved disulfide bond between the two N-terminal domains. This domain rotation is probably caused by differences in the other amino acids at the inter-domain interface between Ig1 and Ig2, as well as a structurally less conserved second Ig domain (Supplementary Fig. 17).

Siglec10 and Siglec11, like MAG, have five Ig domains in total. Whether they can form dimers in a similar fashion to MAG and whether this is related to their function, remains to be investigated.

Additional insights in ligand recognition

One of the two co-purified tetrasaccharide ligands of MAG has a glycolyl variant of sialic acid (Neu5Gc instead of Neu5Ac), that is not biosynthesized by humans and likely originated from the beef digest Primatone that was part of the expression medium. The fact that this low-abundant sugar is prevalent in purified MAG sample suggests that it binds stronger than the N-acetylneuraminic acid variant. This could be explained by an extra hydrogen bond that the hydroxyl group of the glycolyl variant could form with the side chain of conserved residue N125 in MAG. However, this is in conflict with studies showing no binding of MAG to Neu5Gc-containing gangliosides^{5,6}. Also it is interesting that MAG seems to have a preference for tetrasaccharides rather than trisaccharides, even though no density is observed for the fourth sugar in the deglycosylated MAG₁₋₅ crystal form. These observations are relevant for rational drug design efforts, as the ganglioside binding site is an intensively studied drug target⁷.

Glycosylation on Asparagine 406 may serve a regulatory function

We show that the N-linked glycan on N406, that appears to clash with its symmetry-related dimerization partner, reduces dimerization potential in solution. This suggests that the N406 glycosylation site may serve to regulate self-interaction and thereby myelination. For example, MAG can carry HNK-1 containing N-linked glycans on N406, which have a terminal negatively charged glucuronic acid⁸ that could potentially

modulate MAG dimerization by coulombic repulsion. Regulation may occur at the biosynthesis level, in which the expression levels of glycosylation enzymes in the secretory pathway vary during development. Alternatively, extracellular trimming by glycosidase enzymes may spatially and temporally regulate MAG dimerization by acting on N406. A putative candidate glycosidase for such a role is the antiaging factor Klotho, a secreted glycosidase present in the cerebrospinal fluid^{9,10}. It is known to have β -glucuronidase activity and to trim N-linked glycans of neuronal membrane-anchored proteins^{10,11}. Trimming of these charged glucuronic acid groups from the N-linked glycans on MAG N406 by Klotho could reduce the coulombic repulsion and thus enhance MAG dimerization.

In line with this hypothesis, Klotho knockout mice have an impaired myelination phenotype¹². Furthermore, it was shown that downstream intracellular targets of Klotho in oligodendrocyte precursor cells (OPCs) are part of the Akt and Erk signaling pathways¹². These pathways are also downstream of Fyn kinase in OPCs and oligodendrocytes¹³, suggesting that MAG/Fyn could be a transmembrane link connecting extracellular Klotho activity with intracellular signaling events in OPCs. We speculate that in healthy individuals, Klotho could be involved in trimming glucuronic acid-containing N-linked glycans on N406 of MAG, thus regulating MAG dimerization, Fyn signaling and thereby myelination.

Supplementary References

1. Crocker, P. R., Paulson, J. C. & Varki, A. Siglecs and their roles in the immune system. *Nat. Rev. Immunol.* **7**, 255–266 (2007).
2. May, A. P., Robinson, R. C., Vinson, M., Crocker, P. R. & Jones, E. Y. Crystal structure of the N-terminal domain of sialoadhesin in complex with 3' sialyllactose at 1.85 Å resolution. *Mol. Cell* **1**, 719–728 (1998).
3. Alphey, M. S., Attrill, H., Crocker, P. R. & van Aalten, D. M. F. High resolution crystal structures of Siglec-7. Insights into ligand specificity in the Siglec family. *J. Biol. Chem.* **278**, 3372–7 (2003).
4. Zhuravleva, M. a., Trandem, K. & Sun, P. D. Structural Implications of Siglec-5-Mediated Sialoglycan Recognition. *J. Mol. Biol.* **375**, 437–447 (2008).
5. Collins, B. E. *et al.* Sialic acid specificity of myelin-associated glycoprotein binding. *J. Biol. Chem.* **272**, 1248–55 (1997).
6. Collins, B. E., Fralich, T. J., Itonori, S., Ichikawa, Y. & Schnaar, R. L. Conversion of cellular sialic acid expression from N-acetyl- to N-glycolylneuraminic acid using a synthetic precursor, N-glycolylmannosamine pentaacetate: inhibition of myelin-associated glycoprotein binding to neural cells. *Glycobiology* **10**, 11–20 (2000).
7. Schwaradt, O., Kelm, S. & Ernst, B. in *Topics in Current Chemistry* 151–200 (Springer Verlag, 2013). doi:10.1007/128_2013_498
8. Burger, D., Pidoux, L. & Steck, A. J. Identification of the glycosylated sequons of human myelin-associated glycoprotein. *Biochem. Biophys. Res.* **197**, 457–464 (1993).
9. Li, S.-A. *et al.* Immunohistochemical localization of Klotho protein in brain, kidney, and reproductive organs of mice. *Cell Struct. Funct.* **29**, 91–99 (2004).
10. Tohyama, O. *et al.* Klotho Is a Novel β -Glucuronidase Capable of Hydrolyzing Steroid β -Glucuronides. *J. Biol. Chem.* **279**, 9777–9784 (2004).
11. Chang, Q. *et al.* The beta-glucuronidase klotho hydrolyzes and activates the TRPV5 channel. *Science* **310**, 490–493 (2005).
12. Chen, C.-D. *et al.* The antiaging protein Klotho enhances oligodendrocyte maturation and myelination of the CNS. *J. Neurosci.* **33**, 1927–39 (2013).
13. Taveggia, C., Feltri, M. L. & Wrabetz, L. Signals to promote myelin formation and repair. *Nat. Rev. Neurol.* **6**, 276–87 (2010).

Chapter 3

**Nogo Receptor crystal structures with correct disulfide pattern
suggest a novel mode of self-interaction**

Matti F. Pronker¹, Roderick P. Tas^{1,*}, Hedwich C. Vlieg¹ and Bert J.C. Janssen¹

¹: *Crystal and Structural Chemistry, Bijvoet Center for Biomolecular Research, Department of Chemistry, Faculty of Science, Utrecht University, Padualaan 8, 3584 CH Utrecht, The Netherlands*

^{*}: *Current address: Cell Biology, Department of Biology, Faculty of Science, Utrecht University, Padualaan 8, 3584 CH Utrecht, The Netherlands*

manuscript in preparation

Abstract

The Nogo Receptor (NgR) is a glycosphosphatidylinositol (GPI)-anchored cell surface protein and a receptor for three myelin-associated inhibitors of regeneration (MAIs) Myelin-associated glycoprotein (MAG), Nogo66 and Oligodendrocyte Myelin glycoprotein (OMgp). In combination with different co-receptors NgR mediates signaling that reduces neuronal plasticity. Available structures of the NgR ligand-binding leucine-rich repeat (LRR) domain have an artificial disulfide pattern due to C-terminal construct boundaries. NgR was previously shown to self-associate via its LRR domain, but the structural basis of this interaction is elusive. Here, crystal structures of the NgR LRR with a longer C-terminus and native disulfide pattern are presented. An additional C-terminal loop proximal to the C-terminal LRR cap is stabilized by two newly-formed disulfide bonds but is otherwise mostly unstructured in the absence of any stabilizing interactions. NgR crystallized in six unique crystal forms, three of which share a crystal packing interface. We compare NgR crystal packing interfaces from all eight unique crystal forms to explore how NgR could self-interact on the neuronal plasma membrane.

Introduction

NgR is a neuronal cell surface-expressed GPI-anchored protein receptor for ligands that negatively regulate plasticity in the central nervous system (CNS)¹⁻⁴. Knockout of NgR results in prolonged periods of ocular dominance plasticity^{5,6} and anatomical plasticity at dendritic spines and synapses⁷⁻⁹. NgR is part of receptor complexes that mediate signaling by three MAIs that inhibit neurite sprouting and outgrowth and collapse axonal growth cones upon injury in the CNS¹⁻⁴. The three structurally unrelated MAIs Myelin-associated glycoprotein (MAG), Nogo66 and Oligodendrocyte Myelin glycoprotein (OMgp) all bind and signal through NgR to inhibit neurite outgrowth and collapse axonal growth cones¹⁰⁻¹². These three MAIs bind to the N-terminal leucine-rich repeat (LRR) domain of NgR^{11,13-18}. C-terminal of the NgR LRR domain is a heavily glycosylated stalk that contains a disulfide-linked loop¹⁹ followed by a GPI-anchoring sequence that is replaced by a GPI anchor in mature NgR. The stalk of NgR is required but not sufficient for signal transduction and replacing the GPI anchor with a transmembrane helix results in reduced sensitivity of neurons to MAI ligands¹⁴.

Since NgR is GPI-anchored and lacks an intracellular domain for signal transduction into the neuron, it forms signaling complexes together with four different transmembrane co-receptors; the neurotrophin receptor p75^{20,21}, its homologue TROY, LRR and immunoglobulin-like domain-containing NgR-interacting protein 1 (LINGO-1)²² and its homologue Amphoterin-induced gene and open reading frame 3 (AMIGO3). It is not well understood how these co-receptors are able to transduce the signal to the cell interior but several studies have provided useful insights. p75 has a cysteine in its transmembrane region that allows the formation of disulfide-linked dimers, which is important for MAI signal transduction through the membrane²³⁻²⁵. TROY is a more abundant transmembrane co-receptor in adults that can functionally substitute for p75^{26,27} and also has a cysteine in its transmembrane region. LINGO-1 binds to NgR and p75 and confers MAI-sensitivity to non-neuronal COS-7 when co-transfected together with NgR and p75²². AMIGO3 was identified as a functional substitute for LINGO-1, mediating MAI signaling through NgR for the acute effects of MAIs on regeneration²⁸. Thus, NgR forms complexes with either p75 or TROY and either LINGO-1 or AMIGO3 to mediate MAI signaling.

More recent studies have shown that NgR and LINGO-1 compete for p75 binding and that LINGO-1 is mostly expressed in recycling endosomes, whereas NgR and p75 are prevalent on the cell surface²⁹. Also, LINGO-1 was found to bind to NgR via an interface overlapping with that of the MAI ligands¹⁷. These results suggest that NgR and LINGO-1 form complexes with p75 sequentially rather than being in a ternary complex. A mechanism has been proposed in which LINGO-1 displaces NgR from p75 after internalization²⁹.

Structures have been solved of the LRR domain of NgR^{15,30} as well as its paralog NgR2³¹. However, the currently available NgR structures are the result of truncated constructs (residues 26-310 for 1OZN and 27-311³⁰ for 1P8T¹⁵) that result in an artificial disulfide pattern in the C-terminal LRR capping region¹⁹. In these structures, a disulfide bond is observed between cysteines C266 and C309^{15,30}, whereas in full-length NgR, C266 forms a disulfide with C335 and C309 with C336 (mouse NgR numbering, see fig. 1)¹⁹. This generates an extra disulfide-enclosed segment between cysteine 309 and 335 (residues 310-334, hereafter referred to as C-terminal segment). The cysteines C335 and C336 responsible for this arrangement are conserved in NgR orthologs (Fig. 1, bottom panel) but are not conserved in the NgR paralogs NgR2 and NgR3. Deletion of this loop was reported to selectively increase binding of NgR to Nogo66 or OMgp¹⁸. A chimeric protein consisting of the LRR of NgR, in which this loop is replaced with a 13 amino acid sequence from the stalk of NgR2, binds stronger to all three MAIs than either NgR or NgR2¹⁸. The C-terminal segment is expected to be on the convex side of the LRR next to the C-terminal LRR cap¹⁹. However, mutagenesis studies, as well as evolutionary conservation, suggest that it is the concave rather than the convex side of the NgR LRR that is involved in binding all three MAIs as well as LINGO-1^{17,30}. Thus, it remains unclear how the disulfide pattern of the C-terminal LRR capping domain and the extra C-terminal loop influence binding of MAI ligands.

Different NgR truncation constructs, corresponding to the artificially short LRR (res. 27-310), the LRR including the C-terminal segment (res. 27-344) and a construct including most of the glycosylated stalk (res. 27-431) have been compared to determine the region necessary for p75 and TROY binding. For both TROY and p75, binding was observed with just the short LRR, but the affinity was increased by including the C-terminal segment and further enhanced for the third construct²⁷. Other studies found that the short LRR does not support p75 binding, whereas the full extracellular segment of NgR does^{21,30}. These results confirm earlier studies showing that the membrane-attached NgR LRR without the stalk is not sufficient for Nogo66-induced signaling¹⁴. Taken together these data indicated that the artificially short NgR LRR domain supports binding of the three MAI ligands^{11,13-18}, but that the C-terminal loop and the glycosylated stalk are required for efficient co-receptor binding and signal transduction.

NgR has been shown to self-interact via its LRR domain^{14,15,32} at the plasma membrane^{14,15}. These assemblies were previously suggested to represent an inactive signaling state as they can form in the absence of MAI ligands¹⁵. However, the structural basis of this interaction remains elusive, as the available NgR structures do not have any crystal packing interfaces in common^{15,30,33}.

Although a structural model has been proposed for the 310-334 segment and how it interacts with the rest of NgR¹⁹, this model is not supported by any experimental data. Also, it is not clear how the NgR LRR self-interacts^{14,15,32}. Here we describe six

independent crystal structures of NgR with native disulfide bonds, show that the C-terminal segment forms a flexible loop in the absence of any stabilizing ligands and propose a novel mode of NgR self-interaction.

Results

Structures of NgR with correct disulfide pattern show that the C-terminal segment forms a loop that is flexible in the absence of stabilizing ligands.

To study NgR with its native disulfide structure, two constructs were generated that include the extra cysteines necessary for correct disulfide formation. Constructs of the NgR LRR truncated after (mouse) residues 337 and 348 are hereafter referred to as NgRa and NgRb, respectively. The latter includes an extra 11 amino acid sequence (PDAADKASVLE) that is relatively hydrophobic and conserved among orthologues compared to the rest of the glycosylated stalk (Fig. 1). This NgRb construct is very similar (truncated at residue 348 instead of 344) to the construct that previously showed enhanced binding to p75 and TROY compared to the short LRR with the artificial disulfide structure²⁷.

A number of crystal forms were obtained for NgRa (five) and NgRb (three) as glycosylated or Endo-Hf-treated versions. These crystal forms will be referred to as NgRa-1 to NgRa-5 and NgRb-1 to NgRb-3 hereafter (see tables 1 and 2). Counting all NgR molecules in the asymmetric units for all crystal forms, a total of 23 new NgR structures were solved (table 2). The *C*2 and *P*2₁2₁2₁ crystal forms were observed for both NgRa (NgRa-1 and NgRa-3, respectively) and NgRb (NgRb-1 and NgRb-3, respectively). NgRa-3 and NgRb-1 diffracted to the highest resolution (both 1.9 Å), whereas the lowest maximum resolution of 2.5 Å was obtained for NgRa-2, NgRa-4 and NgRb-3. Most often, NgR crystallized as needles in low pH conditions (pH 4-5), but other morphologies and higher pH values (up to pH 6.5) also occurred (see table 2). Three crystallization conditions contained NgR ligands or co-receptors in attempts to obtain crystals of complexes, but these additional molecules were not observed in any of the datasets (see methods section for details).

All structures were solved by molecular replacement using a previously solved structure of the human NgR LRR³⁰ as a search model. Both previously-confirmed N-linked glycans at N82 and N179³⁰ were confirmed in all our structures, as well as an N-linked glycan on N237, which is part of a canonical NxS motif for N-linked glycosylation (Fig. 2). This N-linked glycan was not observed in the three previously-published structures^{15,30,33}. The alternative disulfide pattern that was shown by mass spectrometry¹⁹, with disulfides between C266-C335 and C309-C336 instead of C266-C309, was confirmed in all our structures. The overall structure of the NgR LRR domain, including the C-terminal cap, is not affected by the alternative disulfide structure (Fig. 3a).

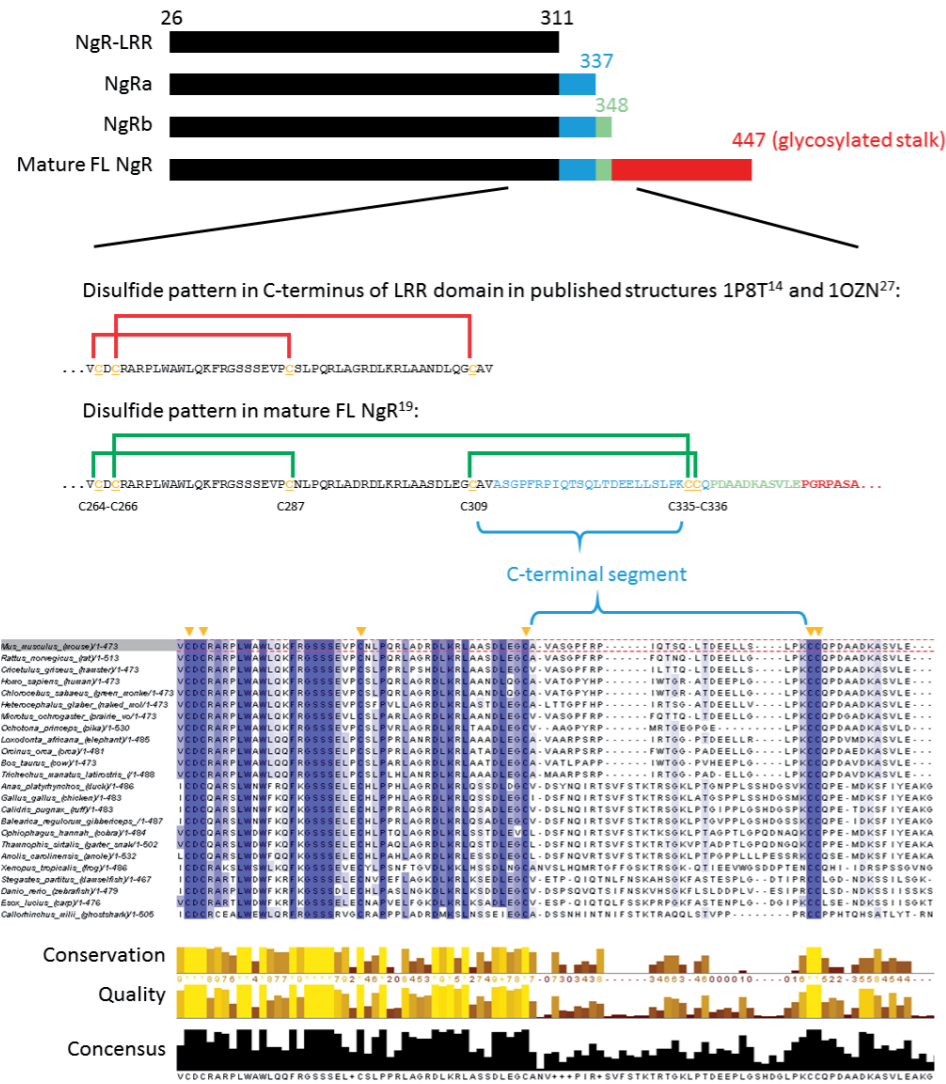


Figure 1: Rationale for construct design

The C-terminal cap of the LRR of NgR in available structures^{15,30} MAG and OMgp limit axonal regeneration after injury of the spinal cord and brain. These cell-surface proteins signal through multi-subunit neuronal receptors that contain a common ligand-binding glycosylphosphatidylinositol-anchored subunit termed the Nogo-66 receptor (NgR has an artificial disulfide pattern due to construct boundaries¹⁹). Therefore, longer constructs of the NgR LRR including C335 and C336 were generated (NgRa and NgRb) that include an extra C-terminal segment (blue) that is enclosed by the C266-C335 and C309-C336 disulfides. NgRb also includes a relatively conserved and hydrophobic sequence C-terminal of these cysteines (green), see bottom panel for sequence alignment of this region in NgR orthologues. Amino acids are colored by percentage identity (blue is more conserved).

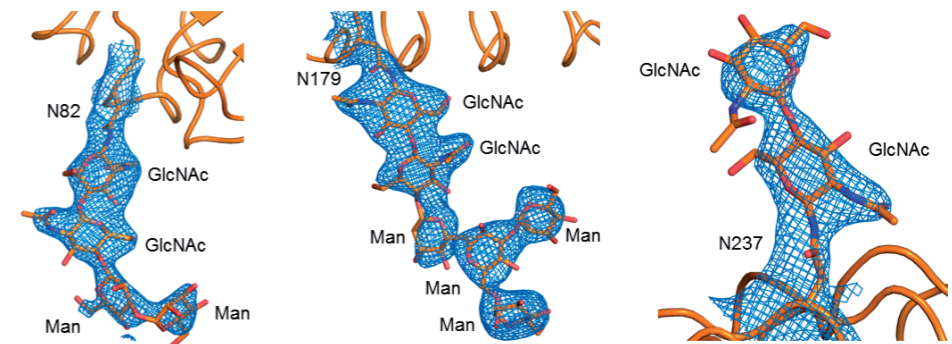


Figure 2: Electron density for the N-linked glycans on the NgR LRR

$2F_o - F_c$ electron density of the glycosylated NgRa-4 crystal form at a contour level of 1.3σ around the N-linked glycans on N82 (left panel), N179 (middle panel) and N237 (right panel), confirming the previously-confirmed glycosylation sites on N82 and N179³⁰ and showing clear electron density for the N-linked glycosylation site at N237.

The C-terminal segment (residues 310-334) forms a loop in our structures. Despite being anchored to the C-terminal Cap by two disulfides C266-C335 and C309-C336, this loop is disordered in most of the structures. Only in one crystal form, NgRa-5, the whole loop could be modeled in the electron density. In this crystal form, eight NgRa molecules are present in the asymmetric unit, related by point group 422 non-crystallographic symmetry. For these NgRa molecules, a relatively large portion of the loop is observed in the electron density (Fig. 3b). For one of the NgRa molecules in the NgRa-5 crystal form (called chain B) the whole loop could be modeled in the relatively weak electron density, with high B-factors in particular for residues 313-318 (Fig. 3c-e). The loop is also relatively well-resolved in the NgRa-4 crystal form (except for residue 317-321), likely due to stabilizing packing interactions. In this crystal form, the loop adopts a conformation similar to that in the NgRa-5 crystal form (Fig. 3). In both NgRa-4 and NgRa-5, α -helical secondary structure can be observed in both the C-terminal segment and the C-terminus (residues C-terminal of C336). The α -helix in the C-terminal segment may represent a native structure. The α -helix observed at the C-terminus, on the other hand, is most likely an artifact, since most residues in this segment (QAAHH) are part of the restriction site and purification tag (AAAHHHHHH). In the full-length protein and in the NgRb construct a proline is present in this segment instead of the first alanine (P338, Fig. 1) that likely perturbs the α -helix³⁴. Indeed, no α -helical structure is observed for the C-terminus in any of the NgRb structures. The fragments of the loop 310-334 that are observed in the electron density of the crystal forms other than NgRa-4 and NgRa-5 are structurally heterogeneous (Fig. 3a). Concluding, the fragmented or absent electron density, the high B-factors and the heterogeneous conformations of the C-terminal segment in the different crystal forms indicate that it is a flexible loop in

the absence of stabilizing interactions (Fig. 3). Nonetheless, a preference for a possibly energetically-favored conformation of this C-terminal loop is suggested by its similar structure in the unrelated NgRa-4 and NgRa-5 crystal forms.

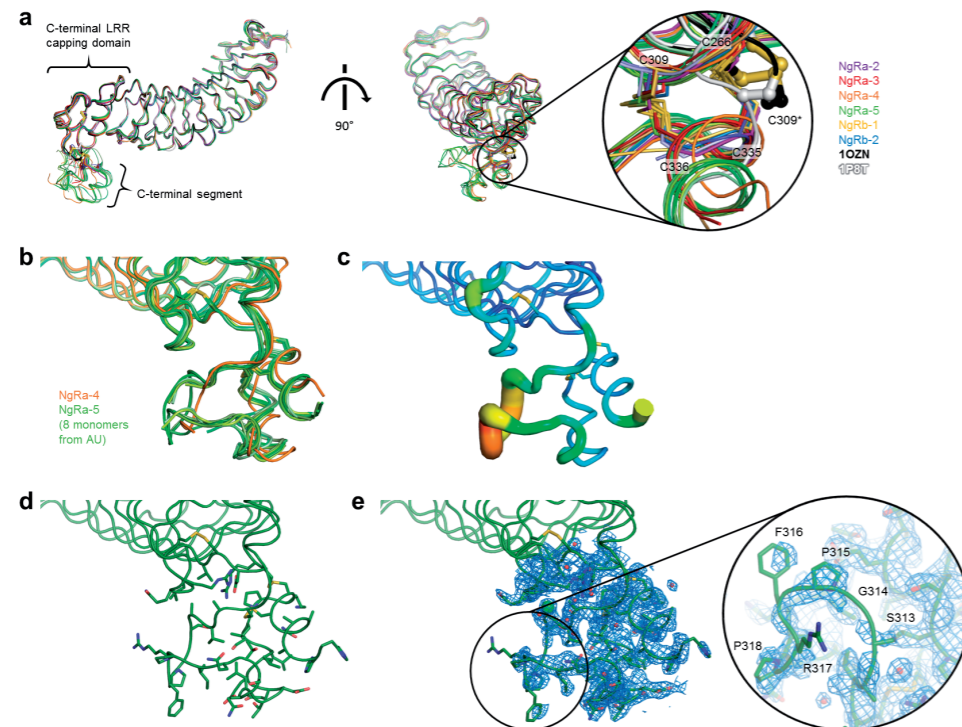


Figure 3: Crystal structures of NgRa and NgRb reveal that the C-terminal loop is mostly flexible. (a) The six different independent crystal forms of NgR with the correct disulfide structure are compared to the currently published structures 1P8T¹⁵ and 1OZN³⁰. The structure of the LRR domain is not altered and confirms the alternative disulfide pattern reported previously¹⁹. The right panel shows a close-up view of the disulfides as in the previously-published structures (thick ball-and-stick) and in the structures of the longer NgRa and NgRb constructs (thin sticks). The asterisk indicates the location of C309 in 1P8T and 1OZN. (b) Comparison of the resolved parts of the C-terminal loop in the NgRa-4 and NgRa-5 crystal forms reveals a similar structure which appears to be flexible. In other crystal forms, this loop could not be resolved. The eight copies of NgRa in the asymmetric unit (AU) of the NgRa-5 crystal form, that are related by point group 422 non-crystallographic symmetry, are colored different shades of green and the single copy from the asymmetric unit of NgRa-4 is orange. (c) Analysis of the B-factors of the C α 's in the C-terminal loop for the best-resolved structure of the loop (chain B from NgRa-5) confirms this loop is flexible. A thick tube and red colors represent high B-factors, a thin tube and blue colors represent low B-factors, using a rainbow gradient. (d) Same representation as panel (c), now showing the sidechains as sticks. It appears that most hydrophobic sidechains pack together in the C-terminal loop. (e) Same representation as panel (d) but with the $2F_o - F_c$ electron density contoured at 1.0σ . Ordered solvent molecules are shown as red spheres and a chloride ion as a green sphere. A close-up view of residues 313-318 shows that this part of the loop in particular is flexible and poorly-resolved.

NgR self-interacts in different crystal forms through a shared interface.

Since NgR was previously shown to self-interact on a cell surface, we analyzed the crystal packing interfaces of all our NgR structures as well as those previously solved by others^{15,30,33}. Remarkably, several different crystal forms of both NgRa and NgRb share a crystal packing interface involving the concave surface of the NgR LRR (NgRa-1, NgRa-3, NgRb-1, NgRb-2 and NgRb-3), hereafter referred to as *interface 1*.

The crystals in which NgR packs via *interface 1* all grew in conditions buffered at pH 5 (table 2). *Interface 1* is part of linear arrays of interacting NgR molecules along a 2_1 screw axis with a pitch of $46.6 \pm 0.3 \text{ \AA}$ (Fig. 4). In some crystal forms, this is a crystallographic screw axis (NgRa-3, NgRb-2 and NgRb-3; space group $P2_12_12_1$, $P2_1$ and $P2_12_12_1$, respectively). In the crystal forms with space group $C2$ (NgRa-1 and NgRb-1) the same interface is formed by the combination of a crystallographic twofold rotation and translation along the b -axis of one unit cell. In these crystal forms, the b -axis has a dimension of 46.6 \AA (see table 1), equivalent to the pitch of the screw axis in NgRa-3, NgRb-2 and NgRb-3. All crystals that showed such NgR arrays had needle-like macroscopic morphology and *vice versa*, suggesting that the screw axes of NgR arrays correspond to the long axes of the needle crystals. However, these arrays are only observed in Endo-Hf-deglycosylated crystal forms and cannot form with native glycosylated NgR, although dimerization via *interface 1* is still possible (Fig. 4). N-linked glycans on asparagines N82 and N179 of NgR molecule n would clash with the LRR of NgR molecule $n+2$. Similarly, the N-linked glycan on asparagine N237 of NgR molecule n would clash with the LRR of NgR molecule $n-2$. However, these glycans are not interfering with dimerization via *interface 1* (n with $n+1$) as observed in these crystals (Fig. 4). Thus, for natively glycosylated NgR, dimers should still be able to form via *interface 1*, whereas further multimerization would be blocked by the three N-linked glycans on the NgR LRR.

Interface 1 is mostly hydrophilic and has a surface area of approximately 750 \AA^2 . The N-terminal LRR cap and concave side of one NgR LRR (the interface spans LRRs 1-7) interacts with the concave face of the C-terminal LRR cap of another NgR molecule (Fig. 5a). The interaction is stabilized by seven salt bridges, ten direct hydrogen bonds and a π - π interaction between the sidechains of Y34 and R279 (see table 3, Fig. 5a and 6b). Three salt bridges are formed by a histidine paired with a negatively-charged amino acid (H136-E284, H210-D295 and H186-D295). This suggests that this interaction could be pH-regulated, since histidine side chains are only positively charged at lower pH values due to pK_a values of their sidechains of approximately 5.5-7.0, depending on the local chemical environment^{35,36}. Apart from the ten direct hydrogen bonds, several indirect ones are formed via ordered water molecules at the interface. As was previously shown by others³⁰, the concave surface of the NgR LRR is also evolutionarily conserved compared to the convex surface (Fig. 5c).

Table 1: Data collection and refinement statistics

	NgRa-1	NgRa-2	NgRa-3	NgRa-4	NgRa-5	NgRb-1	NgRb-2	NgRb-3
Data collection								
Space group	<i>C2</i>	<i>P2₁</i>	<i>P2₁2₁2₁</i>	<i>P4₁</i>	<i>P4₁2₁2</i>	<i>C2</i>	<i>P2₁</i>	<i>P2₁2₁2₁</i>
Cell dimensions								
a, b, c (Å)	151.6, 46.6, 120.7	72.91, 38.6, 119.6	46.6, 112.1, 115.1	90.6, 90.6, 45.6	168.5, 168.5, 256.2	153.2, 46.9, 121.8	132.1, 46.3, 132.2	46.7, 111.6, 114.8
α, β, γ (°)	90.0, 123.45, 90.0	90.0, 106.2, 90.0	90.0, 90.0, 90.0	90.0, 90.0, 90.0	90.0, 90.0, 90.0	90.0, 123.65, 90.0	90.0, 91.9, 90.0	90.0, 90.0, 90.0
Resolution (Å)	43.78-2.30 (2.39-2.30)	38.60-2.51 (2.62-2.51)	56.03-1.90 (1.94-1.90)	90.63-2.50 (2.61-2.50)	70.39-2.20 (2.24-2.20)	44.08-1.92 (1.97-1.92)	45.94-2.40 (2.46-2.40)	46.73-2.50 (2.64-2.50)
No. reflections	31309	20826	48250	13084	185934	54406	60282	21264
R _{sym} or R _{merge}	0.131 (0.724)	0.099 (0.561)	0.129 (1.054)	0.066 (0.912)	0.131 (0.956)	0.086 (1.390)	0.137 (1.044)	0.213 (0.811)
Mean I / σI	5.9 (1.5)	12.2 (3.3)	6.0 (1.5)	13.2 (2.4)	11.4 (2.2)	7.7 (0.6)	5.3 (0.7)	3.8 (1.4)
CC _{1/2}	0.936 (0.546)	0.992 (0.564)	0.994 (0.503)	0.998 (0.704)	0.998 (0.667)	0.998 (0.413)	0.991 (0.270)	0.981 (0.663)
Completeness (%)	98.7 (98.6)	94.6 (89.6)	99.7 (99.8)	100.0 (100.0)	100.0 (100.0)	98.6 (88.8)	95.1 (97.2)	98.8 (99.8)
Redundancy	3.7 (3.6)	2.8 (2.6)	4.6 (4.7)	7.4 (7.6)	8.5 (8.7)	3.5 (3.3)	2.6 (2.4)	3.4 (3.7)
Refinement								
Maximum Resolution (Å)	2.3	2.5	1.9	2.5	2.2	1.9	2.4	2.5
R _{work} / R _{free}	0.179 / 0.234	0.196 / 0.254	0.179 / 0.222	0.207 / 0.245	0.167 / 0.207	0.179 / 0.212	0.212 / 0.266	0.254 / 0.299
No. atoms	4942	4751	5397	2572	21913	4960	9660	4597
Average B-factors (Å ²)								
Protein	36.9	52.8	32.6	100.3	39.7	44.7	49.6	50.0
Ligand/ion	64.2 / 93.1	N.A. / 80.4	N.A.	N.A. / 131.0	73.8 / 53.6	92.6 / 179.1	81.3 / 105.2	57.5 / 41.0
Water	38.4	36.4	38.5	77.9	41.0	48.3	43.0	41.0
R.m.s. deviations								
Bond lengths (Å)	0.002	0.002	0.003	0.003	0.004	0.006	0.002	0.002
Bond angles (°)	0.650	0.650	0.869	0.658	0.850	0.949	0.647	0.657
Molprobit score	1.35	1.64	0.84	1.64	1.76	1.20	1.53	1.90

Table 2: Comparison of crystallization conditions

	Crystal form equivalent to	Interface 1	Crystallization Temp. (°C)	Deglycosylated?	Monomers/AU	pH
NgRa-1	NgRb-1	Y	18	Y	2	5
NgRa-2			4	Y	2	4
NgRa-3	NgRb-3	Y	18	Y	2	5
NgRa-4			18	glycosylated	1	6.5
NgRa-5			4	Y	8	4.5
NgRb-1	NgRa-1	Y	4	Y	2	5
NgRb-2		Y	18	Y	4	5
NgRb-3	NgRa-3	Y	18	Y	2	5

Table 3: Comparison of relevant crystal packing interfaces.

	Interface 1 (Fig. 5)	NgRa-2 (Fig. 7b)	1OZN (Fig. 6a and b)
Surface areas (Å ²):	750	660	860
pH of crystallization condition:	5	4	6.5
predicted ΔG (kcal mol ⁻¹) ³⁷ :	-9.8	-8.2	-7.5
Interface contacts:	D111-R300 D114-R296 H136-E284 D138-R296 R206-D259 H186-D295 H210-D295 Y34-R279 Q45-Q276 R61-R279* R61-G280* R61-S281 H65-Q276 Q109-R300 Q162-A294* H186-A294* Q211-Q291 Y160-E284	R300-D163 R256-D259 R206-E284 H186-D295 S282*-Q211 Y254-D259 Y232-D259 R139-Q291	R131-D114 D176-R189 H202-D259 R227-D259 R250-E284 T243-Q291 GlcNAc2 on N82-Q46

*hydrogen bond to backbone carbonyl. Coloring: blue are salt bridges, green is π-π interaction and yellow are hydrogen bonds

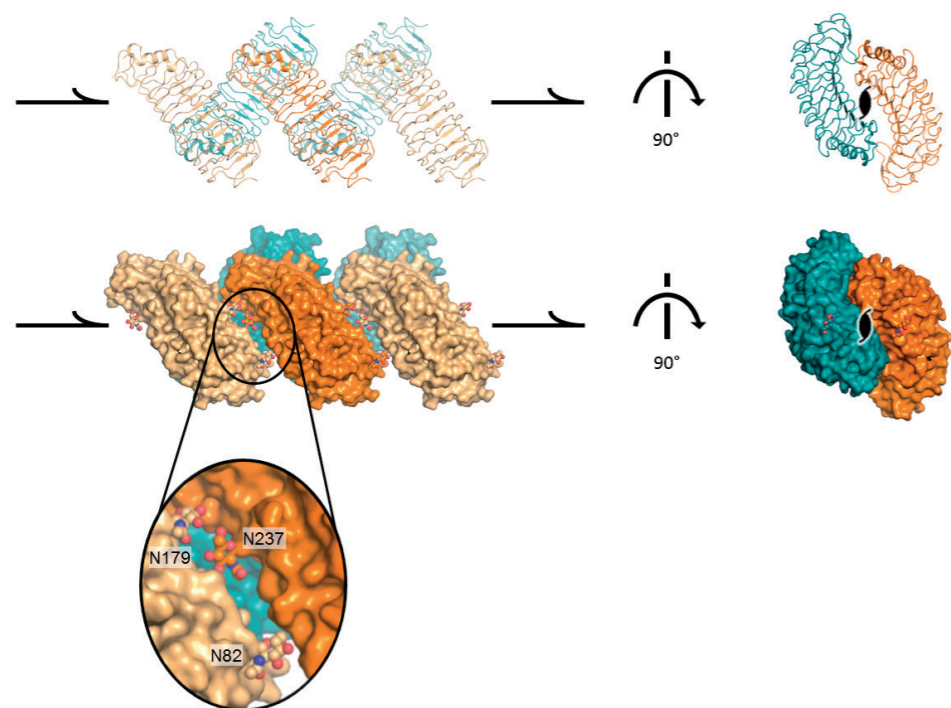


Figure 4: Arrays of NgR molecules in different NgRa and NgRb crystal forms via *interface 1* can only form with deglycosylated protein.

Arrays of NgR molecules are formed around a 2_1 screw axis in the NgRa-1, NgRa-3, NgRb-1, NgRb-2 and NgRb-3 crystal forms (shown is NgRb-1). NgR molecules are shown in cartoon representation in the top panels and in surface representation in the bottom panels. These arrays can only form with Endo- H_7 -deglycosylated material, because the N-linked glycans on N82 and N179 of NgR molecule n would clash with molecule $n+2$ and the N-linked glycan of N237 would clash with molecule $n-2$. Dimerization of NgR via the same interface (n with $n+1$) however is not perturbed by these N-linked glycosylation sites.

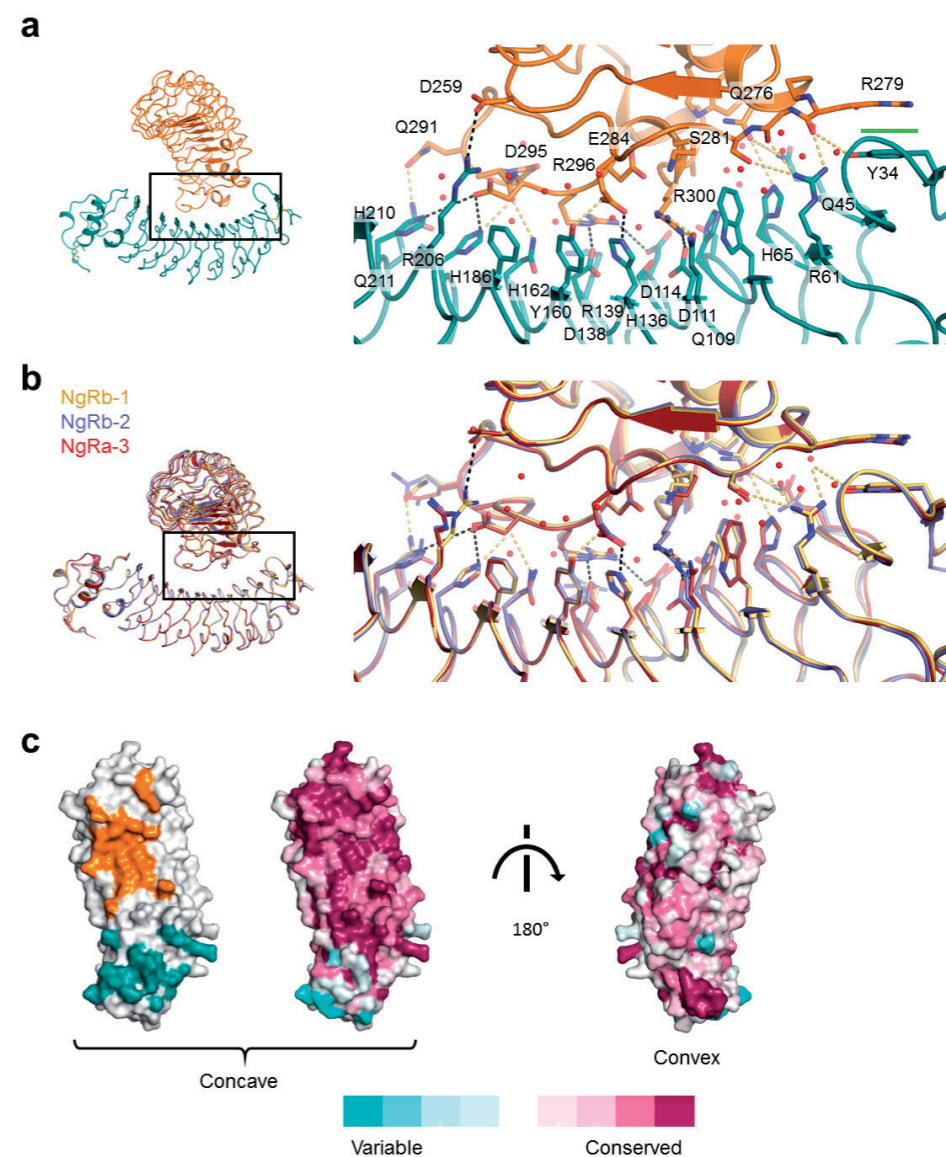


Figure 5: Analysis of *interface 1*

(a) Close up view of *interface 1*. Salt bridges are indicated by black dashed lines, direct hydrogen bonds by yellow dashed lines and the π - π interaction between R279 and Y34 by a green rectangle. Residues at the interface are shown in stick representation and those involved in intermolecular interactions are additionally labeled, other residues at the interface are also shown as sticks. Red spheres represent ordered solvent molecules near the interface. (b) Same representation as (a), comparing the independent crystal forms of NgRb-1, NgRb-2 and NgRa-3 that share this interface. These crystal forms have highly similar orientations of the amino acid sidechains involved in the formation of this interface. (c) Footprints of the interface (left panel, coloring as in (a)) and evolutionary conservation of the surface residues (right panels, purple is more conserved, cyan is less conserved).

Other crystallographic interfaces observed for NgR are less extensive.

Some other crystal forms also have substantial packing interfaces (table 3). Both previously published structures (1OZN and 1P8T) have interfaces with surface areas of $>750 \text{ \AA}^2$. The 1OZN structure has extended crystal packing interfaces on the sides of the LRR domains that would result in parallel arrays (Fig. 6a). This interface has a surface area of 860 \AA^2 and is stabilized by five salt bridges and two direct hydrogen bonds. The N-linked glycans on N82 and N179 also contribute to this interface (Fig. 6a). However, these side faces of the LRR are evolutionarily not as conserved (Fig. 6b), compared to the concave surface of the LRR (Fig. 5c). In the paper describing 1OZN, another interface is suggested for NgR self-interaction³⁰. However, this interface would not be possible for NgR with its native disulfide structure because of steric hindrance (Fig. 6c). In the 1P8T structure¹⁵ MAG and OMgp limit axonal regeneration after injury of the spinal cord and brain. These cell-surface proteins signal through multi-subunit neuronal receptors that contain a common ligand-binding glycosylphosphatidylinositol-anchored subunit termed the Nogo-66 receptor (NgR the biggest interface has a surface area of 790 \AA^2 and is stabilized by one salt bridge and five direct hydrogen bonds, as well as some hydrophobic contacts (Fig. 7a). This interface is formed by the bottom side of the C-terminal LRR cap of one molecule of NgR binding to the N-terminal LRR capping domain and 5 LRRs of another NgR molecule. However, this interface relies on interactions of the artificial disulfide C266-C309 and C-terminus and is thus not likely to be formed for full-length NgR (Fig. 7a).

The NgRa-2 crystal form also has a significant unique interface between two NgR monomers in the asymmetric unit oriented in asymmetric antiparallel fashion (Fig. 7b). This hydrophilic interface has a surface area of 660 \AA^2 and is stabilized by four intermolecular salt bridges and four hydrogen bonds. It involves the evolutionarily conserved concave surface of NgR and is also stabilized by a salt bridge between a histidine (H186) and an aspartate (D295) (Fig. 7b). The NgRa-2 crystal was grown at the lowest pH condition compared to the other crystal forms (pH 4.0, see table 2). All other interfaces were too small or improbable to consider and will not be discussed here.

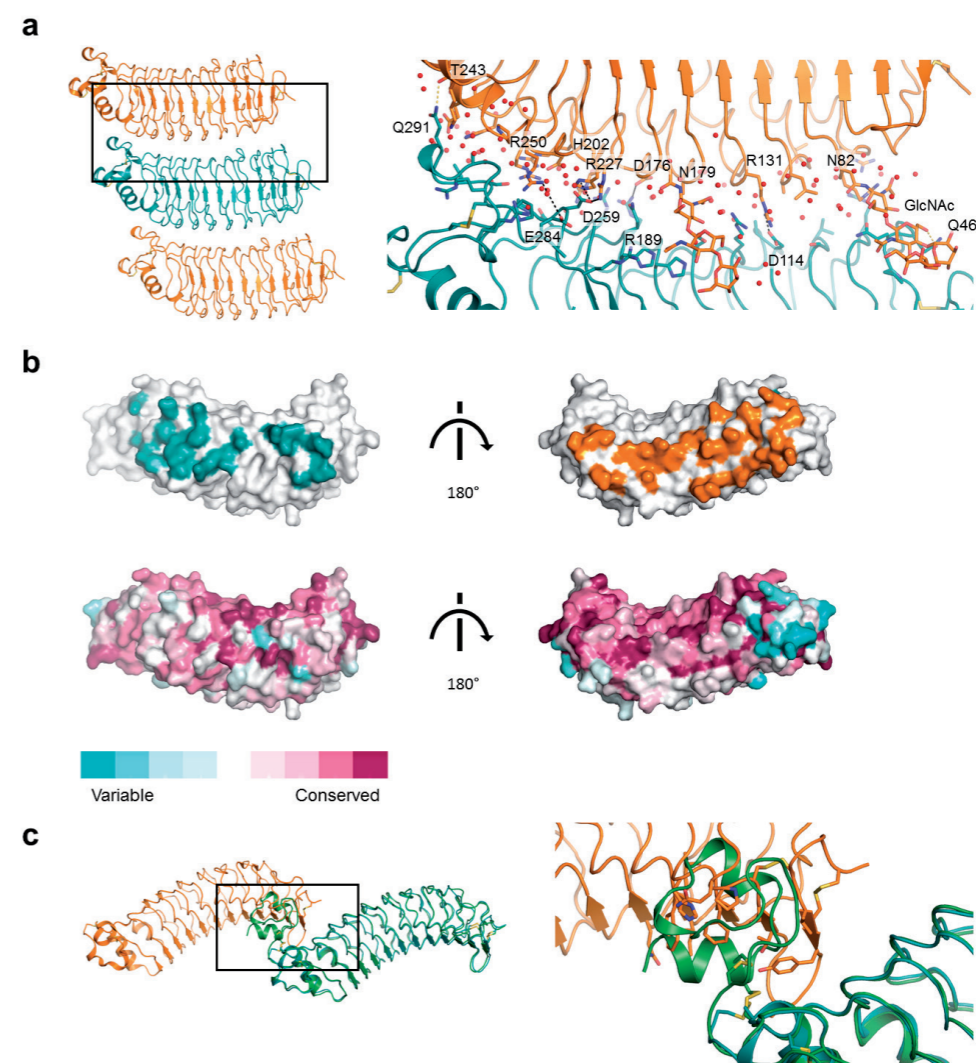


Figure 6: Analysis of interfaces for 1OZN

(a) Close up view of the linear array-forming interface in 1OZN³⁰, same representation as in Fig. 5. N-linked glycans on N82 and N179 are shown as sticks. (b) Footprints of the interface (top panels, coloring as in (a)) and evolutionary conservation of the surface residues (right panels, purple is more conserved, cyan is less conserved). (c) The interface in 1OZN (orange and teal) that was suggested in the accompanying paper to represent the self-interaction of NgR³⁰ cannot be formed if NgR has the correct disulfide pattern because of steric hindrance. The structure of NgRa-5 chain B is overlaid in green to indicate the clashes.

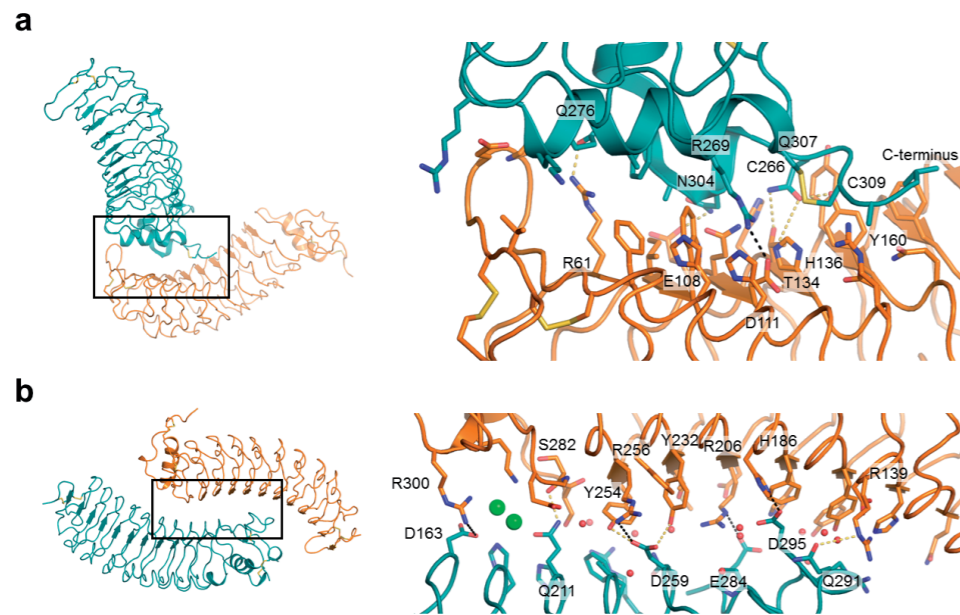


Figure 7: Other crystal packing interfaces that might account for NgR self-interaction
 (a) The largest interface in 1P8T¹⁵, same representation as in Fig. 5. This interface appears to be mostly hydrophobic and is stabilized by the artificial disulfide C266-C309 and C-terminus. (b) View of the interface between two monomers in the asymmetric unit of the NgRa-2 crystal form, same representation as Fig. 5, green spheres represent chloride ions. These crystals appeared in a condition buffered at pH 4.

Discussion

Our structures indicate that the overall structure of the NgR LRR and the C-terminal cap is not altered by the artificial disulfide structure present in the previously-published NgR structures^{15,30} (Fig. 3a). An extra C-terminal loop is formed by the disulfides C266-C335 and C309-C336. This C-terminal loop appears flexible in the absence of any stabilizing interactions. We could model (part of) this loop in two independent crystal forms, which reveals a similar yet flexible structure (Fig. 3b). The structure of the C-terminal loop in these two crystal forms deviates from a previously-proposed model, which was based on the discovery of the alternative disulfide structure in the C-terminal LRR capping domain as a result of truncation¹⁹. This loop is not required for MAI ligand binding^{11,13-18} but previous work shows it contributes to the interaction with the co-receptors p75 and TROY²⁷. Structures of NgR-p75 or NgR-TROY complexes are required to determine if the C-terminal loop indeed adopts a defined structure when interacting with these co-receptors.

To investigate the structural basis of the previously-described NgR self-interaction^{14,15,32}, we compared crystallographic interfaces in six new unique crystal forms of NgRa and NgRb, as well as those of the two previously-published structures (1P8T¹⁵ and 1OZN³⁰). We identify extensive interfaces in the NgRa and NgRb structures, most notably interface 1 found in five of our structures (NgRa-1, NgRa-3, NgRb-1, NgRb-2 and NgRb-3) and three independent crystal forms (space groups $C2$, $P2_1$ and $P2_12_12_1$). This interface has more inter-protein salt bridges (seven) and hydrogen bonds (ten) than any of the other interfaces and is predicted by the PRODIGY server³⁷ to be the most energetically favorable (table 3). Moreover, it is the only interface found in more than one crystallization condition (five out of ten total, eight described here and two previously-published^{15,30}). Several other interfaces have larger surface areas, but are not stabilized by as many contacts (table 3). Some of these can only be formed for NgR constructs with the artificial disulfide pattern in the C-terminal cap (interfaces in 1OZN and 1P8T, see fig. 6c and 7a, respectively). The remaining candidate interfaces have fewer inter-protein salt bridges and hydrogen bonds while not being hydrophobic either (the other interface in 1OZN and the NgRa-2 interface, see table 3), are formed via non-conserved interfaces (interface in 1OZN, see fig. 6b) or are formed at pH 4 (interface in NgRa-2). Although eight independent crystal forms for NgR are now available, there is still a possibility that the previously-demonstrated NgR self-interaction^{14,15,32} is not represented in any of these crystal forms. However, this is unlikely as NgR was crystallized at high concentrations of 250-350 μ M. Therefore, we argue that the interaction via *interface 1* most likely represents the previously reported NgR self-interaction^{14,15,32}. The flexible glycosylated stalk of NgR should allow two NgR LRRs to interact in this fashion on a cell surface *in cis*¹⁴.

Interestingly, NgR self-association via *interface 1* might be pH-controlled, as multiple intermolecular salt bridges are formed between sidechains of pH-sensitive histidine residues^{35,36} and negatively-charged amino acids (aspartate and glutamate) (see table 3). Moreover, these crystals all appeared at pH 5 (see table 2), indicating that this interface is likely more stable at lower pH. Possibly, this could play a role during trafficking of NgR through the secretory pathway or upon internalization, as low pH values occur in both secretory and endosomal compartments³⁸. Ligand-induced internalization has been suggested previously²⁹ and could occur upon binding of shed MAI ligands such as dMAG³⁹. The two previously-published structures were both crystallized at pH 6.5^{15,30}, similar to our NgRa-4 crystal form (table 2 and 3). These three crystal forms share no crystal packing interfaces and the interfaces that are present appear less extensive and less conserved than *interface 1*, as discussed above. This indicates that the interaction interfaces observed in these crystal forms do not likely represent NgR self-interaction on the cell surface, in spite of their more neutral crystallization pH.

Interface 1 involves the concave side of one NgR LRR, whereas for the other NgR LRR

in the dimer this side is still available for interaction with other ligands (Fig. 5a). Previous work has shown, by scanning alanine mutagenesis of surface residues, that Nogo66, MAG and OMgp most likely bind to the concave side of the NgR LRR⁴⁰. In addition, the presence of glutathione S-transferase (GST)-linked Nogo66 did not strongly affect the ability of NgR to self-interact¹⁴. Whether or not the NgR self-interaction via *interface 1* is compatible with ligand binding needs further study.

NgR has been shown to preferentially bind to dimeric disulfide-linked p75 in a conformation with associating intracellular death domains, which likely represents the active MAI signaling state²⁵. These disulfide-linked p75 dimers have been proposed to transduce signaling through the membrane via scissoring mechanisms depending on extracellular ligand binding²³⁻²⁵. These results suggest dimers of NgR can interact with dimeric p75, and depending on the three-dimensional arrangement of their extracellular domains, such complexes could transmit different signals through the membrane. Perhaps, NgR-p75 complexes can be in both active and inactive conformations, depending on the presence of MAI ligand, as suggested previously¹⁵. Interestingly, inactive and active dimers have been reported for plexins⁴¹ and ephRs⁴², both axon guidance receptors that signal via RhoA/ROCK and inhibit CNS regeneration upon injury, similar to NgR⁴³⁻⁴⁶. Further investigation is required to determine if NgR dimers formed via *interface 1* represent an active or an inactive signaling state.

If the dimer that forms via *interface 1* represents an inactive signaling state, this could be a target for pharmacological intervention with small molecule therapeutics. These dimers have significant cavities in between the two monomers that could be exploited by dimer-stabilizing small molecules that keep NgR in a silent signaling state even in the presence of MAIs (Fig. 8). Conversely, if *interface 1* represents an active signaling state, small molecules could be designed that interfere with the formation of the protein-protein interaction interface we report.

Methods

Generation of constructs and mutagenesis

Mouse NgR constructs were generated by polymerase chain reaction (PCR) with the cDNA IMAGE 6397765 as a template and primers to start at UNIPROT residue 26 (after the signal peptide) and end at residue 310 (NgR LRR), 337 (NgRa), 348 (NgRb) or 446 (full extracellular domain, no GPI anchor). All constructs were subcloned using BamHI/NotI sites in pUPE107.03 (cystatin secretion signal peptide, C-terminal His₆-tag).

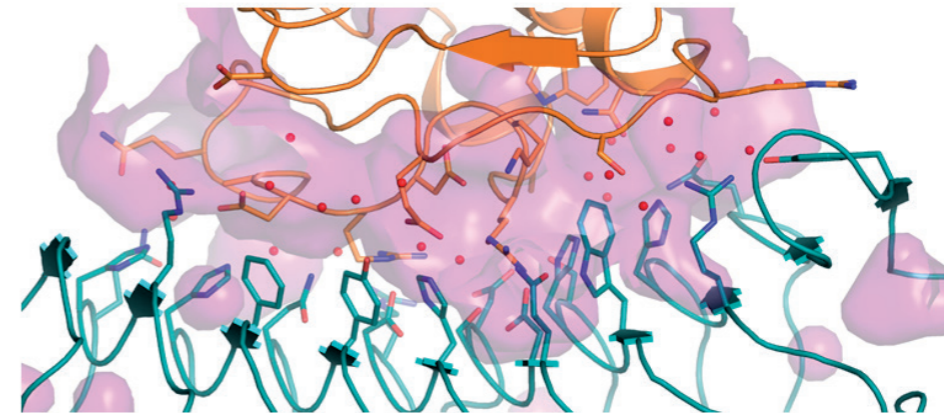


Figure 8: Cavity surface of *interface 1*

Interface represented as in figure 5a. The cavity formed in between the molecules is indicated by a purple surface. If this dimer, formed via *interface 1*, represents an inactive signaling form, these cavities could be exploited to design dimer-stabilizing small molecules to antagonize MAI signaling and enhance regeneration upon CNS injury.

Large-scale expression and purification

Constructs were transiently expressed in N-acetylglucosaminyltransferase I-deficient (GnTI-) Epstein-Barr virus nuclear antigen I (EBNA1)-expressing HEK293 cells in suspension (U-Protein Express). DNA titration by dilution with non-expressing PCR4 DNA was used to boost expression levels, similar to a previously-described approach⁴⁷. DNA was diluted 25× (NgRa), 100× (NgRb), 5× (NgRb D111R) or 5× (NgRb R300E). The medium was harvested six days after transfection and cells were spun down by 10 minutes of centrifugation at 1000× g. Supernatant was concentrated fivefold and diafiltered against 500 mM NaCl, 25 mM HEPES pH 7.5 (IMAC A) using a Quixstand benchtop system (GE Healthcare) with a 10 kDa molecular weight cut-off (MWCO) membrane. Cellular debris was spun down for 10 minutes at 9500× g and the supernatant was filtered with a glass fiber prefilter (Minisart, Sartorius). Protein was purified by Nickel-nitrilotriacetic acid (Ni-NTA) affinity chromatography followed by size exclusion chromatography (SEC) on a Superdex75 Hiload 16/60 column (GE Healthcare) equilibrated with SEC buffer (150 mM NaCl, 20 mM HEPES pH 7.5). Protein was concentrated to 10-15 mg/mL using a 10 kDa MWCO concentrator before plunge freezing in liquid nitrogen and storage at -80 °C.

Crystallization and data collection

For crystallization, glycosylated as well as enzymatically-deglycosylated protein was used. Deglycosylation was performed by overnight treatment with Endo-H_f (1.0×10⁶ U/mL, New England Biolabs, added 1:100 v/v) at 25 °C (NgRa) or 37 °C (NgRb).

Completeness of deglycosylation was analyzed by SDS-PAGE. Sitting-drop vapor diffusion at 4 or 18 °C was used for all crystallization trials, by mixing 150 nL of protein solution with 150 nL of reservoir solution. Crystallization was typically performed at concentrations of 10-13 mg/mL.

NgRa-1 was the result of a co-crystallization trial with Endo-H_f-deglycosylated mouse TROY cysteine-rich domains 1-3 (UNIPROT Q9JLL3, residues 30-152) in SEC buffer, mixed at equimolar stoichiometry. NgRa was also Endo-H_f-deglycosylated. Crystals grew at 18 °C in a condition of 0.05 M citric acid pH 5.0, 15 % (w/v) PEG6000.

NgRa-2 was the result of a co-crystallization trial with the Endo-H_f-deglycosylated extracellular domain of mouse MAG (UNIPROT P20917, residues 20-508) in SEC buffer, mixed at equimolar stoichiometry. NgRa was also Endo-H_f-deglycosylated. Crystals grew at 4 °C in a condition of 0.5 M LiCl, 0.05 M citric acid pH 4.0, 15 % (w/v) PEG6000.

NgRa-3 crystals grew at 18 °C in a condition of 0.05 M MIB buffer (2:3:3 molar ratio of sodium malonate:imidazole:boric acid) pH 5.0, 12.5 % (w/v) PEG1500. NgRa was Endo-H_f-deglycosylated for NgRa-3. The NgRa-3 crystal was soaked with 10 mM N-acetyl-neuraminic acid prior to cryo-protection and freezing.

NgRa-4 was the result of a co-crystallization trial with mouse Nogo54, an extracellular construct derived from the NgR ligand Nogo-A (UNIPROT Q99P72, residues 1025-1078). Nogo54 was purified in 150 mM NaCl, 20 mM HEPES pH 7.0 at a concentration of 3.3 mg/mL and mixed in a 1:1 molar ratio with Endo-H_f-deglycosylated NgRa at a concentration of 10 mg/mL. Crystals grew at 18 °C in a condition of 0.2 M ammonium sulfate, 0.1 M Bis-Tris pH 6.5, 25% (w/v) PEG3350.

NgRa-5 crystals grew at 4 °C in a condition of 2.5 M NaCl, 100 mM NaOAc/AcOH pH 4.5, 200 mM Li₂SO₄. NgRa was Endo-H_f-deglycosylated for NgRa-5.

NgRb-1 crystals grew at 4 °C in a condition of 0.05 M citric acid, 0.05 M Bis-Tris propane pH 5.0, 16 % (w/v) PEG3350. NgRb was Endo-H_f-deglycosylated for NgRb-1.

NgRb-2 crystals grew at 18 °C in a condition of 0.2 M NaH₂PO₄ pH 5, 20 % (w/v) PEG3350. NgRb was Endo-H_f-deglycosylated for NgRb-2.

NgRb-3 crystals grew at 18 °C in a condition of 1.8 M NaH₂PO₄/K₂HPO₄ pH 5.0. NgRb was Endo-H_f-deglycosylated for NgRb-2.

Crystals were cryo-protected with reservoir solution supplemented with 25 % glycerol before plunge-freezing in liquid nitrogen. All data were collected at 100 K at the following beamlines: European Synchrotron Radiation Facility (ESRF) ID23-1 (NgRa-1, NgRa-4, NgRb-1, NgRb-3), ID23-2 (NgRb-2) and ID29 (NgRa-2) and Swiss Light Source (SLS) PX (NgRa-3 and NgRa-5).

Structure solution and refinement

All structures were solved by molecular replacement with PHASER⁴⁸ using the 1OZN structure as a search model³⁰. Structures were modeled by cycles of model building in COOT⁴⁹ and refinement by Refmac⁵⁰ and phenix.refine⁵¹. Eight-fold non-crystallographic symmetry map averaging was used in COOT⁴⁹ to obtain better electron density maps for the C-terminal loop of the NgRa-5 crystal form. Ramachandran statistics were (% Ramachandran favored / % allowed / % outliers): 95/5/0 (NgRa-1), 93.5/6.3/0.2 (NgRa-2), 95.7/4.3/0 (NgRa-3), 92.8/6.2/0 (NgRa-4), 95.4/4.6/0 (NgRa-5), 95.5/4.5/0 (NgRb-1), 93.9/6.1/0 (NgRb-2), 93.8/6.2/0 (NgRb-3).

Structure analysis

Surface areas were calculated by the PISA server⁵². Evolutionary conservation of surface residues was performed using the ConSurf server⁵³. Binding affinities were predicted by the PRODIGY server³⁷. All protein structures were visualized using Pymol⁵⁴.

References

1. Mironova, Y. A. & Giger, R. J. Where no synapses go: gatekeepers of circuit remodeling and synaptic strength. *Trends Neurosci.* **36**, 363–373 (2013).
2. Baldwin, K. T. & Giger, R. J. Insights into the physiological role of CNS regeneration inhibitors. *Front. Mol. Neurosci.* **8**, 1–8 (2015).
3. McGee, A. W. & Strittmatter, S. M. The Nogo-66 receptor: focusing myelin inhibition of axon regeneration. *Trends Neurosci.* **26**, 193–198 (2003).
4. Akbik, F., Cafferty, W. B. J. & Strittmatter, S. M. Myelin associated inhibitors: A link between injury-induced and experience-dependent plasticity. *Exp. Neurol.* **235**, 43–52 (2011).
5. McGee, A. W., Yang, Y., Fischer, Q. S., Daw, N. W. & Strittmatter, S. M. Experience-driven plasticity of visual cortex limited by myelin and Nogo receptor. *Science (80-)*. **309**, 2222–2226 (2005).
6. Stephany, C.-É., Ikrar, T., Nguyen, C., Xu, X. & McGee, A. W. Nogo Receptor 1 Confines a Disinhibitory Microcircuit to the Critical Period in Visual Cortex. *J. Neurosci.* **36**, 11006–11012 (2016).
7. Lee, H. *et al.* Synaptic function for the Nogo-66 receptor NgR1: regulation of dendritic spine morphology and activity-dependent synaptic strength. *J. Neurosci.* **28**, 2753–65 (2008).
8. Raiker, S. J. *et al.* Oligodendrocyte-myelin glycoprotein and Nogo negatively regulate activity-dependent synaptic plasticity. *J. Neurosci.* **30**, 12432–12445 (2010).
9. Akbik, F. V., Bhagat, S. M., Patel, P. R., Cafferty, W. B. J. & Strittmatter, S. M. Anatomical Plasticity of Adult Brain Is Titrated by Nogo Receptor 1. *Neuron* **77**, 859–866 (2013).
10. Fournier, A. E., GrandPré, T. & Strittmatter, S. M. Identification of a receptor mediating Nogo-66 inhibition of axonal regeneration. *Nature* **409**, 341–346 (2001).
11. Liu, B. P., Fournier, A., GrandPré, T. & Strittmatter, S. M. Myelin-associated glycoprotein as a functional ligand for the Nogo-66 receptor. *Science* **297**, 1190–3 (2002).
12. Wang, K. C., Koprivica, V., Kim, J. A. & Sivasankaran, R. Oligodendrocyte-myelin glycoprotein is a Nogo receptor ligand that inhibits neurite outgrowth. *Nature* **417**, 941–944 (2002).
13. Wang, K., Koprivica, V., Kim, J. & Sivasankaran, R. Oligodendrocyte-myelin glycoprotein is a Nogo receptor ligand that inhibits neurite outgrowth. *Nature* **417**, 941–944 (2002).
14. Fournier, A. E., Gould, G. C., Liu, B. P. & Strittmatter, S. M. Truncated soluble Nogo receptor binds Nogo-66 and blocks inhibition of axon growth by myelin. *J. Neurosci.* **22**, 8876–83 (2002).
15. Barton, W. *et al.* Structure and axon outgrowth inhibitor binding of the Nogo-66 receptor and related proteins. *EMBO J.* **22**, 3291–302 (2003).
16. Venkatesh, K. *et al.* The Nogo-66 receptor homolog NgR2 is a sialic acid-dependent receptor selective for myelin-associated glycoprotein. *J. Neurosci.* **25**, 808–822 (2005).
17. Laurén, J. *et al.* Characterization of myelin ligand complexes with neuronal Nogo-66 receptor family members. *J. Biol. Chem.* **282**, 5715–5725 (2007).
18. Robak, L. A. *et al.* Molecular Basis of the Interactions of the Nogo-66 Receptor and Its Homolog NgR2 with Myelin-Associated Glycoprotein : Development of NgR OMNI -Fc , a Novel Antagonist of CNS Myelin Inhibition. *J. Neurosci.* **29**, 5768–5783 (2009).
19. Wen, D. *et al.* Disulfide structure of the leucine-rich repeat C-terminal cap and C-terminal stalk region of Nogo-66 receptor. *Biochemistry* **44**, 16491–16501 (2005).
20. Wong, S. T. *et al.* A p75(NTR) and Nogo receptor complex mediates repulsive signaling by myelin-associated glycoprotein. *Nat. Neurosci.* **5**, 1302–8 (2002).
21. Wang, K. C., Kim, J. a, Sivasankaran, R., Segal, R. & He, Z. P75 interacts with the Nogo receptor as a co-receptor for Nogo, MAG and OMgp. *Nature* **420**, 74–8 (2002).
22. Mi, S. *et al.* LINGO-1 is a component of the Nogo-66 receptor/p75 signaling complex. *Nat. Neurosci.* **7**, 221–228 (2004).
23. Vilar, M. *et al.* Activation of the p75 Neurotrophin Receptor through Conformational Rearrangement of Disulphide-Linked Receptor Dimers. *Neuron* **62**, 72–83 (2009).
24. Vilar, M. *et al.* Ligand-independent signaling by disulfide-crosslinked dimers of the p75 neurotrophin receptor. *J. Cell Sci.* **122**, 3351–3357 (2009).
25. Vilar, M. *et al.* Heterodimerization of p45-p75 modulates p75 signaling: structural basis and mechanism of action. *PLoS Biol.* **12**, e1001918 (2014).
26. Park, J. B. *et al.* A TNF receptor family member, TROY, is a coreceptor with Nogo receptor in mediating the inhibitory activity of myelin inhibitors. *Neuron* **45**, 345–351 (2005).
27. Shao, Z. *et al.* TAJ/TROY, an orphan TNF receptor family member, binds Nogo-66 receptor 1 and regulates axonal regeneration. *Neuron* **45**, 353–359 (2005).
28. Ahmed, Z., Douglas, M. R., John, G., Berry, M. & Logan, A. AMIGO3 is an NgR1/p75 co-receptor signalling axon growth inhibition in the acute phase of adult central nervous system injury. *PLoS One* **8**, e61878 (2013).
29. Meabon, J. S. *et al.* LINGO-1 Interacts with the p75 Neurotrophin Receptor in Intracellular Membrane Compartments. *J. Biol. Chem.* jbc.M114.608018 (2015).
30. He, X. L. *et al.* Structure of the Nogo receptor ectodomain: a recognition module implicated in myelin inhibition. *Neuron* **38**, 177–185 (2003).
31. Semavina, M. *et al.* Crystal structure of the Nogo-receptor-2. *Protein Sci.* **20**, 684–689 (2011).
32. Saha, N., Kolev, M. V., Semavina, M., Himanen, J. & Nikolov, D. B. Ganglioside mediate the interaction between Nogo receptor 1 and LINGO-1. *Biochem. Biophys. Res. Commun.* **413**, 92–97 (2011).
33. Weinreb, P. H. *et al.* Resolution of disulfide heterogeneity in Nogo receptor I fusion proteins by molecular engineering. *Biotechnol. Appl. Biochem.* **57**, 31–45 (2010).
34. Yun, R. H., Anderson, a & Hermans, J. Proline in alpha-helix: stability and conformation studied by dynamics simulation. *Proteins* **10**, 219–28 (1991).
35. Bradbury, J. H. & Scheraga, H. A. Structural studies of ribonuclease. XXIV. The application of nuclear magnetic resonance spectroscopy to distinguish between the histidine residues of ribonuclease. *J. Am. Chem. Soc.* **88**, 4240–4246 (1966).
36. Markley, J. L. Observation of histidine residues in proteins by nuclear magnetic resonance spectroscopy. *Acc. Chem. Res.* **8**, 70–80 (1975).
37. Vangone, A. & Bonvin, A. M. Contacts-based prediction of binding affinity in protein-protein complexes. *Elife* **4**, e07454 (2015).
38. Demaurex, N. pH Homeostasis of cellular organelles. *News Physiol. Sci.* **17**, 1–5 (2002).
39. Tang, S. *et al.* Soluble Myelin-Associated Glycoprotein (MAG) Found in Vivo Inhibits Axonal Regeneration. *Mol. Cell. Neurosci.* **346**, 333–346 (1997).
40. Laurén, J. *et al.* Characterization of myelin ligand complexes with neuronal Nogo-66 receptor family members. *J. Biol. Chem.* **282**, 5715–25 (2007).
41. Kong, Y. *et al.* Structural Basis for Plexin Activation and Regulation. *Neuron* 1–13 (2016). doi:10.1016/j.neuron.2016.06.018
42. Himanen, J. P. *et al.* Crystal structure of an Eph receptor-ephrin complex. *Nature* **414**, 933–8 (2001).
43. Pasterkamp, R. J., Anderson, P. N. & Verhaagen, J. Peripheral nerve injury fails to induce growth of lesioned ascending dorsal column axons into spinal cord scar tissue expressing the axon repellent Semaphorin3A. *Eur. J. Neurosci.* **13**, 457–471 (2001).
44. Benson, M. D. *et al.* Ephrin-B3 is a myelin-based inhibitor of neurite outgrowth. *Proc. Natl. Acad. Sci. U. S. A.* **102**, 10694–9 (2005).
45. Bolsover, S., Fabes, J. & Anderson, P. N. Axonal guidance molecules and the failure of axonal regeneration in the adult mammalian spinal cord. *Restor. Neurol. Neurosci.* **26**, 117–130 (2008).
46. Kolodkin, A. L. & Tessier-Lavigne, M. Mechanisms and molecules of neuronal wiring: A primer. *Cold Spring Harb. Perspect. Biol.* **3**, 1–14 (2011).
47. Half, E. F., Versteeg, M., Brondijk, T. H. C. & Huizinga, E. G. When less becomes more: Optimization of protein expression in HEK293-EBNA1 cells using plasmid titration - A case study for NLRs. *Protein Expr. Purif.* **99**, 27–34 (2014).
48. McCoy, A. J. *et al.* Phaser crystallographic software. *J. Appl. Crystallogr.* **40**, 658–674 (2007).
49. Emsley, P. & Cowtan, K. Coot: Model-building tools for molecular graphics. *Acta Crystallogr. Sect. D Biol. Crystallogr.* **60**, 2126–2132 (2004).
50. Murshudov, G. N. *et al.* REFMAC5 for the refinement of macromolecular crystal structures. *Acta Crystallogr. Sect. D Biol. Crystallogr.* **67**, 355–367 (2011).
51. Afonine, P. V. *et al.* Towards automated crystallographic structure refinement with phenix.refine. *Acta Crystallogr. Sect. D Biol. Crystallogr.* **68**, 352–367 (2012).
52. Krissinel, E. & Henrick, K. Inference of Macromolecular Assemblies from Crystalline State. *J. Mol. Biol.* **372**, 774–797 (2007).
53. Glaser, F. *et al.* ConSurf: Identification of functional regions in proteins by surface-mapping of phylogenetic information. *Bioinformatics* **19**, 163–164 (2003).
54. The PyMOL Molecular Graphics System, Version 1.5 Schrödinger.

Acknowledgements

We thank the staff of the European Synchrotron Radiation Facility (ESRF) beamlines ID23-1, ID23-2 and ID29 and Swiss Light Source (SLS) beamline PX for assistance with diffraction data collection.

Author contributions

M.F.P. and B.J.C.J. designed experiments. M.F.P. generated constructs, purified proteins, performed crystallization and solved and refined structures. R.J.T., H.C.V. and M.F.P. purified proteins and set up crystals that resulted in the NgRa-4 structure. B.J.C.J. supervised the project. M.F.P. and B.J.C.J. wrote the manuscript. This work was funded by a Vidi grant (723.012.002) from the Netherlands Organization for Scientific Research to B.J.C.J..

Chapter 4

Olfactomedin-1 has a V-shaped disulfide-linked tetrameric structure

Matti F. Pronker¹, Trusanne G.A.A. Bos¹, Thomas H. Sharp³, Dominique M.E. Thies-Weesie², Bert J.C. Janssen¹

¹: *Crystal and Structural Chemistry, Bijvoet Center for Biomolecular Research, Department of Chemistry, Faculty of Science, Utrecht University 3584 CH Utrecht, The Netherlands*

²: *Van't Hoff Laboratory for Physical and Colloid Chemistry, Debye Institute of Nanomaterials Science, Department of Chemistry, Faculty of Science, Utrecht University 3584 CH Utrecht, The Netherlands*

³: *Section Electron Microscopy, Department of Molecular Cell Biology, Leiden University Medical Center, 2300 RC Leiden, The Netherlands*

Journal of Biological Chemistry **290**, 15092–15101 (2015).

Abstract

Olfactomedin-1 (Olfm1; also known as noelin, pancortin) is a member of the olfactomedin domain-containing superfamily and a highly expressed neuronal glycoprotein important for nervous system development. It binds a number of secreted proteins and cell-surface bound receptors to induce cell signaling processes. Using a combined approach of X-ray crystallography, solution scattering, analytical ultracentrifugation and electron microscopy we determine that full-length Olfm1 forms disulfide-linked tetramers with a distinctive V-shaped architecture. The base of the “V” is formed by two disulfide-linked dimeric N-terminal domains. Each of the two V-legs consists of a parallel dimeric disulfide-linked coiled coil with at the tips a C-terminal β -propeller dimer. This agrees with our crystal structure of a C-terminal coiled-coil segment and β -propeller combination (Olfm1^{coil-Olf}), which reveals a disulfide-linked dimeric arrangement with the β -propeller top faces in an outward exposed orientation. Similar to its family member myocilin, Olfm1 is stabilized by calcium. The dimer-of-dimers architecture suggests a role for Olfm1 in clustering receptors to regulate signaling and informs on the conformation of several other olfactomedin domain family members.

Introduction

Olfm1 is a secreted oligomerized glycoprotein highly expressed in the developing and adult nervous system¹. It is involved in signaling processes that regulate neuronal development. It has been shown to stimulate neurogenesis and influences the timing of neuronal differentiation in several vertebrates^{2,3}. Olfm1 also modulates cortical cell migration and neural crest formation^{4,5} and Olfm1 has been recognized as a regulator of axon growth and elongation^{6,7}. More recently, aberrant Olfm1 function was also linked to mouse behavioral abnormalities⁸. These results suggest Olfm1 is an important signaling protein in the developing and adult nervous system.

It is not known how Olfm1 regulates these processes but it has been shown that Olfm1 interacts with a number of proteins that are implicated in these neuronal signaling processes. Olfm1 binds to secreted Wnt Inhibitory Factor 1 (WIF-1), receptors Nogo Receptor (NgR) and Amyloid Precursor Protein (APP) and neuronal cation channel proteins GluR2 AMPA receptor and Cav2.1 voltage-gated calcium channel. These proteins are part of several signaling pathways and interfering with these interactions, by mutation, overexpression or knockdown of Olfm1, leads to neuronal developmental defects^{4,6,7}. Mutation of Olfm1 disrupts interactions with the AMPA receptor and Cav2.1 channel and increases intracellular calcium levels. This results in a multitude of signaling malfunctions, culminating in brain dystrophy and behavioral changes⁸. How Olfm1 interacts with this diverse set of proteins and how this leads to signaling events that control neuronal developments is not clear.

Olfm1 is a member of the olfactomedin superfamily, of which the conserved olfactomedin domain is a defining feature^{9,10}. Other well-known members are the Olfm1 paralogs Olfm2, Olfm3, Olfm4 (56%, 67% and 22% sequence identity respectively), gliomedin, myocilin and latrophilin1, -2 and -3. These proteins have been shown to bind to ligands on the cell surface. The olfactomedin domain is often implicated in interaction with ligands and many members are believed to be oligomerized. The four Olfms paralogs and myocilin are oligomerized through coiled-coil domains whereas gliomedin is oligomerized through a collagen-like domain. Oligomerization of these molecules is important for function¹⁰ and Olfm1 can form complexes with Olfm2 and Olfm3^{11,12}. However, it is not clear how Olfm1 or the paralog (Olfm2, 3 and 4) oligomers are structurally arranged.

As a result of alternative splicing, four isoforms of Olfm1 are differentially expressed during development (Fig. 1a)¹³. All 4 isoforms of Olfm1 are known to be present in the ER as well as being secreted, in spite of isoforms 1 and 3 having a C-terminal -RSEDEL quasi-ER-retention motif^{3,4}. The most complete isoform of Olfm1, isoform 1 (also called BMX), is most similar to the other Olfm paralogs. This isoform comprises a disulfide-containing C-terminal olfactomedin domain, which has recently been shown to be a

five-bladed β -propeller in myocilin, gliomedin and latrophilin3¹⁴⁻¹⁶. The olfactomedin domain is preceded by a conserved cysteine and a 132-residues-long coiled-coil domain. N-terminal of the coiled-coil domain is a 77 residue large region that contains three conserved cysteines in a C-X-C-X₂-C arrangement. The first two cysteines (Cys73 and Cys75) have been found to be essential for Olfm1 oligomerization¹⁷. In isoform 2 and 4, the C-terminal β -propeller domain and a large part of the coiled coil are absent, whereas isoform 3 and 4 have an alternative signal sequence and lack the first 35 amino acids of mature Olfm1 (Fig. 1a). Thus, essentially isoform 1 represents the full mature Olfm1 protein whereas the other three isoforms are lacking regions at the termini.

The structure of Olfm1 and its paralog is not known. It is not clear how the domains are arranged, which interactions mediate oligomerization nor whether it adopts a defined quaternary structure. Olfm1 interacts with a diverse set of proteins for its signaling functions, but how it performs these various roles is unknown. Lack of structural data has hampered progress in the field. In this study we determine the structure of the olfactomedin domain of Olfm1 and the quaternary arrangement and architecture of the full-length protein, using a combined approach of X-ray crystallography, electron microscopy and biophysical characterization.

Results

Olfm1 forms disulfide-linked homotetramers

Recombinantly expressed Olfm1 lacking the C-terminal ER-retention signal was purified from HEK293 supernatant for structural studies. Size exclusion chromatography as part of the purification strategy suggested a defined oligomeric assembly larger than a trimer. Analysis by reducing and non-reducing SDS-PAGE showed that this oligomer was disulfide-linked, as seen by others^{17,18} (Fig. 1b).

The oligomeric assembly was independently shown to be tetrameric by size-exclusion chromatography coupled to multi-angle light scattering (SEC-MALS), analytical ultracentrifugation (AUC) sedimentation velocity and SAXS (Fig. 1c-f). In SEC-MALS, a mass of approximately 260 kDa was determined from the light scattering signal (Fig. 1c). This correlates well with the theoretical mass of 256 kDa for a fully glycosylated tetrameric Olfm1 (without any glycans the mass of a tetramer would be 217 kDa). In AUC, the tetramer had a sedimentation coefficient of 7.67 S and a frictional ratio f/f_0 of 1.98, indicating an extended shape and corresponding to a molecular mass of 242 kDa (Fig. 1d). Further confirmation of a concentration-independent tetramer came from SAXS (Fig. 1e, table 1); the molecular weight estimated from the I_0 value of the Guinier plot of 249 kDa indicated a tetramer (Fig. 1f). The presence of monomers, dimers or higher oligomeric species was not observed in any of these experiments.

To show that the sole presence of Olfm1 tetramers was not an artifact of purification, Western blot with α -His antibody was performed directly on the expression medium. This confirmed the presence of a disulfide-linked tetramer, yet showed no bands for other disulfide-linked oligomers (Fig. 1b).

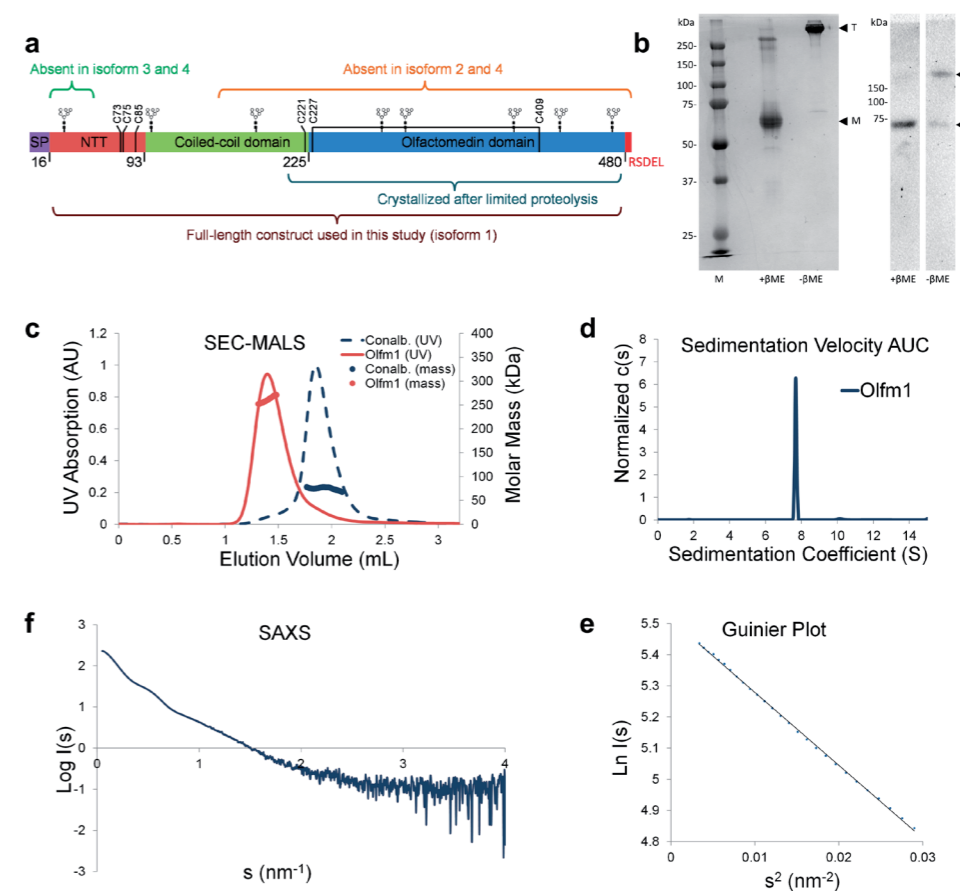


Figure 1. Olfm1 forms disulfide-linked tetramers.

(a) Isoforms and domains of Olfm1. In this study isoform 1 was used. Cysteines are shown as vertical black lines. (b) Non-reducing SDS-PAGE (Coomassie-stained purified protein, left and Western-blotted expression medium, right) shows a shift to >250 kDa, whereas reducing SDS-PAGE shows Olfm1 running at the expected height of 64 kDa for a (fully glycosylated) monomer. (c) SEC-MALS shows a mass of approximately 260 kDa for the Olfm1 peak, which elutes before conalbumin (78 kDa). The plotted UV signal was recorded at 280 nm. (d) AUC sedimentation velocity experiments give a mass of 242 kDa, a sedimentation coefficient of 7.67 S and a frictional ratio of 1.98 (RMSD= 0.005). E. SAXS log I(s) vs. s plot of Olfm1 at 3.55 mg/mL. F. Guinier plot from SAXS curve agrees with a tetramer ($I_0 = 249$, $R_g = 8.5$ nm).

Table 1. SAXS parameters

I_0 (normalized and referenced)	249
R_g from Guinier plot (nm)	8.5
R_g from $P(r)$ (nm)	8.8
D_{max} from $P(r)$ (nm)	30
V_{pore} (nm ³)	616
Protein concentration (mg/mL)	3.55
SASBDB accession code	SASDAS7

Crystal structure of a covalent dimeric Olfm1^{coil-Olf}

Crystallization attempts of the full-length protein yielded no crystals, so we employed limited proteolysis by α -chymotrypsin as a crystallization aid to remove unstructured regions. This yielded diffraction-quality crystals and a dataset to 2.4 Å resolution (see Table 2). Crystal structures of the olfactomedin domain of gliomedin¹⁴ allowed us to do molecular replacement.

The structure revealed a disulfide-linked dimer of β -propellers in the asymmetric unit, related by a pseudo-twofold rotation of 178° (Fig. 2a). As expected, each β -propeller corresponds to a C-terminal olfactomedin domain. In addition to the β -propellers, a segment of the coiled-coil domain (residues Val211 to Leu225) was visible in the electron density (Fig. 2b). Cys221 in this coiled-coil segment forms an interprotein disulfide, covalently linking the two β -propellers. The coiled coil is predicted to be longer (Fig. 3) but we do not observe additional residues N-terminal of Val211. Most likely, the segment of coiled coil absent from the crystals was hydrolyzed by α -chymotrypsin prior to crystallization. The Val211-Leu225 segment appears to be inaccessible for proteolysis due to steric hindrance by the two β -propellers. The dimer contacts are exclusively formed by the coiled coils; the two β -propellers are not contacting each other directly. Cys227, the first residue of the β -propeller, forms an intraprotein disulfide with Cys409 as predicted¹⁵; this disulfide bond appears to close the β -propeller fold and lock it in a fixed orientation with respect to the coiled coil (Fig. 2a and 2b). The β -propeller is tilted with respect to the coiled coil with an angle of 30° between the β -propeller plane and the coiled coil axis. Hence, the two β -propellers in the covalent dimer have a 60° angle between each other resulting in an exposed outward orientation of the β -propeller top faces.

The Olfm1 β -propeller

The olfactomedin domain of Olfm1 forms a five-bladed β -propeller similar in structure to the recently solved olfactomedin domains of gliomedin, myocilin and latrophilin^{3,14-16}. Each of the five blades in Olfm1 consists of four β strands. The N-terminal segment of the β -propeller (Lys229-Thr241) forms a β strand that completes the fifth β -propeller

and closes the β -propeller fold (in addition to the intramolecular disulfide bond Cys227-Cys409; Fig. 2a, 2b and 2c). The two β -propellers in the dimer are very similar in structure (rmsd of 0.4 Å and 0.9 Å over all $C\alpha$'s and all atoms, respectively) with largest differences in the N- and C-termini.

Table 2. Crystallographic data collection and refinement

	Olfm1 ^{coil-Olf}
Data collection	
Space group	C2
Cell dimensions	
a, b, c (Å)	160.2, 43.94, 104.1
α, β, γ (°)	90, 114.2, 90
Resolution (Å)	50.3-2.4 (2.5-2.4)
No. of reflections	26050
R_{merge}	0.096 (0.936)
Mean I/σ	7.7 (1.2)
Completeness (%)	98.9 (99.4)
Redundancy	3.4 (3.5)
$CC_{1/2}$	0.996 (0.489)
Refinement	
Resolution (Å)	2.4
R_{work}/R_{free}	0.241/0.258
No. of atoms	4304
Average B-factor (Å ²)	
Protein	69.3
Ligand	92.7
Water	51.2
R.M.S. deviations	
Bond lengths (Å)	0.005
Bond angles (°)	0.884
Molprobrity score	1.84

Highest resolution shell is shown in parentheses.

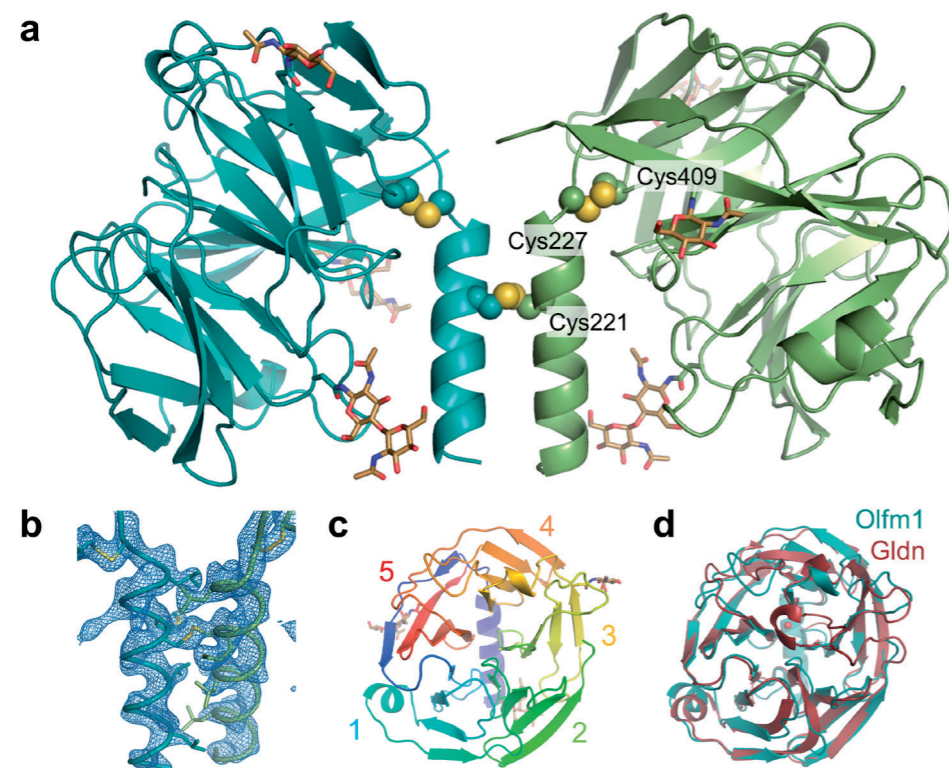


Figure 2. Structural characterization of a limited proteolysis fragment of Olfm1

(a) Structure of the Olfm1^{coil-off} dimer. The inter- and intraprotein disulfides (shown as spheres) link the two monomers together and lock the β -propellers to the coiled coil, respectively. (b) Close-up view of the coiled coil and disulfides of the Olfm1^{coil-off} dimer, showing the hydrophobic side chains in the coiled coil as sticks. The $2F_o - F_c$ electron density map was plotted at 1.2σ . (c) View down the top face of a single β -propeller shows five blades, which are numbered accordingly. (d) The structure of the olfactomedin domain of gliomedin (Gldn; red) is very similar to the olfactomedin domain of Olfm1 (teal, rmsd of 1.3 Å over 226 aligned C α 's).

We compared the olfactomedin domain of Olfm1 to that of gliomedin¹⁴ and latrophilin3¹⁶ (PDB codes 4D77 and 5AFB, respectively). The three olfactomedin domain structures are very similar to each other with an rmsd of 1.3 Å for gliomedin and 1.1 Å for latrophilin3 over 226 aligned C α 's (Fig. 2d and 5a). These scores are also reflected in the respective sequence identities of 32 and 42% for the olfactomedin domain. Largest differences are apparent in three loops at the top face of the β -propeller (within and between blades 3, 4 and 5) and in one loop in blade 1 at the β -propeller bottom face that interfaces with the coiled coil in Olfm1.

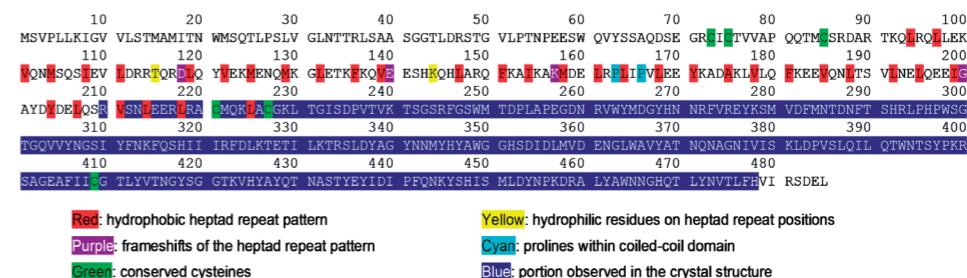


Figure 3. Analysis of the hydrophobic heptad-repeat pattern in the coiled-coil domain of Olfm1.

The full amino acid sequence of mouse Olfm1 is shown. Hydrophobic heptad repeat residues have been indicated, based on the register of coiled coil residues 210 to 225, which were observed in the crystal structure. Also indicated are possible disturbances from an ideal coiled coil, such as frameshifts, hydrophilic residues on heptad repeat positions and prolines in the coiled coil.

Most likely, all of the five predicted N-linked glycosylation sites in the β -propeller (Asn288, -307, -394, -431 and -473) are glycosylated as we observed at least some density for the five glycans in one of the two β -propellers. Remarkably, all glycosylation sites are located at either the side or the bottom of the β -propellers, whereas the top faces are free from glycans and completely exposed (Fig. 4a). Furthermore, the top face of the β -propellers is evolutionarily more conserved than the sides or the bottom (Fig. 4b). These observations, together with an exposed outward orientation, suggest a role for the β -propeller top face in ligand binding.

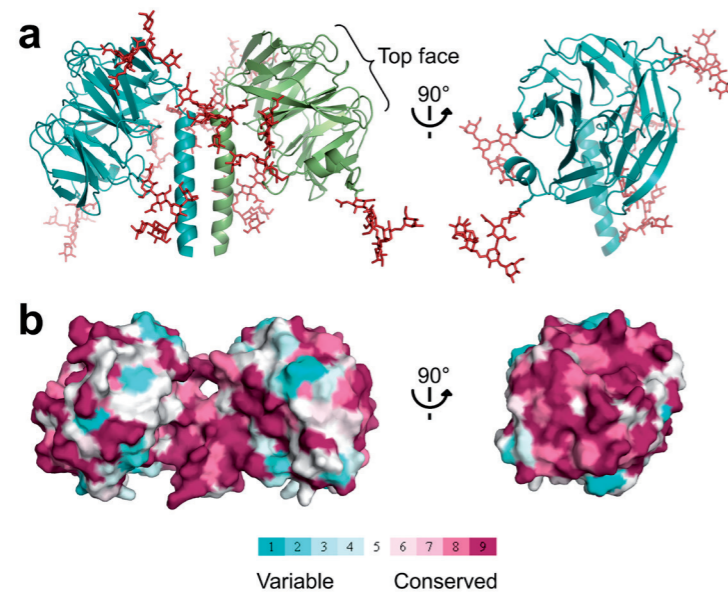


Figure 4. The top face of the Olfm1 β -propeller could be important for receptor binding.

(a) Olfm1^{coil-Olf} dimer with modeled full glycans (red) and longer coiled coils shows that all glycans are localized to the side and bottom face of the β -propeller, whereas the top face is accessible. (b) Conservation plot indicates that the top face of the β -propeller has a higher degree of sequence conservation than the sides, suggesting this interface might be important for ligand binding. Conservation scores were calculated with an alignment of 35 vertebrate Olfm1 orthologs using ConSurf⁴².

Calcium stabilizes Olfm1

A cation binding site is present in the center of the olfactomedin domain β -propeller of gliomedin¹⁴ myocilin¹⁵, and latrophilin3¹⁶. In myocilin and latrophilin3 a calcium and sodium ion are located next to each other in this site whereas in gliomedin one sodium ion is present. The Olfm1 cation binding site resembles that of myocilin and latrophilin3; two of the three cation coordinating sidechains are identical in the three proteins (Asp356 and Asp453, Olfm1 residue numbering) and one, Glu404, is replaced by Asn in myocilin and latrophilin3 (Fig. 5a). We observed a positive 5σ peak at this site in the $F_o - F_c$ difference electron density map after initial refinement, but cannot confidently place a calcium ion here even at lowered occupancies. Thermal denaturation assays showed that excess calcium stabilized the protein at concentrations as low as 1 mM, whereas EDTA destabilized it (Fig. 5b). Based on cation binding site similarity to myocilin and latrophilin3 and our observation that calcium stabilizes Olfm1, we hypothesize that Olfm1 also has a calcium binding site located at this site in the center of the β -propeller.

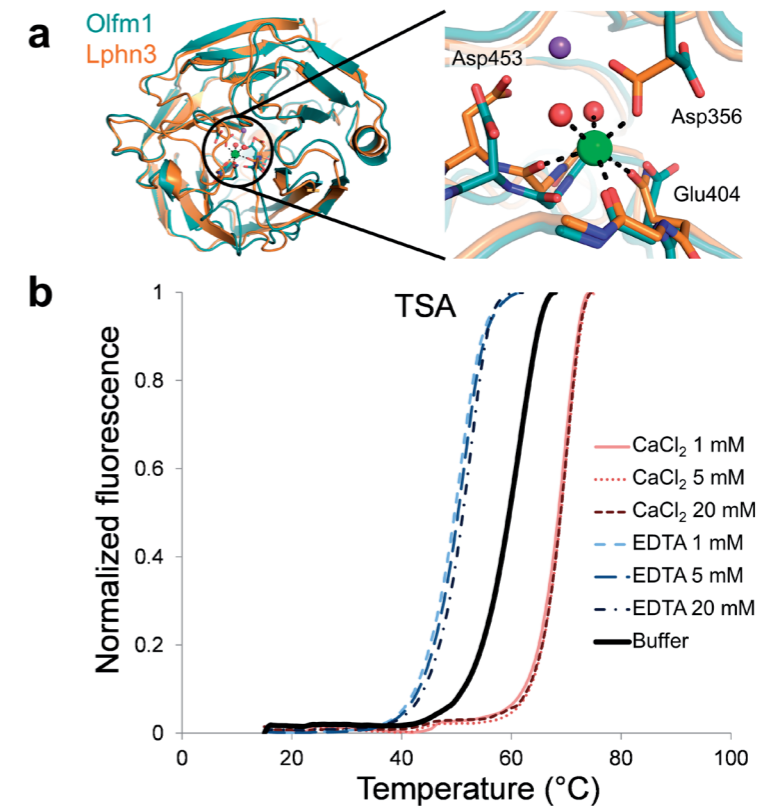


Figure 5. Calcium stabilizes the Olfm1 β -propeller

(a) Comparison of the calcium-binding olfactomedin domain of latrophilin3 (Lphn3; orange) and Olfm1 (teal). Likely, Olfm1 can also accommodate a calcium ion at the center of the β -propeller. The latrophilin3-coordinated calcium ion (green) and neighboring sodium ion (purple) are shown. (b) TSA shows a pronounced stabilizing effect of Olfm1 by calcium, shifting the melting temperature 8 °C higher, whereas EDTA destabilizes Olfm1 (shift to 10.5 °C lower). Buffer indicates TSA buffer without calcium or EDTA added.

The Olfm1 tetramer is arranged as a V-shaped dimer of dimers

Analysis of the full-length Olfm1 tetramer in solution by SAXS and by negative stain ET indicates that Olfm1 has a V-shaped architecture. The SAXS data show that Olfm1 has a rather rigid structure, as the Kratky plot has low values at higher scattering angles¹⁹ (Fig. 6a). The pair distance distribution function $P(r)$ remarkably shows two maxima at 5 and 14 nm (Fig. 6b and 6d), indicative of a dumbbell-like shape. *Ab initio* modeling by DAMMIF²⁰ with imposed two-fold rotational symmetry suggested a V-shaped arrangement (Fig. 6c and 6d). Likewise, ET analysis revealed a V-shaped architecture with varying angles between the legs. A bilobal shape is observed at the base of the V in the tomograms, which is likely formed by the N-terminal tetramerization region (Fig. 6e). This suggests that this region forms a folded domain, which we refer to as the N-terminal tetramerization (NTT) domain.

In the DAMMIF bead model, the two tips of the V are separated by 21 nm, whereas in the ET maps this distance varies from 13 to 28 nm. The D_{\max} from SAXS indicates a maximum distance of 30 nm in the Olfm1 tetramer, correlating with the maximum distance from the ET data of approximately 32 nm. Thus, we observed a V-shaped architecture for the full-length Olfm1 tetramer both in SAXS and ET experiments with similar dimensions for the tetramer between the two techniques (Fig. 6).

The V shape of Olfm1 agrees well with our crystal structure of the dimeric Olfm^{1coil-Olf} and with our data on tetramerization of Olfm1. The two tips of the V legs each appear as a bulky feature in both the SAXS and ET data and are readily identifiable as one β -propeller dimer each. The V legs are both formed by a coiled-coil dimer whereas the base of the V is formed by four copies of the NTT domain (Fig. 6f). This tetramer of NTT domains is arranged in a bilobal shape and harbors cysteines Cys73 and Cys75, shown previously to be essential for oligomerization¹⁷. It is noteworthy that we constructed this model with a dimeric β -propeller at the tips of the V-shape before we solved the crystal structure. The dimeric Olfm^{1coil-Olf} structure essentially validated this model.

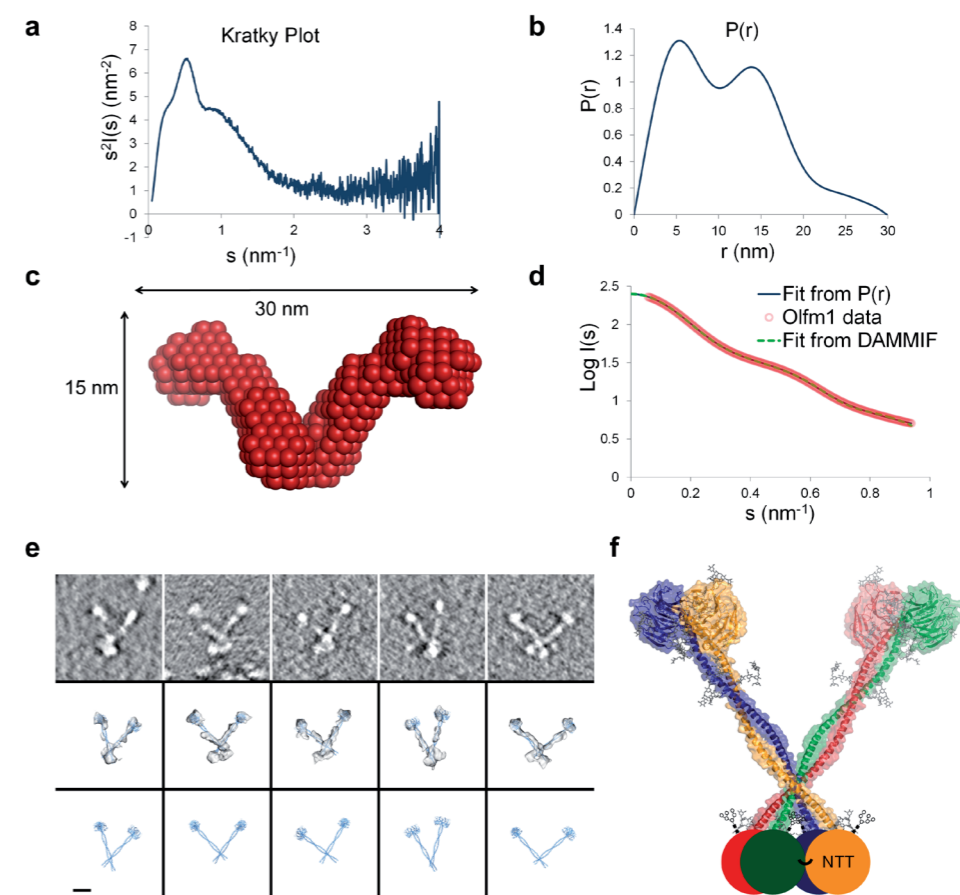


Figure 6. The full-length Olfm1 tetramer has a V-shaped architecture.

(a) The Kratky plot shows no signs of large unstructured regions¹⁹. (b) The SAXS pair distance distribution function $P(r)$ indicates a dumbbell-like shape. (c) *Ab initio* modeling by DAMMIF with imposed twofold rotational symmetry reveals a V-shaped architecture. A single (non-averaged) DAMMIF model is shown that is representative of the average structure generated from 50 models without applying twofold symmetry. (d) Fit from the $P(r)$ and the DAMMIF *ab initio* modeling ($\chi^2=4.313$). (e) ET shows V-shapes with varying angles between the legs. The dimensions of the coiled coil and the double β -propeller from the crystal structure fit those of the ET densities. Top panels: central slice through the tomograms showing the V-shapes. Middle panels: fit of two double β -propellers with modeled coiled-coil domains in the ET density. Bottom panels: same as middle panels but without the ET densities. Scale bar indicates 10 nm. (f) Model of the full-length Olfm1 tetramer. Each monomer is represented by a different color. In the NTT domains, one of the interprotein disulfides necessary for tetramerization is indicated.

Discussion

Although others have shown that Olfm1 forms covalent oligomers *in vivo*, the stoichiometry of the assembly has not hitherto been reported. We show that Olfm1 consistently forms stable covalent tetramers and is not further covalently oligomerized as was previously suggested by others^{9,18}. Interestingly, myocilin also has a coiled coil N-terminal of the olfactomedin domain and others have shown that it forms covalent dimers and tetramers²¹. Similarly, gliomedin has a trimerizing collagen-like helix N-terminal of its olfactomedin domain²². It has been shown that Olfm1 co-purifies with Olfm2, which also co-purifies with Olfm3¹². It is not clear whether these strongly related paralogs form mixed heterotetramers with a similar arrangement, or whether they interact non-covalently. Nonetheless, we show that Olfm1 can form stable homotetramers and likely also does so *in vivo*.

The combination of our ET data, the P(r) and ab-initio modeling by SAXS and the crystal structure of the Olfm1^{coil-Olf} dimers agrees with a V-shaped dimer-of-dimers architecture for the full-length Olfm1 tetramer. The ET data suggests some flexibility of the two legs of the V, which may be caused by two proline residues, found in a P-X-X-P motif at Pro163 and Pro166 within the coiled coil. Whilst these do not interrupt the heptad repeat pattern of the coiled coil (Fig. 3), it is known that prolines disrupt hydrogen bonding within α -helices, allowing a kink in the rod-like coiled coil and affecting the overall V-shape of the tetramer. In addition, there may be flexibility in the connection between the NTT domains and the coiled coils, that affects the angle between the V legs. Cys73 and Cys75, located in the NTT domain, have been shown previously to be essential for oligomerization¹⁷. The ET data show a bilobal shape at the base of the V, suggesting that the NTT domains are also arranged as a dimer-of-dimers. However, the detailed structure of the NTT domain and a portion of the coiled coil remain elusive.

Olfm1 has not previously been described as a calcium-binding protein. It has a site similar to the myocilin and latrophilin3 calcium binding site consisting of two aspartates (Asp356 and Asp453) and a glutamate (Glu404). These residues are the same in Olfm1 paralogs Olfm2 and Olfm3, whereas Glu404 and Asp453 are both asparagine in Olfm4. TSA shows that excess calcium indeed stabilizes Olfm1 whereas EDTA is destabilizing. Most likely, Olfm1 contains a calcium binding site as do Olfm2 and Olfm3. Whether the calcium is only structurally stabilizing the protein or serves a regulatory purpose remains to be determined.

The V-shaped tetrameric conformation we observed for full-length Olfm1 is possibly adopted by several other olfactomedin family members. Sequence analysis indicates that the features that define this architecture; two or more cysteines near the N-terminus, a central coiled coil domain and a C-terminal β -propeller, are also present in Olfm2, Olfm3, Olfm4 and myocilin (Fig. 7). In addition, the Olfm1 paralogs (Olfm2, 3 and 4)

also have a cysteine equivalent to Cys221 in Olfm1 that covalently links the C-terminal end of the coiled coil domain and two β -propellers. Myocilin does not have a cysteine in this region and, possibly, the β -propellers in myocilin have more flexibility with respect to the coiled coil. Taken together, the data suggest that the V-shaped conformation with two β -propellers dimers attached to each other via a coiled-coil domain is more common within the olfactomedin superfamily.

The striking architecture of Olfm1, encompassing two exposed and substantially separated β -propellers dimers with conserved top faces, is likely important for function. Olfm1 interacts with a diverse set of proteins, many of which are cell-surface attached receptors. Possibly, Olfm1-receptor interactions are mediated by the β -propellers (i.e. the olfactomedin domains), although for NgR it has been shown that interaction does not rely on the olfactomedin domain⁶. This way, Olfm1 can engage multiple receptor molecules simultaneously and may bring receptors together or induce receptor clustering to regulate signaling.

The oligomeric state of many olfactomedin family members has been shown to be important for function¹⁰. Besides Olfm1-4 and myocilin, that are likely to form tetramers with separated β -propellers, also gliomedin has substantially separated β -propellers in a trimerized form¹⁴. Latrophilin3, on the other hand, is not known to oligomerize and lacks a coiled coil or collagen domain. The binding and signaling mode between Olfm1-4, myocilin and gliomedin is possibly related and as we hypothesize for Olfm1, may involve oligomerization or clustering of receptors.

Olfm1 has been reported to be a binding partner of cation channels such as the AMPA receptor complex and the Cav2.1 voltage-gated calcium channel. Moreover, genetic deletion of a part of the coiled-coil region leads to elevated calcium concentrations in the cytosol as well as developmental and behavioral defects⁸. Since both the AMPA receptor and Olfm1 form homotetramers with a 2x2 arrangement, it is tempting to hypothesize that Olfm1 plays a role in AMPA receptor complex stabilization or regulation. Alternatively, an Olfm1 tetramer may bind two or even four AMPA receptor complexes and play a role in the supramolecular organization of these complexes, by providing a scaffold for the formation of larger clusters of AMPA receptors.

Olfm2 has been shown to have a similar role in AMPA receptor binding or regulation¹¹. Gliomedin is also known to be involved in sodium channel clustering and maintenance^{23,24}. Remarkably, whereas Olfm1 and Olfm2 bind calcium channels and likely a calcium ion within the β -propeller, gliomedin binds sodium channels and sodium in its β -propeller. It is noteworthy that all of them seem to share a cation binding site and an oligomerization domain N-terminal of their olfactomedin domains. Whether other olfactomedin domain-containing proteins such as Olfm3 or myocilin could have a similar role in ion channel stabilization or regulation needs further investigation.

In conclusion, we show that Olfm1 forms disulfide-linked homotetramers with a

V-shaped architecture and provide high-resolution data for the C-terminal Olfm1^{coil-Olf}. This sheds light on the structure and quaternary organization of full-length Olfm1 as well as family members and provides new insights into function.

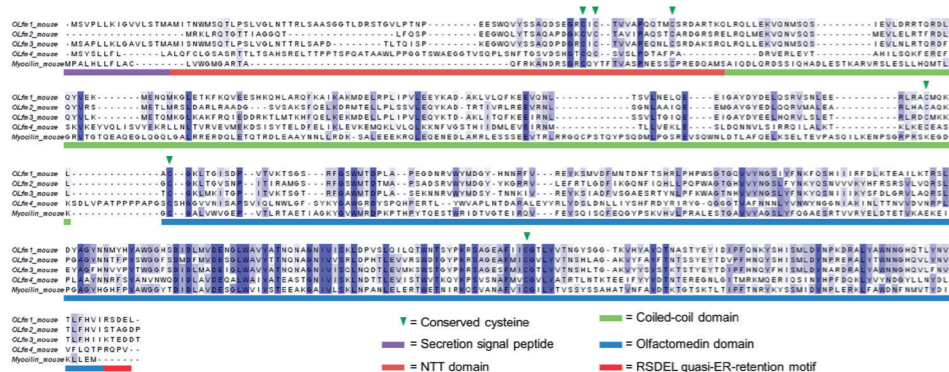


Figure 7. Sequence alignment of Olfm1 and paralogous

Olfm1 is aligned with the closely related (mouse) paralogous Olfm2, Olfm3, Olfm4 and myocilin. Domain boundaries are indicated with the same color scheme as figure 1A. Conserved cysteines are indicated by arrowheads. Residues are colored to percentage sequence identity (blue means conserved, white means variable).

Methods

Protein Expression and Purification

Mouse Olfm1 (NCBI Reference Sequence: NP_062371) residues 17-478 (isoform 1), from cDNA IRAVp968C0174D (Source Bioscience) were subcloned using BamHI/NotI sites in pUPE107.03 (N-terminal cystatin secretion signal, C-terminal His₆). We call this construct full-length Olfm1 although the C-terminal VIRSDEL segment is not included. 6 days after transient expression in N-acetylglucosaminyltransferase I-deficient (GnTI⁻) Epstein-Barr virus nuclear antigen I (EBNA1)-expressing HEK293 cells (U-Protein Express), the medium was harvested and fivefold concentrated using a 10 kDa molecular weight cut-off (MWCO) membrane. Protein was purified by Ni-NTA affinity chromatography followed by gel filtration on a Superdex200 column (GE Healthcare) equilibrated in gel filtration (GF) buffer (150 mM NaCl, 20 mM HEPES pH 7.5). Protein was concentrated to 6 mg/mL using a 30 kDa MWCO concentrator before plunge freezing in liquid nitrogen.

SDS-PAGE and Western blot

2 μ L of purified protein was diluted with 8 μ L H₂O and denatured by boiling with 5

μ L SDS loading dye with or without 6% (v/v) β -mercaptoethanol for reducing and non-reducing SDS-PAGE respectively. For Western blot analysis, 10 μ L expression medium supernatant was denatured by boiling with 5 μ L (non-)reducing loading dye. Samples were run on standard Laemmli 12.5% (w/v) polyacrylamide tris-glycine gels. Gels were either stained with Coomassie PAGE blue or for Western blot, blotted on a polyvinylidene difluoride (PVDF) membrane (BioRad). Proteins were detected with a mixture of Qiagen mouse anti-penta-his, Sigma mouse anti-polyhistidine and Dako rabbit anti-mouse-HRP antibodies.

Crystallization and Data Collection

Since initial crystallization attempts were fruitless, limited proteolysis by α -Chymotrypsin was used for crystallization. α -Chymotrypsin (stock of 1 mg/mL in 1 mM HCl and 2 mM CaCl₂) was added 1:100 (v/v) to 6 mg/ml of Olfm1 in 150 mM NaCl and 20 mM HEPES pH 7.5. After 30 minutes incubation at room temperature, crystallization screens were set up using the sitting drop method by mixing 150 nL of protein/protease mixture (6 mg/mL) with 150 nL of reservoir solution. Crystals were grown at 20°C in a condition containing 1 M LiCl, 20% PEG6000 (w/v) and 100 mM Tris pH8.5.

Crystals from the original condition were cryo-protected with reservoir solution supplemented with 25% (v/v) glycerol and plunge-cooled in liquid nitrogen. A dataset was collected at 100 K at the European Synchrotron Radiation Facility (ESRF) beamline ID23-1, operated at a wavelength of 0.97242 Å. Crystals diffracted to 2.4 Å. Data were integrated with iMosflm²⁵ and scaled and merged with Pointless/Aimless/Ctruncate (CCP4 suite)^{26,27}.

Structure Solution and Refinement

The structure was solved by molecular replacement with the gliomedin β -propeller crystal structure (PDB: 4D77¹⁴) using PHASER²⁸. Subsequent rounds of manual model building and refinement were performed with Coot²⁹ and REFMAC5³⁰. Final refinement was performed with PHENIX³¹ and validation with MolProbity³². A large portion, 209 residues of a total of 463 residues for the mature full-length protein is missing in the electron density most likely due to α -Chymotrypsin treatment of Olfm1. The final model consists of residues Val211-Phe477 and Arg210-Ala480 (the last two alanines Ala479 and Ala480 are from the NotI restriction site) for chain A and B respectively, excluding loops Ala339-His352 in both chains. Ramachandran statistics were (% Ramachandran favored / % allowed / % outliers): 97/3/0.

SEC-MALS

Size-exclusion chromatography with multi-angle light scattering (SEC-MALS) was performed at room temperature using an analytical Superdex200 5/150 column (GE

Healthcare) equilibrated with GF buffer. SEC was performed with online static light scattering (miniDAWN TREOS, Wyatt Technology) and differential refractive index (dRI, Shimadzu RID-10A) on an ÄKTAmicro system equipped with a triple wavelength UV detector (GE Healthcare). Data were analyzed using the ASTRA software suite (Wyatt Technology). The dRI signal was combined with the light scattering to determine the molecular mass using standard protocols. A dn/dc of 0.178 was calculated for Olfm1, based on 8 predicted N-linked glycans. Conalbumin was injected at 10 mg/mL as a control and calibration standard (for Conalbumin a dn/dc of 0.185 was used).

Small angle X-ray scattering

Small-angle X-ray scattering (SAXS) was performed at the ESRF BM29 BioSAXS beamline equipped with a 2D Pilatus 1M detector (DECTRIS, Switzerland), operated at an energy of 12.5 keV. Full-length Olfm1 was diluted with and dialyzed against GF buffer using a 10 kDa MWCO membrane. The concentration of Olfm1 was determined by UV-Vis spectroscopy on a nanodrop ND-1000 spectrophotometer to be 3.55 mg/mL. SAXS data were collected at 20 °C. 18 successive 0.056-second frames were collected. The data were radially averaged, normalized to the intensity of the transmitted beam, exposure time and sample concentration and the scattering of the solvent-blank (GF buffer) was subtracted. The curve was scaled using a BSA reference so that the I_0 represents the Olfm1 molecular mass. Radiation damage was monitored by comparing curves collected on the same sample; no evidence for radiation damage was observed. Data were analyzed by PRIMUS³³, GNOM³⁴ and DAMMIF²⁰ of the ATSAS suite³⁵.

Analytical ultracentrifugation

Full-length Olfm1 was dialyzed against GF buffer using a 10 kDa MWCO membrane. Protein was diluted with GF buffer to a concentration of 1.71 mg/mL. AUC sedimentation velocity was performed in a Beckman Coulter Proteomelab XL-I analytical ultracentrifuge using a 3 mm centerpiece, quartz windows and an An-60 Ti rotor (Beckman). Absorption measurements were made at 42000 rpm and 20 °C every minute at 280 nm wavelength and with GF buffer as reference. \bar{V} , buffer density and viscosity were determined by SEDNTERP as 0.71006 mL/g, 0.99823 g/mL and 0.001002 Pa·s respectively. Measurements were analyzed by SEDFIT using continuous $c(s)$ mode^{36,37}.

Thermofluor stability assays

Thermofluor stability assays were performed using full-length Olfm1 diluted with TSA buffer (20 mM NaCl, 50 mM HEPES pH 7.5) to concentrations of 1.2 mg/mL. Diluted protein or GF buffer was mixed 1:1 with 125× diluted Sypro Orange (Sigma-Aldrich) in TSA buffer. 12.5 μ L of Sypro-Protein mixture was mixed with 12.5 μ L assay conditions,

consisting of 1, 5 or 20 mM $CaCl_2$ or Ethylenediaminetetraacetic acid (EDTA) in TSA buffer or just TSA buffer. Denaturing curves were recorded on a MyiQ real-time PCR thermocycler (BioRad). A temperature ramp of 288-369 K was performed at 3 K/min. All measurements were performed in triplicate; curves were blank subtracted, baseline corrected, normalized to maximum fluorescence and averaged.

Negative stain electron tomography

Full-length Olfm1 was diluted with Milli-Q water to a concentration of 65 μ g/mL. Carbon-coated mesh copper grids (EMS, CF200-Cu) were glow discharged for 15 sec before incubation with protein for 30 sec. Excess protein was wicked away with filter paper before grids were briefly washed two times with 5 μ L Milli-Q water and then stained for 30 sec with a freshly prepared filtered 2% uranyl formate solution.

Electron tomography (ET) was performed with a Tecnai F20 (FEI company) at 200 kV and images acquired with a Gatan Ultrascan 4000 camera (Gatan Inc.). Tomographic tilt series were collected at a nominal magnification of $\times 30k$ with a final pixel size of 4.57 Å/pix after $\times 2$ binning. Tomograms were processed using IMOD³⁸ and phase CTF correction was performed on the tilt series using IMOD prior to reconstruction by weighted back-projection.

Sub-tomogram particles were manually picked using `e2spt_boxer.py` from EMAN2³⁹. Each particle was normalized and masked with a sharp spherical mask to remove background density not associated with the protein. Particles were then filtered to 20 Å with a low-pass Gaussian filter, before a tight mask was applied to the remaining density. An Olfm1 coiled coil- β -propeller dimer was modeled using the crystal structure of Olfm1^{coil-Olf} and the homodimeric parallel coiled coil from myosin-V (PDB 2DFS,⁴⁰) to the predicted length of the Olfm1 coiled coil (Fig. 3), adding full N-linked glycans to all predicted positions. Models were fitted manually by treating each Olfm1 dimer as one rigid body using UCSF Chimera⁴¹.

References

1. Snyder, D. a, Rivers, a M., Yokoe, H., Menco, B. P. & Anholt, R. R. Olfactomedin: purification, characterization, and localization of a novel olfactory glycoprotein. *Biochemistry* **30**, 9143–9153 (1991).
2. Moreno, T. a & Bronner-Fraser, M. The secreted glycoprotein Noelin-1 promotes neurogenesis in *Xenopus*. *Dev. Biol.* **240**, 340–360 (2001).
3. Moreno, T. a. & Bronner-Fraser, M. Noelins modulate the timing of neuronal differentiation during development. *Dev. Biol.* **288**, 434–447 (2005).
4. Rice, H. C. *et al.* Pancortins interact with amyloid precursor protein and modulate cortical cell migration. *Development* **139**, 3986–3996 (2012).
5. Barembaum, M., Moreno, T. a, LaBonne, C., Sechrist, J. & Bronner-Fraser, M. Noelin-1 is a secreted glycoprotein involved in generation of the neural crest. *Nat. Cell Biol.* **2**, 219–225 (2000).
6. Nakaya, N., Sultana, A., Lee, H. S. & Tomarev, S. I. Olfactomedin 1 interacts with the Nogo A receptor complex to regulate axon growth. *J. Biol. Chem.* **287**, 37171–37184 (2012).
7. Nakaya, N., Lee, H.-S., Takada, Y., Tzchori, I. & Tomarev, S. I. Zebrafish olfactomedin 1 regulates retinal axon elongation in vivo and is a modulator of Wnt signaling pathway. *J. Neurosci.* **28**, 7900–7910 (2008).
8. Nakaya, N. *et al.* Deletion in the N-terminal half of olfactomedin 1 modifies its interaction with synaptic proteins and causes brain dystrophy and abnormal behavior in mice. *Exp. Neurol.* **250**, 205–218 (2013).
9. Anholt, R. R. H. Olfactomedin proteins: central players in development and disease. *Front. Cell Dev. Biol.* **2**, 1–10 (2014).
10. Tomarev, S. I. & Nakaya, N. Olfactomedin domain-containing proteins: Possible mechanisms of action and functions in normal development and pathology. *Mol. Neurobiol.* **40**, 122–138 (2009).
11. Sultana, A. *et al.* Deletion of olfactomedin 2 induces changes in the AMPA receptor complex and impairs visual, olfactory, and motor functions in mice. *Exp. Neurol.* **261**, 802–811 (2014).
12. Sultana, A., Nakaya, N., Senatorov, V. V. & Tomarev, S. I. Olfactomedin 2: Expression in the eye and interaction with other olfactomedin domain-containing proteins. *Investig. Ophthalmol. Vis. Sci.* **52**, 2584–2592 (2011).
13. Nagano, T. *et al.* A2-pancortins (Pancortin-3 and -4) are the dominant Pancortins during neocortical development. *J. Neurochem.* **75**, 1–8 (2000).
14. Han, H. & Kursula, P. The olfactomedin domain from gliomedin is a β -propeller with unique structural properties. *J. Biol. Chem.* **290**, 3612–21 (2015).
15. Donegan, R. K. *et al.* Structural basis for misfolding in myocilin-associated glaucoma. *Hum. Mol. Genet.* 1–14 (2014). doi:10.1093/hmg/ddu730
16. Jackson, V. A. *et al.* Structural Basis of Latrophilin-FLRT Interaction. *Structure* 1–8 (2015).
17. Ando, K. *et al.* Expression and characterization of disulfide bond use of oligomerized A2-Pancortins: Extracellular matrix constituents in the developing brain. *Neuroscience* **133**, 947–957 (2005).
18. Yokoe, H. & Anholt, R. R. Molecular cloning of olfactomedin, an extracellular matrix protein specific to olfactory neuroepithelium. *Proc. Natl. Acad. Sci. U. S. A.* **90**, 4655–4659 (1993).
19. Bernadó, P. & Svergun, D. I. Structural analysis of intrinsically disordered proteins by small-angle X-ray scattering. *Mol. Biosyst.* **8**, 151 (2012).
20. Franke, D. & Svergun, D. I. DAMMIF, a program for rapid ab-initio shape determination in small-angle scattering. *J. Appl. Crystallogr.* **42**, 342–346 (2009).
21. Nguyen, T. D. *et al.* Gene structure and properties of TIGR, an olfactomedin-related glycoprotein cloned from glucocorticoid-induced trabecular meshwork cells. *J. Biol. Chem.* **273**, 6341–6350 (1998).
22. Maertens, B. *et al.* Cleavage and oligomerization of gliomedin, a transmembrane collagen required for node of Ranvier formation. *J. Biol. Chem.* **282**, 10647–10659 (2007).
23. Amor, V. *et al.* Long-term maintenance of Na⁺ channels at nodes of Ranvier depends on glial contact mediated by gliomedin and NrCAM. *J. Neurosci.* **34**, 5089–98 (2014).
24. Feinberg, K. *et al.* A Glial Signal Consisting of Gliomedin and NrCAM Clusters Axonal Na⁺ Channels during the Formation of Nodes of Ranvier. *Neuron* **65**, 490–502 (2010).
25. Batty, T. G. G., Kontogiannis, L., Johnson, O., Powell, H. R. & Leslie, A. G. W. iMOSFLM: A new graphical interface for diffraction-image processing with MOSFLM. *Acta Crystallogr. Sect. D Biol. Crystallogr.* **67**, 271–281 (2011).
26. Evans, P. R. An introduction to data reduction: Space-group determination, scaling and intensity statistics. *Acta Crystallogr. Sect. D Biol. Crystallogr.* **67**, 282–292 (2011).
27. Evans, P. R. & Murshudov, G. N. How good are my data and what is the resolution? *Acta Crystallogr. Sect. D Biol. Crystallogr.* **69**, 1204–1214 (2013).
28. McCoy, A. J. *et al.* Phaser crystallographic software. *J. Appl. Crystallogr.* **40**, 658–674 (2007).
29. Emsley, P. & Cowtan, K. Coot: Model-building tools for molecular graphics. *Acta Crystallogr. Sect. D Biol. Crystallogr.* **60**, 2126–2132 (2004).
30. Murshudov, G. N. *et al.* REFMAC5 for the refinement of macromolecular crystal structures. *Acta Crystallogr. Sect. D Biol. Crystallogr.* **67**, 355–367 (2011).
31. Afonine, P. V. *et al.* Towards automated crystallographic structure refinement with phenix.refine. *Acta Crystallogr. Sect. D Biol. Crystallogr.* **68**, 352–367 (2012).
32. Chen, V. B. *et al.* MolProbity: All-atom structure validation for macromolecular crystallography. *Acta Crystallogr. Sect. D Biol. Crystallogr.* **66**, 12–21 (2010).
33. Konarev, P. V., Volkov, V. V., Sokolova, A. V., Koch, M. H. J. & Svergun, D. I. PRIMUS: A Windows PC-based system for small-angle scattering data analysis. *J. Appl. Crystallogr.* **36**, 1277–1282 (2003).
34. Svergun, D. I. Determination of the regularization parameter in indirect-transform methods using perceptual criteria. *J. Appl. Crystallogr.* **25**, 495–503 (1992).
35. Petoukhov, M. V. *et al.* New developments in the ATSAS program package for small-angle scattering data analysis. *J. Appl. Crystallogr.* **45**, 342–350 (2012).
36. Schuck, P. Size-distribution analysis of macromolecules by sedimentation velocity ultracentrifugation and lamm equation modeling. *Biophys. J.* **78**, 1606–1619 (2000).
37. Brown, P. H. & Schuck, P. Macromolecular size-and-shape distributions by sedimentation velocity analytical ultracentrifugation. *Biophys. J.* **90**, 4651–4661 (2006).
38. Kremer, J. R., Mastronarde, D. N. & McIntosh, J. R. Computer visualization of three-dimensional image data using IMOD. *J. Struct. Biol.* **116**, 71–76 (1996).
39. Tang, G. *et al.* EMAN2: An extensible image processing suite for electron microscopy. *J. Struct. Biol.* **157**, 38–46 (2007).
40. Liu, J., Taylor, D. W., Kremntsova, E. B., Trybus, K. M. & Taylor, K. a. Three-dimensional structure of the myosin V inhibited state by cryoelectron tomography. *Nature* **442**, 208–211 (2006).
41. Pettersen, E. F. *et al.* UCSF Chimera - A visualization system for exploratory research and analysis. *J. Comput. Chem.* **25**, 1605–1612 (2004).
42. Celniker, G. *et al.* ConSurf: Using evolutionary data to raise testable hypotheses about protein function. *Isr. J. Chem.* **53**, 199–206 (2013).

Acknowledgements

We would like to thank Deniz Ugurlar and Camilla De Nardis for their assistance with EM preparation and Louris Feitsma for assistance with TSA experiments. The SAXS and diffraction experiments were performed on the BM29 and ID23-1 beamlines respectively at the European Synchrotron Radiation Facility (ESRF), Grenoble, France. We are grateful to Local Contacts at ESRF for providing assistance in using beamlines BM29 and ID23-1.

Author contributions

M.F.P. and B.J.C.J. designed the experiments. T.G.A.A.B. and M.F.P. designed constructs and purified proteins. M.F.P. performed crystallization and X-ray diffraction experiments and solved the structure, performed SAXS, SEC-MALS and TSA experiments and data analysis and prepared negative stain EM grids. M.F.P. and D.T.W. performed AUC experiments and analyzed the data. T.H.S. recorded tomograms and analyzed ET data. B.J.C.J. supervised the project. M.F.P. and B.J.C.J. wrote the manuscript with input from all authors.

Data accessibility

The atomic coordinates and structure factors have been deposited in the Protein Data Bank (<http://www.pdb.org/>) with PDB ID 5AMO. The SAXS experimental data and bead model have been deposited in the SASBDB (<http://www.sasbdb.org/>) with SASDAS7. The ET data have been deposited in the EMDB (<http://www.emdatabank.org/>) with EMD-2940, EMD-2941, EMD-2942, EMD-2943, EMD-2944.

Chapter 5

General discussion

Matti F. Pronker

While regeneration upon injury can be robust in the peripheral nervous system (PNS)¹, regeneration in the central nervous system (CNS) of vertebrates is generally very limited^{2,3}. This is in part due to the signaling of three myelin-associated inhibitors of regeneration (MAIs) – myelin-associated glycoprotein (MAG), Nogo and Oligodendrocyte Myelin glycoprotein (OMgp) – through the neuronal Nogo Receptor (NgR)³. This signaling erects an external barrier to neurite outgrowth and other regeneration processes and is postulated to have a physiological role in consolidating neuronal circuitry in the adult nervous system^{4,5}. Although different aspects of this signaling have been intensely studied, the initial events at the neuronal membrane remain poorly understood on the molecular level. In this thesis, structural studies of NgR, its MAI ligand MAG and the antagonist of MAI signaling Olfactomedin-1 (Olfm1) are described. Biophysical techniques and cell-based assays were used to validate possible mechanisms based on crystal structures of these proteins. Here, general implications of these studies are discussed and novel hypotheses are proposed.

Oligomerization of ligands and receptors

Receptor oligomerization or clustering at the plasma membrane is a common mechanism for signal transduction of many extracellular cues^{6,7}. MAI signaling appears to be no exception to this rule, as oligomeric states have been reported for almost all neuronal receptors and co-receptors involved in MAI signaling. NgR was previously reported to self-associate on the neuronal cell surface^{8,9}, although the exact stoichiometry of this interaction has not been shown. NgR crystal structures described in chapter three suggest it forms dimers via the leucine-rich repeat domain. The NgR co-receptor p75 was shown to form covalent dimers via a conserved cysteine in the transmembrane helix^{10–12}, which is also conserved in the p75 substitute in MAI signaling TROY. LINGO-1, another co-receptor of NgR, was crystallized as a *cis* tetramer that could be confirmed in solution¹³. Finally, the extracellular domain of the LINGO-1 substitute in MAI signaling AMIGO3 was shown to form dimers in solution¹⁴.

MAIs, as well as non-myelin-associated NgR ligands, have the potential to induce receptor clustering. The MAI and NgR ligand Nogo was reported to form heteromeric complexes of the three different splice forms Nogo-A, Nogo-B and Nogo-C¹⁵, which all contain the NgR-binding extracellular segment known as Nogo66^{16,17}, suggesting a possibility of multivalent receptor binding. Several other ligands of NgR involved in regeneration-inhibitory signaling form oligomers or could otherwise cluster receptors on the neuronal cell surface. The non-myelin-associated NgR ligand BlyS inhibits neurite outgrowth and collapses axonal growth cones similar to MAIs¹⁸. BlyS forms homotrimers^{19,20} that could further assemble into icosahedral 60-mers in its membrane-

detached form^{21,22}. Chondroitin sulfate proteoglycans (CSPGs) also confer non-myelin-associated regeneration-inhibiting signaling through NgR and its paralog NgR3²³. The long linear negatively-charged glycosaminoglycan chains of these proteoglycans are responsible for this signaling²³, which are likely able to bind to several NgR or NgR3 molecules at the same time.

In chapter 2 we describe that MAG forms low-affinity dimers in solution and that dimerization of MAG is important for its neurite outgrowth-inhibiting properties. Whether the third MAI OMgp forms dimers or higher order oligomers remains to be determined.

In chapter 4 we show that the NgR ligand Olfm1 forms disulfide-linked tetramers that stay tetrameric regardless of concentration. However, the signaling of Olfm1 antagonizes axonal growth cone collapse induced by MAI signaling²⁴, so in spite of its potential to cluster NgR molecules, the outcome is reversed compared to BlyS, CSPGs, Nogo and MAG. This could be explained by the fact that Olfm1 competes for NgR binding with the co-receptors p75 and LINGO-1²⁴. Thus, these data indicate that clustering of only NgR is not enough, co-receptor (co-)clustering is also necessary for the signal transduction of MAIs.

MAI-induced lipid raft localization of p75

Several studies have shown involvement of lipid rafts in the signal transduction of MAIs. Both gangliosides such as GT1b and GPI-anchored proteins such as NgR have previously been shown to preferentially reside in lipid rafts²⁵. Indeed, both for NgR and GT1b expressed on neurons, lipid raft localization was observed²⁶⁻²⁸. Furthermore, replacing the GPI-anchoring sequence of NgR with a regular transmembrane helix made neurons less sensitive to MAI ligands⁸.

p75 co-localizes with and binds to GT1b gangliosides, NgR and externally added Fc-dimerized extracellular domain of MAG (MAG₁₋₅-Fc) on neurons and in lipid rafts²⁷⁻³⁰. p75 binding to NgR was enhanced in the presence of MAG₁₋₅-Fc³¹ and addition of MAG₁₋₅-Fc or a Nogo66-derived peptide could recruit p75 to lipid rafts²⁷. Moreover, even anti-GT1b antibodies could induce recruitment of p75 to lipid rafts²⁷ and elicit neurite outgrowth inhibition³², similar to MAG₁₋₅-Fc. These results suggest MAIs signal by recruiting p75 to GT1b-NgR lipid rafts.

We show in chapter 2 that both the dimerization of MAG as observed in the crystal structures as well as its ganglioside binding properties are essential for neurite outgrowth inhibition. This is in agreement with the findings described above and further strengthens the notion of MAG-induced recruitment of p75 to lipid rafts to transmit the extracellular signal across the membrane. We observe that a concentration-independent dimeric

MAG construct that cannot bind to GT1b gangliosides (MAG₁₋₅-Fc R118A) enhances regeneration instead of inhibiting it. This could be explained by p75 being clustered without being recruited to lipid rafts. Since receptor clustering can enhance lipid raft formation and *vice versa*²⁵, it is likely that co-clustering of NgR, GT1b and p75 in lipid rafts by oligomeric or multivalent ligands such as MAG, Nogo, BlyS or CSPGs could trigger downstream signaling. Additional evidence for this model comes from the fact that disruption of lipid rafts by the cholesterol-sequestering agent β -methylcyclodextrin abolishes Nogo66-mediated RhoA activation²⁸ and axonal growth cone collapse by MAG and Nogo66²⁷.

A cysteine in the transmembrane helix of p75 covalently dimerizes the protein, which was found to be important for neurotrophin signaling¹⁰⁻¹². Mutating this cysteine rendered p75-expressing cells insensitive to neurotrophins. Furthermore, cells co-expressing NgR, LINGO-1 and a p75 mutant lacking this cysteine were less sensitive to MAI signaling¹⁰. Neurotrophins elicit opposite downstream signaling effects compared to MAI signaling^{33,34}. Based on live-cell Förster resonance energy transfer (FRET) studies¹⁰ and structural data of the intracellular death domain (DD) and its complex with RhoGDI and RhoA³⁵, a scissoring mechanism was proposed in which dimeric neurotrophins bring the extracellular domains of p75 together^{10,35}. This would then separate the intracellular DDs and release RhoA from RhoGDI.

NgR preferentially binds dimeric p75 in the conformation with associating intracellular DDs¹², as opposed to the neurotrophin-bound conformation¹⁰. Perhaps in MAI signaling, the p75 response is not a scissoring movement induced by ligand binding to the extracellular domains of p75. Instead, MAIs can recruit p75 to lipid rafts²⁷, which have greater membrane thickness than normal plasma membrane²⁵. Thus, lipid raft recruitment of p75 by MAIs might trigger rearrangement of the disulfide-linked transmembrane helices (to prevent hydrophobic mismatch) and thereby association of the intracellular DDs of p75 to initiate RhoA/RhoGDI signaling.

Other co-receptors

TROY, like p75 a member of the tumor necrosis factor receptor superfamily, was previously shown independently by two groups to be a functional substitute for p75 in the nervous system^{36,37}. In the transmembrane helix of TROY, a cysteine is present at a similar depth in the membrane compared to the dimerizing cysteine in p75, suggesting it might form disulfide-linked dimers similar to p75. TROY was recently shown to directly bind to RhoGDI with its intracellular domain and this interaction was potentiated by Nogo66, similar to p75. Moreover, Nogo66 signaling via TROY-RhoGDI could activate RhoA in cell lines deficient of p75³⁸. These results further confirm TROY could

functionally substitute for p75 and transduce the signal by a similar mechanism.

In contrast with the classic picture of MAI receptor complexes of NgR-p75/TROY-LINGO-1 on the neuronal plasma membrane^{3,39,40}, it was recently shown that LINGO-1 is not expressed at the cell surface but instead exclusively in endosomal compartments⁴¹. The notion of tripartite signaling complexes of NgR-p75/TROY-LINGO-1 was further undermined by the fact that LINGO-1 competes with NgR for p75 binding⁴¹. LINGO-1 might still play a role in the downstream signaling of MAI-induced regeneration inhibition, but likely is not involved in the initial signal transduction events at the neuronal plasma membrane.

Whether or not the recently-identified amphotericin-induced gene and open reading frame 3 (AMIGO3)⁴² is expressed at the cell surface or forms a tripartite complex with NgR and p75/TROY remains to be determined. Interestingly, binding between AMIGO3 and p75 was only observed in the presence of NgR⁴², whereas LINGO-1 competes with NgR for p75 binding⁴¹. Thus, AMIGO3 may be involved in mediating downstream signaling of MAIs by a distinct mechanism compared to LINGO-1.

In brief, p75/TROY appear to be the most important players in MAI signal transduction through the neuronal plasma membrane. AMIGO3 could also play a role in this signaling but this needs to be studied further, whereas LINGO-1 likely functions more downstream in the signaling cascade as it is absent from the plasma membrane.

MAG is important for myelin formation and stability

Similar to the local structure of the nervous system itself, myelin in the CNS is not static but can restructure for decades into adulthood. White matter structure changes during many complex learning processes, which has been proposed to be an additional layer of activity-dependent plasticity involved in learning and memory, possibly by modifying the conductance velocity of axons⁴³. The important role of MAG in myelin formation and stability^{44,45} suggests MAG could play a role in activity-dependent myelination.

Different studies have shown that proper MAG functioning is essential for myelin ultrastructure, myelin-axon interaction and axonal protection in the adult nervous system⁴⁶⁻⁵². In chapter two we describe a dimeric arrangement of MAG that provides a mechanism for MAG-imposed regulation of the intermembrane spacing between myelin and axon (the periaxonal diameter). By binding to axonal gangliosides *in trans* and dimerizing *in cis*, the orientation of two rod-like MAG extracellular domains is locked in place by interactions between the membrane-proximal Immunoglobulin domains 4 and 5. MAG was previously shown to regulate this distance⁴⁶⁻⁴⁸ and the membrane spacing based on our crystal structures of 10 nm is in agreement with distances of 9-12 nm found in recent electron microscopy studies on high-pressure-frozen myelin tissue⁵³.

Thus, the *cis* dimerization of MAG combined with ganglioside binding *in trans* could restrict the myelin-axon spacing to 9-12 nm, in analogy to a molecular leaf spring.

Two isoforms of MAG, L-MAG and S-MAG, differ only in their cytoplasmic domains and are expressed differentially during development⁵⁴. L-MAG binds to and signals via the myelination regulator Fyn kinase^{55,56}. S-MAG on the other hand binds to zinc⁵⁷, tubulin and microtubules⁵⁸. Therefore, L-MAG has been postulated to be important for signaling during myelination, whereas S-MAG could have a structural role in mature myelin^{57,58}. L-MAG is essential for proper CNS but not PNS myelination⁵⁹ and could not be detected in the adult PNS⁶⁰. L-MAG is present only in trace amounts in the developing PNS, in contrast with the highly-expressed S-MAG isoform⁶⁰. In the adult CNS on the other hand, the L-MAG isoform is still abundantly expressed in overlapping yet unique populations of oligodendrocytes compared to S-MAG^{54,60}.

L-MAG clustering by antibodies triggers its partitioning to lipid rafts⁵⁶ and results in activation of the cytosolic non-receptor tyrosine kinase Fyn⁵⁵. Fyn activation is essential for the initiation of the myelination process⁶¹. The dimerization of MAG as described in chapter two places the C-terminal transmembrane helices at a distance of 5.4 nm, providing a possible mechanism for Fyn activation. Fyn activation could be triggered by extracellular dimerization of MAG as a result of *trans* interaction with axonal gangliosides and elevation of the local concentration (because of the local abundance of ganglioside ligand). A similar mechanism has been suggested for immune cells, in which Fyn can be activated by extracellular clustering of the transmembrane immune receptor Signaling lymphocytic activation molecule (SLAM)⁶².

How and whether MAG signaling is downregulated is currently not clear. MAG serves both adhesion and signaling functions and it remains present at the myelin-axon interface after axons are fully myelinated⁶⁴. Perhaps MAG signals constitutively while it provides contacts between myelin and axon. Another possibility is that Fyn is inactivated by downstream cytosolic feedback mechanisms. Alternatively, upregulation of local production of S-MAG, that does not signal via Fyn, may take over the adhesion role of L-MAG, competing with L-MAG dimers and thus downregulating L-MAG signaling. Activity-dependent myelin plasticity has been demonstrated in the brain and has been linked to memory and learning processes⁴³. White matter in the PNS, on the other hand, is not involved in learning processes and is therefore expected to be more static once established. The signaling L-MAG isoform remains abundant in the adult CNS^{54,60}, whereas in the adult PNS only the structural S-MAG isoform is found⁶⁰. This suggests L-MAG could play a role in activity-dependent myelin plasticity. In a recent study, a link was found between MAG and the membrane protein monogenic audiogenic seizure susceptible 1 (MASS1)⁶³. MASS1 has 35 extracellular calcium binding domains and a transmembrane G protein-coupled receptor domain. Mutation of MASS1 causes epilepsy in mice and is linked to a dramatic decrease in MAG expression levels⁶³. MASS1

was found to regulate MAG ubiquitination and degradation in a calcium-dependent manner, elevating MAG surface expression levels in the presence of extracellular calcium⁶³. These results provide a direct link between local electrochemical activity in the CNS and MAG expression levels. Concluding, both the abundance of L-MAG in the CNS compared to the PNS and the calcium-dependent surface expression levels of MAG suggest MAG could be involved in activity-dependent myelin plasticity.

In summary, MAG is widely recognized as an important protein for myelin formation and stability. Our crystal structures suggest a mechanism for MAG-imposed myelin-axon spacing, by dimerizing *in cis* and binding axonal gangliosides *in trans*. Dimerization of L-MAG also provides a putative mechanism for axon-to-myelin signaling through Fyn, which is important during myelin formation. Finally, MAG may play a role in activity-dependent myelin plasticity, as L-MAG is abundant in the adult CNS and not in the PNS. Activity-dependence may be orchestrated by MASS1, which links electrochemical activity to MAG expression levels.

Putative mechanism for axon engagement by myelin

Apart from MAG, several other molecules have been implicated in forming axon-myelin trans interactions. L1 cell adhesion molecule (L1CAM) and neuronal cell adhesion molecule (NCAM) can form *homo-trans*-interactions and are expressed by both myelin cells and axons⁶⁴. Whereas NCAM and MAG are present in both CNS and PNS, L1CAM is only detected in the Schwann cells of the PNS and not on the oligodendrocytes of the CNS⁶⁵. Multiply-myelinated axons (oligodendrocytes myelinating already myelinated axons) have been observed for MAG knockout mice^{66,67}. This has been explained by compensatory overexpression of NCAM, since the *homo-trans* binding mechanism does not allow discrimination of axons from myelin cells⁶⁷.

More recently, Nectin-like (Necl) family members Necl1 and Necl4 were shown to form *hetero-trans*-interactions at the myelin-axon interface along the internode, with Necl1 expressed on the axon and Necl4 on the myelinating cells^{68,69}. Necl4 co-localizes with MAG, but neither Necl1 nor Necl4 binds to MAG⁶⁹. While Necl4 was shown to be upregulated in mature oligodendrocytes during myelination, knockout of Necl4 shows that it is not essential for myelination⁷⁰. Although there seems to be functional redundancy between NCAM, Necl1/4 and the MAG-ganglioside interaction, it is noteworthy that MAG expression in mature myelin appears about tenfold higher than the Necl proteins and twice as high as NCAM⁷¹.

Comparing the cell adhesion molecules at the myelin-axon interface, there are indications of sequential interactions during the engagement and wrapping of the axon by the myelin cell^{64,66}. L1CAM, for example, is only present on myelinating cells of the PNS

during the initial stages of myelination. In mice at postnatal day 8 (P8), when myelin cells have wrapped the axon approximately 1.5 times on average, MAG expression increases as L1CAM disappears and NCAM is downregulated⁶⁴. The expression levels of Necl4 in the spinal cord were later found to be the highest between P7 and P15, after which expression was downregulated⁷⁰. MAG remains highly expressed at the adaxonal membrane in mature myelin⁶⁴. The homo interactions of L1CAM and NCAM and the interaction of MAG with axonal gangliosides were previously proposed to be sequentially involved in mediating the axon-myelin interaction^{64,66}.

Based on a combination of available crystal structures and electron microscopy data, we can estimate the preferential intermembrane distances for L1CAM⁷², NCAM^{73,74}, Necl1/475 and MAG (this work, chapter two) (Fig. 1). Combining these preferential intermembrane distances with the data concerning the timing of expression at the myelin-axon interface, a sequential periaxonal compaction model can be constructed (Fig. 1). First L1CAM (only in the PNS) and NCAM engage in *homo-trans*-interactions, forming interactions at >30 nm. Subsequently, Necl1 and Necl4 form *hetero-trans*-interactions at 15–30 nm, leading to compaction of the periaxonal diameter. Thereafter, at ca. 1.5 myelin wrappings, MAG monomers diffuse into the interface and can engage ganglioside ligands on the axon at 16 nm intermembrane distance. Simultaneously, L1CAM is expelled from the interface (in the PNS) and NCAM and Necl1/4 are downregulated. Finally, the *trans* stabilization of MAG leads to elevation of the local MAG concentration at the interface, so that MAG dimers can be formed, completing and rigidifying the compaction of the axon-myelin interaction at 10 nm intermembrane distance (Fig. 1).

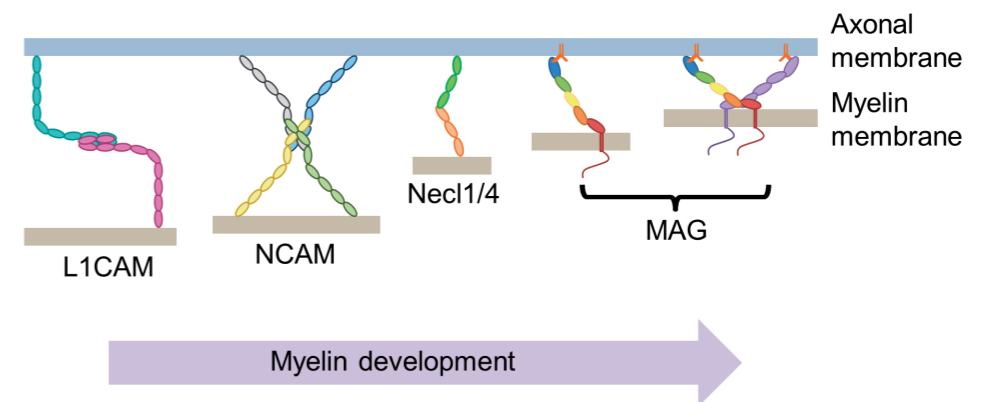


Figure 1: Model for sequential periaxonal compaction

First, the larger extracellular domains of L1CAM (only in the PNS) and NCAM engage in *homo-trans*-interactions at intermembrane distances of up to 32 nm. Later, Necl1/4 could mediate *hetero-trans*-interactions at distances of 15–30 nm (shown is 20 nm). MAG monomers can reach out approximately 16 nm and could even span greater distances by binding to α 2,3-sialylated N-linked and O-linked glycans of axonal surface glycoproteins. Finally, as the local concentration of MAG molecules is elevated because of the high local concentration of available (ganglioside) ligands, MAG dimers are formed that reduce the periaxonal diameter to 10 nm, as is observed in mature myelin⁵³. Sizes and distances are represented to scale.

Roles for NgR and Olfm1 at the synapse

Chemical synapses are contact sites where information transfer occurs between two neurons. The connections are formed between axonal boutons or terminals of a signaling neuron and dendritic spines or the cell body (*soma*) of a receiving neuron. When an action potential reaches the pre-synapse, the content of neurotransmitter vesicles is released into the synaptic cleft. This allows neurotransmitter molecules to diffuse to post-synaptic ligand-gated ion channels, causing them to open their transmembrane ion channel domains to allow currents to flow along the electrochemical gradient. This can be the start of a new action potential in the receiving neuron.

Apart from its role as a receptor for regeneration-inhibiting factors, NgR plays a physiological role at synapses. NgR (as well as its paralogs NgR2 and NgR3) was found to restrict the number of synapses in the developing brain⁷⁶. It does so by signaling through TROY and RhoA at the post-synaptic side⁷⁶, similar to MAI signal transduction. NgR knockout studies using long-term monocular deprivation confirm that NgR functions post-synaptically rather than at axonal synaptic boutons or terminals in consolidating circuitry⁷⁷. However, it is not clear to what extracellular cue NgR responds for this function.

A role for NgR was also found in restricting α -amino-3-hydroxy-5-methyl-4-isoxazole propionic acid (AMPA) receptor delivery to synapses to limit plasticity⁷⁸. AMPA receptors are glutamate-gated ion channels that function in the post-synaptic membranes of excitatory synapses⁷⁹. Their trafficking has been linked to synaptic plasticity, memory and learning⁷⁹. Another post-synaptic membrane protein that was found to interact with NgR is amyloid precursor protein (APP)⁸⁰, although it remains unclear what the physiological function of this interaction is (Fig. 2).

Interestingly, the NgR ligand Olfm1 has also been suggested to have functions at the synapse⁸¹. Similar to NgR, Olfm1 interacts with APP, which was found to be important during nervous system development⁸². Olfm1 was also found to interact with other synaptic proteins, such as AMPA receptors, voltage-gated calcium channels and Teneurin^{4,81,83,84}. A mutation that results in deletion of part of the coiled-coil domain of Olfm1 influenced these interactions, changed calcium signaling upon stimulation with AMPA or glutamate and resulted in abnormal behavior and brain dystrophy in mice⁸¹. The fact that both AMPA receptors and Olfm1 form tetramers with a dimer-of-dimers architecture, as described in chapter four, suggests Olfm1 might be involved in regulating AMPA receptor mobility, clustering or gating (Fig. 2).

AMPA receptors are organized opposed to pre-synaptic vesicles and voltage-gated calcium channels on a sub-synaptic scale as “nanocolumns”^{85–87}. The synaptic cleft proteins responsible for such organization have not been identified. Olfm1 binds to both pre-synaptic voltage-gated calcium channels and post-synaptic AMPA receptors⁸¹,

has the potential to bind multiple copies of both, has a calcium binding site that could regulate interactions and combined with the extracellular domains of these proteins, has the right dimensions to span the 24 nm spacing of the synaptic cleft^{88,89}. This makes Olfm1 an interesting candidate as an extracellular organizer of such nanocolumns.

The fact that NgR and Olfm1 interact with each other as well as with post-synaptic AMPA receptors and APP (Fig. 2) suggests complex mechanisms involving these proteins might be at play to regulate activity-dependent synaptic plasticity. Determining how and why these synaptic proteins interact could be an interesting new direction to shed light on the molecular basis of memory and learning.

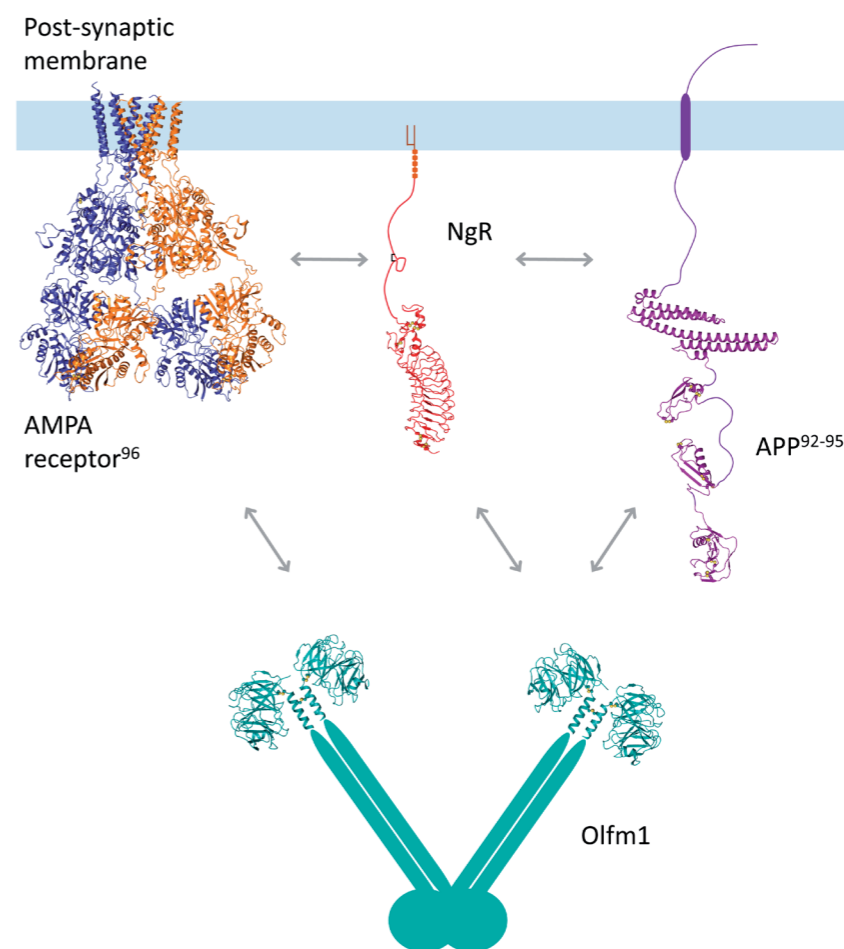


Figure 2: Illustration of NgR and Olfm1 synaptic binding partners

Schematic representation of NgR, Olfm1 and their shared synaptic binding partners APP and AMPA receptors. Previously-reported interactions are shown as grey arrows. Structures of APP^{92–95}, AMPA receptor⁹⁶, NgR and Olfm1 (this work) are shown as cartoon with disulfides as ball and stick.

Conclusion

The structural studies described in this thesis provide new insights into the molecular mechanisms of MAI signaling, as well as myelin formation and stability. Nevertheless, important questions remain and new ones are raised. Whether MAI-receptor-co-receptor complexes have a defined stoichiometry and what this stoichiometry is remains unclear. For MAG, NgR, GT1b and p75/TROY we propose hypothetical mechanisms for signal transduction through the membrane, but these mechanisms remain, for the moment, unverified. Structures of MAI-receptor complexes or receptor-co-receptor complexes are required to answer these questions. Fast developments in the fields of cryogenic electron microscopy and tomography could help in obtaining structural data for these low-affinity complexes. The current availability of high-resolution structures of almost all of the individual components should be helpful in such studies, as these models could be docked into lower-resolution density maps. Rapid developments in super-resolution microscopy and live cell imaging could also assist in determining the exact mechanisms of MAI signal transduction into neurons, for example by visualizing MAI-induced (co-)receptor clustering and determining the stoichiometry of ligands, receptors and co-receptors on the neuronal cell surface.

As the field of MAI signaling is maturing, clinical application is no longer solely a futuristic dream. The fact that compounds targeting MAG (a monoclonal antibody)⁹⁰ and NgR (a NgR LRR domain-Fc fusion)⁹¹ to enhance recovery of spinal cord injury are in (pre-)clinical trials, demonstrates the feasibility of pharmacological interference with MAI signaling to promote recovery upon CNS damage. The structural insights into MAG-ganglioside interaction we present in chapter two, as well as our observation that MAG_{1,5}-Fc R118A enhances neurite outgrowth, provide new handles for drug development to enhance recovery upon CNS damage. Concluding, although there might still be questions, there is light on the horizon for victims of spinal cord or brain injury.

References

1. Fawcett, J. W. & Keynes, R. J. Peripheral nerve regeneration. *Annu. Rev. Neurosci.* **13**, 43–60 (1990).
2. Kim, W.-Y. & Snider, W. D. Neuroscience. Overcoming inhibitions. *Science* **322**, 869–72 (2008).
3. Akbik, F., Cafferty, W. B. J. & Strittmatter, S. M. Myelin associated inhibitors: A link between injury-induced and experience-dependent plasticity. *Exp. Neurol.* **235**, 43–52 (2011).
4. Mironova, Y. A. & Giger, R. J. Where no synapses go: gatekeepers of circuit remodeling and synaptic strength. *Trends Neurosci.* **36**, 363–373 (2013).
5. Baldwin, K. T. & Giger, R. J. Insights into the physiological role of CNS regeneration inhibitors. *Front. Mol. Neurosci.* **8**, 1–8 (2015).
6. Alberts, B. *et al.* *Molecular Biology of the Cell.* (2002).
7. Wu, H. Higher-Order Assemblies in a New Paradigm of Signal Transduction. *Cell* **153**, 287–292 (2013).
8. Fournier, A. E., Gould, G. C., Liu, B. P. & Strittmatter, S. M. Truncated soluble Nogo receptor binds Nogo-66 and blocks inhibition of axon growth by myelin. *J. Neurosci.* **22**, 8876–83 (2002).
9. Barton, W. *et al.* Structure and axon outgrowth inhibitor binding of the Nogo-66 receptor and related proteins. *EMBO J.* **22**, 3291–302 (2003).
10. Vilar, M. *et al.* Activation of the p75 Neurotrophin Receptor through Conformational Rearrangement of Disulphide-Linked Receptor Dimers. *Neuron* **62**, 72–83 (2009).
11. Vilar, M. *et al.* Ligand-independent signaling by disulfide-crosslinked dimers of the p75 neurotrophin receptor. *J. Cell Sci.* **122**, 3351–3357 (2009).
12. Vilar, M. *et al.* Heterodimerization of p45-p75 modulates p75 signaling: structural basis and mechanism of action. *PLoS Biol.* **12**, e1001918 (2014).
13. Mosyak, L. *et al.* The structure of the Lingo-1 ectodomain, a module implicated in central nervous system repair inhibition. *J. Biol. Chem.* **281**, 36378–90 (2006).
14. Kajander, T., Kuja-Panula, J., Rauvala, H. & Goldman, A. Crystal Structure and Role of Glycans and Dimerization in Folding of Neuronal Leucine-Rich Repeat Protein AMIGO-1. *J. Mol. Biol.* **413**, 1001–1015 (2011).
15. Dodd, D. *et al.* Nogo-A, -B, and -C are found on the cell surface and interact together in many different cell types. *J. Biol. Chem.* **280**, 12494–12502 (2005).
16. Fournier, A. E., GrandPré, T. & Strittmatter, S. M. Identification of a receptor mediating Nogo-66 inhibition of axonal regeneration. *Nature* **409**, 341–346 (2001).
17. GrandPré, T., Nakamura, F., Vartanian, T. & Strittmatter, S. M. Identification of the Nogo inhibitor of axon regeneration as a Reticulon protein. *Nature* **7199**, 439–444 (2000).
18. Zhang, L. *et al.* Identification of BLYS (B lymphocyte stimulator), a non-myelin-associated protein, as a functional ligand for Nogo-66 receptor. *J. Neurosci.* **29**, 6348–6352 (2009).
19. Karpusas, M. *et al.* Crystal structure of extracellular human BAFF, a TNF family member that stimulates B lymphocytes. *J. Mol. Biol.* **315**, 1145–54 (2002).
20. Oren, D. *et al.* Structural basis of BLYS receptor recognition. *Nat. Struct. Biol.* **9**, 288–292 (2002).
21. Liu, Y. *et al.* Crystal structure of sTALL-1 reveals a virus-like assembly of TNF family ligands. *Cell* **108**, 383–394 (2002).
22. Kim, H. M. *et al.* Crystal structure of the BAFF-BAFF-R complex and its implications for receptor activation. *Nat. Struct. Biol.* **10**, 342–348 (2003).
23. Dickendesher, T. L. *et al.* NgR1 and NgR3 are receptors for chondroitin sulfate proteoglycans. *Nat. Neurosci.* **15**, (2012).
24. Nakaya, N., Sultana, A., Lee, H. S. & Tomarev, S. I. Olfactomedin 1 interacts with the Nogo A receptor complex to regulate axon growth. *J. Biol. Chem.* **287**, 37171–37184 (2012).
25. Simons, K. & Toomre, D. Lipid rafts and signal transduction. *Nat. Rev. Mol. Cell Biol.* **1**, 31–39 (2000).
26. Pignot, V. *et al.* Characterization of two novel proteins, NgRH1 and NgRH2, structurally and biochemically homologous to the Nogo-66 receptor. *J. Neurochem.* **85**, 717–728 (2003).
27. Fujitani, M. *et al.* Binding of soluble myelin-associated glycoprotein to specific gangliosides induces the association of p75NTR to lipid rafts and signal transduction. *J. Neurochem.* **94**, 15–21 (2005).
28. Yu, W., Guo, W. & Feng, L. Segregation of Nogo66 receptors into lipid rafts in rat brain and inhibition of Nogo66 signaling by cholesterol depletion. *FEBS Lett.* **577**, 87–92 (2004).
29. Yamashita, T., Higuchi, H. & Tohyama, M. The p75 receptor transduces the signal from myelin-associated glycoprotein to Rho. *J. Cell Biol.* **157**, 565–70 (2002).

30. Vinson, M. *et al.* Lipid rafts mediate the interaction between myelin-associated glycoprotein (MAG) on myelin and MAG-receptors on neurons. *Mol. Cell. Neurosci.* **22**, 344–352 (2003).
31. Wang, K. C., Kim, J. a, Sivasankaran, R., Segal, R. & He, Z. P75 interacts with the Nogo receptor as a co-receptor for Nogo, MAG and OMgp. *Nature* **420**, 74–8 (2002).
32. Vinson, M. *et al.* Myelin-associated glycoprotein interacts with ganglioside GT1b. A mechanism for neurite outgrowth inhibition. *J. Biol. Chem.* **276**, 20280–5 (2001).
33. Cai, D., Shen, Y., De Bellard, M., Tang, S. & Filbin, M. T. Prior exposure to neurotrophins blocks inhibition of axonal regeneration by MAG and myelin via a cAMP-dependent mechanism. *Neuron* **22**, 89–101 (1999).
34. Williams, G. *et al.* Overcoming the inhibitors of myelin with a novel neurotrophin strategy. *J. Biol. Chem.* **280**, 5862–5869 (2005).
35. Lin, Z. *et al.* Structural basis of death domain signaling in the p75 neurotrophin receptor. *Elife* **4**, 1–21 (2015).
36. Shao, Z. *et al.* TAJ/TROY, an orphan TNF receptor family member, binds Nogo-66 receptor 1 and regulates axonal regeneration. *Neuron* **45**, 353–359 (2005).
37. Park, J. B. *et al.* A TNF receptor family member, TROY, is a coreceptor with Nogo receptor in mediating the inhibitory activity of myelin inhibitors. *Neuron* **45**, 345–51 (2005).
38. Lu, Y. *et al.* TROY interacts with Rho guanine nucleotide dissociation inhibitor α (RhoGDI α) to mediate Nogo-induced inhibition of neurite outgrowth. *J. Biol. Chem.* **288**, 34276–86 (2013).
39. Saha, N., Kolev, M. & Nikolov, D. B. Structural Features of the Nogo receptor Signaling Complexes at the Neuron/Myelin Interface. *Neurosci. Res.* **87**, 1–7 (2014).
40. Schwab, M. E. Functions of Nogo proteins and their receptors in the nervous system. *Nat. Rev. Neurosci.* **11**, 799–811 (2010).
41. Meabon, J. S. *et al.* LINGO-1 Interacts with the p75 Neurotrophin Receptor in Intracellular Membrane Compartments. *J. Biol. Chem.* jbc.M114.608018 (2015).
42. Ahmed, Z., Douglas, M. R., John, G., Berry, M. & Logan, A. AMIGO3 is an NgR1/p75 co-receptor signalling axon growth inhibition in the acute phase of adult central nervous system injury. *PLoS One* **8**, e61878 (2013).
43. Fields, R. D. A new mechanism of nervous system plasticity: activity-dependent myelination. *Nat. Rev. Neurosci.* **16**, 756–67 (2015).
44. Quarles, R. H. Myelin-associated glycoprotein (MAG): past, present and beyond. *J. Neurochem.* **100**, 1431–1448 (2007).
45. Lopez, P. H. H. Role of myelin-associated glycoprotein (siglec-4a) in the nervous system. *Adv. Neurobiol.* **9**, 245–62 (2014).
46. Trapp, B. D. & Quarles, R. H. Presence of the myelin-associated glycoprotein correlates with alterations in the periodicity of peripheral myelin. *J. Cell Biol.* **92**, 877–882 (1982).
47. Trapp, B. D., Quarles, R. H. & Suzuki, K. Immunocytochemical studies of quaking mice support a role for the myelin-associated glycoprotein in forming and maintaining the periaxonal space and periaxonal cytoplasmic collar of myelinating Schwann cells. *J. Cell Biol.* **99**, 594–606 (1984).
48. Li, C. *et al.* Myelination in the absence of myelin-associated glycoprotein. *Nature* **369**, 747–50 (1994).
49. Nguyen, T. *et al.* Axonal protective effects of the myelin-associated glycoprotein. *J. Neurosci.* **29**, 630–7 (2009).
50. Mehta, N. R., Nguyen, T., Bullen, J. W., Griffin, J. W. & Schnaar, R. L. Myelin-associated glycoprotein (MAG) protects neurons from acute toxicity using a ganglioside-dependent mechanism. *ACS Chem. Neurosci.* **1**, 215–222 (2010).
51. Lopez, P. H. H. *et al.* Myelin-associated glycoprotein protects neurons from excitotoxicity. *J. Neurochem.* **116**, 900–908 (2011).
52. Kinter, J. *et al.* An essential role of MAG in mediating axon-myelin attachment in Charcot-Marie-Tooth 1A disease. *Neurobiol. Dis.* **0**, 221–231 (2013).
53. Snaidero, N. *et al.* Myelin Membrane Wrapping of CNS Axons by PI(3,4,5)P3-Dependent Polarized Growth at the Inner Tongue. *Cell* **156**, 277–290 (2014).
54. Butt, a M., Ibrahim, M., Gregson, N. & Berry, M. Differential expression of the L- and S-isoforms of myelin associated glycoprotein (MAG) in oligodendrocyte unit phenotypes in the adult rat anterior medullary velum. *J. Neurocytol.* **27**, 271–80 (1998).
55. Umemori, H., Sato, S., Yagi, T., Aizawa, S. & Yamamoto, T. Initial events of myelination involve Fyn tyrosine kinase signalling. *Nature* **367**, 572–576 (1994).
56. Marta, C. B. *et al.* Myelin associated glycoprotein cross-linking triggers its partitioning into lipid rafts, specific signaling events and cytoskeletal rearrangements in oligodendrocytes. *Neuron Glia Biol.* **1**, 35–46 (2004).
57. Kursula, P., Meriläinen, G., Lehto, V. P. & Heape, A. M. The small myelin-associated glycoprotein is a zinc-binding protein. *J. Neurochem.* **73**, 2110–2118 (1999).
58. Kursula, P., Lehto, V. P. & Heape, A. M. The small myelin-associated glycoprotein binds to tubulin and microtubules. *Mol. Brain Res.* **87**, 22–30 (2001).
59. Fujita, N. *et al.* The cytoplasmic domain of the large myelin-associated glycoprotein isoform is needed for proper CNS but not peripheral nervous system myelination. *J. Neurosci.* **18**, 1970–1978 (1998).
60. Erb, M. *et al.* Unraveling the differential expression of the two isoforms of myelin-associated glycoprotein in a mouse expressing GFP-tagged S-MAG specifically regulated and targeted into the different myelin compartments. *Mol. Cell. Neurosci.* **31**, 613–27 (2006).
61. Yamauchi, J. *et al.* Phosphorylation of Cytohesin-1 by Fyn Is Required for Initiation of Myelination and the Extent of Myelination During Development. *Sci. Signal.* **5**, ra69-ra69 (2012).
62. Chan, B. *et al.* SAP couples Fyn to SLAM immune receptors. *Nat Cell Biol* **5**, 155–160 (2003).
63. Shin, D., Lin, S.-T., Fu, Y.-H. & Ptáček, L. J. Very large G protein-coupled receptor 1 regulates myelin-associated glycoprotein via G α s/G α q-mediated protein kinases A/C. *Proc. Natl. Acad. Sci. U. S. A.* **110**, 19101–6 (2013).
64. Martini, R. & Schachner, M. Immunoelectron microscope localization of neural cell adhesion molecules (L1, N-CAM, MAG) and their carbohydrate epitope and myelin basic protein (MBP) in developing sciatic nerve. *J. Cell Biol.* **103**, 2439–2448 (1986).
65. Bartsch, U., Kirchhoff, F. & Schachner, M. Immunohistological localization of the adhesion molecules L1, N-CAM, and MAG in the developing and adult optic nerve of mice. *J. Comp. Neurol.* **284**, 451–62 (1989).
66. Li, C., Trapp, B., Ludwin, S., Peterson, A. & Roder, J. Myelin associated glycoprotein modulates glia-axon contact in vivo. *J. Neurosci. Res.* **51**, 210–7 (1998).
67. Schachner, M. & Bartsch, U. Multiple functions of the myelin-associated glycoprotein MAG (siglec-4a) in formation and maintenance of myelin. *Glia* **29**, 154–165 (2000).
68. Maurel, P. *et al.* Nectin-like proteins mediate axon-Schwann cell interactions along the internode and are essential for myelination. *J. Cell Biol.* **178**, 861–874 (2007).
69. Spiegel, I. *et al.* A central role for Necl4 (SynCAM4) in Schwann cell–axon interaction and myelination. *Nat. Neurosci.* **10**, 861–869 (2007).
70. Zhu, Y. *et al.* Necl-4/SynCAM-4 Is Expressed in Myelinating Oligodendrocytes but Not Required for Axonal Myelination. *PLoS One* **8**, 4–11 (2013).
71. Ishii, A. *et al.* Human myelin proteome and comparative analysis with mouse myelin. *Proc. Natl. Acad. Sci. U. S. A.* **106**, 14605–14610 (2009).
72. He, Y., Jensen, G. J. & Bjorkman, P. J. Cryo-Electron Tomography of Homophilic Adhesion Mediated by the Neural Cell Adhesion Molecule L1. *Structure* **17**, 460–471 (2009).
73. Soroka, V. *et al.* Structure and interactions of NCAM Ig1-2-3 suggest a novel zipper mechanism for homophilic adhesion. *Structure* **11**, 1291–1301 (2003).
74. Hall, A. K. & Rutishauser, U. Visualization of neural cell adhesion molecule by electron microscopy. *J. Cell Biol.* **104**, 1579–86 (1987).
75. Harrison, O. J. *et al.* Nectin ectodomain structures reveal a canonical adhesive interface. *Nat. Struct. Mol. Biol.* **19**, 906–15 (2012).
76. Wills, Z. P. *et al.* The Nogo Receptor Family Restricts Synapse Number in the Developing Hippocampus. *Neuron* **73**, 466–481 (2012).
77. Frantz, M. G., Kast, R. J., Dorton, H. M., Chapman, K. S. & McGee, a. W. Nogo Receptor 1 Limits Ocular Dominance Plasticity but not Turnover of Axonal Boutons in a Model of Amblyopia. *Cereb. Cortex* 1–11 (2015). doi:10.1093/cercor/bhv014
78. Jitsuki, S. *et al.* Nogo Receptor Signaling Restricts Adult Neural Plasticity by Limiting Synaptic AMPA Receptor Delivery. *Cereb. cortex* **26**, 427–39 (2016).
79. Chater, T. E. & Goda, Y. The role of AMPA receptors in postsynaptic mechanisms of synaptic plasticity. *Front. Cell. Neurosci.* **8**, 1–14 (2014).
80. Park, J. H. *et al.* Alzheimer precursor protein interaction with the Nogo-66 receptor reduces amyloid-beta plaque deposition. *J. Neurosci.* **26**, 1386–1395 (2006).
81. Nakaya, N. *et al.* Deletion in the N-terminal half of olfactomedin 1 modifies its interaction with synaptic proteins and causes brain dystrophy and abnormal behavior in mice. *Exp. Neurol.* **250**, 205–218 (2013).

82. Rice, H. C. *et al.* Pancortins interact with amyloid precursor protein and modulate cortical cell migration. *Development* **139**, 3986–3996 (2012).
83. Schwenk, J. *et al.* High-Resolution Proteomics Unravel Architecture and Molecular Diversity of Native AMPA Receptor Complexes. *Neuron* **74**, 621–633 (2012).
84. Shanks, N. F. *et al.* Differences in AMPA and Kainate Receptor Interactomes Facilitate Identification of AMPA Receptor Auxiliary Subunit GSG1L. *Cell Rep.* **1**, 590–598 (2012).
85. Tang, A. *et al.* A trans-synaptic nanocolumn aligns neurotransmitter release to receptors. *Nature* 1–21 (2016). doi:10.1038/nature19058
86. Frank, T. *et al.* Bassoon and the synaptic ribbon organize Ca²⁺ channels and vesicles to add release sites and promote refilling. *Neuron* **68**, 724–738 (2010).
87. Ermolyuk, Y. S. *et al.* Differential triggering of spontaneous glutamate release by P/Q-, N- and R-type Ca²⁺ channels. *Nat. Publ. Gr.* **16**, 1754–1763 (2013).
88. Pronker, M. F., Bos, T. G. A. A., Sharp, T. H., Thies-Weesie, D. M. E. & Janssen, B. J. C. Olfactomedin-1 Has a V-shaped Disulfide-linked Tetrameric Structure. *J. Biol. Chem.* **290**, 15092–15101 (2015).
89. Lucić, V., Yang, T., Schweikert, G., Förster, F. & Baumeister, W. Morphological characterization of molecular complexes present in the synaptic cleft. *Structure* **13**, 423–34 (2005).
90. Abila, B., Cunningham, E. & Simeoni, M. First-time-in-human study with GSK249320, a myelin-associated glycoprotein inhibitor, in healthy volunteers. *Clin. Pharmacol. Ther.* **93**, 163–9 (2013).
91. Wang, X. *et al.* Human NgR-Fc Decoy Protein via Lumbar Intrathecal Bolus Administration Enhances Recovery from Rat Spinal Cord Contusion. *J. Neurotrauma* **31**, 1955–1966 (2014).
92. Barnham, K. J. *et al.* Structure of the Alzheimer's disease amyloid precursor protein copper binding domain. A regulator of neuronal copper homeostasis. *J. Biol. Chem.* **278**, 17401–17407 (2003).
93. Rossjohn, J. *et al.* Crystal structure of the N-terminal, growth factor-like domain of Alzheimer amyloid precursor protein. *Nat. Struct. Biol.* **6**, 327–331 (1999).
94. Wang, Y. & Ha, Y. The X-ray structure of an antiparallel dimer of the human amyloid precursor protein E2 domain. *Mol. Cell* **15**, 343–353 (2004).
95. Hynes, T. R., Randal, M., Kennedy, L. A., Eigenbrot, C. & Kossiakoff, A. A. X-ray crystal structure of the protease inhibitor domain of Alzheimer's amyloid β -protein precursor. *Biochemistry* **29**, 10018–10022 (1990).
96. Dürr, K. L. *et al.* Structure and dynamics of AMPA receptor GluA2 in resting, pre-open, and desensitized states. *Cell* **158**, 778–792 (2014).

English summary

In most parts of the body, nerves can regenerate well upon injury. However, in the brain and spinal cord regeneration is very limited. One of the causes of this lack of regeneration is the presence of myelin proteins that inhibit outgrowth of neuronal projections. Myelin is the fatty substance wrapped around the output projections of neurons called axons, to enhance conduction velocity and reduce electrical capacitance. Three myelin-associated inhibitors of regeneration (MAIs) have been identified; myelin-associated glycoprotein (MAG), Nogo and oligodendrocyte myelin glycoprotein. These MAIs signal to nerve cells (neurons) via receptor complexes at the neuronal cell surface. In this work, molecular mechanisms of this MAI signaling are described. The focus of this dissertation is on the initial signaling events that happen at the neuronal cell surface. Three proteins were studied by structural biology techniques: the MAI ligand MAG, the neuronal Nogo Receptor (NgR) and an antagonist of MAG signaling via NgR; Olfactomedin-1 (Olfm1).

Apart from their role in MAI signaling, these proteins also serve various physiological functions in the nervous system. MAG is recognized as a cell adhesion molecule at the myelin-axon interface along the internode. MAG is involved in myelin formation and required for stability of myelin and axon. Moreover, it maintains the correct spacing between myelin and neuronal membranes and is engaged in axon-to-myelin signaling. NgR is a receptor for diverse plasticity-inhibiting ligands and functions in consolidating neuronal circuitry and memory. Olfm1 is a secreted protein vital for proper brain development and function. The signaling mechanisms of MAG, NgR and Olfm1 and how they perform their physiological functions are the subject of this dissertation.

Chapter one introduces MAI signaling, focusing on NgR and the initial signal transduction events at the neuronal plasma membrane. The currently available literature is reviewed and the roles of MAG, NgR and Olfm1 in MAI signaling are described.

In chapter two, the three-dimensional structure of the extracellular segment of MAG is described. Structures of MAG-oligosaccharide complexes and biophysical techniques combined with site-directed mutagenesis reveal how MAG recognizes neuronal gangliosides (glycolipids). Dimers of MAG, formed by association between immunoglobulin domains four and five, were observed in different crystal forms. Site-directed mutagenesis and different solution-state techniques were used to validate this interface. Neurite outgrowth assays evaluated the role of MAG dimerization and ganglioside binding in regeneration-inhibiting signaling. Both dimerization and ganglioside binding were found to be required for the regeneration-inhibiting properties of MAG. The combination of dimerization of MAG on the myelin membrane and ganglioside binding on the opposing neuronal membrane provides a mechanism for regulation of the myelin-axon spacing. The rod-like MAG extracellular segment has

angular freedom with respect to the myelin membrane as a monomer. However, it is locked in a specific orientation by dimerization and ganglioside binding, maintaining the myelin-axon spacing like a molecular leaf spring. Dimerization as a result of axon engagement also provides a putative mechanism for axon-to-myelin signaling. It brings the intracellular domains of MAG within six nanometer distance of each other, which could trigger auto-activation of the cytosolic MAG-binding non-receptor tyrosine kinase Fyn. Fyn activation is required for the initiation of myelination. Thus, dimerization and ganglioside binding of MAG as observed in our structures are required for myelin-to-axon signaling (regeneration inhibition), maintaining the myelin-axon spacing and potentially also for axon-to-myelin signaling via Fyn during myelination.

Chapter three describes crystal structures of the leucine-rich repeat (LRR) domain of NgR, for the first time with the correct disulfide structure. An extra C-terminal loop, which is important for co-receptor binding, is observed but appears mostly flexible in the absence of stabilizing interactions. NgR was shown previously to self-interact on the neuronal cell surface. We compare different crystal forms to establish the structural basis of NgR self-interaction. One extensive dimerization interface was observed in different crystal forms, which we argue represents the NgR self-interaction on the neuronal cell surface.

In chapter four, Olfm1 is shown to form disulfide-linked tetramers. Limited proteolysis was combined with X-ray crystallography to determine the structure of a double olfactomedin (Olf) domain and coiled coil. We show that this Olf domain is stabilized by calcium and use a combination of techniques to provide the architecture of the full-length tetramer. The V-shaped dimer-of-dimers architecture suggests a role of Olfm1 in receptor clustering at cell surfaces.

In chapter five, the general implications of these results are discussed and collated with regard to old and new literature. Novel hypotheses based on the findings are proposed and an outlook on the future of the MAI field is provided.

In summary, we provide the first structures of MAG, suggesting mechanisms for bi-directional signaling and maintenance of the correct myelin-axon spacing. NgR was crystallized for the first time with native disulfide bonds in many different crystal forms, allowing us to compare interfaces to investigate NgR self-interaction on the neuronal cell surface. Finally, we show that Olfm1 forms disulfide-linked tetramers with a V-shaped dimer-of-dimers architecture and provide the structure of a dimeric Olf domain and coiled-coil segment. These results provide novel insights in MAI signaling mechanisms, myelin formation and stability and nervous system development and plasticity.

Keywords: central nervous system, regeneration, myelin, development, signaling, molecular mechanisms, structural biology, X-ray diffraction, protein crystallography, biophysics

Nederlandse samenvatting

In het grootste gedeelte van het lichaam kunnen zenuwen zichzelf herstellen na schade. In het brein en ruggenmerg is het herstellend vermogen echter beperkt. Eén van de redenen hiervoor is de aanwezigheid van myeline eiwitten die uitgroei van neuronale uitlopers remmen. Myeline is de vettige substantie die is opgerold rondom axonen, de uitlopers van zenuwcellen (neuronen) die verantwoordelijk zijn voor hun outputsignalen. Myeline verhoogt de geleidingssnelheid van de axon en vermindert de elektrische capaciteit. Drie eiwitten zijn geïdentificeerd als myeline-geassocieerde inhibitoren van regeneratie (MAIs); myeline-geassocieerd glycoproteïne (MAG), Nogo en oligodendrocyet myeline glycoproteïne (OMgp). Deze MAIs signaleren naar neuronale cellen via receptor complexen op het neuronale cel oppervlak. In dit proefschrift worden moleculaire mechanismes verantwoordelijk voor MAI signalering beschreven. Drie eiwitten zijn bestudeerd met behulp van structuurbiologische technieken om een beter begrip te krijgen van deze signalering: het MAI ligand MAG, de neuronale Nogo Receptor (NgR) en een antagonist van MAG signalering via NgR; Olfactomedin-1 (Olfm1).

Naast hun rol in MAI signalering na schade aan het zenuwstelsel, hebben deze eiwitten ook verscheidene functies onder fysiologische condities. MAG is een celadhesie molecuul in het myeline-axon grensvlak ter hoogte van het internodium. MAG is betrokken bij myelinevorming en is benodigd voor stabiliteit van myeline en axon. Bovendien reguleert MAG de afstand tussen de membranen van neuron en myeline cel en speelt een rol in axon-naar-myeline signalering. NgR is een receptor voor verschillende plasticiteit-inhiberende liganden en fungeert in de consolidatie van neuronale circuits en het vormen van herinneringen en geheugen. Olfm1 is een uitgescheiden eiwit dat essentieel is voor het naar behoren ontwikkelen en functioneren van het brein. De signaleringsmechanismen van MAG, NgR en Olfm1 en hoe ze hun fysiologische functies uitoefenen zijn het onderwerp van deze dissertatie.

Hoofdstuk één introduceert MAI signalering, waarin de focus ligt op NgR en de initiële signaaltransductiemechanismen ter hoogte van het neuronale plasmamembraan. De beschikbare literatuur wordt besproken en de rollen van MAG, NgR en Olfm1 in MAI signalering komen aan bod.

In hoofdstuk twee wordt de driedimensionale structuur van het extracellulaire segment van MAG beschreven. Structuren van MAG-oligosaccharide complexen en biofysische technieken gecombineerd met mutagenese laten zien hoe MAG neuronale gangliosides (glycolipiden) herkent. Dimeren van MAG, gevormd door associatie van de immunoglobuline domeinen vier en vijf, werden geobserveerd in verschillende kristalvormen. Mutagenese en technieken uitgevoerd in oplossing werden gebruikt om deze interactie te valideren. Neuriet uitgroei proeven lieten zien dat zowel dimeervorming en gangliosidebinding nodig zijn voor de regeneratie-inhiberende eigenschappen van

MAG. De combinatie van dimeervorming van MAG op het myelinemembraan en gangliosidebinding op het tegenoverliggende neuronale membraan laat zien hoe MAG de afstand tussen beide membranen kan reguleren. Het staafvormige extracellulaire segment van MAG heeft als monomeer rotatievrijheid ten opzichte van het myeline membraan. Dit segment wordt echter vastgezet wanneer het een dimeer vormt met een ander MAG molecuul en gangliosides op het tegenoverliggend membraan bindt, zodat het de afstand tussen de twee membranen reguleert als een moleculaire bladveer. MAG dimeervorming als gevolg van contact met de axon is ook een mogelijke verklaring voor hoe MAG axon-naar-myeline signalering verzorgt. In een MAG dimeer komen de intracellulaire domeinen van MAG binnen zes nanometer van elkaar, wat auto-activatie van de cytoplasmatische MAG bindingspartner Fyn kinase zou kunnen bewerkstelligen. Fyn activatie is nodig voor het in gang zetten van de myelinatie. Zodoende zijn de dimeervorming en gangliosidebinding van MAG zoals geobserveerd in de kristalstructuren nodig voor myeline-naar-axon signalering (regeneratie inhibitie), voor het reguleren van de correcte myeline-axon afstand en mogelijk ook voor axon-naar-myeline signalering via Fyn tijdens myelinatie.

Hoofdstuk drie beschrijft kristalstructuren van het leucine-rijke herhaling domein van NgR, voor het eerst met de correcte zwavelbrugstructuur. Een extra C-terminale lus die belangrijk is voor co-receptor binding werd geobserveerd maar is flexibel in de afwezigheid van stabiliserende interacties. Eerder werk liet zien dat NgR zelfinteractie aangaat op het neuronale celoppervlak. We vergelijken verschillende kristalvormen om de structurele basis van deze zelfinteractie vast te stellen. Eén extensief interactie grensvlak werd geobserveerd in verschillende kristalvormen, welke wij verantwoordelijk houden voor NgR zelf-interactie op het neuronale celoppervlak zoals eerder geobserveerd.

In hoofdstuk vier wordt beschreven hoe Olfm1 met zwavelbruggen verbonden tetrameren vormt. Gelimiteerde proteolyse werd gecombineerd met Röntgenkristallografie om de structuur te bepalen van een dubbel olfactomedin (Olf) domein en dubbelspiraal. We laten zien dat dit Olf domein wordt gestabiliseerd door calcium en gebruiken een combinatie van technieken om de organisatie van de volledige tetrameer te bepalen. De V-vormige dimeer-van-dimeren organisatie suggereert een rol voor Olfm1 in het clusteren van receptoren op het plasmamembraan van cellen.

In hoofdstuk vijf worden de algemene implicaties van deze resultaten bediscussieerd en vergeleken met beschikbare oude en nieuwe literatuur. Nieuwe hypothesen worden geponeerd en er wordt een perspectief geschetst van de mogelijkheden in de toekomst voor het MAI veld.

Samengevat laten we de eerste structuren zien van MAG, die mechanismen suggereren voor het in twee richtingen signaleren en voor handhaving van de correcte myeline-axon afstand. NgR is voor het eerst gekristalliseerd met de correcte disulfide structuur in verschillende kristalvormen, wat ons in staat stelde om interactie grensvlakken te

vergelijken om zo te bepalen hoe NgR zelf-associatie aangaat op het neuronale celoppervlak. Tenslotte laten we zien dat Olfm1 tetrameren vormt, die met zwavelbruggen verbonden zijn. We beschrijven de structuur van een dubbel Olf domein en dubbelspiraal segment en laten zien dat het volledige eiwit georganiseerd is als een V-vormige dimeer-van-dimeren. Deze resultaten bieden nieuwe inzichten in MAI signalering, myelinevorming en -stabiliteit en in ontwikkeling en plasticiteit van het zenuwstelsel.

Trefwoorden: centraal zenuwstelsel, regeneratie, myeline, ontwikkeling, signalering, moleculaire mechanismes, structuurbiologie, Röntgendiffractie, eiwitkristallografie, biofysica

Acknowledgements

I have had a great time during my PhD, not least because of the very collegial and supportive atmosphere in the K&S lab. This book would not have been possible without the contributions, scientific or otherwise, of many people. Therefore I would like to express my deep gratitude to these people.

Ten eerste wil ik mijn begeleider, Bert, bedanken. Afgezien van een uitstekende begeleider, was je ook een fijne baas en ben ik blij dat we regelmatig goed hebben kunnen lachen. Ondanks mijn eigenwijsheid hebben we veel goede en constructieve discussies gehad over wetenschappelijke vragen, de richting van projecten en het schrijven van artikelen. Je was altijd beschikbaar voor een vraag of een praatje en nam mijn ideeën serieus. Piet, mijn promotor, bij jou kon ik terecht voor enkele wijze adviezen en mooie verhalen over wetenschap “behind the scenes”.

Essentieel voor de totstandkoming van deze dissertatie waren mijn paranimfen, Hedwich en Remco. Remco, ganjaman, fawaka? No spang, everything real big in 808. Succes met je carrière in data-analyse! Hedwich, myelin inhibitor buddy, ik herinner me nog dat we al met het scheikunde introkamp in hetzelfde groepje zaten, het kan geen toeval zijn dat we op dezelfde dag aan onze PhD begonnen bij Bert. Succes met de laatste loodjes! Also part of Team Structural Neurobiology from the beginning was Nadia. I had a great time in Bretagne, you were a fantastic host! Bonne chance pour tes publications et futurs plans de carrière. The newer members Dimphna, Lukas and Matthieu completed the team. Dimphna; getver, this is unacceptable. Beste postdoc van Team Structural Neurobiology! Matthieu and Lucas, the new flagbearers of the team, bonne chance pour vos projects!

Also a huge thank you to all my collaborators. A surprising amount is from the mass spec lab; thanks Joost, Mirjam, Fan, Celine, Simone and Albert, you have helped me a great deal with many different projects! Dominique, bedankt voor alle hulp met de AUC experimenten, die een belangrijke bijdrage waren aan mijn twee publicaties. Eugene and Lucas, I feel like we've exhausted almost all available fluorescence microscopy techniques investigating MAG, thanks for your tireless efforts. Tevens op de 5^e verdieping, Roderik Tas, bedankt voor je bijdrage aan hoofdstuk 3 en de eerste neurite outgrowth testjes. Suzanne en Jeroen, jullie hebben een grote bijdrage geleverd voor hoofdstuk 2, wat resulteerde in belangrijke nieuwe inzichten in MAI signaling in deze thesis. Hartstikke bedankt! Thom, thanks a bunch for helping me out with the electron microscopy, good luck with your tenure track! Jonas and Mike, thanks for your assistance in preparing ganglioside liposomes and doing DLS with them, this was very useful for my studies on MAG.

Mijn oude bachelor- en masterstage begeleiders Arjen en Eric, jullie hebben me ingewijd in de wereld van Röntgenkristallografie en eiwitstructuren. Eric, het was erg prettig dat

jij het kantoor deelde met Bert, als de wetenschappelijke discussies in N810 interessant begonnen te worden had je vaak nuttige inbreng.

Already crystallography buddies since my bachelor (your pre-master) and an 808 veteran is Deniz. I have many good memories from the Instruct biennial meeting, holiday in Istanbul and in general in 808. Kapsalon, kapsalon, jin bon bon! Speaking of veterans, Louris and Xiaoguang were two great examples for me and always available for questions or discussions, especially when working in the terminal room. Loutje, heb je nog zo'n antafloetje? Nogmaals bedankt voor je hulp met de TSA! X to the G, I will never forget our "honeymoon" to Heidelberg. Also terminal room mentors in the beginning of my PhD were Federico, Tom and Peng. Thanks for all your tips and tricks in linux, phenix, CCP4, Coot and pymol, hope to see you again someday at a conference or in Italy/UK/USA! Thanks for the table tennis sessions, XG, Peng, Pramod and Christoph. Terminal master Tim, bedankt voor de snoepjes en xset b off.

Let's not forget the newer members of the 808 gang, Viviana and Ramon. Viviana, pausa cafe? Ramon, ramon, turn the radio on, nog bedankt voor het fruit! En natuurlijk voormalig 808-er Wout, ik ben trots op zo'n toegewijde nieuwe Borrel Boss. Camilla, thanks for helping me with screening olfactomedin EM grids, congratz with the JBC paper! Revina, de hardst werkende persoon in het Kruytgebouw, ik weet zeker dat het zich zal uitbetalen.

Loes en Martin, bedankt voor alle inzichten in Röntgenkristallografie en nuttige tips over twinning, scattering, data integratie etc. Martin, de trip naar het Schwarzwald was, ondanks het weer, een avontuur dat ik niet snel zal vergeten. Arie, Joke en Toine, hartstikke bedankt voor alle support op het gebied van kristallografie, moleculaire biologie en IT voorzieningen. Zonder jullie loopt het lab binnen no time vast. Hetzelfde geldt voor Noortje en haar voorgangers Cecile en Caroline, bedankt voor alle administratieve hulp. Een heel erg groot dankjewel voor de collega's van UPE; Wieger, Roland, Lucio, Smiriti en Zalan; jullie hebben misschien wel de grootste bijdrage aan dit proefschrift geleverd met alle HEK culturen en vectoren. K&S gaat jullie ongetwijfeld heel erg missen.

Also a shoutout to all of the structural biology buddies at NMR and EM. In particular, Siddarth and Gydo for co-organizing the starwars structural drinks, may the forcefield be with you. Tessa, tot ziens in Cambridge! Also, many thanks to Robert and Laura for helping me with my electron tomography data.

Verder wil ik mijn voormalige studenten Trusanne en Hugo heel erg bedanken, jullie hebben fantastisch werk geleverd voor het olfactomedin project. Hoofdstuk 4 was er waarschijnlijk niet geweest als jij mijn project niet had gekozen, Trusanne. Hugo, succes met je PhD in Duitsland, ik ben trots dat je voor de wetenschap hebt gekozen.

Wie ik zeker niet moet vergeten is Aike, voor wetenschappelijke discussies onder het genot van goed eten en een lekker (zelfgebrouwen) biertje. Klaar voor Cuba? Uiteraard ook een shoutout naar de rest van HULK, Wesley en Christian, when I say kip, y'all

say ...? En natuurlijk mijn bandgenoten van Roots Palmera voor de nodige muzikale afleiding en een fantastische tour op de ABC eilanden. Ivo, Roque, Jean-Carlos, Marc, Tarek, Lino en Alex, nos ta topa! Voor muzikale afleiding moet ik ook mijn Scherzogenoten, Jesse en Sebastiaan, bedanken. Succes met jullie muzikale carrières! Niet te vergeten ook zijn mijn ex-huisgenoten (maar nog steeds homies) van de vrijmiborrel, Marc, Hans, Karolien, Pim ;), Floriek, Anna, Yolanda, Nicky, Eleanor, ik ga jullie heel erg missen in Engeland. Vincent-san, arigato gozaimasu, je was een geweldige gastheer in Tokio!

Tot slot nog mijn familie, pap en mam, Anne en Jenny, superbedankt voor al jullie steun. Ik kon altijd bij jullie terecht en jullie interesse in mijn onderzoek was erg fijn. Zonder jullie zou deze dissertatie er niet zijn. And last but not least, Lan, thanks for always being there for me. Our weekends and longer periods together were the best parts of my PhD period, I can't express how much I'm looking forward to living together with you. I love you all!

Curriculum Vitae

Matti Pronker was born in Leiderdorp (the Netherlands) on the 15th of June, 1989. From 2007 to 2010, he studied chemistry at Utrecht University, for which the Bachelor of Science degree was awarded *cum laude* (GPA 4.0). He performed his Bachelor thesis in the Biomolecular Mass Spectrometry and Proteomics laboratory at Utrecht University under the supervision of Nikolai Mischerikow, Ph.D., and Shabaz Mohammed, Ph.D., studying lysine acetylation in *Saccharomyces Cerevisiae* by Gcn5. He subsequently completed a research master in the program Molecular and Cellular Life Sciences, also at Utrecht University, from 2010 to 2012. As part of his master program, he did a 9-month research internship in the Crystal and Structural Chemistry laboratory at Utrecht University under the supervision of Arjen Jakobi, Ph.D., and Eric Huizinga, Ph.D., studying the hemostatic protein von Willebrand Factor. He also did a 6-month research internship in the Department of Biochemistry, University of Cambridge, in the lab of Prof. Ernest Laue, Ph.D., investigating the structural mechanisms of replication-dependent chromatin assembly using nuclear magnetic resonance spectroscopy and other biophysical techniques. During his Master program, he completed the extracurricular honours program “Xtrack” and his degree was awarded *cum laude* (GPA 4.0). After obtaining his Master’s degree, he returned to the Crystal and Structural Chemistry laboratory in 2012 to work for his current supervisor and co-promotor Bert Janssen, Ph.D., the results of which are described in this thesis. In January 2017, he will start to work in the lab of Ingo Greger, Ph.D., in the Laboratory of Molecular Biology of the Medical Research Council (MRC-LMB), University of Cambridge, United Kingdom.

List of abbreviations

ADP:	Atomic displacement factor
AMIGO3:	Amphoterin-induced gene and open reading frame 3
AMPA:	α -amino-3-hydroxy-5-methyl-4-isoxazole propionic acid
APP:	Amyloid precursor protein
AUC:	Analytical ultracentrifugation
BSA:	Buried surface area
CNS:	Central nervous system
CSPG:	Chondroitin sulfate proteoglycan
DD:	Death domain
DLS:	Dynamic light scattering
DPC:	Dodecylphosphocholine
EM:	Electron microscopy
ET:	Electron tomography
FGF:	Fibroblast growth factor
GPI:	Glycophosphatidylinositol
HEPES:	4-(2-hydroxyethyl)-1-piperazineethanesulfonic acid
Ig:	Immunoglobulin
IMAC:	Immobilized metal affinity chromatography
L1CAM:	L1 cell adhesion molecule
LGI1:	Leucine-rich glioma inactivated 1
LOTUS:	Lateral olfactory tract usher substance
LRP1:	Low-density lipoprotein receptor-related protein-1
LINGO-1:	Leucine-rich repeat and immunoglobulin-like domain-containing Nogo receptor-interacting protein 1
LRP1:	Low density lipoprotein receptor-related protein 1
LRR:	Leucine-rich repeat
MAG:	Myelin-associated glycoprotein
MAI:	Myelin-associated inhibitor (of regeneration)
MALS:	Multi-angle light scattering
MWCO:	Molecular weight cut-off
NCAM:	Neuronal cell adhesion molecule
Nectl:	Nectin-like
NgR:	Nogo Receptor
NTT:	N-terminal tetramerization
Olf:	Olfactomedin
Olfm1:	Olfactomedin-1
OMgp:	Oligodendrocyte myelin glycoprotein

PBS:	Phosphate-buffered saline
PEG:	Polyethylene glycol
PirB:	Paired immunoglobulin receptor B
PNS:	Peripheral nervous system
RhoA:	Ras homolog gene family, member A
RhoGDI:	Rho GDP dissociation inhibitor
RhoGEF:	Rho GDP/GTP exchange factors
R.M.S.:	Root mean square
ROCK:	Rho-associated, coiled-coil-containing protein kinase
SAXS:	Small-angle X-ray scattering
SDS:	Sodium Dodecyl Sulfate
SDS-PAGE:	SDS Polyacrylamide gel electrophoresis
SE-AUC:	Sedimentation equilibrium analytical ultracentrifugation
SEC:	Size exclusion chromatography
SPR:	Surface plasmon resonance
SV-AUC:	Sedimentation velocity analytical ultracentrifugation
Tris:	Tris(hydroxymethyl)aminomethane
TSA:	Thermofluor stability assay
WNK1:	With no lysine 1
WT:	Wild type